

SYNTHESIS AND CHARACTERIZATION OF NEW LANTHANIDE
CHALCOGENIDES

Except where reference is made to the work of others, the work described in this dissertation is my own or was done in collaboration with my advisory committee. This dissertation does not include proprietary or classified information.

Geng Bang Jin

Certificate of Approval:

Thomas R. Webb
Associate Professor
Chemistry and Biochemistry

Thomas E. Albrecht-Schmitt, Chair
Professor
Chemistry and Biochemistry

Andreas J. Illies
Professor
Chemistry and Biochemistry

Peter D. Livant
Associate Professor
Chemistry and Biochemistry

Joe F. Pittman
Interim Dean
Graduate School

SYNTHESIS AND CHARACTERIZATION OF NEW LANTHANIDE
CHALCOGENIDES

Geng Bang Jin

A Dissertation

Submitted to

the Graduate Faculty of

Auburn University

in Partial Fulfillment of the

Requirements for the

Degree of

Doctor of Philosophy

Auburn, Alabama
August 4, 2007

SYNTHESIS AND CHARACTERIZATION OF NEW LANTHANIDE
CHALCOGENIDES

Geng Bang Jin

Permission is granted to Auburn University to make copies of this dissertation at its discretion, upon request of individuals or institutions and at their expense. The author reserves all publication rights.

Signature of Author

Date of Graduation

VITA

Geng Bang Jin, son of Biao Sheng Jin and Xian Xiang Jin, was born October 8, 1981, in Donyang, Zhejiang, China. He graduated from Donyang Second High School in 1999. He attended East China University of Science and Technology in Shanghai for four years, where he graduated in July of 2003, with a Bachelor of Science degree in Applied Chemistry. In August of 2003, he entered Graduate School at Auburn University pursuing a doctoral degree in Chemistry under the tutelage of Dr. Thomas E. Albrecht-Schmitt. He married Pan Chen, daughter of Wang Heng Chen and Xiao Xiang Li, on January 26, 2007.

DISSERTATION ABSTRACT
SYNTHESIS AND CHARACTERIZATION OF NEW LANTHANIDE
CHALCOGENIDES

Geng Bang Jin

Doctor of Philosophy, August 4, 2007
(B.S., East China University of Science and Technology, 2003)

299 Typed Pages

Directed by Thomas E. Albrecht-Schmitt

A large number of new ternary and quaternary lanthanide chalcogenides have been synthesized through solid-state reactions of corresponding elements with the aid of alkali metal halides and Sb_2Q_3 ($\text{Q} = \text{S}, \text{Se}$) fluxes. Molten Sb_2Q_3 ($\text{Q} = \text{S}, \text{Se}$) fluxes have been valuable media for accessing interlanthanide chalcogenides. The structures of these compounds were determined by single crystal X-ray diffraction. Their optical and magnetic properties were characterized by UV-vis-NIR diffuse reflectance spectroscopy, magnetic susceptibility measurements, and Mössbauer spectroscopy. Their structures and physical properties depend highly on the choices of lanthanides and chalcogenides. They have shown a variety of structures including ordered and disordered types under different reaction conditions. Most compounds are semiconductors with wide tunable

band gaps. Different magnetic behaviors have been found in these systems, namely Curie-Weiss type paramagnetism, van Vleck paramagnetism, antiferromagnetism, ferromagnetism, and spin glass performance. Possible spin-frustrations in some of these interlanthanide compounds were also discussed.

ACKNOWLEDGMENTS

There are a lot of people to whom I would like to express my sincere gratitude. I feel so lucky to have met you all during my four years in Auburn. First of all, I would like to thank my advisor, Professor Thomas E. Albrecht-Schmitt, without whom none of this would have been possible. Thank you for your support, your guidance, and most importantly, your friendship. You have been so much more than an advisor to me. Also, I want to thank my committee members, Dr. Illies, Dr. Webb, and Dr. Livant for the valuable suggestions they have provided.

I am also indebted to all my group members and collaborators. You have all been so nice to me and have shown great patience. I know I could be quite trying at times with my long list of questions. Tyler, Shehee, Daniel, and Phil, thank you for helping me get my research started when I first came to the lab. Ling Jie, Tanya, Noel, Yaqin, Anna, and Andrea, thank you for all of your support. Travis, I want to thank you most for what you have done outside of work. You have been so helpful for fixing my car, teaching me English, and helping me assimilate American culture...I would like to thank Dr. Choi and Dr. Booth for their substantial help in magnetic property measurements all along the way.

Finally, I would like to thank my family. Dad and Mom, thank you for being supportive of every choice I've made. Pan, your companionship and encouragement have helped me to keep doing my best in my studies and work.

Style manual or journal used:

American Chemical Society Style

Computer software used:

Microsoft Word 2000, Microsoft Excel, Atoms v.5.0, & 6.0, CorelDRAW 10, Microcal
Origin 6.0

TABLE OF CONTENTS

| | |
|--|------|
| LIST OF FIGURES | xvii |
| LIST OF TABLES | xxv |
| CHAPTER 1. INTRODUCTION | 1 |
| SOLID STATE SYNTHESIS | 3 |
| STRUCTURES | 7 |
| MAGNETIC PROPERTIES | 16 |
| OPTICAL PROPERTIES | 23 |
| REFERENCE | 28 |
| CHAPTER 2. SYNTHESIS, STRUCTURE, AND MAGNETIC PROPERTIES OF THE NONCENTROSYMMETRIC TERNARY RARE-EARTH ANTIMONY POLYSULFIDE $\text{Eu}_6\text{Sb}_6\text{S}_{17}$ | 34 |
| ABSTRACT | 34 |
| INTRODUCTION | 35 |
| EXPERIMENTAL | 36 |
| SYNTHESES | 36 |
| CRYSTALLOGRAPHIC STUDIES | 36 |
| MAGNETISM | 41 |
| RESULTS AND DISCUSSION | 41 |

| | |
|--|----|
| STRUCTURE | 41 |
| MAGNETIC SUSCEPTIBILITY | 43 |
| REFERENCES | 50 |
| CHAPTER 3. SYNTHESSES, STRUCTURES, AND MAGNETIC | |
| PROPERTIES OF THE EUROPIUM(II) SELENIDO PNICTOGENATES(III), | |
| EuPnSe ₃ (Pn = Sb, Bi) | 52 |
| ABSTRACT..... | 52 |
| INTRODUCTION | 53 |
| EXPERIMENTAL..... | 54 |
| SYNTHESSES | 54 |
| EuPnSe ₃ | 54 |
| CRYSTALLOGRAPHIC STUDIES | 55 |
| MAGNETISM | 56 |
| ¹⁵¹ Eu AND ¹²¹ Sb Mössbauer SPECTROSCOPY | 56 |
| RESULTS AND DISCUSSION | 56 |
| STRUCTURE of EuPnSe ₃ (Pn = Sb, Bi)..... | 56 |
| MAGNETIC SUSCEPTIBILITY | 68 |
| ¹⁵¹ Eu Mössbauer SPECTROSCOPY | 68 |
| ¹²¹ Sb Mössbauer SPECTROSCOPY | 72 |
| CONCLUSIONS..... | 73 |
| REFERENCES | 78 |
| CHAPTER 4. SYNTHESSES, STRUCTURE, MAGNETISM, AND OPTICAL | |
| PROPERTIES OF THE ORDERED MIXED-LANTHANIDE | |

| | |
|---|-----|
| SULFIDES, γ -LnLn'S ₃ (Ln = La, Ce; Ln' = Er, Tm, Yb)..... | 81 |
| ABSTRACT..... | 81 |
| INTRODUCTION | 82 |
| EXPERIMENTAL..... | 83 |
| MATERIALS..... | 83 |
| SYNTHESES of γ -LnLn'S ₃ (Ln = La, Ce; Ln' = Er, Tm, Yb)..... | 84 |
| CRYSTALLOGRAPHIC STUDIES | 84 |
| POWDER X-RAY DIFFRACTION | 85 |
| MAGNETIC SUSCEPTIBILITY MEASUREMENT | 88 |
| UV-vis-NIR DIFFUSE REFLECTANCE | |
| SPECTROSCOPY..... | 88 |
| RESULTS AND DISCUSSION | 88 |
| EFFECTS OF SYNTHETIC PARAMETERS ON | |
| PRODUCT COMPOSITION AND STRUCTURE..... | 88 |
| STRUCTURAL FEATURES OF | |
| γ -LnLn'S ₃ (Ln = La, Ce; Ln' = Er, Tm, Yb)..... | 91 |
| MAGNETIC PROPERTIES OF | |
| γ -LnLn'S ₃ (Ln = La, Ce; Ln' = Er, Tm, Yb)..... | 98 |
| OPTICAL PROPERTIES OF | |
| γ -LnLn'S ₃ (Ln = La, Ce; Ln' = Er, Tm, Yb)..... | 103 |
| CONCLUSIONS..... | 105 |
| REFERENCES | 109 |

CHAPTER 5. SYNTHESSES, STRUCTURE, MAGNETISM, AND

OPTICAL PROPERTIES OF THE INTERLANTHANIDE SULFIDES

| | |
|---|-----|
| δ -Ln _{2-x} Lu _x S ₃ (Ln = Ce, Pr, Nd)..... | 114 |
| ABSTRACT | 114 |
| INTRODUCTION | 115 |
| EXPERIMENTAL..... | 116 |
| STARTING MATERIALS | 116 |
| SYNTHESES OF δ -Ln _{2-x} Lu _x S ₃ (Ln = Ce, Pr, Nd)..... | 116 |
| CRYSTALLOGRAPHIC STUDIES | 117 |
| POWDER X-RAY DIFFRACTION | 123 |
| MAGNETIC SUSCEPTIBILITY MEASUREMENT | 123 |
| UV-vis-NIR DIFFUSE REFLECTANCE SPECTROSCOPY | 123 |
| RESULTS AND DISCUSSION | 124 |
| STRUCTURES OF δ -Ln _{2-x} Lu _x S ₃ (Ln = Ce, Pr, Nd)..... | 124 |
| MAGNETIC SUSCEPTIBILITY | 128 |
| OPTICAL PROPERTIES | 133 |
| CONCLUSIONS..... | 133 |
| REFERENCES | 136 |

CHAPTER 6. SYNTHESSES, STRUCTURE, MAGNETISM,

AND OPTICAL PROPERTIES OF LUTETIUM-BASED

| | |
|---------------------------------|-----|
| INTERLANTHANIDE SELENIDES | 138 |
| ABSTRACT..... | 138 |
| INTRODUCTION | 139 |
| EXPERIMENTAL..... | 140 |

| | |
|--|-----|
| STARTING MATERIALS | 140 |
| SYNTHESES | 140 |
| CRYSTALLOGRAPHIC STUDIES | 141 |
| POWDER X-RAY DIFFRACTION | 147 |
| MAGNETIC SUSCEPTIBILITY MEASUREMENT | 147 |
| UV-vis-NIR DIFFUSE REFLECTANCE SPECTROSCOPY | 147 |
| RESULTS AND DISCUSSION | 148 |
| SYNTHESIS OF Ln/Ln'/Q using Sb ₂ Q ₃ fluxes (Q = S, Se)..... | 148 |
| STRUCTURE OF Ln _x Lu _y Se _z (Ln = La, Ce, Pr, Nd, Sm, Gd)..... | 148 |
| MAGNETIC SUSCEPTIBILITY | 159 |
| OPTICAL PROPERTIES | 170 |
| CONCLUSIONS..... | 170 |
| REFERENCES | 173 |
| CHAPTER 7. SYNTHESSES, STRUCTURE, MAGNETISM, AND OPTICAL PROPERTIES OF THE PARTIALLY ORDERED QUATERNARY INTERLANTHANIDE SULFIDES PrLnYb ₂ S ₆ (Ln = Tb, Dy)..... | |
| ABSTRACT | 176 |
| INTRODUCTION | 177 |
| EXPERIMENTAL | 178 |
| STARTING MATERIALS | 178 |
| SYNTHESES | 178 |
| CRYSTALLOGRAPHIC STUDIES | 179 |
| POWDER X-RAY DIFFRACTION | 185 |

| | |
|---|-----|
| MAGNETIC SUSCEPTIBILITY MEASUREMENT | 185 |
| UV-vis-NIR DIFFUSE REFLECTANCE SPECTROSCOPY | 185 |
| RESULTS AND DISCUSSION | 185 |
| STRUCTURE OF PrLnYb ₂ S ₆ (Ln = Pr/Yb, Tb, Dy) | 185 |
| MAGNETIC SUSCEPTIBILITY | 187 |
| OPTICAL PROPERTIES | 194 |
| CONCLUSION | 194 |
| REFERENCES | 197 |
| | |
| CHAPTER 8. SYNTHESSES, STRUCTURE, MAGNETISM, AND OPTICAL PROPERTIES OF THE ORDERED INTERLANTHANIDE COPPER CHALCOGENIDES Ln ₂ YbCuQ ₅ (Ln = La, Ce, Pr, Nd, Sm; Q = S, Se) | 200 |
| ABSTRACT | 200 |
| INTRODUCTION | 201 |
| EXPERIMENTAL | 202 |
| STARTING MATERIALS | 202 |
| SYNTHESSES | 202 |
| CRYSTALLOGRAPHIC STUDIES | 203 |
| POWDER X-RAY DIFFRACTION | 204 |
| MAGNETIC SUSCEPTIBILITY MEASUREMENT. | 204 |
| UV-vis-NIR DIFFUSE REFLECTANCE SPECTROSCOPY | 207 |
| RESULTS AND DISCUSSION | 207 |
| STRUCTURE OF Ln ₂ YbCuQ ₅ (Ln = La, Ce, Pr, Nd, Sm; Q = S, Se) | 207 |

| | |
|---|-----|
| MAGNETIC SUSCEPTIBILITY | 217 |
| OPTICAL PROPERTIES | 217 |
| CONCLUSION | 224 |
| REFERENCES | 226 |
| CHAPTER 9. PARTIALLY-FILLED MIXED-LANTHANIDE VARIANTS | |
| OF THE $K_2Tm_{23.33}S_{36}$ STRUCTURE-TYPE: STRUCTURE AND PROPERTIES | |
| OF $Cs_xLn_yYbS_2$ ($x = 0.14 - 0.16$; $Ln = La-Nd, Sm-Yb$; $y = 0.26 - 0.33$)..... | 230 |
| ABSTRACT..... | 230 |
| INTRODUCTION | 231 |
| EXPERIMENTAL..... | 232 |
| STARTING MATERIALS | 232 |
| $Cs_{0.14-0.17}Ln_{0.26-0.33}YbS_2$ | |
| (Ln = La, Ce, Pr, Nd, Sm, Eu, Gd) | 233 |
| $Cs_{0.14-0.17}Ln_{0.26-0.33}YbS_2$ | |
| (Ln = Tb, Dy, Ho, Er, Tm, Yb)..... | 233 |
| CRYSTALLOGRAPHIC STUDIES | 234 |
| POWDER X-RAY DIFFRACTION | 235 |
| MAGNETISM | 235 |
| X-RAY ABSORPTION NEAR EDGE | |
| SPECTROSCOPY (XANES) | 239 |
| UV-vis-NIR DIFFUSE REFLECTANCE SPECTROSCOPY..... | 239 |
| RESULTS AND DISCUSSION | 239 |
| CRYSTAL STRUCTURES..... | 239 |

| | |
|---------------------------|-----|
| MAGNETIC PROPERTIES | 248 |
| XANES | 254 |
| OPTICAL PROPERTIES | 257 |
| CONCLUSION..... | 259 |
| REFERENCES | 260 |
| CHAPTER 10. SUMMARY..... | 266 |

LIST OF FIGURES

| | |
|--|----|
| Figure 1.1. Typical coordination geometries for lanthanides (green) bound to chalcogenides (yellow) | 10 |
| Figure 1.2. Common connectivities between coordination polyhedra of lanthanide (green) chalcogenides (yellow)..... | 11 |
| Figure 1.3. General building units for structures of lanthanide chalcogenides: one-dimensional chains of lanthanide coordination polyhedra..... | 12 |
| Figure 1.4. Connectivities between one-dimensional chains of lanthanide coordination polyhedra..... | 13 |
| Figure 1.5. A view of the two-dimensional structure of β -LaYbS ₃ along the <i>a</i> axis. La-S bonds have been omitted for clarity | 14 |
| Figure 1.6. An illustration of the three-dimensional channel structure of EuYb ₂ S ₄ down the <i>b</i> axis. Eu-S bonds have been omitted for clarity | 15 |
| Figure 1.7. Inverse molar magnetic susceptibility vs temperature for Gd _{1.87} Lu _{2.13} Se ₆ under an applied magnetic field of 0.1 T between 2 and 300 K..... | 20 |
| Figure 1.8. The temperature dependence of the reciprocal molar magnetic susceptibility for β -NdLuSe ₃ under an applied magnetic field of 0.1 T between 2 and 300 K..... | 21 |

| | |
|---|----|
| Figure 1.9. Inverse molar magnetic susceptibility as a function of temperature for $\text{Sm}_{1.82}\text{Lu}_{2.18}\text{Se}_6$ under an applied magnetic field of 0.1 T between 2 and 300 K..... | 22 |
| Figure 1.10. Variation of the band gap E_g of Ln_2Q_3 (Q = O, S, Se) in the lanthanide series: 1) oxides; 2) sulphides; 3) selenides | 26 |
| Figure 1.11. Variation of the dissociation (atomization) energy D of Ln_2O_3 in the lanthanide series..... | 27 |
| Figure 2.1. A view of the $[\text{Sb}_3\text{S}_7]^{5-}$ anions that consist of a trimer of corner-sharing SbS_3 units in $\text{Eu}_6\text{Sb}_6\text{S}_{17}$. 50% probability ellipsoids are depicted..... | 44 |
| Figure 2.2. A depiction of the local environments of the six crystallographically unique Eu^{2+} cations in $\text{Eu}_6\text{Sb}_6\text{S}_{17}$. 50% probability ellipsoids are depicted. | 47 |
| Figure 2.3. An illustration of the three-dimensional channel structure of $\text{Eu}_6\text{Sb}_6\text{S}_{17}$ viewed down the a axis. Eu–S bond have been omitted for clarity | 48 |
| Figure 2.4. Plots of dc magnetic susceptibility and its inverse for $\text{Eu}_6\text{Sb}_6\text{S}_{17}$. The straight line shows a fit of the inverse susceptibility to the Curie-Weiss law..... | 49 |
| Figure 3.1. Illustrations of the nine-coordinate tricapped trigonal prismatic environments around the Eu centers in EuSbSe_3 | 61 |
| Figure 3.2. A view of the one-dimensional rectangular columns formed from | |

| | |
|--|-----|
| Pn (Pn = Sb, Bi) and Se in EuPnSe ₃ | 66 |
| Figure 3.3. A depiction of the Pn/Se columns in EuPnSe ₃ (Pn = Sb, Bi) that are formed from two opposing nets of square pyramidal PnSe ₅ units that are linked by PnSe ₆ octahedra | 67 |
| Figure 3.4. Plots of dc magnetic susceptibility (●) and its inverse (χ) for EuSbSe ₃ | 69 |
| Figure 3.5. Plots of dc magnetic susceptibility (●) and its inverse (χ) for EuBiSe ₃ | 70 |
| Figure 3.6. Experimental and simulated ¹⁵¹ Eu Mössbauer spectra of EuSbSe ₃ at various temperatures | 75 |
| Figure 3.7. Experimental and simulated ¹⁵¹ Eu Mössbauer spectra of EuBiSe ₃ at various temperatures..... | 76 |
| Figure 3.8. Experimental and simulated ¹²¹ Sb Mössbauer spectrum of EuSbSe ₃ at 77 K..... | 77 |
| Figure 4.1. Views of the structures of a) α-LnLn'S ₃ , b) β-LnLn'S ₃ , and c) γ-LnLn'S ₃ (Ln = La, Ce; Ln' = Er, Tm, Yb)..... | 92 |
| Figure 4.2. A depiction of an individual ² / _∞ [Ln' ₃ S ₉] ⁹⁻ (Ln' = Er, Tm, Yb) layer viewed down the <i>a</i> axis in γ-LnLn'S ₃ (Ln = La, Ce; Ln' = Er, Tm, Yb) | 93 |
| Figure 4.3. Illustrations of the coordination environments for the larger lanthanides, La ³⁺ and Ce ³⁺ , in γ-LnLn'S ₃ (Ln = La, Ce; Ln' = Er, Tm, Yb) | 94 |
| Figure 4.4. Temperature dependence of the reciprocal molar magnetic susceptibility for γ-LnLn'S ₃ (Ln = La, Ce; Ln' = Er, Tm, Yb) under an applied magnetic field of 0.1 T | 100 |

| | |
|--|-----|
| Figure 4.5. a) A view of the layers in Sm-based triangles in β -SmYbSe ₃ . | |
| b) A depiction of the interconnection of the Sm layers by Yb ³⁺ ions..... | 101 |
| Figure 4.6. a) An illustration of the square and triangular networks in γ -CeYbS ₃ . | |
| b) A drawing of the complex three-dimension network in γ -CeYbS ₃ | 102 |
| Figure 4.7. UV-vis diffuse reflectance spectra of γ -LnLn'S ₃ | |
| (Ln = La, Ce; Ln' = Er, Tm, Yb)..... | 107 |
| Figure 5.1. A view down the <i>b</i> axis shows the complex three-dimensional | |
| structure of δ -Ce _{1.30} Lu _{0.70} S ₃ | 125 |
| Figure 5.2. A plot of inverse molar cerium magnetic susceptibility for | |
| δ -Ce _{1.30} Lu _{0.70} S ₃ between 2 and 300 K..... | 129 |
| Figure 5.3. Temperature dependence of the reciprocal molar praseodymium | |
| magnetic susceptibility for δ -Pr _{1.29} Lu _{0.71} S ₃ under an applied | |
| magnetic field of 0.1 T between 2 and 300 K..... | 130 |
| Figure 5.4. Inverse molar neodymium magnetic susceptibility vs. T | |
| for δ -Nd _{1.33} Lu _{0.67} S ₃ under an applied magnetic field of | |
| 0.1 T between 2 and 300 K..... | 131 |
| Figure 5.5. UV-vis diffuse reflectance spectra of δ -Ln _{2-x} Lu _x S ₃ | |
| (Ln = Ce, Pr, Nd; x = 0.67 – 0.71)..... | 135 |
| Figure 6.1. An illustration of the three-dimensional structure of La ₃ LuSe ₆ | |
| down the <i>c</i> axis..... | 151 |
| Figure 6.2. Unit cell of β -PrLuSe ₃ viewed along the <i>a</i> axis | 154 |
| Figure 6.3. A depiction of an individual LuSe ₆ octahedra layer viewed | |
| down the <i>b</i> axis in β -PrLuSe ₃ | 155 |

| | |
|--|-----|
| Figure 6.4. A view of the three-dimensional channel structure of $\text{Sm}_{1.82}\text{Lu}_{2.18}\text{Se}_6$ along the b axis..... | 156 |
| Figure 6.5. Illustrations of the coordination environments for Pr ions in $\beta\text{-PrLuSe}_3$ and Sm(1)/Lu(1) ions in $\text{Sm}_{1.82}\text{Lu}_{2.18}\text{Se}_6$ | 157 |
| Figure 6.6. The temperature dependence of the reciprocal molar magnetic susceptibility for $\beta\text{-PrLuSe}_3$ and $\beta\text{-NdLuSe}_3$, under an applied magnetic field of 0.1 T between 2 and 300 K..... | 161 |
| Figure 6.7. Molar magnetic susceptibility vs temperature between 2 and 300 K for $\text{Sm}_{1.82}\text{Lu}_{2.18}\text{Se}_6$ | 163 |
| Figure 6.8. Inverse molar magnetic susceptibility vs temperature for $\text{Gd}_{1.87}\text{Lu}_{2.13}\text{Se}_6$ under an applied magnetic field of 0.1 T between 2 and 300 K..... | 165 |
| Figure 6.9. The magnetization for $\text{Gd}_{1.87}\text{Lu}_{2.13}\text{Se}_6$ as a function of applied field at 2 K..... | 166 |
| Figure 6.10. Inverse molar magnetic susceptibility as a function of temperature for Ce_3LuSe_6 under an applied magnetic field of 0.1 T between 2 and 300 K..... | 167 |
| Figure 6.11. Molar magnetic susceptibility as a function of temperature for Ce_3LuSe_6 under ZFC and FC conditions with an applied magnetic field of 0.01 T between 2 and 25 K..... | 168 |
| Figure 6.12. The magnetization for Ce_3LuSe_6 as a function of applied field at 2 K..... | 169 |
| Figure 6.13. UV-vis diffuse reflectance spectra of $\text{Ln}_x\text{Lu}_y\text{Se}_z$ | |

| | |
|---|-----|
| (Ln = La, Ce, Pr, Nd, Sm, Gd)..... | 172 |
| Figure 7.1. An illustration of the three-dimensional structure of PrTbYb ₂ S ₆ along the <i>b</i> axis..... | 186 |
| Figure 7.2. Bicapped trigonal prismatic coordination environment of the Pr ions in PrTbYb ₂ S ₆ | 188 |
| Figure 7.3. Inverse molar magnetic susceptibility plotted against temperature between 2 and 300 K for Pr _{1.34} Yb _{2.66} S ₆ | 190 |
| Figure 7.4. The plot of the inverse molar magnetic susceptibility vs T for PrTbYb ₂ S ₆ under an applied magnetic field of 0.1 T between 2 and 300 K..... | 191 |
| Figure 7.5. The temperature dependence of the reciprocal molar magnetic susceptibility for PrDyYb ₂ S ₆ under an applied magnetic field of 0.1 T between 2 and 300 K..... | 192 |
| Figure 7.6. UV-vis diffuse reflectance spectra of PrLnYb ₂ S ₆ (Ln = Pr/Yb, Tb, Dy) | 196 |
| Figure 8.1. A view the three-dimensional structure of La ₂ YbCuS ₅ along the <i>b</i> axis. La-S bonds have been omitted for clarity..... | 208 |
| Figure 8.2. Illustrations of the coordination environments for La ions in La ₂ YbCuS ₅ | 209 |
| Figure 8.3. Illustrations of the coordination environments for Cu ions in La ₂ YbCuS ₅ | 210 |
| Figure 8.4. Depictions of various connectivities of [CuQ ₅] (Q = S, Se, Te) trigonal bipyramids in different compounds: a) La ₂ YbCuS ₅ ; b) Gd ₃ Cu ₂ Te ₇ ; c) Sm ₃ CuSe ₆ ; d) LaCu _{0.28} Te ₂ | 215 |

| | |
|---|-----|
| Figure 8.5. Unit cell of $\text{La}_3\text{CuO}_2\text{S}_3$ viewed along the b axis | 216 |
| Figure 8.6. Molar magnetic susceptibility vs temperature between 2 and 300 K for $\text{La}_2\text{YbCuS}_5$, $\text{Ce}_2\text{YbCuS}_5$, and $\text{Pr}_2\text{YbCuS}_5$ | 218 |
| Figure 8.7. The temperature dependence of the reciprocal molar magnetic susceptibility for $\text{Nd}_2\text{YbCuS}_5$ under an applied magnetic field of 0.1 T between 2 and 300 K | 219 |
| Figure 8.8. Molar magnetic susceptibility as a function of temperature for $\text{La}_2\text{YbCuSe}_5$ and $\text{Ce}_2\text{YbCuS}_5$ under an applied magnetic field of 0.1 T between 2 and 300 K..... | 220 |
| Figure 8.9. UV-vis diffuse reflectance spectra of $\text{Ln}_2\text{YbCuQ}_5$ (Ln = La, Ce, Pr, Nd, Sm; Q = S, Se) | 223 |
| Figure 9.1. A view down the c axis shows the three-dimensional channel structure of $\text{Cs}_{0.14}\text{La}_{0.30}\text{YbS}_2$ | 240 |
| Figure 9.2. a) A polyhedral representation of EuYb_2S_4 structure projected along the b axis; b) A polyhedral view of $\text{Cs}_{0.14}\text{La}_{0.30}\text{YbS}_2$ structure projected along the c axis. S(3) atoms have been removed for clarity | 242 |
| Figure 9.3. Depictions of the CsS_9 and LaS_9 tricapped trigonal prismatic geometries in $\text{Cs}_{0.14}\text{La}_{0.30}\text{YbS}_2$ and distorted EuS_9 tricapped trigonal prismatic environment in $\text{Cs}_{0.16}\text{Eu}_{0.33}\text{YbS}_2$ | 243 |
| Figure 9.4. Unit cell volumes (\AA^3) and Yb~Yb distances (\AA) vs the number of f electrons for $\text{Cs}_{0.14-0.17}\text{Ln}_{0.26-0.33}\text{YbS}_2$ (Ln = La, Ce, Pr, Nd, Sm, Eu, Gd, Tb, Dy, Ho, Er, Tm)..... | 247 |
| Figure 9.5. a) An illustration of the Yb^{3+} cations network along the b axis | |

| | |
|---|-----|
| with Yb-Yb distances labeled for EuYb_2S_4 . b) An drawing of the Yb^{3+} cations network along the c axis with Yb-Yb distances labeled for $\text{Cs}_{0.14}\text{La}_{0.30}\text{YbS}_2$ | 249 |
| Figure 9.6. a) Plots of dc inverse molar magnetic susceptibility for $\text{Cs}_{0.14-0.17}\text{Ln}_{0.26-0.33}\text{YbS}_2$ (Ln = La, Ce, Pr, Nd, Sm, Gd, Tb) under an applied field of 0.5 T | 251 |
| Figure 9.6. b) Plots of dc inverse molar magnetic susceptibility for $\text{Cs}_{0.14-0.17}\text{Ln}_{0.26-0.33}\text{YbS}_2$ (Ln = Dy, Ho, Er, Tm, Yb) under an applied field of 0.5 T | 252 |
| Figure 9.7. Ce, Nd, and Sm L_{III} edge x-ray absorption spectra of (a) $\text{Cs}_{0.14}\text{Ce}_{0.30}\text{YbS}_2$, (b) $\text{Cs}_{0.14}\text{Nd}_{0.29}\text{YbS}_2$, and (c) $\text{Cs}_{0.15}\text{Sm}_{0.29}\text{YbS}_2$, respectively | 255 |
| Figure 9.8. (a) Yb L_{III} edge spectra of the same samples in Fig. 7, and (b) the derivative of these spectra | 256 |
| Figure 9.9. UV-vis diffuse reflectance spectra of $\text{Cs}_{0.14-0.17}\text{Ln}_{0.26-0.33}\text{YbS}_2$ (Ln = La, Ce, Pr, Nd, Sm, Gd, Tb, Dy, Ho, Er, Tm) | 258 |

LIST OF TABLES

| | |
|--|----|
| Table 1.1. The ground-state electron configurations and radius of the lanthanides | 2 |
| Table 1.2. Melting points (°C) of common fluxes used in solid state reactions | 6 |
| Table 1.3. Crystal structures of Ln ₂ S ₃ . α : orthorhombic Gd ₂ S ₃ -type; β : tetragonal Pr ₁₀ S ₁₄ O-type; γ : cubic Th ₃ P ₄ -type; δ : monoclinic Er ₂ S ₃ -type; ϵ : rhombohedral Al ₂ O ₃ -type; τ : cubic Tl ₂ O ₃ -type | 9 |
| Table 1.4. Calculated and measured effective magnetic moments (μ) for the trivalent lanthanide ions | 17 |
| Table 2.1. Crystallographic data for Eu ₆ Sb ₆ S ₁₇ | 38 |
| Table 2.2. Atomic Coordinates and Equivalent Isotropic Displacement Parameters for Eu ₆ Sb ₆ S ₁₇ | 39 |
| Table 2.3. Eu–S, Sb–S, and S–S Bond Distances (Å) for Eu ₆ Sb ₆ S ₁₇ | 45 |
| Table 3.1. Crystallographic Data for EuSbSe ₃ and EuBiSe ₃ | 57 |
| Table 3.2. Atomic Coordinates and Equivalent Isotropic Displacement Parameters for EuSbSe ₃ | 58 |
| Table 3.3. Atomic Coordinates and Equivalent Isotropic Displacement Parameters for EuBiSe ₃ | 59 |
| Table 3.4. Selected Bond Distances (Å) for EuSbSe ₃ | 62 |

| | |
|--|-----|
| Table 3.5. Selected Bond Distances (Å) for EuBiSe ₃ | 64 |
| Table 3.6. Fitting parameters of ¹⁵¹ Eu Mössbauer measurements of EuBiSe ₃ and EuSbSe ₃ | 74 |
| Table 4.1. Crystallographic Data for γ-LnLn'S ₃ (Ln = La, Ce; Ln' = Er, Tm, Yb)..... | 86 |
| Table 4.2. Atomic Coordinates and Equivalent Isotropic Displacement Parameters for γ-LaYbS ₃ | 87 |
| Table 4.3. Selected Bond Distances (Å) for γ-LnLn'S ₃ (Ln = La, Ce; Ln' = Er, Tm, Yb)..... | 96 |
| Table 4.4. Comparisons of Ternary Interlanthanide Sesquichalcogenides that Form in a Sb ₂ Q ₃ (Q = S, Se) Flux at 1000 °C | 108 |
| Table 5.1. Crystallographic Data for δ-Ln _{2-x} Lu _x S ₃ (Ln = Ce, Pr, Nd; x = 0.67 – 0.71)..... | 118 |
| Table 5.2. Atomic Coordinates and Equivalent Isotropic Displacement Parameters for δ-Ce _{1.30} Lu _{0.70} S ₃ | 119 |
| Table 5.3. Atomic Coordinates and Equivalent Isotropic Displacement Parameters for δ-Pr _{1.29} Lu _{0.71} S ₃ | 120 |
| Table 5.4. Atomic Coordinates and Equivalent Isotropic Displacement Parameters for δ-Nd _{1.33} Lu _{0.67} S ₃ | 121 |
| Table 5.5. Selected Bond Distances (Å) for δ-Ln _{2-x} Lu _x S ₃ (Ln = Ce, Pr, Nd; x = 0.67 – 0.71)..... | 126 |
| Table 5.6. Magnetic Parameters for δ-Ln _{2-x} Lu _x S ₃ (Ln = Ce, Pr, Nd; x = 0.67 – 0.71)..... | 132 |
| Table 6.1. Crystallographic Data for Ln _x Lu _y Se _z (Ln = La, Ce, Pr, Nd, Sm, Gd)..... | 143 |

| | |
|--|-----|
| Table 6.2. Atomic Coordinates and Equivalent Isotropic Displacement | |
| Parameters for La_3LuSe_6 | 144 |
| Table 6.3. Atomic Coordinates and Equivalent Isotropic Displacement | |
| Parameters for $\beta\text{-PrLuSe}_3$ | 145 |
| Table 6.4. Atomic Coordinates and Equivalent Isotropic Displacement | |
| Parameters for $\text{Sm}_{1.82}\text{Lu}_{2.18}\text{Se}_6$ | 146 |
| Table 6.5. Ternary Interlanthanide Sulfides Prepared Using Sb_2S_3 Flux | |
| at 1000 °C. | 149 |
| Table 6.6. Ternary Interlanthanide Selenides Prepared Using Sb_2Se_3 Flux | |
| at 1000 °C. | 150 |
| Table 6.7. Selected Bond Distances (Å) for Ln_3LuSe_6 (Ln = La, Ce)..... | 153 |
| Table 6.8. Selected Bond Distances (Å) for $\beta\text{-LnLuSe}_3$ (Ln = Pr, Nd)..... | 158 |
| Table 6.9. Selected Bond Distances (Å) for $\text{Ln}_x\text{Lu}_{4-x}\text{Se}_6$ | |
| (Ln = Sm, Gd; x = 1.82, 1.87)..... | 160 |
| Table 6.10. Magnetic Parameters for Ce_3LuSe_6 , $\beta\text{-PrLuSe}_3$, $\beta\text{-NdLuSe}_3$, | |
| and $\text{Gd}_{1.87}\text{Lu}_{2.13}\text{Se}_6$ | 162 |
| Table 7.1. Crystallographic Data for $\text{PrLnYb}_2\text{S}_6$ (Ln = Pr/Yb, Tb, Dy)..... | 181 |
| Table 7.2. Atomic Coordinates and Equivalent Isotropic Displacement | |
| Parameters for $\text{Pr}_{1.34}\text{Yb}_{2.66}\text{S}_6$ | 182 |
| Table 7.3. Atomic Coordinates and Equivalent Isotropic Displacement | |
| Parameters for $\text{PrTbYb}_2\text{S}_6$ | 183 |
| Table 7.4. Atomic Coordinates and Equivalent Isotropic Displacement | |
| Parameters for $\text{PrDyYb}_2\text{S}_6$ | 184 |

| | |
|---|-----|
| Table 7.5. Selected Bond Distances (Å) for PrLnYb ₂ S ₆ (Ln = Pr/Yb, Tb, Dy) | 189 |
| Table 7.6. Magnetic Parameters for PrLnYb ₂ S ₆ (Ln = Pr/Yb, Tb, Dy)..... | 193 |
| Table 8.1. Crystallographic Data for Ln ₂ YbCuQ ₅ (Ln = La, Ce, Pr, Nd, Sm; Q = S, Se) | 205 |
| Table 8.2. Atomic Coordinates and Equivalent Isotropic Displacement Parameters for La ₂ YbCuS ₅ | 206 |
| Table 8.3. Selected Bond Distances (Å) and Angles (deg) for Ln ₂ YbCuQ ₅ (Ln = La, Ce, Pr, Nd, Sm; Q = S, Se) | 211 |
| Table 8.4. Magnetic Parameters for Ln ₂ YbCuQ ₅ (Ln = La, Ce, Pr, Nd, Sm; Q = S, Se) | 221 |
| Table 9.1. a. Crystallographic Data for Cs _{0.14-0.17} Ln _{0.26-0.33} YbS ₂ (Ln = La, Ce, Pr, Nd, Sm, Eu, Gd) | 236 |
| b. Crystallographic Data for Cs _{0.14-0.17} Ln _{0.26-0.33} YbS ₂ (Ln = Tb, Dy, Ho, Er, Tm, Yb)..... | 237 |
| Table 9.2. Positional and Thermal parameters for Cs _{0.14} La _{0.30} YbS ₂ and Cs _{0.16} Eu _{0.33} YbS ₂ | 238 |
| Table 9.3. a. Selected Bond Distances (Å) for Cs _{0.14-0.17} Ln _{0.26-0.33} YbS ₂ (Ln = La, Ce, Pr, Nd, Sm, Eu, Gd) | 244 |
| b. Selected Bond Distances (Å) for Cs _{0.14-0.17} Ln _{0.26-0.33} YbS ₂ (Ln = Tb, Dy, Ho, Er, Tm, Yb)..... | 245 |
| Table 9.4. Magnetic Parameters for Cs _{0.14-0.17} Ln _{0.26-0.33} YbS ₂ (Ln = La, Ce, Pr, Nd, Sm, Gd, Tb, Dy, Ho, Er, Tm, Yb) | 253 |
| Table 10.1 A list of new compounds and some of their properties, contained in this | |

dissertation267

CHAPTER 1

INTRODUCTION

Lanthanide chalcogenides have been the focus of intense interest not only because of their remarkably complex structures,¹ but also because of the variety of physical properties that they exhibit including tunable band gaps,²⁻¹³ atypical magnetism,¹⁴⁻²⁰ superconductivity,²¹⁻²⁵ charge-density waves,²⁶⁻²⁹ and thermoelectricity.^{30,31}

The most striking fact about lanthanide chemistry is the extraordinary homogeneity in properties of all the elements across the series. This arises because the 4f shell of electrons is being filled along the lanthanide series, while the number of outer valence electrons remains unchanged. The 4f atomic orbitals are deeply buried and thus play a small role in chemical bonding. The ionization beyond the Ln^{3+} ion is usually not energetically favorable leading to the characteristic trivalent state across the whole series. As shown in Table 1.1, the electronic configurations for trivalent lanthanides are $4f^n$, where n goes from 0 to 14, regardless of which configuration, $4f^n 5d 6s^2$ or $4f^{n+1} 6s^2$, is the ground state of the neutral atom. The trivalent lanthanides show a general decrease of ionic radius along the series of elements La-Lu. This is usually referred to as lanthanide contraction and is due to the imperfect shielding of one electron by another in the same sub-shell.

Three configurations for trivalent lanthanides are especially stable. The first and most stable is that of La^{3+} with its unfilled 4f orbitals and a 1S ground state. The second

Table 1.1. The ground-state electron configurations and radii of the lanthanides.

| Element | | Electronic configuration | | | Radius/Å | |
|---------|--------------|--|----------------------|----------------------|----------|------------------|
| | | Ln | Ln ²⁺ | Ln ³⁺ | Ln | Ln ³⁺ |
| La | lanthanum | [Xe]6s ² 5d ¹ | | [Xe] 4f ⁰ | 1.88 | 1.16 |
| Ce | cerium | [Xe]4f ¹ 6s ² 5d ¹ | | [Xe]4f ¹ | 1.83 | 1.14 |
| Pr | praseodymium | [Xe]4f ³ 6s ² | | [Xe]4f ² | 1.82 | 1.13 |
| Nd | neodymium | [Xe]4f ⁴ 6s ² | | [Xe]4f ³ | 1.81 | 1.11 |
| Pm | promethium | [Xe]4f ⁵ 6s ² | | [Xe]4f ⁴ | 1.81 | 1.09 |
| Sm | samarium | [Xe]4f ⁶ 6s ² | [Xe]4f ⁶ | [Xe]4f ⁵ | 1.80 | 1.08 |
| Eu | europium | [Xe]4f ⁷ 6s ² | [Xe]4f ⁷ | [Xe]4f ⁶ | 1.99 | 1.07 |
| Gd | gadolinium | [Xe]4f ⁷ 6s ² 5d ¹ | | [Xe]4f ⁷ | 1.80 | 1.05 |
| Tb | terbium | [Xe]4f ⁹ 6s ² | | [Xe]4f ⁸ | 1.78 | 1.04 |
| Dy | dysprosium | [Xe]4f ¹⁰ 6s ² | | [Xe]4f ⁹ | 1.77 | 1.03 |
| Ho | holmium | [Xe]4f ¹¹ 6s ² | | [Xe]4f ¹⁰ | 1.76 | 1.02 |
| Er | erbium | [Xe]4f ¹² 6s ² | | [Xe]4f ¹¹ | 1.75 | 1.00 |
| Tm | thulium | [Xe]4f ¹³ 6s ² | [Xe]4f ¹³ | [Xe]4f ¹² | 1.74 | 0.99 |
| Yb | ytterbium | [Xe]4f ¹⁴ 6s ² | [Xe]4f ¹⁴ | [Xe]4f ¹³ | 1.94 | 0.99 |
| Lu | lutetium | [Xe]4f ¹⁴ 6s ² 5d ¹ | | [Xe]4f ¹⁴ | 1.73 | 0.98 |

stable electronic arrangement is that of Gd^{3+} with the 4f shell half filled ($4f^7$). According to Hund's rule this arrangement has the maximum multiplicity possible ($2S + 1 = 8$) and must consequently be an S state ($L = 0$) through the Pauli Exclusion Principle. The third is that of Lu^{3+} with a completed 4f shell and as a consequence, also a 1S state.

It has been known for some time that an oxidation state other than trivalent is possible for many rare earths. Because of the stability of full and half-filled shells, Yb and Eu might appear in the divalent form while Ce and Tb may be quadrivalent as well. Samarium would be expected to have a less stable divalent state than Eu.

In the chalcogenides, no tetravalent lanthanide has been observed owing to the low electronegativity of the anions. In contrast, the divalent state can be stabilized for the same reason. For example, in case of europium, for which the regular oxide is $Eu_2(III)O_3$, the corresponding $Eu_2(III)S_3$ does not exist. Instead, $Eu(II)S$ can be easily obtained.^{32,33} However, mixed-valent europium ions were found in some chalcogenides, especially in ternary phases including Eu_2BiSe_4 ,³⁴ Eu_2CuS_3 ,^{35,36} $EuPd_3S_4$,³⁷ $Eu_5Sn_3S_{12}$,³⁸ and $Eu_4Sn_2S_9$.³⁹

With ytterbium, a similar behavior is observed, but with a greater stability of the trivalent state. The ubiquitous sulfide is $Yb_2(III)S_3$,⁴⁰ but it is easily dissociated by heat into mixed-valent Yb_3S_4 .⁴¹ Ytterbium selenide is also stable in the form of Yb_3Se_4 ,⁴² while only one binary telluride is known, $Yb(II)Te$.⁴³

SOLID STATE SYNTHESIS

Lanthanide chalcogenides have been synthesized through a variety of solid state synthetic methods. Because the starting materials are usually solids, classical solid-state

synthesis requires high-temperature ($> 600\text{ }^{\circ}\text{C}$) to cause sufficient diffusion for a reaction to occur. As a result of the high reaction temperatures, thermodynamically stable products are generally formed. These products are usually the simplest binary or ternary compounds with high lattice stability. They become synthetic road blocks that are hard to avoid. Furthermore, the high temperature reactions only involve building blocks on the atomic level. Molecules, as starting materials, will be reduced back to atoms at high temperature. Therefore, solid-state synthesis has much less predictability than other areas of chemical synthesis.

There have been many attempts to develop methodology that allow for greater diffusion of reactants and lower reaction temperatures to circumvent thermodynamic traps. Solid state reactions performed at low temperatures are able to produce new kinetically stable compounds and can also employ molecular assemblies as building blocks to incorporate into solid state structures.

Hydro(solvo)thermal synthesis⁴⁴ and chemical vapor deposition (CVD)⁴⁵ are two major synthetic methods that are performed at low temperatures. The hydro(solvo)thermal synthesis employs various solvents under high pressure that enhance the solubility of the reactants in the reaction matrix. The reaction temperatures are usually between the boiling temperature and the critical point of solvents. Polyatomic species can be used as building units for reaction products. The solubility and the diffusion of reactants can be further improved by adding mineralizers or using supercritical solvents.⁴⁶ CVD is commonly used to synthesize known solid-state compounds as thin film. The chemical process involves the intimate gas-phase mixing of

volatile precursors leading, upon pyrolysis, to deposition of solid state intermetallic materials on various substrates. Therefore, CVD is limited to using elemental reactants.

Molten salts can also be used as solvents to increase the diffusion of reactants and lower the reaction temperature.⁴⁷ Compared to CVD and hydro(solvo)thermal techniques, reactions using molten salts are easier to conduct. Most salts are soluble in many common polar solvents. This allows for easy isolation of products since excess flux can simply be washed away. One group of low-melting salts that have been rapidly developed over the last twenty years is the alkali metal polychalcogenides, A_2Q_x (A = alkali metal; Q = chalcogenide).^{48,49} They are usually referred to as reactive fluxes owing to their high reactivity with reactants. The low melting points of A_2Q_x fluxes have led to the isolation of many new kinetically stable multinary polychalcogenides. Another class of well-known fluxes that have been employed for over 100 years for high-temperature single-crystal growth is alkali metal halides.⁴⁷ Although many halides are high-melting species, as shown in Table 1.2, eutectic combinations of different salts often have melting points well below the temperatures of classical solid-state synthesis, making possible their use in the exploration of new chemistry at intermediate temperatures. In some cases, alkali metal halides act not only as solvents, but also as reactants, providing species that can be incorporated into the final product.

A method of using Sb_2Q_3 ($Q = S, Se$) fluxes has been developed in our group to prepare interlanthanide chalcogenides.⁵⁰ The desired products can be separated from the flux during the cooling process by slightly tilting the furnace, which allows the flux to flow to the bottom of the tubes leaving crystals behind, minimizing the need for manual separation of solids. Molten Sb_2Q_3 ($Q = S, Se$) fluxes turn out to be valuable media to

Table 1.2. Melting points (°C) of common fluxes used in solid state reactions.

| Flux | Melting points | Flux | Melting points | Flux | Melting points |
|---------------------------------|----------------|------|----------------|---------------------------------|----------------|
| Na ₂ S ₂ | 490 | LiCl | 605 | RbI | 647 |
| Na ₂ S ₃ | 228.8 | NaCl | 801 | CsCl | 646 |
| Na ₂ Se ₂ | 495 | NaBr | 747 | CsBr | 636 |
| K ₂ S ₂ | 470 | KCl | 773 | CsI | 626 |
| K ₂ S ₄ | 145 | KBr | 743 | SrCl ₂ | 873 |
| K ₂ Se ₂ | 460 | KI | 681 | BaCl ₂ | 963 |
| Rb ₂ S | 530 | RbCl | 718 | Sb ₂ S ₃ | 550 |
| Rb ₂ S ₄ | 160 | RbBr | 693 | Sb ₂ Se ₃ | 611 |

access ternary and quaternary interlanthanide chalcogenides. Eight different structure types and more than fifty compounds have been identified for ternary interlanthanide chalcogenides prepared by employing these fluxes. The limitations of using Sb_2Q_3 (Q = S, Se) fluxes to prepare $\text{LnLn}'\text{Q}$ include: 1) Attempts to make interlanthanide tellurides have not succeeded; 2) It is difficult to get high yield and high-quality single crystals when the ionic radii of the two Ln^{3+} ions approach equality; 3) Occasionally, distinguishing and separating products from Sb_2Q_3 (Q = S, Se) fluxes proves tricky.

STRUCTURES

Lanthanide chalcogenides exhibit a large number of crystal structure types that are related to the variety of coordination environments of lanthanide ions and diverse connectivities between these coordination polyhedra.¹ The structural complexity of lanthanide chalcogenides can be exemplified by simple binary sesquisulfides, which are found in at least six different modifications, as shown in Table 1.3. These include orthorhombic Gd_2S_3 -type (α),⁵¹ tetragonal $\text{Pr}_{10}\text{S}_{14}\text{O}$ -type (β),⁵²⁻⁵⁵ cubic Th_3P_4 -type (γ),⁵⁶ monoclinic Er_2S_3 -type (δ),^{40,57-59} rhombohedral Al_2O_3 -type (ϵ),^{40,60,61} and cubic Tl_2O_3 -type (τ).⁶²⁻⁶⁴

Figure 1.1 presents the common coordination environments for lanthanides found in lanthanide chalcogenides with coordination number ranging from 6 to 9. Coordination polyhedra for smaller lanthanide ions, e.g. monocapped trigonal prismatic or octahedral Yb^{3+} , have lower coordination number and are usually edge-sharing or corner-sharing with neighbors. In contrast, larger ions prefer higher coordination

numbers, and their coordination polyhedra, such as bicapped or tricapped trigonal prisms, can even share faces with each other (Figure 1.2).

Most structures for lanthanide chalcogenides, except cubic phases, are constructed from one-dimensional chains of lanthanide coordination polyhedra along the crystal growth axis. As shown in Figure 1.3, small polyhedra are usually edge-sharing and large polyhedra are face-sharing down the chain-propagation direction. The polyhedra can share corners or edges with each other to form two-dimensional or three-dimensional structures (Figure 1.4). Figures 1.5 and 1.6 illustrate the two-dimensional layer structure of β -LaYbS₃^{65,66} and three-dimensional channel structure of EuYb₂S₄.^{67,68} The structure of β -LaYbS₃ includes YbS₆ octahedra layers that alternate with layers of LaS₈ bicapped trigonal prisms along the *b* axis. The YbS₆ octahedra are edge-sharing down the *a* axis to form one-dimensional chains that are corner-sharing along the *c* axis. The La-based layers consist of face-sharing one-dimensional chains of LaS₈ bicapped trigonal prisms that share edges with identical neighbors. The structure of EuYb₂S₄ is constructed from two different edge-shared double rutile chains of YbS₆ octahedra along the *b* axis. Each double chain is joined at the vertices to four other chains to form open channels of capped trigonal prismatic sites wherein Eu²⁺ ions reside.

The introduction of other metal ions into the lanthanide chalcogenide system may result in even more complex structures. D-block and main-group metals normally have smaller radii than lanthanides ions, and therefore lower coordination numbers. Typical coordination environments include trigonal planar, tetrahedral, and octahedral moieties. In contrast, alkali metals and alkaline-earth metals are more loosely bound to chalcogenides and have higher coordination numbers. Because of their distinct oxidation

Table 1.3. Crystal structures of Ln_2S_3 . α : orthorhombic Gd_2S_3 -type; β : tetragonal $\text{Pr}_{10}\text{S}_{14}\text{O}$ -type; γ : cubic Th_3P_4 -type; δ : monoclinic Er_2S_3 -type; ε : rhombohedral Al_2O_3 -type; τ : cubic Tl_2O_3 -type.

| La | Ce | Pr | Nd | Sm | Eu | Gd | Tb | Dy | Ho | Er | Tm | Yb | Lu |
|----------|----|----|----|----|----|----|----|----|----------|----|---------------|----|----|
| α | | | | | | | | | | | | | |
| β | | | | | | | | | | | | | |
| γ | | | | | | | | | | | | | |
| | | | | | | | | | δ | | | | |
| | | | | | | | | | | | ε | | |
| | | | | | | | | | | | τ | | |

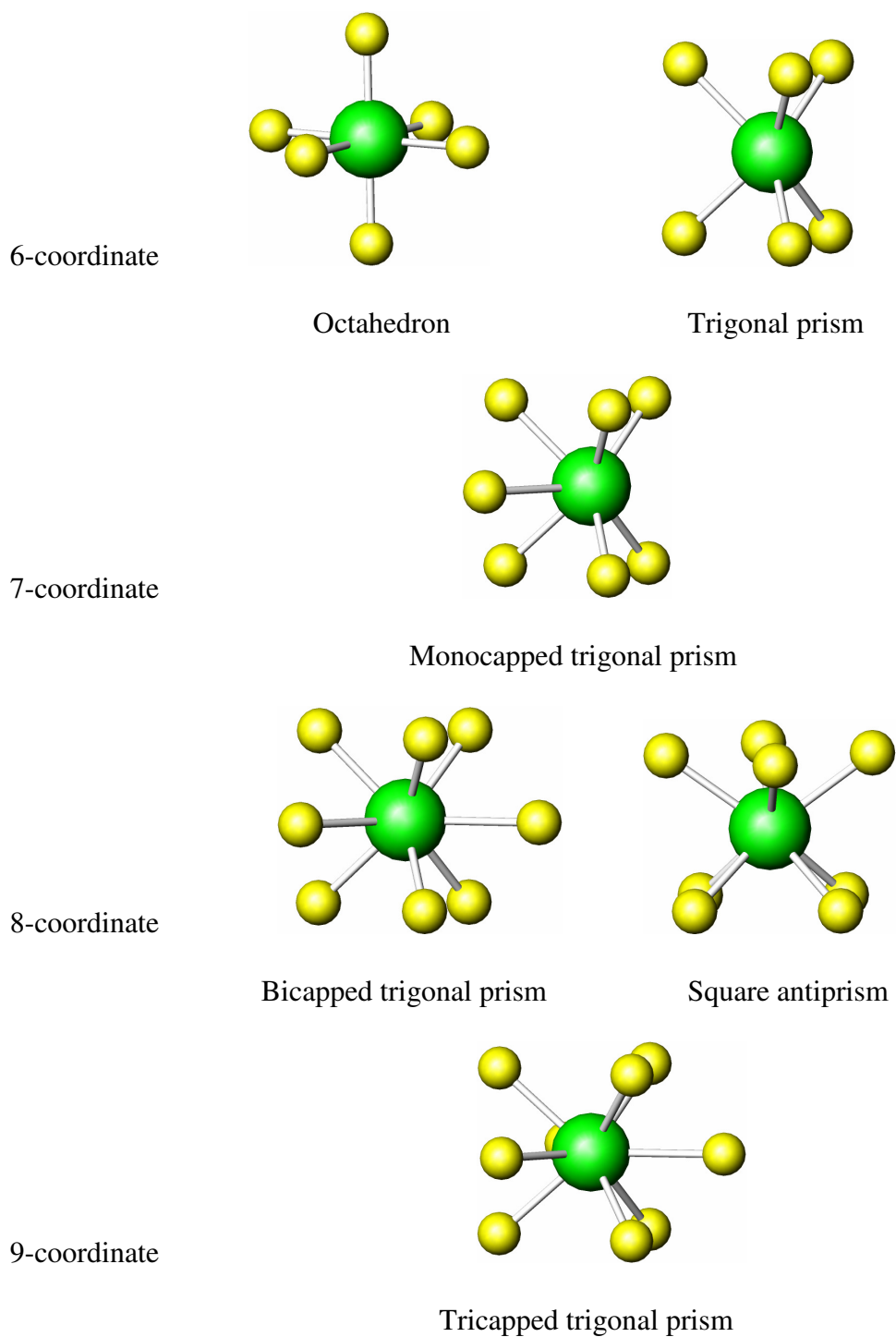
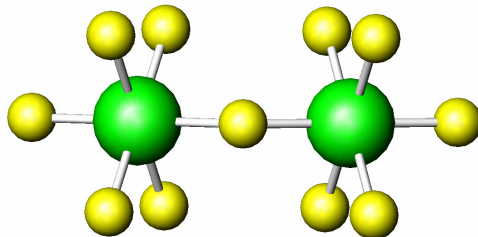
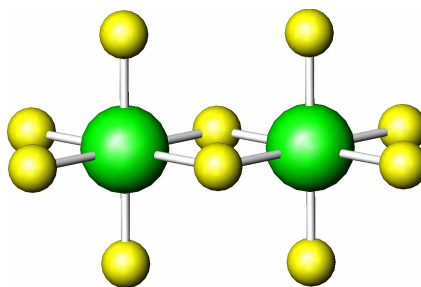


Figure 1.1. Typical coordination geometries for lanthanides (green) bound to chalcogenides (yellow).

Corner-sharing



Edge-sharing



Face-sharing

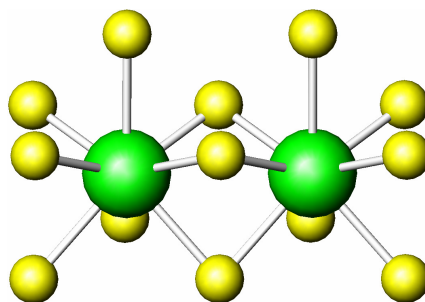
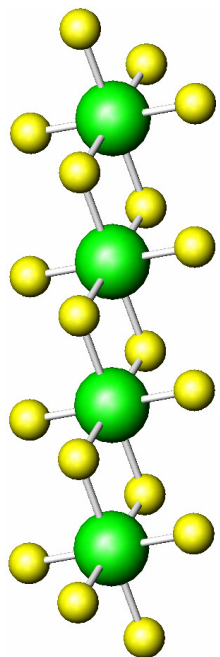
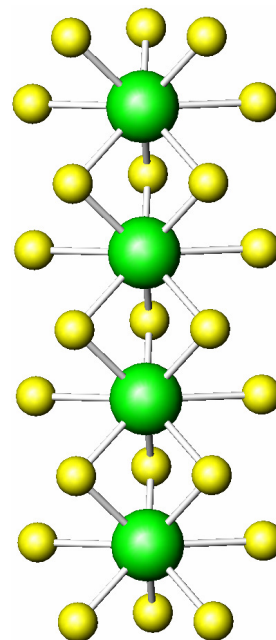


Figure 1.2. Common connectivities between coordination polyhedra of lanthanide (green) chalcogenides (yellow).

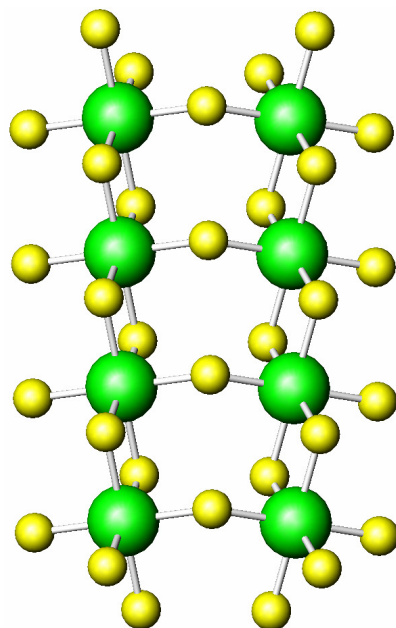


Edge-sharing octahedral chain

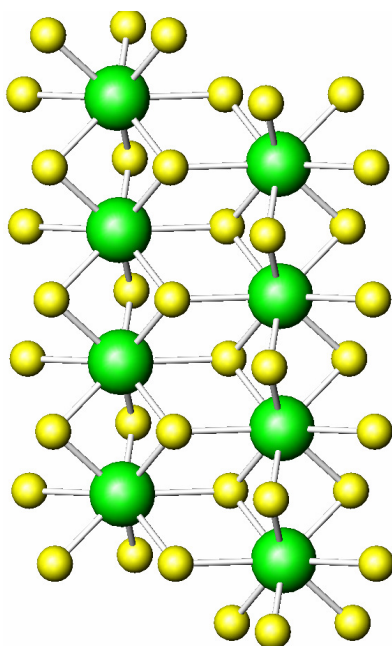


Face-sharing bicapped trigonal prismatic chain.

Figure 1.3. General building units for structures of lanthanides chalcogenide: one-dimensional chains of lanthanide coordination polyhedra.



Corner-sharing between one-dimensional octahedral chains



Face-sharing between one-dimensional bicapped trigonal prismatic chains

Figure 1.4. Connectivities between one-dimensional chains of lanthanide coordination polyhedra.

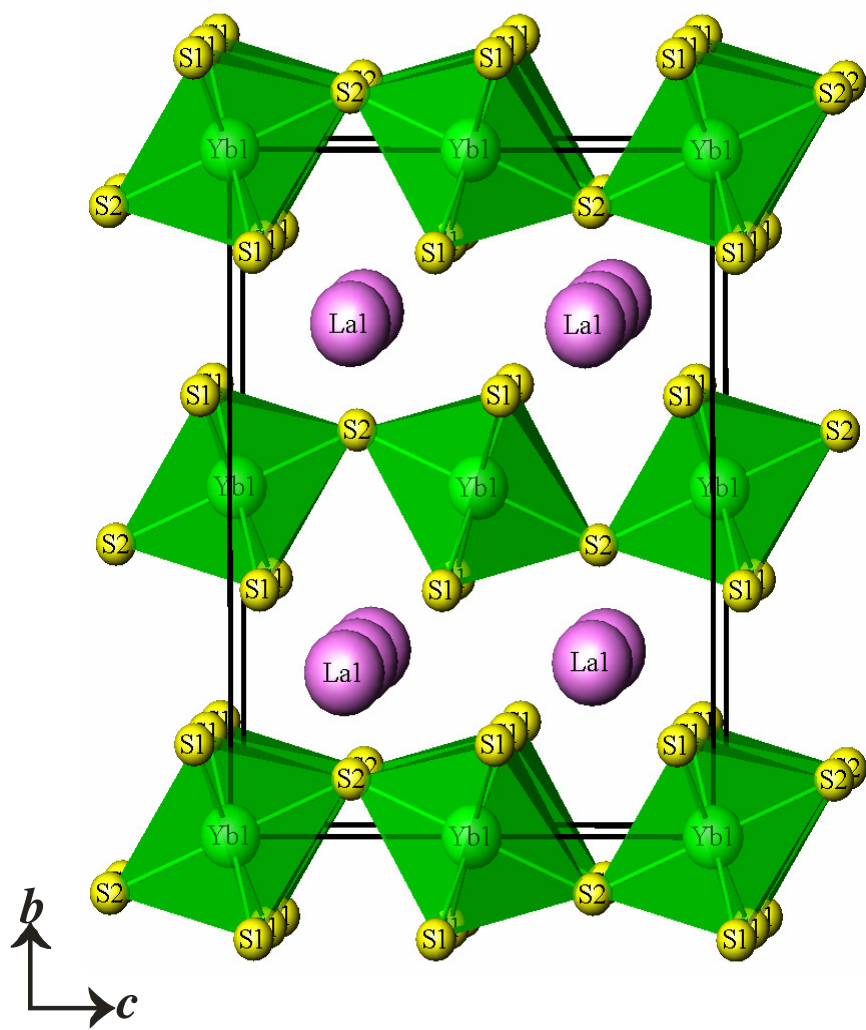


Figure 1.5. A view of the two-dimensional structure of β -LaYbS₃ along the a axis. La-S bonds have been omitted for clarity.

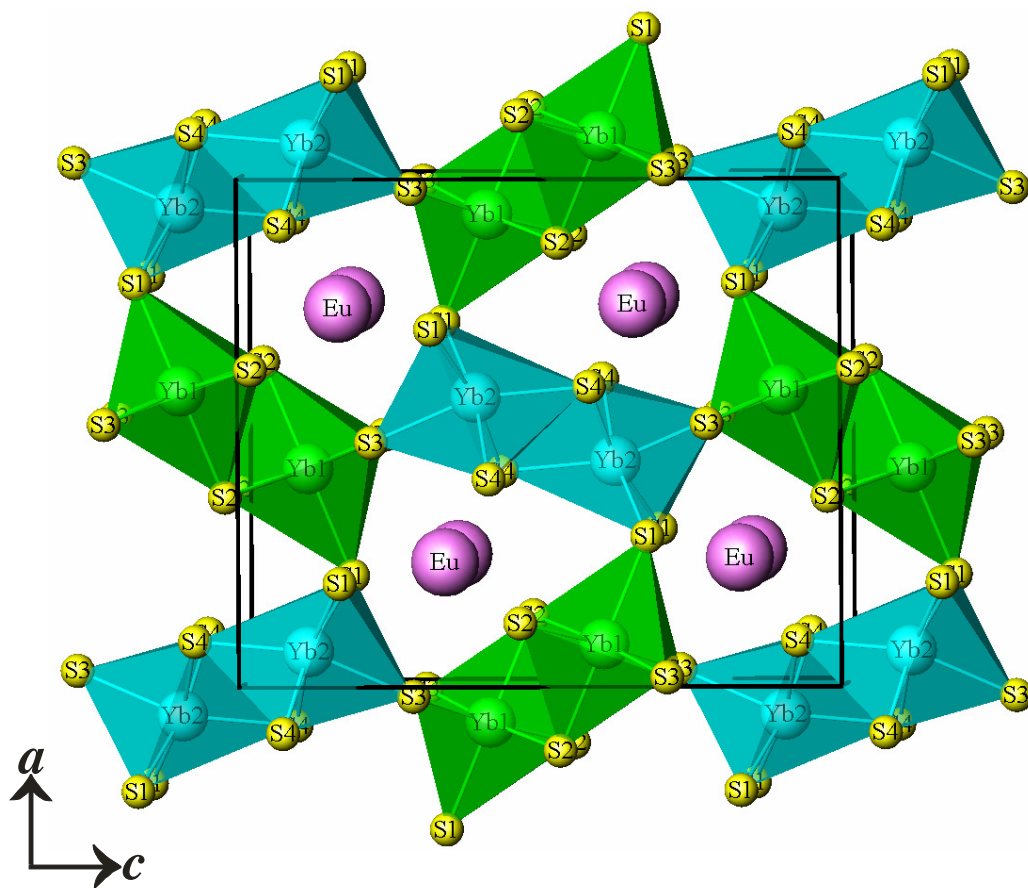


Figure 1.6. An illustration of the three-dimensional channel structure of EuYb_2S_4 down the b axis. Eu-S bonds have been omitted for clarity.

states (I or II), these metals usually occupy different crystallographic sites from lanthanides, even though their coordination geometries are quite similar.

MAGNETIC PROPERTIES

One of the outstanding properties of the lanthanides is the strong paramagnetism displayed by the metals and their compounds. This trait can be attributed to the presence of unpaired 4f electrons. Not only have magnetic methods been valuable for identification and the determination of purity, but also they have also cast considerable light on the configurations of the ions and possible magnetic interactions between ions in the solid state.

Most lanthanides have unpaired 4f electrons, as shown in Table 1.4, except diamagnetic La^{3+} and Lu^{3+} ions. The magnetic moment of each unpaired electron includes spin angular momentum and orbital angular momentum. For transition metals, the partially filled d-shells are the outermost electronic shells, and are therefore strongly influenced by their environment. The orbital angular momentum in the case of many first row d-block metal ions is actually quenched by the crystal field. This is a particular example of a general phenomenon known as crystal-field splitting. The magnetic moment, μ , can be expressed as the so-called spin-only formula (equation 1.1).⁶⁹

$$\mu \text{ (spin-only)} = 2 [S(S+1)]^{1/2} \quad (1.1)$$

In contrast, crystal field splitting is unimportant for lanthanides, because the partially filled 4f shells lie deep inside the ion (beneath filled 5s and 5p shells). The effective

Table 1.4. Calculated and measured effective magnetic moments (μ) for the trivalent lanthanide ions

| Element | | Electronic configuration | Ground-state term | $\mu_{\text{cal}}/\mu_{\text{B}}$ | $\mu_{\text{mea}}/\mu_{\text{B}}$ |
|---------|--------------|--------------------------|--------------------------------|-----------------------------------|-----------------------------------|
| La | lanthanum | [Xe] 4f ⁰ | ¹ S | 0.00 | diamagnetic |
| Ce | cerium | [Xe]4f ¹ | ² F _{5/4} | 2.54 | 2.4 |
| Pr | praseodymium | [Xe]4f ² | ³ H ₄ | 3.58 | 3.5 |
| Nd | neodymium | [Xe]4f ³ | ⁴ I _{9/2} | 3.62 | 3.5 |
| Pm | promethium | [Xe]4f ⁴ | ⁵ I ₄ | 2.68 | - |
| Sm | samarium | [Xe]4f ⁵ | ⁶ H _{5/2} | 0.84 | 1.5 |
| Eu | europium | [Xe]4f ⁶ | ⁷ F ₀ | 0.00 | 3.4 |
| Gd | gadolinium | [Xe]4f ⁷ | ⁸ S _{7/2} | 7.94 | 8.0 |
| Tb | terbium | [Xe]4f ⁸ | ⁷ F ₆ | 9.72 | 9.5 |
| Dy | dysprosium | [Xe]4f ⁹ | ⁶ H _{15/2} | 10.63 | 10.6 |
| Ho | holmium | [Xe]4f ¹⁰ | ⁵ I ₈ | 10.60 | 10.4 |
| Er | erbium | [Xe]4f ¹¹ | ⁴ I _{15/2} | 9.59 | 9.5 |
| Tm | thulium | [Xe]4f ¹² | ³ H ₆ | 7.57 | 7.3 |
| Yb | ytterbium | [Xe]4f ¹³ | ² F _{7/2} | 4.54 | 4.5 |
| Lu | lutetium | [Xe]4f ¹⁴ | ¹ S | 0.00 | diamagnetic |

magnetic moment, μ_{eff} , for lanthanides, given by equation 1.2, takes into account both spin angular momentum and orbital angular momentum.

$$\mu_{\text{eff}} = g_J [J(J+1)]^{1/2} \quad (1.2)$$

where g_J is the Zeeman factor, $g_J = 3/2 + [(S(S+1) - L(L+1))/2J(J+1)]$. μ_{eff} can be obtained from the experimentally measured molar magnetic susceptibility, χ_m , and is expressed in Bohr magnetons (μ_B) according to equation 1.3.

$$\mu_{\text{eff}} = [3k_B\chi_m T / (L\mu_0\mu_B^2)]^{1/2} \quad (1.3)$$

where k_B is Boltzmann constant; L is Avogadro's number; μ_0 is vacuum permeability; T is temperature in Kelvin. Table 1.4 presents the calculated effective magnetic moments, based on equation 1.2, that generally agree well with experimental values.

For most of the trivalent lanthanides, the energy difference between $^{2S+1}L_J$ free-ion ground state and the first excited state is much larger than the thermal energy ($k_B T$), therefore only the ground state is thermally populated at room temperature and below. In the free-ion approximation, the molar magnetic susceptibility is then given by equation 1.4.⁷⁰

$$\chi_m = L(g_J\mu_B)^2 J(J+1) / 3k_B T + 2L\mu_B^2 (g_J - 1)(g_J - 2) / 3\lambda \quad (1.4)$$

where λ is the spin-orbit coupling constant. The second term in the above equation is a temperature independent component due to the coupling between ground and excited states through the Zeeman perturbation. Equation 1.4 can be rewritten as modified Curie-Weiss law (equation 1.5), where C is Curie constant, $C = L(g_J\mu_B)^2 J(J+1) / 3k_B$; θ is Weiss constant; $\chi_0 = 2L\mu_B^2 (g_J - 1)(g_J - 2) / 3\lambda$.

$$\chi_m = \chi_0 + C / (T - \theta) \quad (1.5)$$

The magnetic susceptibility behavior for lanthanides does not always follow the Curie-Weiss law, especially at low temperatures. Because of the crystal-field effect that splits the $^{2S+1}L_J$ ground state into several Stark sublevels, at high temperatures all Stark sublevels are thermally populated, while as the temperature decreases, a depopulation of these sublevels occurs causing the deviation from Curie-Weiss law. For Eu^{3+} and Sm^{3+} ions, their first excited states are thermally populated, because the energy difference between the first excited state and ground state is comparable to the thermal energy. Considering the contribution from excited states, the magnetic susceptibility for Eu^{3+} and Sm^{3+} would not follow equation 1.5.

$\text{Gd}_{1.87}\text{Lu}_{2.13}\text{Se}_6$, $\beta\text{-NdLuSe}_3$, and $\text{Sm}_{1.82}\text{Lu}_{2.18}\text{Se}_6$ are given as examples to illustrate the typical magnetic susceptibility behaviors of lanthanide chalcogenides.⁷¹ Since the Lu^{3+} ions are diamagnetic, Gd^{3+} , Nd^{3+} , and Sm^{3+} are the only magnetic ions in these compounds. Gd^{3+} ion is rather unique in the lanthanides series with a ground state of $^8S_{7/2}$ ($L = 0$). It does not have orbital angular momentum, so the ground state is not perturbed by crystal field effect. Furthermore, its first excited state $^6P_{7/2}$ is fully depopulated even at room temperature. The temperature dependence of magnetic susceptibility for Gd^{3+} follows the Curie-Weiss law, as shown in Figure 1.7. $\text{Gd}_{1.87}\text{Lu}_{2.13}\text{Se}_6$ undergoes an antiferromagnetic transition around 4 K. It is worth noting that some Gd-based compounds have some small crystal field splitting at very low temperature because of the spin-orbital coupling between $^8S_{7/2}$ and $^6P_{7/2}$.

The ground state of Nd^{3+} is $^4I_{9/2}$ that would be influenced by the crystal field. Figure 1.8 shows the inverse molar magnetic susceptibility as a function of temperature

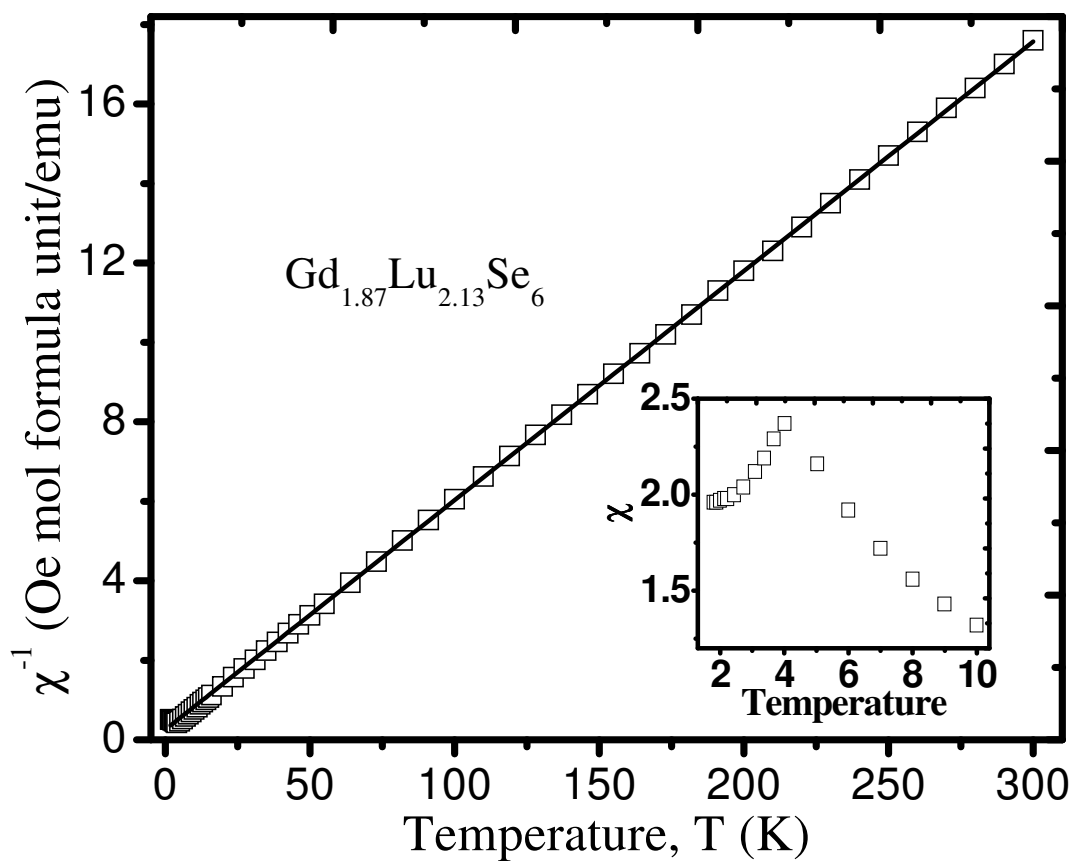


Figure 1.7. Inverse molar magnetic susceptibility vs temperature for $\text{Gd}_{1.87}\text{Lu}_{2.13}\text{Se}_6$ under an applied magnetic field of 0.1 T between 2 and 300 K. The solid line represents the fit to Curie-Weiss law in the range of 100-300 K. Inset shows the molar magnetic susceptibility at low temperature.

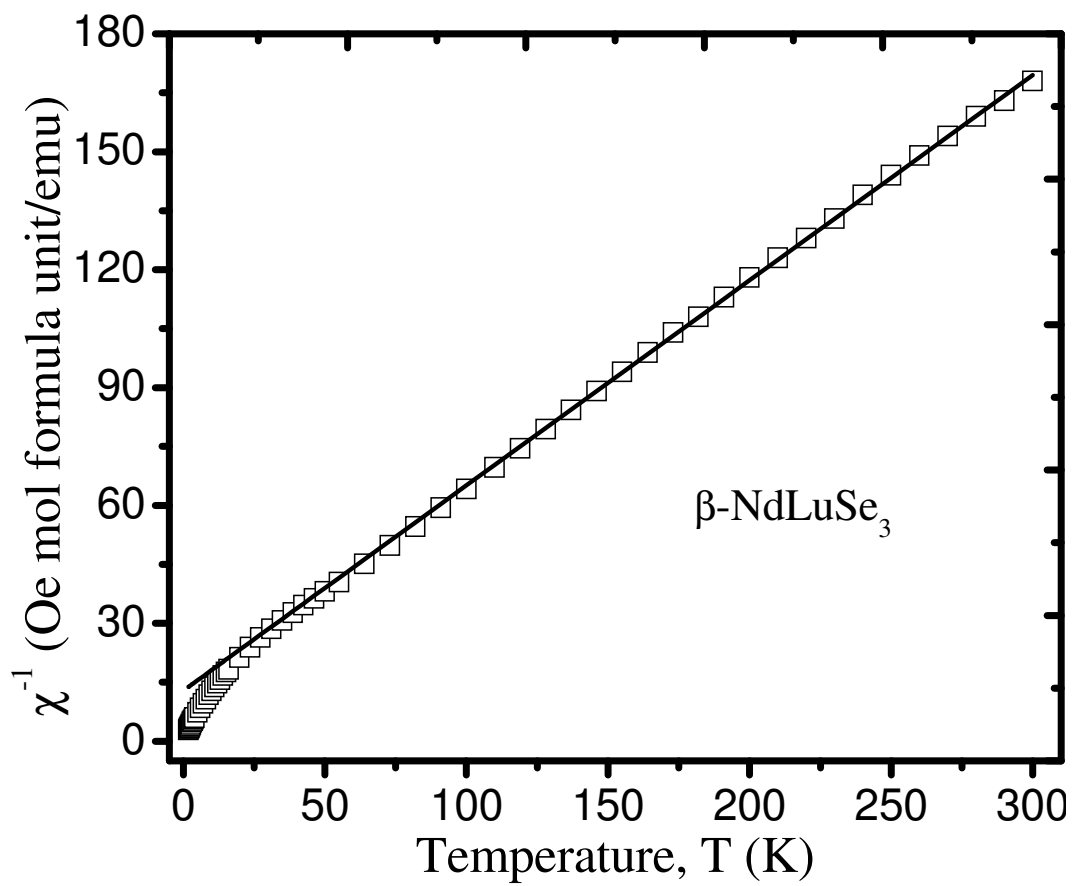


Figure 1.8. The temperature dependence of the reciprocal molar magnetic susceptibility for β -NdLuSe₃ under an applied magnetic field of 0.1 T between 2 and 300 K. The straight line represents the fit to Curie-Weiss law in the range of 100-300 K.

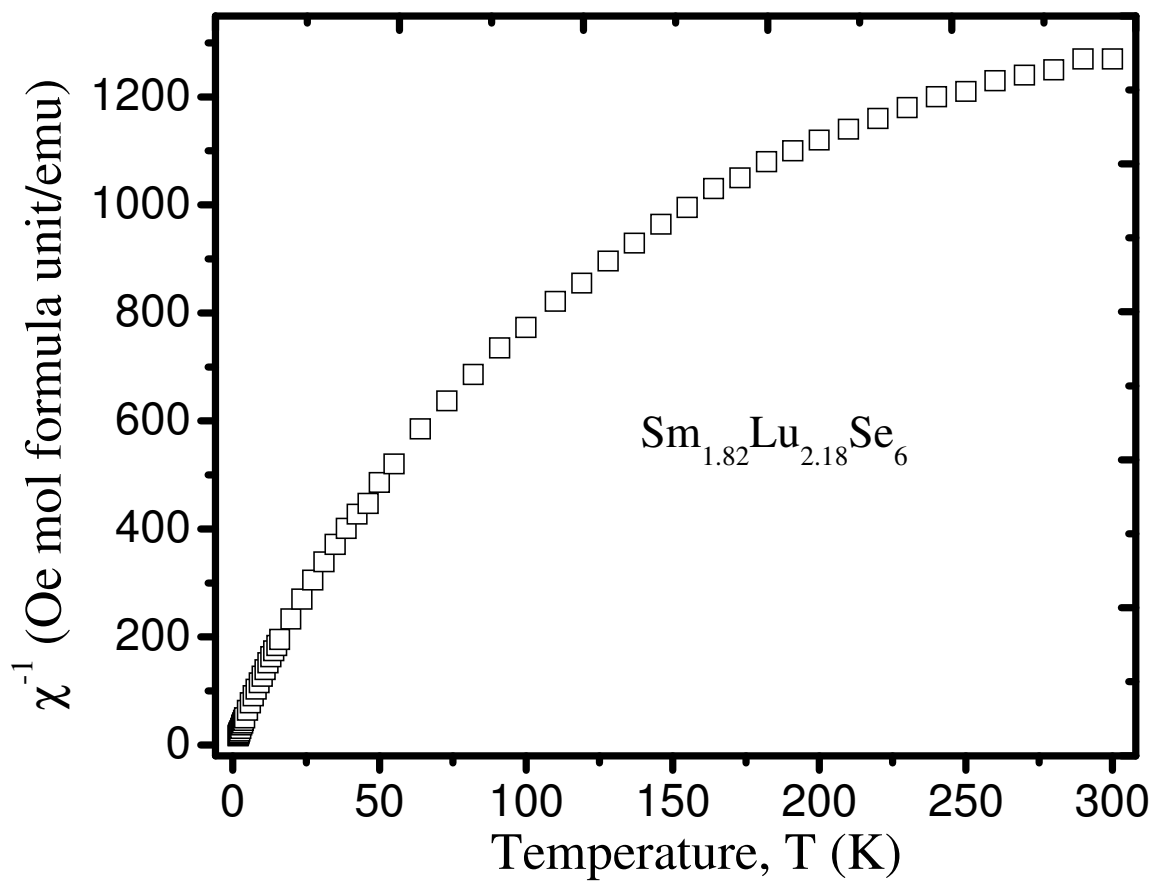


Figure 1.9. Inverse molar magnetic susceptibility as a function of temperature for $\text{Sm}_{1.82}\text{Lu}_{2.18}\text{Se}_6$ under an applied magnetic field of 0.1 T between 2 and 300 K.

for β -NdLuSe₃. It deviates from the Curie-Weiss law below 40 K owing to depopulation of Stark sublevels of higher energy. For Sm³⁺ ions, the difference between the ground state (⁶H_{5/2}) and the first excited state (⁶H_{7/2}) is not large compared to thermal energy ($k_B T$). Therefore, the excited states make significant contributions to the magnetic susceptibility at high temperature. The magnetic susceptibility of Sm³⁺ is given by equation 1.6.

$$\chi_m = \frac{[C^{2.14} + 3.67/\gamma + (42.9 + 0.82/\gamma) e^{-7\gamma} + (142 - 0.33/\gamma) e^{-16\gamma} + \dots]}{[T(3 + 4e^{-7\gamma} + 5e^{-16\gamma})]} \quad (1.6)$$

where $C = L\mu_B 2/(3k_B)$; γ is the ratio between the multiplet width and the thermal energy, $\gamma = \lambda/(k_B T)$. The magnetic susceptibility of Sm_{1.82}Lu_{2.18}Se₆ (Figure 1.9) shows a typical van Vleck paramagnetic behavior that does not follow the Curie-Weiss law.⁷²

OPTICAL PROPERTIES

One of the most promising applications of the lanthanide chalcogenides is the ability to systematically change the band gap of these semiconductors. The variation of their optical gaps across the series often exhibits certain periodicity. The well-studied compounds, Ln₂Q₃ (Q = O, S, Se), are typical examples of this character.^{73,74}

The band gap (E_g) for binary lanthanide chalcogenides is the gap between the valence band, usually composed of the np states of chalcogenides, and conduction band that is formed by the 5d(6s) states of lanthanides ions. Figure 1.10 shows the variation of the band gap for Ln₂Q₃ (Q = O, S, Se).⁷⁴ There are two apparent minima for cerium and terbium. Both of them have one excess 4f electron from the most stable 4f⁰ and 4f⁷ configurations. Ce-based compounds have the smallest gaps in the whole series because

of their high-energy $4f^1$ state that overlaps the forbidden band. The absorption edge is determined by optical transition from the $4f$ band to the conduction band. The energies of the $4f$ -shells start to decrease after Ce^{3+} causing the increase of band gaps in the sequence of Ce_2O_3 - Pr_2O_3 - Nd_2O_3 - Sm_2O_3 . The same thing happens for Tb_2O_3 - Dy_2O_3 - Ho_2O_3 . La-, Gd-, and Lu-containing compounds have the maximum gaps. The empty $4f$ band for La^{3+} is located much higher than the bottom of the conduction band, while the $4f$ bands for Gd^{3+} and Lu^{3+} are buried deeply in the valence band owing to the high stability of half- and fully-filled $4f$ shells. The band gaps for Er and Tm oxides are close to the values for La, Gd, and Lu oxides because, as the $4f$ band enters the valence band, the E_g become constant. The E_g minima for Eu_2O_3 and Yb_2O_3 are because of their low dissociation energy (D), which is presented in Figure 1.11.⁷⁴ The lower D values for these two compounds may indicate some bivalent character of Eu and Yb ions. Because the sequence of energy levels of p orbitals is $2p$ (O) < $3p$ (S) < $4p$ (Se), the periodicity of the variation of band gaps becomes less obvious in sulfides and selenides. The $4f$ bands in lanthanide oxides that lie in the forbidden band might drop into the valence band in the cases of sulfides and selenides.

The band gaps of lanthanide chalcogenides with same composition highly depend on their structures as well. For instance, β - $LaYbS_3$ crystals are yellow,⁶⁶ while γ - $LaYbS_3$ crystals are dark red with smaller band gaps.⁵⁰ Both β - $LaYbS_3$ and γ - $LaYbS_3$ adopt two-dimensional layer structures, but the structure of γ - $LaYbS_3$ is more condensed.

Including other metals will have a substantial effect on the band gaps of lanthanide chalcogenides. Alkali metal and alkaline-earth cations are more electropositive than lanthanides and have almost no contribution to the electronic states

near the Fermi level, although they usually lift the energy of conduction band and give rise to larger band gaps.⁷⁵⁻⁷⁷ In contrast, transition metal ions and main group metal ions are more electronegative than lanthanides and form more covalent bonds with chalcogenides. The band gaps are usually smaller and are dominated by the interactions between transition metal ions (or main group metal ions) and chalcogenides.⁷⁸⁻⁸⁰

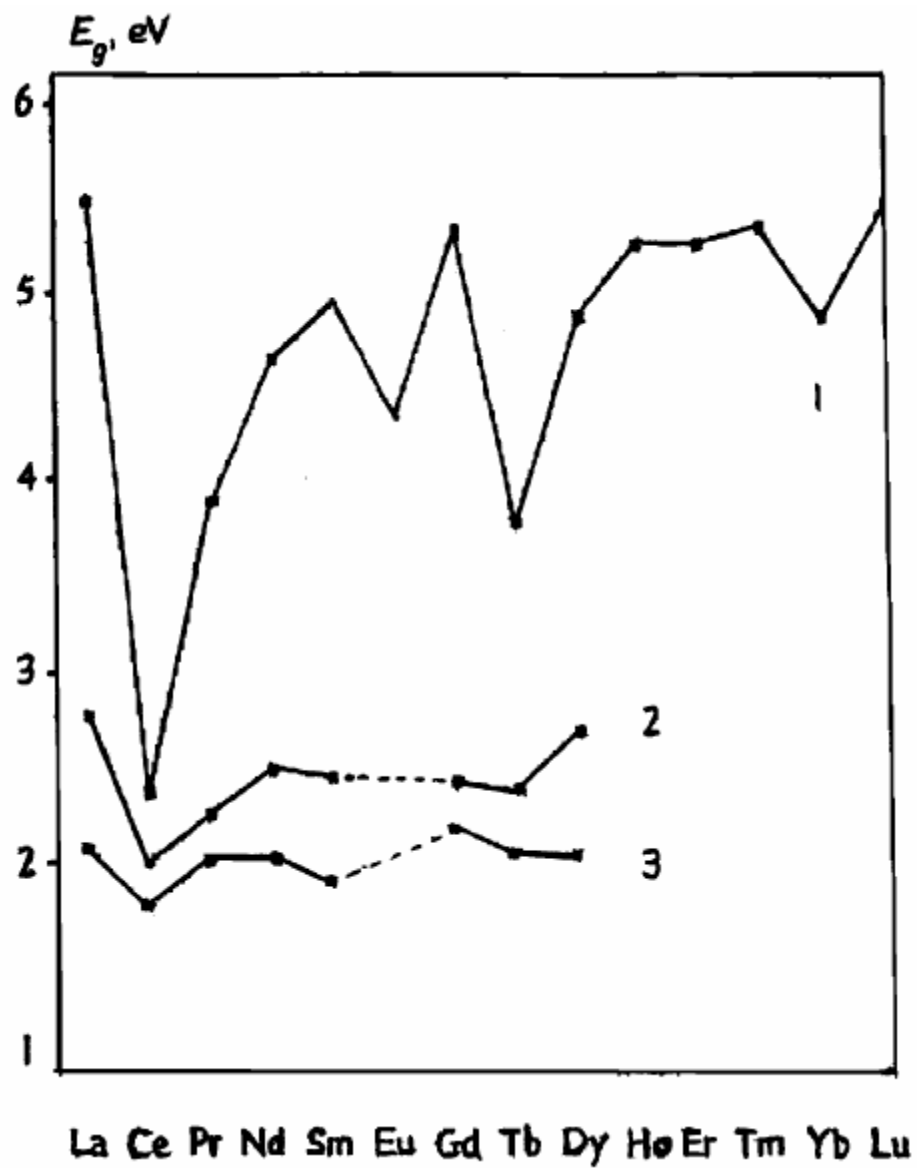


Figure 1.10. Variation of the band gap E_g of Ln_2Q_3 ($\text{Q} = \text{O}, \text{S}, \text{Se}$) in the lanthanide series: 1) oxides; 2) sulfides; 3) selenides.

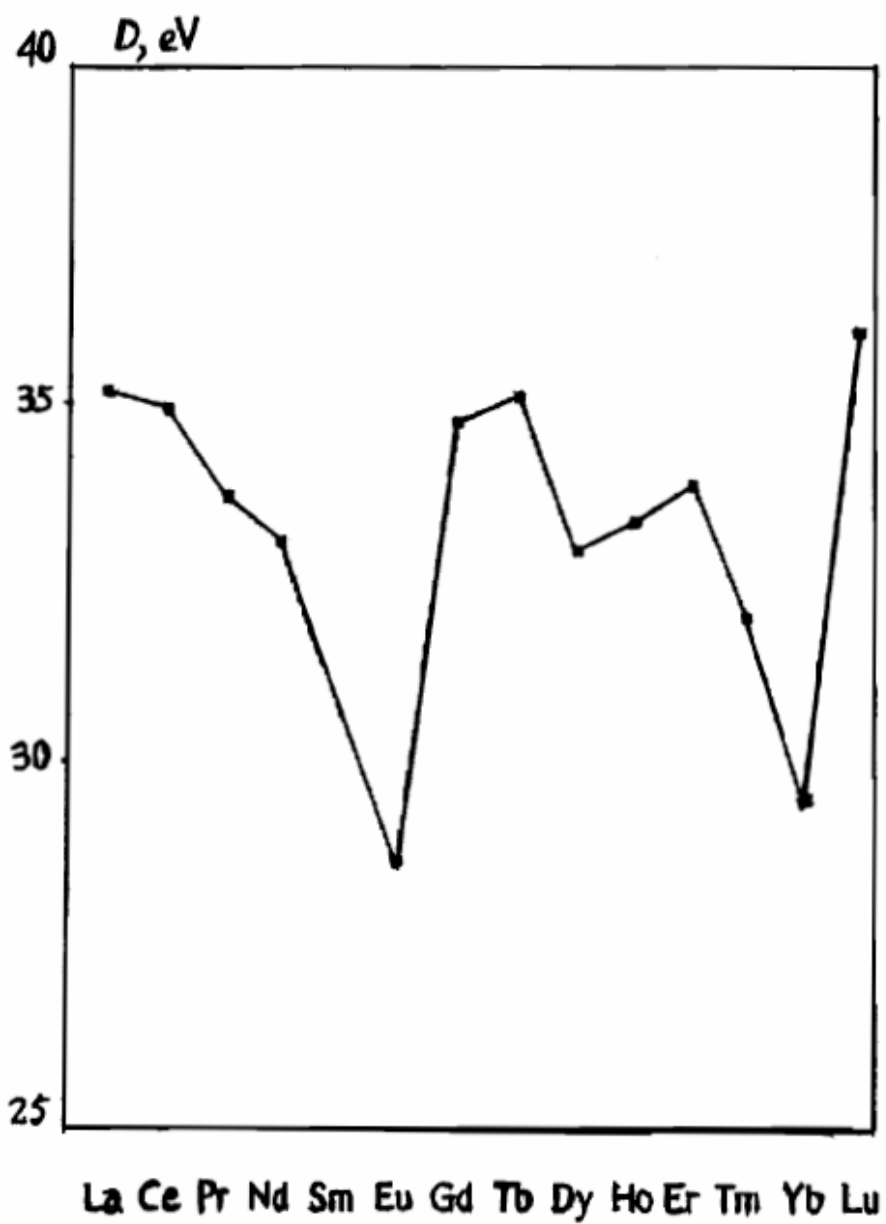


Figure 1.11. Variation of the dissociation (atomization) energy D of Ln_2O_3 in the lanthanide series.

REFERENCES

1. Gschneidner Jr., K. A.; Eyring, L. R. Eds. *Handbook on the Physics and Chemistry of Rare Earths*; North-Holland Physics Publishing: New York, **1979**; Vol. 4, pp 1-88.
2. Isaacs, T. J.; Hopkins, R. H.; Kramer, W. E. *J. Electron. Mater.* **1975**, *4*, 1181.
3. Hautala, J.; Taylor, P. C. *J. Non-Cryst. Solids* **1992**, *141*, 24.
4. Lowe-Ma, C. K.; Vanderah, T. A.; Smith, T. E. *J. Solid State Chem.* **1995**, *117*, 363.
5. Huang, F. Q.; Mitchell, K.; Ibers, J. A. *Inorg. Chem.* **2001**, *40*, 5123.
6. Inoue, S.; Ueda, K.; Hosono, H.; Hamada, N. *Phys. Rev. B* **2001**, *64*, 245211.
7. Ueda, K.; Inoue, S.; Hosono, H.; Sarukura, N.; Hirano, H. *Appl. Phys. Lett.* **2001**, *78*, 2333.
8. Mitchell, K.; Ibers, J. A. *Chem. Rev.* **2002**, *102*, 1929-1952.
9. Mitchell, K.; Haynes, C. L.; McFarland, A. D.; Van Duyne, R. P.; Ibers, J. A. *Inorg. Chem.* **2002**, *41*, 1199.
10. Mitchell, K.; Huang, F. Q.; McFarland, A. D.; Haynes, C. L.; Somers, R. C.; Van Duyne, R. P.; Ibers, J. A. *Inorg. Chem.* **2003**, *42*, 4109.
11. Ueda, K.; Takafuji, K.; Hiramatsu, H.; Ohta, H.; Kamiya, T.; Hirano, M.; Hosono, H. *Chem. Mater.* **2003**, *15*, 3692.
12. Yao, J.; Deng, B.; Sherry, L. J.; McFarland, A. D.; Ellis, D. E.; Van Duyne, R. P.; Ibers, J. A. *Inorg. Chem.* **2004**, *43*, 7735.

13. Mitchell, K.; Huang, F. Q.; Caspi, E. N.; McFarland, A. D.; Haynes, C. L.; Somers, R. C.; Jorgensen, J. D.; Van Duyne, R. P.; Ibers, J. A. *Inorg. Chem.* **2004**, *43*, 1082.
14. Furuuchi, F.; Wakeshima, M.; Hinatsu, Y. *J. Solid State Chem.* **2004**, *177*, 3853.
15. Sutorik, A. C.; Albritton-Thomas, J.; Hogan, T.; Kannewurf, C. R.; Kanatzidis, M. *G. Chem. Mater.* **1996**, *8*, 751.
16. Tougait, O.; Ibers, J. A. *Inorg. Chem.* **2000**, *39*, 1790.
17. Bronger, W.; Miessen, H.-J.; Schmitz, D. *J. Less-Common Met.* **1983**, *95*, 275.
18. Wakeshima, M.; Hinatsu, Y.; Oikawa, K.; Shimojo, Y.; Morii, Y. *J. Mater. Chem.* **2000**, *10*, 2183.
19. Meng, F.; Hughbanks, T. *Inorg. Chem.* **2001**, *40*, 2482.
20. Wakeshima, M.; Hinatsu, Y.; Ishii, Y.; Shimojo, Y.; Morii, Y. *J. Mater. Chem.* **2002**, *12*, 631.
21. Bozorth, R. M.; Holtzberg, F.; Methfessel S. *Phys. Rev. Lett.* **1965**, *14*, 952.
22. Westerholt, K.; Bach, H.; Wendemuth, R.; Methfessel, S. *Solid State Commun.* **1979**, *31*, 961.
23. Westerholt, K.; Timmer, F.; Bach, H. *Phys. Rev. B* **1985**, *32*, 2985.
24. Fischer, O. *Springer Ser. Solid-State Sci.* **1990**, *90*, 96-112.
25. Kang, J. -S.; Nahm, K.; Kim, C. K.; Olson, C. G.; Pelzl, J.; Shim, J. H.; Min, B. I. *Phys. Rev. B* **2002**, *66*, 075108.
26. Foran, B.; Lee, S.; Aronson, M. C. *Chem. Mater.* **1993**, *5*, 974.
27. DiMasi, E.; Foran, B.; Aronson, M. C.; Lee, S. *Chem. Mater.* **1994**, *6*, 1867.

28. Prodan, A.; Marinkovic, V.; Boswell, F. W.; Bennett, J. C.; Remskar, M. *J. Alloys Compd.* **1995**, *219*, 69-72.
29. Malliakas, C. D.; Kanatzidis, M. G. *J. Am. Chem. Soc.* **2006**, *128*, 12612.
30. Aliev, O. M.; Rustamov, P. G.; Guseinov, G. G.; Guseinov, M. S.; *Nauk SSSR, Izvest. Akad. Neorgan. Mater.* **1978**, *14*, 1346.
31. Tritt, T. M. *Science* **1999**, *283*, 804-805.
32. Nowacki, W. *Naturwissenschaften* **1938**, *26*, 495.
33. Gschneidner Jr., K. A.; Eyring, L. R. Eds. *Handbook on the Physics and Chemistry of Rare Earths*; North-Holland Physics Publishing: New York, **1979**; Vol. 2, pp 507-575.
34. Lemoine, P.; Guittard, M. *Acta Cryst.* **1982**, *B38*, 727.
35. Lemoine, P.; Carré, D.; Guittard, M. *Acta Cryst.* **1986**, *C42*, 390.
36. Furuuchi, F.; Wakeshima, M.; Hinatsu, Y. *J. Solid State Chem.* **2004**, *177*, 3853.
37. Wakeshima, M.; Fujino, T.; Sato, N.; Yamada, K.; Masuda, H. *J. Solid State Chem.* **1997**, *129*, 1.
38. Jaulmes, S.; Julien-Pouzol, M. *Acta Cryst.* **1977**, *C33*, 1191.
39. Flahaut, J.; Laruelle, P.; Guittard, M.; Jaulmes, S.; Julien-Pouzol, M.; Lavenant, C. *J. Solid State Chem.* **1979**, *29*, 125.
40. Flahaut, J.; Domange, L.; Pardo, M. P. *Inorg. Chem.* **1968**, *7*, 2282.
41. Chevalier, R.; Laruelle, P.; Flahaut, J. *Bulletin de la Societe Francaise de Mineralogie et de Cristallographie* **1967**, *90*, 564.
42. Pouzol, J.; Jaulmes, M.; Wintenberger, M.; Guittard, M. *Mater. Res. Bull.* **1987**, *22*, 95.

43. Noda, Y.; Matsumoto, K.; Ohba, S.; Saito, Y. *Acta Crystallogr.* **1987**, *43*, 1433.
44. Rabenau, A. *Angew. Chem. Int. Ed. Engl.* **1985**, *24*, 1026.
45. Steigerwald, M. L. *Inorganomet. Chem.* **1992**, 333.
46. Wood, P. T.; Pennington, W. T.; Kolis, J. W. *J. Am. Chem. Soc.* **1992**, *114*, 9233.
47. Elwell, D.; Scheel, H. J. *Crystal Growth from High-Temperature Solutions*; Academic, New York, 1975.
48. Sunshine, S. A.; Kang, D.; Ibers, J. A. *J. Am. Chem. Soc.* **1987**, *109*, 6202.
49. Kanatzidis, M. G.; Sutorik, A. C. *Prog. Inorg. Chem.* **1995**, *43*, 151.
50. Jin, G. B.; Choi, E. S.; Guertin, R. P.; Brooks, J. S.; Bray, T. H.; Booth, C. H.; Albrecht-Schmitt, T. E. *Chem. Mater.* **2007**, *19*, 567.
51. Prewitt, C. T.; Sleight, A. W. *Inorg. Chem.* **1968**, *7*, 1090.
52. Besancon, P.; Laruelle, P. *C. R. Acad. Sci. Paris, Ser. C* **1969**, 268, 48.
53. Besancon, P. *J. Solid State Chem.* **1973**, *7*, 232.
54. Carre, D.; Laruelle, P.; Besancon, P. *C. R. Acad. Sci. Paris, Ser. C* **1970**, 270, 537.
55. Schleid, T.; Lissner, F. *J. Less-Common Met.* **1991**, *175*, 309.
56. Zachariasen, W. H. *Acta Crystallogr.* **1949**, *2*, 57.
57. White, J. G.; Yocom, P. N.; Lerner, S. *Inorg. Chem.* **1967**, *6*, 1872.
58. Fang, C. M.; Meetsma, A.; Wiegers, G. A.; Boom, G. *J. Alloys Compd.* **1993**, *201*, 255.
59. Landa-Canovas, A. R.; Amador, U.; Otero-Diaz, L. C. *J. of Alloys Compd.* **2001**, *323*, 91.

60. Flahaut, J.; Domange, L.; Pardo, M. P. *Comptes Rendus Hebdomadaires des Seances de l'Academie des Sciences* **1964**, 258, 594.
61. El Fadli, Z.; Lemoine, P.; Guittard, M.; Tomas, A. *Acta Crystallogr.* **1994**, C50, 166.
62. Kuzmicheva, G. M.; Efremov, V. A.; Khlyustova, S. Yu.; Eliseev, A. A. *Zhurnal Neorganicheskoi Khimii* **1986**, 31, 2210.
63. Kuz'micheva, G. M.; Smarina, E. I.; Khlyustova, S. Yu.; Chernyshev, V. V. *Zhurnal Neorganicheskoi Khimii* **1990**, 35, 869.
64. Schleid, T.; Lissner, F. *J. Alloys Compd.* **1992**, 189, 69.
65. Rodier, N.; Julien, R.; Tien, V. *Acta Crystallogr. C* **1983**, 39, 670.
66. Mitchell, K.; Somers, R. C.; Huang, F. Q.; Ibers, J. A. *J. Solid State Chem.* **2004**, 177, 709.
67. Hulliger, F.; Vogt, O. *Phys. Lett.* **1966**, 21, 138.
68. Lugscheider, W.; Pink, H.; Weber, K.; Zinn, W. *Zeitschrift fuer Angewandte Physik* **1970**, 30, 36.
69. Kittel, C. *Introduction to Solid State Physics*; 6th Ed., Wiley, New York, 1986.
70. Andruh, M.; Bakalbassis, E.; Kahn, O.; Trombe, J. C.; Porcher, P. *Inorg. Chem.* **1993**, 32, 1616.
71. Jin, G. B.; Choi, E. S.; Guertin, R. P.; Brooks, J. S.; Bray, T. H.; Booth, C. H.; Albrecht-Schmitt, T. E. *Inorg. Chem.* submitted.
72. Van Vleck, J. H. *The Theory of Electric and Magnetic Susceptibilities*; Oxford University Press: London, 1932.

73. Prokofiev, A. V.; Shelykh, A. I.; Golubkov, A. V.; Smirnov, I. A. *J. Alloys Compd.* **1995**, *219*, 172.
74. Prokofiev, A. V.; Shelykh, A. I.; Melekh, B. T. *J. Alloys Compd.* **1996**, *242*, 41.
75. Bronger, W.; Eyck, J.; Kruse, K.; Schmitz, D. *Eur. J. Solid State Inorg. Chem.* **1996**, *33*, 213.
76. Sutorik, A. C.; Kanatzidis, M. G. *Chem. Mater.* **1997**, *9*, 387.
77. Deng, B.; Ellis, D. E.; Ibers, J. A. *Inorg. Chem.* **2002**, *41*, 5716.
78. Ueda, K.; Hosono, H.; Hamada, N. *J. Phys.: Condens. Matter* **2004**, *16*, 5179.
79. Chan, G. H.; Deng, B.; Bertoni, M.; Ireland, J. R.; Hersam, M. C.; Mason, T. O.; Van Duyne, R. P.; Ibers, J. A. *Inorg. Chem.* **2006**, *45*, 8264.
80. Liu, M. L.; Wu, L. B.; Huang, F. Q.; Chen, L. D.; Ibers, J. A. *J. Solid State Chem.* **2007**, *180*, 62.

CHAPTER 2

**SYNTHESIS, STRUCTURE, AND MAGNETIC PROPERTIES OF THE
NONCENTROSYMMETRIC TERNARY RARE-EARTH ANTIMONY
POLYSULFIDE $\text{Eu}_6\text{Sb}_6\text{S}_{17}$**

ABSTRACT

$\text{Eu}_6\text{Sb}_6\text{S}_{17}$ is isostructural with $\text{Sr}_6\text{Sb}_6\text{S}_{17}$ and can be treated as consisting of two isolated $[\text{Sb}_3\text{S}_7]^{5-}$ anions and a S_3^{2-} polysulfide anion that are joined together by Eu^{2+} cations. There are six crystallographically unique Eu^{2+} cations bound by sulfide and polysulfide anions in seven-, eight-, and nine-coordinate environments. Each of the $[\text{Sb}_3\text{S}_7]^{5-}$ anions consists of a trimer of corner-sharing SbS_3 units. The $[\text{Sb}_3\text{S}_7]^{5-}$ anions are connected by long (~ 3.1 Å) Sb–S interactions, forming one-dimensional ribbons running down the a axis and packed with opposing directions of polarity. The bent S_3^{2-} anions stack in columns along the a axis, oriented in opposing directions with respect to one another. The overall structure is three-dimensional and has channels running down the a axis to house the stereochemically active lone-pair of electrons on the Sb^{3+} centers. The presence of Eu^{2+} ions is supported by both magnetic measurements and bond valence calculations. Crystallographic data (193 K, Mo $K\alpha$, $\lambda = 0.71073$): orthorhombic, space

group $P2_12_12_1$, $a = 8.236(2) \text{ \AA}$, $b = 15.237(3) \text{ \AA}$, $c = 22.724(5) \text{ \AA}$, $Z = 4$, $R(F) = 3.11\%$ for 264 parameters with 7062 reflections with $I > 2\sigma(I)$.)

INTRODUCTION

Ternary rare-earth thioantimonites have been known for more than twenty years since the initial report of the synthesis and crystal structure of $\text{Eu}_3\text{Sb}_4\text{S}_9$.¹ Despite this early success, the chemistry of thioantimonites is relatively undeveloped compared to that of thiophosphates,² and there is still a dearth of understanding in the structure-property relationships in this system. There has been renewed interest in ternary and quaternary chalcantimonites and chalcobismuthites owing to their potential applications as thermoelectric materials. Based on structural analogies with Pn_2Q_3 phases ($\text{Pn} = \text{Sb, Bi}$; $\text{Q} = \text{S, Se, Te}$), a series of ternary phases such as EuSb_2Q_4 , EuSb_2Q_7 , and EuBi_2Te_4 has been prepared and their transport properties measured.³ EuBi_2Te_4 displays a thermoelectric figure of merit comparable with that of Bi_2Te_3 .³ Eu_2BiS_4 is also of particular interest because it contains Eu(II) and Eu(III) in different coordination environments.⁴ Other ternary rare-earth thioantimonites such as $\text{Pr}_8\text{Sb}_2\text{S}_{15}$,⁵ $\text{Ln}_3\text{Sb}_3\text{S}_{10}$ ($\text{Ln} = \text{La, Ce}$),⁶ and $\text{Ln}_6\text{Sb}_8\text{S}_{21}$ ($\text{Ln} = \text{La, Ce}$)⁷ have been characterized from single-crystal and powder X-ray diffraction data. EuSb_4S_7 has also been reported, but only its lattice constants are known.⁸

More recently there has been attention paid to preparing quaternary rare-earth chalcantimonites and chalcobismuthites, e.g. $\text{K}_2(\text{Ln}_{2-x})\text{Sb}_{4+x}\text{Se}_{12}$ ($\text{Ln} = \text{La, Ce, Pr, Gd}$),⁹ $\text{K}_2\text{Gd}_2\text{Sb}_2\text{Se}_9$,¹⁰ $\text{K}_2\text{La}_2\text{Sb}_2\text{S}_9$,¹⁰ $\text{Na}_9\text{Gd}_5\text{Sb}_8\text{S}_{26}$,¹¹ $\text{BaLaBi}_2\text{S}_6$,¹² $\text{ALn}_{1\pm x}\text{Bi}_{4\pm x}\text{S}_8$ ($\text{A} = \text{K, Rb}$; La, Ce, Pr, Nd),¹³ and $\text{Pb}_2\text{Eu}_2\text{Bi}_6\text{Se}_{13}$.¹⁴ These compounds possess complex structures

owing to the combination of the high coordination numbers found for lanthanides with discrete PnQ_3^{3-} , PnQ_{3+1}^{3-} , and PnQ_4^{5-} anions as well as extended networks of chalcocantimonites and chalcobismuthites. Herein we report the preparation, crystal structure, and magnetic properties of $\text{Eu}_6\text{Sb}_6\text{S}_{17}$, a new ternary thioantimonite that is isostructural $\text{Sr}_6\text{Sb}_6\text{S}_{17}$,¹⁵ and which contains Eu(II) and a polysulfide linkage. The information in this chapter has been published as a full paper in *Acta Crystallographica*.¹⁶

EXPERIMENTAL

Syntheses. The single crystal used for X-ray diffraction experiments was isolated from the reaction of Eu foil (99.9%, Alfa-Aesar), Sb (99.5%, Alfa-Aesar), and S (99.5%, Alfa-Aesar) that were loaded in a fused-silica tube in a molar ratio of 3:5:12 with a total mass of 0.250 g. The following heating profile was used: 5 °C/min to 850 °C for 1 d, 5 °C/min to 1000 °C for 7 d, 0.5 °C/min to 600 °C for 5 d, and 0.25 °C/min to 22 °C. The product consisted of small black block-shaped crystals of $\text{Eu}_6\text{Sb}_6\text{S}_{17}$ and acicular crystals of Sb_2S_3 . The yields were generally low (~10%), and were not improved by quenching the reactions. Semi-quantitative SEM/EDX analysis was performed on crystals of $\text{Eu}_6\text{Sb}_6\text{S}_{17}$ using a JEOL 840/Link Isis instrument. Eu, Sb, and S percentages were calibrated against standards, and a Eu:Sb:S ratio of close to 1:1:2.8 (20%:23%:57%) was found.

Crystallographic Studies. A single crystal of $\text{Eu}_6\text{Sb}_6\text{S}_{17}$ was mounted on a glass fiber with epoxy and aligned on a Bruker SMART APEX CCD X-ray diffractometer. Intensity measurements were performed using graphite-monochromated Mo $K\alpha$ radiation from a sealed tube with a monocapillary collimator. SMART was used for preliminary

determination of the cell constants and data-collection control. The intensities of reflections of a sphere were collected by a combination of three sets of exposures (frames). Each set had a different ϕ angle for the crystal and each exposure covered a range of 0.3° in ω . A total of 1800 frames were collected with an exposure time per frame of 30 s.

Determination of integrated intensities and global cell refinement were performed with the Bruker SAINT (v 6.02) software package using a narrow-frame integration algorithm. A face-indexed absorption (Gaussian) correction was initially applied using XPREP.¹⁷ Individual shells of unmerged data were corrected and exported in the same format. These files were subsequently treated with a semi-empirical absorption correction by SADABS.¹⁸ The program suite SHELXTL (v 5.1) was used for space group determination (XPREP), direct methods structure solution (XS), and least-squares refinement (XL).¹⁷ The final refinements included anisotropic displacement parameters for all atoms and a secondary extinction parameter. Some crystallographic details are listed in Table 2.1. Atomic coordinates and equivalent isotropic displacement parameters are given in Table 2.2.

Inspection of the atomic positions (Table 2.2) reveals that they come in symmetry-related pairs (e.g., Eu1–Eu2, Eu3–Eu4, Eu5–Eu6) and the presence of additional pseudosymmetry elements is confirmed by PLATON.¹⁹ The structure can be refined in *Pmnb* to a residual of $R(F) = 0.11$ if a large number of systematic absence exceptions are excluded. The structure in *Pmnb* is identical to the structure in *P2₁2₁2₁*, except that the S_3^{2-} groups are in a disordered arrangement. We conclude, in agreement

Table 2.1. Crystallographic data for Eu₆Sb₆S₁₇.

| | |
|--|--|
| Compound | Eu ₆ Sb ₆ S ₁₇ |
| Formula mass (amu) | 2187.28 |
| Color and habit | black, prism |
| Crystal system | orthorhombic |
| Space group | <i>P</i> 2 ₁ 2 ₁ 2 ₁ (No. 19) |
| <i>a</i> (Å) | 8.236(2) |
| <i>b</i> (Å) | 15.237(3) |
| <i>c</i> (Å) | 22.724(5) |
| <i>V</i> (Å ³) | 2851.7(11) |
| <i>Z</i> | 4 |
| <i>T</i> (°C) | −80 |
| λ (Å) | 0.71073 |
| $2\theta_{\max}$ | 56.64 |
| ρ_{calcd} (g cm ^{−3}) | 5.095 |
| $\mu(\text{Mo } K\alpha)$ (cm ^{−1}) | 198.01 |
| Flack parameter | 0.699(16) |
| $R(F)$ for $F_o^2 > 2\sigma(F_o^2)$ ^a | 0.0311 |
| $R_w(F_o^2)$ ^b | 0.0615 |

^a $R(F) = \frac{\sum ||F_o| - |F_c||}{\sum |F_o|}$.

^b $R_w(F_o^2) = \left[\frac{\sum [w(F_o^2 - F_c^2)^2]}{\sum wF_o^4} \right]^{1/2}$.

Table 2.2. Atomic Coordinates and Equivalent Isotropic Displacement Parameters for $\text{Eu}_6\text{Sb}_6\text{S}_{17}$.

| Atom | x | y | z | $U_{\text{eq}} (\text{\AA}^2)^a$ |
|-------|-------------|--------------|--------------|----------------------------------|
| Eu(1) | -0.24890(7) | -0.44990(4) | 0.21293(3) | 0.01187(13) |
| Eu(2) | 0.25359(6) | -0.44487(4) | 0.21124(2) | 0.01138(13) |
| Eu(3) | 0.25743(6) | -0.55805(4) | 0.04396(2) | 0.01101(13) |
| Eu(4) | 0.75051(6) | -0.56076(4) | 0.04524(2) | 0.01075(12) |
| Eu(5) | 0.75622(6) | -0.66597(4) | -0.12281(2) | 0.01029(13) |
| Eu(6) | 0.24942(6) | -0.66659(4) | -0.12393(2) | 0.01054(13) |
| Sb(1) | -0.02334(8) | -0.20669(4) | 0.23203(2) | 0.01337(14) |
| Sb(2) | 0.01222(9) | -0.31758(4) | 0.08537(2) | 0.01276(12) |
| Sb(3) | 0.49364(9) | -0.32492(4) | 0.05958(2) | 0.01261(12) |
| Sb(4) | 0.53432(7) | -0.42215(4) | -0.09216(3) | 0.01265(14) |
| Sb(5) | 0.01938(8) | -0.42766(4) | -0.10816(2) | 0.01144(13) |
| Sb(6) | 0.99997(9) | -0.80859(3) | -0.25011(2) | 0.01199(12) |
| S(1) | 0.0001(4) | -0.34890(13) | 0.28152(9) | 0.0120(4) |
| S(2) | -0.2157(3) | -0.26825(19) | 0.15715(13) | 0.0126(6) |
| S(3) | 0.2297(3) | -0.2702(2) | 0.14998(14) | 0.0139(6) |
| S(4) | 0.0029(3) | -0.47102(14) | 0.11941(8) | 0.0114(4) |
| S(5) | 0.5040(3) | -0.46228(14) | 0.11727(8) | 0.0110(4) |
| S(6) | 0.2759(3) | -0.3737(2) | -0.00482(13) | 0.0140(6) |
| S(7) | 0.7240(3) | -0.37670(19) | -0.00959(13) | 0.0122(6) |
| S(8) | 0.5070(3) | -0.56906(13) | -0.05339(8) | 0.0099(4) |
| S(9) | 0.0089(3) | -0.56270(14) | -0.05055(8) | 0.0117(4) |

| | | | | |
|-------|-----------|--------------|--------------|-----------|
| S(10) | 0.7675(3) | -0.4741(2) | -0.16414(14) | 0.0131(6) |
| S(11) | 0.2424(3) | -0.4778(2) | -0.17007(13) | 0.0133(6) |
| S(12) | 0.7490(3) | -0.84651(18) | -0.19195(12) | 0.0109(5) |
| S(13) | 0.2119(3) | -0.85439(19) | -0.18205(13) | 0.0139(6) |
| S(14) | 0.9982(4) | -0.65447(13) | -0.22023(8) | 0.0104(4) |
| S(15) | 0.5012(3) | -0.79586(13) | -0.07184(8) | 0.0116(4) |
| S(16) | 0.3593(3) | -0.75150(16) | -0.00157(10) | 0.0113(5) |
| S(17) | 0.4964(3) | -0.70617(13) | 0.06972(8) | 0.0120(4) |

^a U_{eq} is defined as one-third of the trace of the orthogonalized \mathbf{U}_{ij} tensor.

with Choi et al.,¹⁵ that the correct space group is indeed $P2_12_12_1$. The sole atom that breaks the mirror symmetry is S(16).

Magnetism. A 15-mg sample consisting of ground aggregates of $\text{Eu}_6\text{Sb}_6\text{S}_{17}$ crystals was collected for magnetic studies. Magnetic susceptibility measurements were made between 2 and 300 K under zero-field-cooled conditions in an applied field of 0.1 T on a Quantum Design 9T-PPMS dc magnetometer/ac susceptometer. The susceptibility was corrected for contributions from the holder diamagnetism and the underlying sample diamagnetism. (Magnetic susceptibility measurements were performed by Shane J. Crerar and Arthur Mar at University of Alberta)

RESULTS AND DISCUSSION

Structure. Although three-dimensional in nature, the structure of $\text{Eu}_6\text{Sb}_6\text{S}_{17}$ can be treated as consisting of two isolated $[\text{Sb}_3\text{S}_7]^{5-}$ anions and a S_3^{2-} polysulfide anion that are joined together by Eu^{2+} cations. Analogous to $\text{Sr}_6\text{Sb}_6\text{S}_{17}$,¹⁵ to which $\text{Eu}_6\text{Sb}_6\text{S}_{17}$ is isostructural, charge balance is attained in a straightforward manner by assuming the presence of six Eu^{2+} cations, six Sb^{3+} cations, fourteen S^{2-} anions, and one S_3^{2-} anion. The $[\text{Sb}_3\text{S}_7]^{5-}$ anion consists of a trimer of corner-sharing SbS_3 units as shown in Figure 2.1. Other anions formed from the linking of SbS_n units include $[\text{Sb}_2\text{S}_4]^{2-}$ in BaSb_2S_4 ²⁰ and $[\text{Sb}_2\text{S}_5]^{4-}$ in $\text{Sr}_2\text{Sb}_2\text{S}_5 \cdot 15\text{H}_2\text{O}$.²¹ The Sb-S bond distances are given in Table 2.3 and range from 2.416(2) to 2.644(3) Å. As in $\text{Sr}_6\text{Sb}_6\text{S}_{17}$,¹⁵ the $[\text{Sb}_3\text{S}_7]^{5-}$ anions are connected by long (3.105(3) to 3.106(3) Å) Sb-S interactions to form one-dimensional ribbons running down the a axis. Each of the Sb^{3+} cations possesses a stereochemically active lone-pair of electrons. Although space group $P2_12_12_1$, in which this compound

crystallizes, is enantiomorphic and not polar, there is approximate alignment of the lone pair of electrons on the individual Sb^{3+} cations along the b axis. However, the $[\text{Sb}_3\text{S}_7]^{5-}$ anions are packed with opposing directions of polarity (i.e. the lone-pairs on different anions are aligned in opposite directions). The S_3^{2-} anion is bent with S–S bond distances of 2.091(3) and 2.092(3) Å, and an S–S–S bond angle of 113.34(15)°. Although the polysulfide anions do stack in oriented columns along the a -axis, the columns are oriented in opposing directions with respect to one another, canceling any polarity.

The six crystallographically unique Eu^{2+} cations are found in a variety of coordination environments, as shown in Figure 2.2. Eu–S bond distances are given in Table 2.3. Eu(1) and Eu(2) are found in seven-coordinate monocapped trigonal prismatic environments with Eu–S bond distances ranging from 2.984(3) to 3.087(3), and 2.962(3) to 3.209(3) Å, respectively. Eu(3) is bound by eight sulfide anions with bond distances ranging from 2.968(2) to 3.235(3) Å. The geometry around Eu(3) is heavily distorted from a bicapped trigonal prism, a square antiprism, or a dodecahedron because two of the sulfide nearest neighbors are part of the polysulfide linkage creating a very short edge on the polyhedron. Eu(4), Eu(5), and Eu(6) are all found in nine-coordinate geometries that are quite distorted from idealized tricapped trigonal prismatic symmetry because of the presence of a polysulfide linkage within their inner spheres. Eu(5)–S, Eu(6)–S, Eu(7)–S bond distances range from 3.005(3) to 3.382(3) Å, 2.980(2) to 3.208(2) Å, and 2.988(3) to 3.197(3) Å, respectively. Bond-valence sum calculations provide values ranging from 1.87 to 2.10 for the Eu centers in $\text{Eu}_6\text{Sb}_6\text{S}_{17}$, which are consistent with Eu^{2+} in this compound.^{22,23} A packing diagram for the complete structure of $\text{Eu}_6\text{Sb}_6\text{S}_{17}$ is shown in Figure 2.3. When the structure is viewed down the a -axis, it becomes apparent that

$\text{Eu}_6\text{Sb}_6\text{S}_{17}$ adopts a channel structure. These channels house the stereochemically active lone pair of electrons on the Sb^{3+} centers. A similar channel motif is also observed for $\text{Eu}_3\text{Sb}_4\text{S}_9$.¹

Magnetic Susceptibility. The dc magnetic susceptibility of $\text{Eu}_6\text{Sb}_6\text{S}_{17}$ between 2 and 300 K at an applied field of 0.1 T is shown in Figure 2.4. In the high-temperature regime, the susceptibility can be fit to the Curie-Weiss law with $\theta = -3.3$ K and $C = 35.5$ $\text{cm}^3 \text{mol}^{-1}$ K. The effective magnetic moment is $7.0 \mu_{\text{B}}/\text{Eu}$, which is somewhat lower than the expected free-ion moment of $7.9 \mu_{\text{B}}$ for Eu^{2+} . We attribute this to the presence of minor amounts of diamagnetic Sb_2S_3 , which is difficult to separate cleanly from $\text{Eu}_6\text{Sb}_6\text{S}_{17}$, as revealed by a powder X-ray diffraction analysis of the sample used for the magnetic measurements. The negative Weiss constant is consistent with antiferromagnetic coupling of the Eu^{2+} ions (the closest Eu–Eu separations are 4.1 Å), and is close to the 3.2 K transition observed in the susceptibility curve.

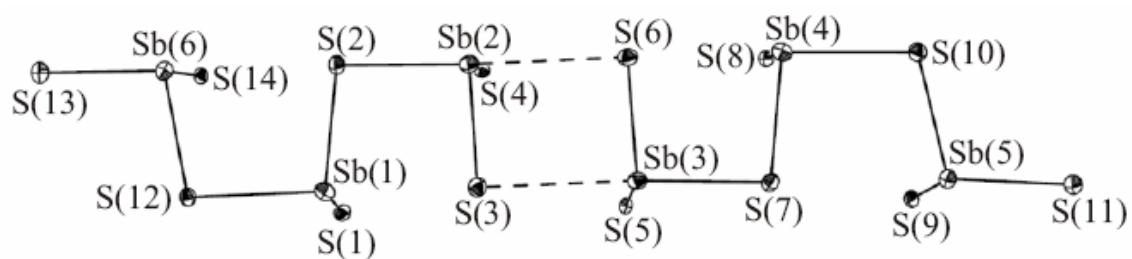


Figure 2.1. A view of the $[\text{Sb}_3\text{S}_7]^{5-}$ anions that consist of a trimer of corner-sharing SbS_3 units in $\text{Eu}_6\text{Sb}_6\text{S}_{17}$. 50% probability ellipsoids are depicted.

Table 2.3. Eu–S, Sb–S, and S–S Bond Distances (Å) for Eu₆Sb₆S₁₇.

| | | | |
|-------------|----------|-------------|----------|
| Eu(1)–S(1) | 3.000(3) | Eu(4)–S(8) | 3.010(2) |
| Eu(1)–S(2) | 3.056(3) | Eu(4)–S(9) | 3.044(2) |
| Eu(1)–S(4) | 2.987(3) | Eu(4)–S(13) | 3.382(3) |
| Eu(1)–S(5) | 2.984(3) | Eu(4)–S(15) | 3.066(3) |
| Eu(1)–S(10) | 3.028(3) | Eu(4)–S(16) | 3.157(3) |
| Eu(1)–S(13) | 3.081(3) | Eu(4)–S(17) | 3.098(3) |
| Eu(1)–S(14) | 3.009(3) | Eu(5)–S(1) | 3.039(3) |
| Eu(2)–S(1) | 3.008(3) | Eu(5)–S(8) | 2.980(2) |
| Eu(2)–S(3) | 3.010(3) | Eu(5)–S(9) | 3.082(2) |
| Eu(2)–S(4) | 2.962(3) | Eu(5)–S(10) | 3.073(3) |
| Eu(2)–S(5) | 2.981(2) | Eu(5)–S(12) | 3.168(3) |
| Eu(2)–S(11) | 2.944(3) | Eu(5)–S(14) | 2.984(3) |
| Eu(2)–S(12) | 3.209(3) | Eu(5)–S(15) | 3.110(3) |
| Eu(2)–S(14) | 2.982(3) | Eu(5)–S(16) | 3.208(2) |
| Eu(3)–S(4) | 3.015(3) | Eu(5)–S(17) | 3.027(2) |
| Eu(3)–S(5) | 3.005(3) | Eu(6)–S(1) | 2.988(3) |
| Eu(3)–S(6) | 3.023(3) | Eu(6)–S(8) | 3.046(2) |
| Eu(3)–S(8) | 3.024(2) | Eu(6)–S(9) | 3.035(2) |
| Eu(3)–S(9) | 2.968(2) | Eu(6)–S(11) | 3.063(3) |
| Eu(3)–S(15) | 3.132(3) | Eu(6)–S(13) | 3.167(3) |
| Eu(3)–S(16) | 3.235(3) | Eu(6)–S(14) | 3.017(3) |
| Eu(3)–S(17) | 3.051(3) | Eu(6)–S(15) | 3.095(2) |
| Eu(4)–S(4) | 3.005(3) | Eu(6)–S(16) | 3.197(3) |

| | | | |
|-------------|----------|-------------|----------|
| Eu(4)–S(5) | 3.009(2) | Eu(6)–S(17) | 3.101(3) |
| Eu(4)–S(7) | 3.077(3) | | |
| <hr/> | | | |
| Sb(1)–S(1) | 2.449(2) | Sb(4)–S(8) | 2.416(2) |
| Sb(1)–S(2) | 2.507(3) | Sb(4)–S(10) | 2.644(3) |
| Sb(1)–S(12) | 2.664(3) | Sb(5)–S(9) | 2.440(2) |
| Sb(2)–S(2) | 2.598(3) | Sb(5)–S(10) | 2.534(3) |
| Sb(2)–S(3) | 2.426(3) | Sb(5)–S(11) | 2.436(3) |
| Sb(2)–S(4) | 2.464(2) | Sb(6)–S(12) | 2.520(3) |
| Sb(3)–S(5) | 2.471(2) | Sb(6)–S(13) | 2.434(3) |
| Sb(3)–S(6) | 2.431(3) | Sb(6)–S(14) | 2.445(2) |
| Sb(3)–S(7) | 2.587(3) | S(15)–S(16) | 2.091(3) |
| Sb(4)–S(7) | 2.537(3) | S(16)–S(17) | 2.092(3) |
| <hr/> | | | |

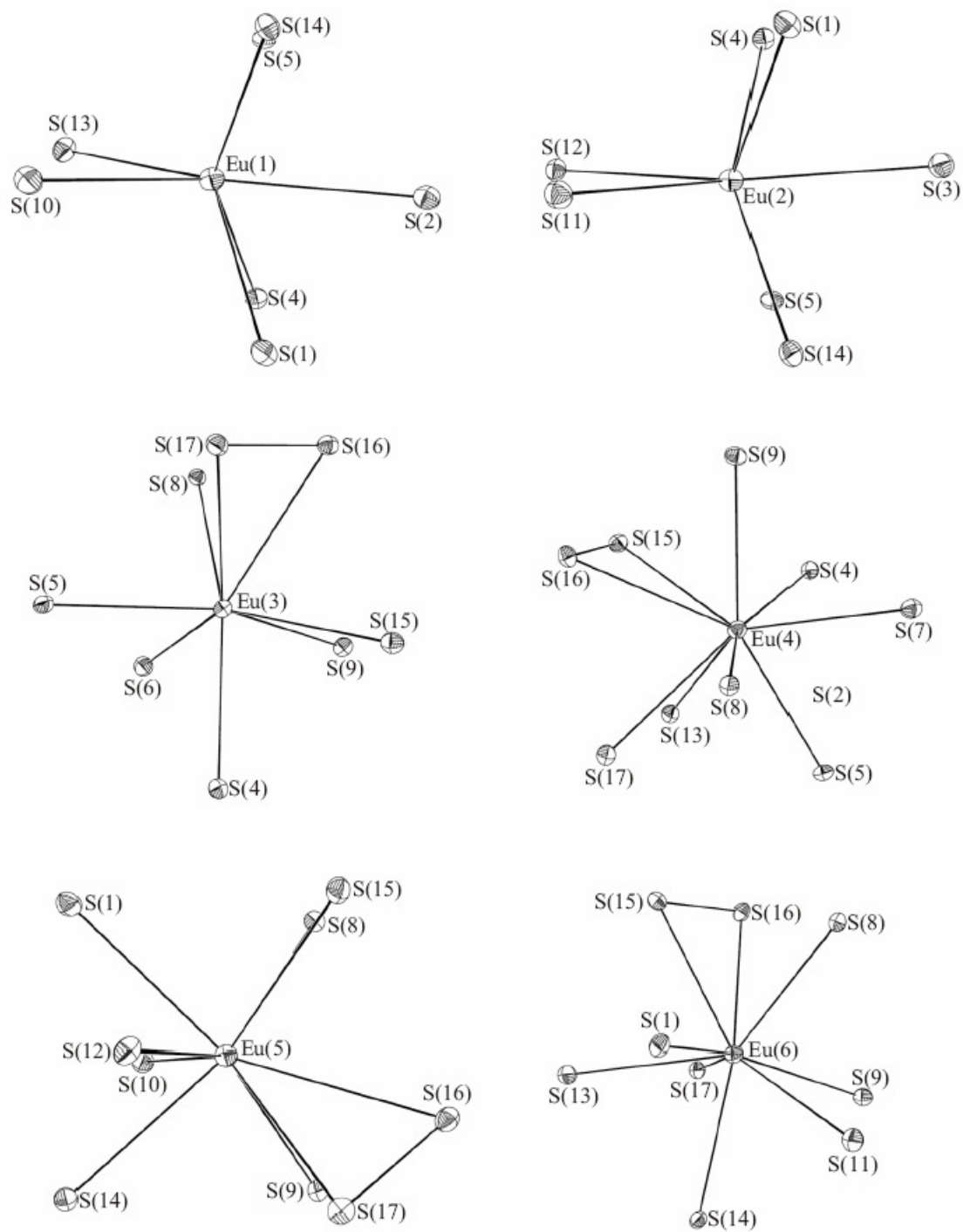


Figure 2.2. A depiction of the local environments of the six crystallographically unique Eu^{2+} cations in $\text{Eu}_6\text{Sb}_6\text{S}_{17}$. 50% probability ellipsoids are depicted.

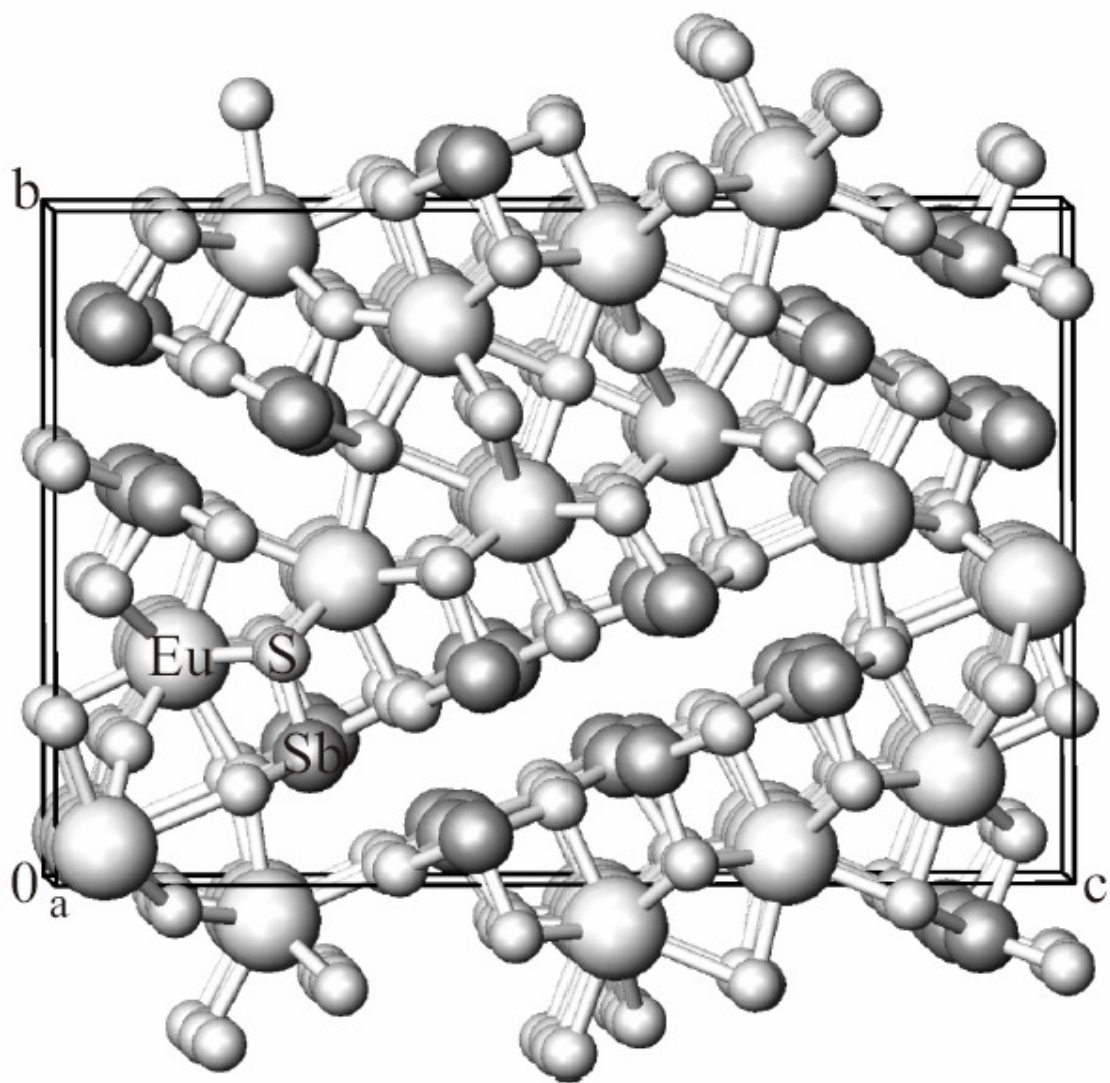


Figure 2.3. An illustration of the three-dimensional channel structure of $\text{Eu}_6\text{Sb}_6\text{S}_{17}$ viewed down the a axis. Eu-S bond have been omitted for clarity.

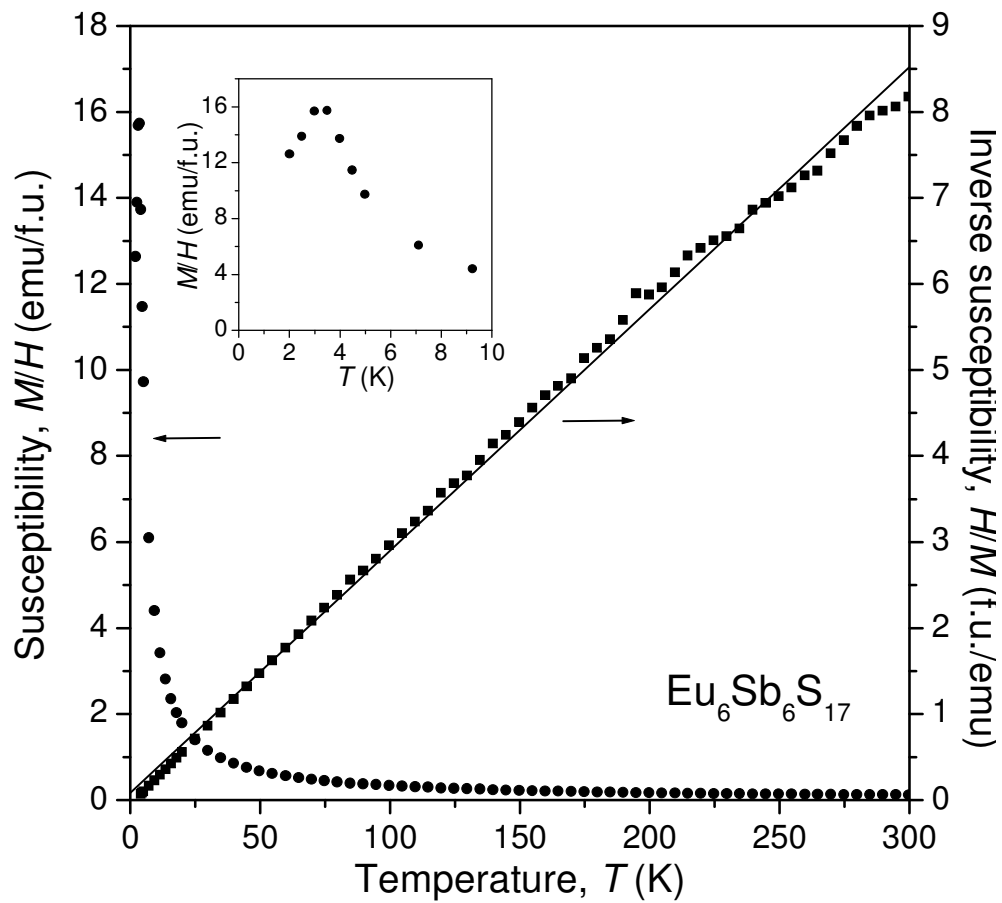


Figure 2.4. Plots of dc magnetic susceptibility and its inverse for $\text{Eu}_6\text{Sb}_6\text{S}_{17}$. The straight line shows a fit of the inverse susceptibility to the Curie-Weiss law.

REFERENCES

1. Lemoine, P.; Carré, D.; Guittard, M. *Acta Crystallogr.* **1981**, *B37*, 1281.
2. a) Evenson, C. R.; Dorhout, P. K. *Inorg. Chem.* **2001**, *40*, 2884. b) Kanatzidis, M. G. *Curr. Opin. Solid State Mater. Sci.* **1997**, *2*, 139.
3. a) Godzhaev, É. M.; Rustamov, P. G.; Guseinov, M. S.; Aliev, O. M. *Inorg. Mater.* **1997**, *13*, 512. (b) Harman, T. C.; Honig, J. M. *Thermoelectric and Thermomagnetic Effects and Applications*; McGraw Hill, New York, 1967.
4. Carré, D.; Guittard, M.; Jaulmes, S.; Julien-Pouzul, M.; Lemoine, P.; Laurelle, P.; Flahaut, J. J. *Less-Common Met.* **1985**, *110*, 349.
5. Guseinov, G. G.; Mamedov, F. K.; Amirasanov, I. R.; Mamedov, Kh. S. *Kristallografiya* **1981**, *26*, 831.
6. Gao, J.-Z.; Nakai, I.; Nagashima, K. *Bull. Chem. Soc. Jpn.* **1983**, *56*, 2615.
7. Gao, J.-Z.; Nakai, I.; Nagashima, K. *Bull. Chem. Soc. Jpn.* **1984**, *57*, 875.
8. Aliev, O. M.; Rustamov, P. G.; Guseinov, G. G.; Guseinov, M. S. *Izv. Akad. Nauk SSSR, Neorg. Mater.* **1978**, *14*, 1346.
9. Chen, J. H.; Dorhout, P. K. *J. Alloys and Compd.* **1997**, *249*, 199.
10. Choi, K.-S.; Hanko, J. A.; Kanatzidis, M. G. *J. Solid State Chem.* **1999**, *147*, 309.
11. Park, S.; Kim, S.-J. *J. Solid State Chem.* **2001**, *161*, 129.
12. Choi, K.-S.; Iordanidis, L.; Chondroudis, K.; Kanatzidis, M. G. *Inorg. Chem.* **1997**, *36*, 3804.
13. Iordanidis, L.; Schindler, J. L.; Kannewurf, C. R.; Kanatzidis, M. G. *J. Solid State Chem.* **1999**, *143*, 151.

14. Chung, D.-Y.; Iordanidis, L.; Choi, K.-S.; Kanatzidis, M. G. *Bull. Kor. Chem. Soc.* **1998**, *19*, 1283.
15. Choi, K.-S.; Kanatzidis, M. G. *Inorg. Chem.* **2000**, *39*, 5655.
16. Jin, G. B.; Wells, D. M.; Crerar, Shane J.; Shehee, T. C.; Mar, A.; Albrecht-Schmitt, T. E. *Acta Crystallogr.* **2005**, *E61*, i116.
17. Sheldrick, G. M. SHELXTL PC, Version 6.12, An Integrated System for Solving, Refining, and Displaying Crystal Structures from Diffraction Data; Siemens Analytical X-Ray Instruments, Inc.: Madison, WI 2001.
18. Sheldrick, G. M. SADABS 2001, Program for absorption correction using SMART CCD based on the method of Blessing; Blessing, R. H. *Acta Crystallogr.* **1995**, *A51*, 33.
19. Spek, A. L. *J. Appl. Crystallogr.* **2003**, *36*, 7.
20. Cordier, G.; Schäfer, H. *Z. Naturforsch.* **1979**, *34b*, 1053.
21. Schwidetzky, C. W. D. *Zur Struckturchemie der Alkali- und Erdalkali- Thio und Selenopnictate (III)*; Tech. Hochschule Darmstadt, 1985.
22. Brown, I. D.; Altermatt, D. *Acta Crystallogr.* **1985**, *B41*, 244.
23. Brese, N. E.; O’Keeffe, M. *Acta Crystallogr.* **1991**, *B47*, 192.

CHAPTER 3

SYNTHESES, STRUCTURES, AND MAGNETIC PROPERTIES OF THE EUROPIUM(II) SELENIDO PNICTOGENATES(III), EuPnSe_3 (Pn = Sb, Bi)

ABSTRACT

EuPnSe_3 (Pn = Sb, Bi) have been synthesized through the reaction of Eu with Pn_2Se_3 (Pn = Sb, Bi) and Se at 850 to 900 °C. These compounds are isotypic with SrPnSe_3 (Pn = Sb, Bi) and consist of square pyramidal PnSe_5 units and distorted PnSe_6 octahedra that form hollow columns that extend along the c axis. These columns are separated by Eu^{2+} cations that occur as nine-coordinate tricapped trigonal prisms. There are also additional V-shaped triselenide Se_3^{2-} anions between the columns that bind the Eu^{2+} cations. The Se...Se contacts (in EuSbSe_3) in these units are 2.4584(11) and 2.4359(11) Å, which are consistent with Se–Se single bonds. The overall structure is chiral. Bond-valence sum calculations indicate that this compound contains Eu^{2+} . Magnetic susceptibility measurements provide values of 7.66 μ_{B}/Eu for EuSbSe_3 and 7.64 μ_{B}/Eu for EuBiSe_3 , which are close to the expected free-ion moment for Eu^{2+} . These compounds follow essentially Curie behavior from 300 K to 5 K, and undergo an apparently antiferromagnetic transition below 5 K. ^{151}Eu and ^{121}Sb Mössbauer spectra of EuSbSe_3 and EuBiSe_3 were measured at different temperatures. The

presence of divalent europium and trivalent antimony were confirmed. The largely negative values of the isomer shift in ^{151}Eu spectrum show highly ionic bonding within these two compounds. Both of them show magnetic hyperfine field splitting at 4.2 K, which indicates a change in the orientation of the EFG principal axis with respect to the magnetic hyperfine field direction. EuSbSe_3 has slightly smaller electron density at the antimony nuclei, compared to Sb_2Se_3 . Crystallographic data: EuSbSe_3 , orthorhombic, space group $P2_12_12_1$, $a = 32.936(2) \text{ \AA}$, $b = 15.406(1) \text{ \AA}$, $c = 4.2622(3) \text{ \AA}$, $V = 2162.7(2) \text{ \AA}^3$, $Z = 16$, $R(F) = 2.63\%$ for 183 parameters and 5095 reflections with $I > 2\sigma(I)$; EuBiSe_3 , orthorhombic, space group $P2_12_12_1$, $a = 33.307(2) \text{ \AA}$, $b = 15.5804(9) \text{ \AA}$, $c = 4.2274(2) \text{ \AA}$, $V = 2193.7(2) \text{ \AA}^3$, $Z = 16$, $R(F) = 2.68\%$ for 183 parameters and 4895 reflections with $I > 2\sigma(I)$.

INTRODUCTION

Ternary europium pnictogen chalcogenide compounds form a rich group that is currently represented by EuPn_2Q_4 ($\text{Pn} = \text{Sb, Bi}$; $\text{Q} = \text{S, Se, Te}$),^{1,2} EuSb_4S_7 ,² $\text{Eu}_3\text{Sb}_4\text{S}_9$,³ $\text{Eu}_{1.1}\text{Bi}_2\text{S}_4$,⁴ Eu_2BiS_4 ,⁵ EuPn_4Q_7 ($\text{Pn} = \text{Sb, Bi}$; $\text{Q} = \text{S, Se}$),⁶ $\text{Eu}_3\text{Pn}_4\text{Q}_9$ ($\text{Pn} = \text{Sb, Bi}$; $\text{Q} = \text{S, Se, Te}$),⁶ $\text{Eu}_6\text{Sb}_6\text{S}_{17}$,⁷ and the metal-rich phase $\text{Eu}_4\text{Bi}_2\text{Te}$.⁸ The structures and properties of many of these compounds have been reviewed by Carré and co-workers.⁹ In addition to adopting novel structure types, these compounds possess interesting electronic properties that are often associated with the divalent or mixed-valent character of the Eu ions. Many of the aforementioned compounds contain Eu(II), which can be rationalized by the stability of the half-filled $4f^7$ shell. Eu_2BiS_4 contains both Eu(II) and Eu(III) in different crystallographic sites.⁵ The transport and magnetic properties of many of these

compounds have been measured. In this regard, one of the more interesting phases is Eu_2BiS_4 , which displays semi-metallic behavior ascribed to the mobility of electrons inside hexagonal channels within the structure.⁹

While europium pnictogen sulfides have good representation, less is known about selenides and tellurides. In an effort to better understand this system we have prepared the new phases EuPnSe_3 (Pn = Sb, Bi), which proved to be isotypic with SrPnSe_3 (Pn = Sb, Bi),^{10,11} determined their crystal structures, and measured their magnetic properties and ^{151}Eu and ^{121}Sb Mössbauer spectra, which are reported herein. The information in this chapter has been reported as full papers in *Journal of Solid-State Chemistry*.^{12,13}

EXPERIMENTAL

Syntheses. Eu (99.9%, Alfa-Aesar), Sb (99.5%, Alfa-Aesar), Bi (99.5%, Alfa-Aesar), and Se (99.5%, Alfa-Aesar) were used as received. Sb_2Se_3 and Bi_2Se_3 were prepared from the direct reaction of the elements in sealed fused-silica ampoules at 850 °C.

EuPnSe₃. *EuSbSe₃*: Eu (0.0595 g, 0.392 mmol), Sb_2Se_3 (0.0941 g, 0.196 mmol), and Se (0.0464 g, 0.588 mmol) or for *EuBiSe₃*: Eu (0.0508 g, 0.334 mmol), Bi_2Se_3 (0.1095 g, 0.167 mmol), and Se (0.0396 g, 0.501 mmol) were loaded into fused-silica ampoules that were then sealed under vacuum. The following heating profiles were used: *EuSbSe₃* - 2 °C/min from room temperature to 500 °C where it was held for 1 h, 0.5 °C/min to 850 °C where it was held for 6 d, 0.04 °C/min to 400 °C where it was held 2 d, and 0.5 °C/min to 24 °C; *EuBiSe₃*: 2 °C/min to 600 °C where it was held for 1 h, 0.5 °C/min to 900 °C where it was held for 4 d, 0.03 °C/min to 500 °C where it was held for

1 d, and 0.5 °C/min to 24 °C. In both cases the products consisted of thin black needles up to 2 mm in length. PXRD measurements confirmed phase purity by comparison with powder patterns calculated from the single crystal X-ray structures. Semi-quantitative SEM/EDX analyses were performed using a JEOL 840/Link Isis instrument. Eu, Sb, Bi, and Se percentages were calibrated against standards. The Eu:Pn(Sb, Bi):Se ratio determined from EDX analyses was approximately 1:1:3.

Crystallographic Studies. Single crystals of EuSbSe₃ and EuBiSe₃ were mounted on glass fibers and aligned on a Bruker SMART APEX CCD X-ray diffractometer and cooled to 193 K using an Oxford Cryostat. Intensity measurements were performed using graphite monochromated Mo K α radiation from a sealed tube and monocapillary collimator. SMART (v 5.624) was used for preliminary determination of the cell constants and data-collection control. The intensities of reflections of a sphere were collected by a combination of 3 sets of exposures (frames). Each set had a different ϕ angle for the crystal and each exposure covered a range of 0.3° in ω . A total of 1800 frames were collected with an exposure time per frame of 30 s for both compounds.

For EuSbSe₃ and EuBiSe₃ determination of integrated intensities and global refinement were performed with the Bruker SAINT (v 6.02) software package using a narrow-frame integration algorithm. A face-indexed numerical absorption correction was initially applied using XPREP.¹⁴ These data were subsequently treated with a semiempirical absorption correction by SADABS.¹⁵ The program suite SHELXTL (v 6.12) was used for space group determination (XPREP), direct methods structure solution (XS), and least-squares refinement (XL).¹⁴ The final refinements included anisotropic displacement parameters for all atoms and secondary extinction. Some crystallographic

details are given in Table 3.1. Atomic coordinates and equivalent isotropic displacement parameters for EuSbSe_3 and EuBiSe_3 can be found in Tables 3.2 and 3.3, respectively.

Magnetism. Magnetic susceptibility measurements were made between 2 and 300 K under zero-field-cooled conditions in an applied field of 0.5 T on a Quantum Design 9T-PPMS dc magnetometer / ac susceptometer. The susceptibility was corrected for contributions from the holder diamagnetism and the underlying sample diamagnetism. (Magnetic susceptibility measurements were performed by Shane J. Crerar and Arthur Mar at University of Alberta)

^{151}Eu and ^{121}Sb Mössbauer spectroscopy. The 21.53 keV transition of ^{151}Eu with an activity of 130 MBq (2% of the total activity of a $^{151}\text{Sm}:\text{EuF}_3$ source) and a $\text{Ba}^{121\text{m}}\text{SnO}_3$ source were used for the Mössbauer spectroscopic experiments, which were conducted in the usual transmission geometry. The measurements were performed with a commercial helium bath cryostat. The temperature of the absorber was varied between 4.2 K and room temperature, while the source was kept at room temperature. The temperature was controlled by a resistance thermometer (± 0.5 K accuracy). The samples were placed within a thin-walled PVC container at a thickness corresponding to about 10 Eu/cm^2 , respectively. (The Mössbauer spectroscopic experiments were conducted by Falko M. Schappacher and Rainer Pöttgen at Westfälische Wilhelms-Universität Münster)

RESULTS AND DISCUSSION

Structures of EuPnSe_3 (Pn = Sb, Bi). EuSbSe_3 and EuBiSe_3 are isotypic with SrPnSe_3 (Pn = Sb, Bi).^{10,11} The structure of EuSbSe_3 will be discussed with values for the Bi analog given parenthetically where important. There are four crystallographically

Table 3.1. Crystallographic Data for EuSbSe₃ and EuBiSe₃.

| | | |
|---|--|--|
| Formula | EuSbSe ₃ | EuBiSe ₃ |
| Formula Mass | 510.59 | 597.82 |
| Color and habit | Black needle | black needle |
| Crystal System | orthorhombic | orthorhombic |
| Space group | <i>P</i> 2 ₁ 2 ₁ 2 ₁ (No. 19) | <i>P</i> 2 ₁ 2 ₁ 2 ₁ (No. 19) |
| <i>a</i> (Å) | 32.936(2) | 33.307(2) |
| <i>b</i> (Å) | 15.406(1) | 15.5804(9) |
| <i>c</i> (Å) | 4.2622(3) | 4.2274(2) |
| <i>V</i> (Å ³) | 2162.7(2) | 2193.7(2) |
| <i>Z</i> | 16 | 16 |
| <i>T</i> (K) | 193 | 193 |
| λ (Å) | 0.71073 | 0.71073 |
| Maximum 2 θ (deg.) | 56.74 | 56.58 |
| R(int) | 0.0430 | 0.0494 |
| Reflections (total) | 21782 | 22502 |
| Reflections (ind.) | 5410 | 5470 |
| Parameter | 182 | 183 |
| Weighting scheme | 0.0298 | 0.0190 |
| Res. electron den. (min,max) | -3.029, 2.044 | -1.721, 2.856 |
| ρ_{calcd} (g cm ⁻³) | 6.273 | 7.240 |
| μ (Mo <i>K</i> α) (cm ⁻¹) | 365.10 | 631.10 |
| $R(F)$ for $F_o^2 > 2\sigma(F_o^2)$ | 0.0263 | 0.0268 |
| $R_w(F_o^2)^b$ | 0.0612 | 0.0538 |

$$^a R(F) = \frac{\sum ||F_o| - |F_c||}{\sum |F_o|}. \quad ^b R_w(F_o^2) = \left[\frac{\sum [w(F_o^2 - F_c^2)^2]}{\sum wF_o^4} \right]^{1/2}.$$

Table 3.2. Atomic Coordinates and Equivalent Isotropic Displacement Parameters for EuSbSe₃.

| Atom (site) | <i>x</i> | <i>y</i> | <i>z</i> | $U_{\text{eq}} (\text{\AA}^2)^a$ |
|-------------|--------------|------------|-------------|----------------------------------|
| Eu(1) | 0.576979(10) | 0.57063(2) | 0.49241(10) | 0.01218(8) |
| Eu(2) | 0.296366(10) | 0.13685(2) | 0.02213(11) | 0.01185(8) |
| Eu(3) | 0.328241(11) | 0.78806(2) | 0.55498(9) | 0.01190(8) |
| Eu(4) | 0.540637(11) | 0.22202(3) | 0.98005(11) | 0.01640(9) |
| Sb(1) | 0.863350(19) | 0.94069(4) | 0.97073(16) | 0.02636(13) |
| Sb(2) | 0.73758(2) | 0.87685(4) | 0.95831(17) | 0.03376(17) |
| Sb(3) | 0.522404(14) | 0.96358(3) | 0.48936(14) | 0.01751(11) |
| Sb(4) | 0.612807(16) | 0.80824(3) | 0.95840(15) | 0.01861(12) |
| Se(1) | 0.58106(2) | 0.02102(6) | 0.9515(3) | 0.0280(2) |
| Se(2) | 0.68091(2) | 0.84877(5) | 0.4793(3) | 0.0260(2) |
| Se(3) | 0.80227(2) | 0.91220(6) | 0.4644(4) | 0.0344(3) |
| Se(4) | 0.28659(2) | 0.98044(4) | 0.5007(2) | 0.01259(14) |
| Se(5) | 0.63578(2) | 0.65000(4) | 0.9772(2) | 0.01173(14) |
| Se(6) | 0.26013(2) | 0.78192(5) | 0.03648(19) | 0.01229(15) |
| Se(7) | 0.43833(2) | 0.27777(5) | 0.0203(2) | 0.01714(16) |
| Se(8) | 0.38870(2) | 0.71799(5) | 0.0379(2) | 0.01347(15) |
| Se(9) | 0.39990(2) | 0.92243(5) | 0.5091(2) | 0.01271(14) |
| Se(10) | 0.51079(2) | 0.61894(5) | 0.0084(2) | 0.01391(14) |
| Se(11) | 0.47580(2) | 0.89768(5) | 0.9407(2) | 0.0219(2) |
| Se(12) | 0.34292(2) | 0.94859(5) | 0.14871(18) | 0.01230(16) |

Table 3.3. Atomic Coordinates and Equivalent Isotropic Displacement Parameters for EuBiSe₃.

| Atom (site) | <i>x</i> | <i>y</i> | <i>z</i> | U_{eq} (Å ²) ^a |
|-------------|--------------|------------|-------------|--|
| Eu(1) | 0.423100(13) | 0.43651(3) | 0.50871(15) | 0.01152(10) |
| Eu(2) | 0.703237(13) | 0.86713(3) | 0.97886(15) | 0.01120(10) |
| Eu(3) | 0.673097(14) | 0.21559(3) | 0.44798(12) | 0.01090(11) |
| Eu(4) | 0.457513(14) | 0.78660(3) | 0.01679(16) | 0.01635(11) |
| Bi(1) | 0.139593(10) | 0.05145(2) | 0.01155(12) | 0.01252(8) |
| Bi(2) | 0.265127(10) | 0.12156(2) | 0.01405(12) | 0.01250(8) |
| Bi(3) | 0.478387(10) | 0.04741(2) | 0.51028(11) | 0.01252(8) |
| Bi(4) | 0.389701(10) | 0.19634(2) | 0.01923(12) | 0.01215(8) |
| Se(1) | 0.41803(3) | 0.98808(6) | 0.0436(3) | 0.0124(2) |
| Se(2) | 0.32141(3) | 0.15262(6) | 0.5316(3) | 0.0127(2) |
| Se(3) | 0.20035(3) | 0.08477(6) | 0.5422(3) | 0.0118(2) |
| Se(4) | 0.71366(2) | 0.02172(6) | 0.5002(3) | 0.01103(18) |
| Se(5) | 0.36444(3) | 0.35747(6) | 0.0229(3) | 0.01081(19) |
| Se(6) | 0.74097(3) | 0.21586(6) | 0.9655(3) | 0.0109(2) |
| Se(7) | 0.55806(3) | 0.73215(6) | 0.9767(3) | 0.01188(19) |
| Se(8) | 0.61263(3) | 0.28598(6) | 0.9668(3) | 0.0116(2) |
| Se(9) | 0.60217(3) | 0.08292(6) | 0.4901(3) | 0.01185(19) |
| Se(10) | 0.48925(3) | 0.38643(6) | -0.0049(3) | 0.01159(18) |
| Se(11) | 0.52751(3) | 0.11325(6) | 0.0509(2) | 0.0119(2) |
| Se(12) | 0.65795(3) | 0.05528(7) | -0.1459(2) | 0.0106(2) |

unique Eu atoms in the structures of EuPnSe_3 . All four Eu sites are nine-coordinate and occur as tricapped trigonal prisms. Eu–Se bond distances range from 3.0846(9) to 3.2950(9) Å (3.0907(12) to 3.3240(11) Å), 3.0516(8) to 3.3496(9) Å (3.0587(11) to 3.4417(11) Å), 3.0419(8) to 3.5712(9) Å (3.0449(11) to 3.5773(12) Å), and 3.1052(9) to 3.7031(10) Å (3.1042(12) to 3.7447(10) Å) for Eu(1), Eu(2), Eu(3), and Eu(4), respectively. These polyhedra are shown in Figure 3.1. Selected bond distances can be found in Tables 3.4 and 3.5. Bond-valence sum calculations provide values for the four Eu sites ranging from 1.60 to 2.27, implying Eu(II) character.^{16,17}

The coordination environments around the Sb centers are challenging to describe owing to the extreme variability in the Sb–Se bond lengths. For example, for Sb(3) there are three relatively short Sb–Se bonds of 2.6312(9), 2.6621(10), 2.8974(12) Å. If these are the sole contacts used then the geometry could be described as a distorted trigonal pyramid with a stereochemically active lone pair of electrons. However, there are three longer contacts ranging from 2.9759(11) to 3.1414(9) Å. It is probably best to describe this unit as a distorted octahedron. For Sb(1), Sb(2), and Sb(4) the sixth potential Sb···Se contact exceeds 3.4 Å, and these units are probably best described as square pyramids. The Sb and Se atoms form rectangular columns that extend down the *c* axis as is shown in Figure 3.2. These columns are formed from two opposing nets of square pyramidal SbSe_5 units that are linked by the SbSe_6 units (Figure 3.3). The lone pair of electrons on the Sb(III) centers appear to be contained within these columns. These rock-salt-like fragments are known from other ternary antimony and bismuth chalcogenide phases such as $\text{CsBi}_{3.67}\text{Se}_6$,¹⁸ $\text{Sr}_4\text{Bi}_6\text{Se}_{13}$,¹⁹ $\text{A}_{1+x}\text{Pb}_{4-2x}\text{Sb}_{7+x}\text{Se}_{15}$ ($\text{A} = \text{K}, \text{Rb}; 0 < x < 2$).²

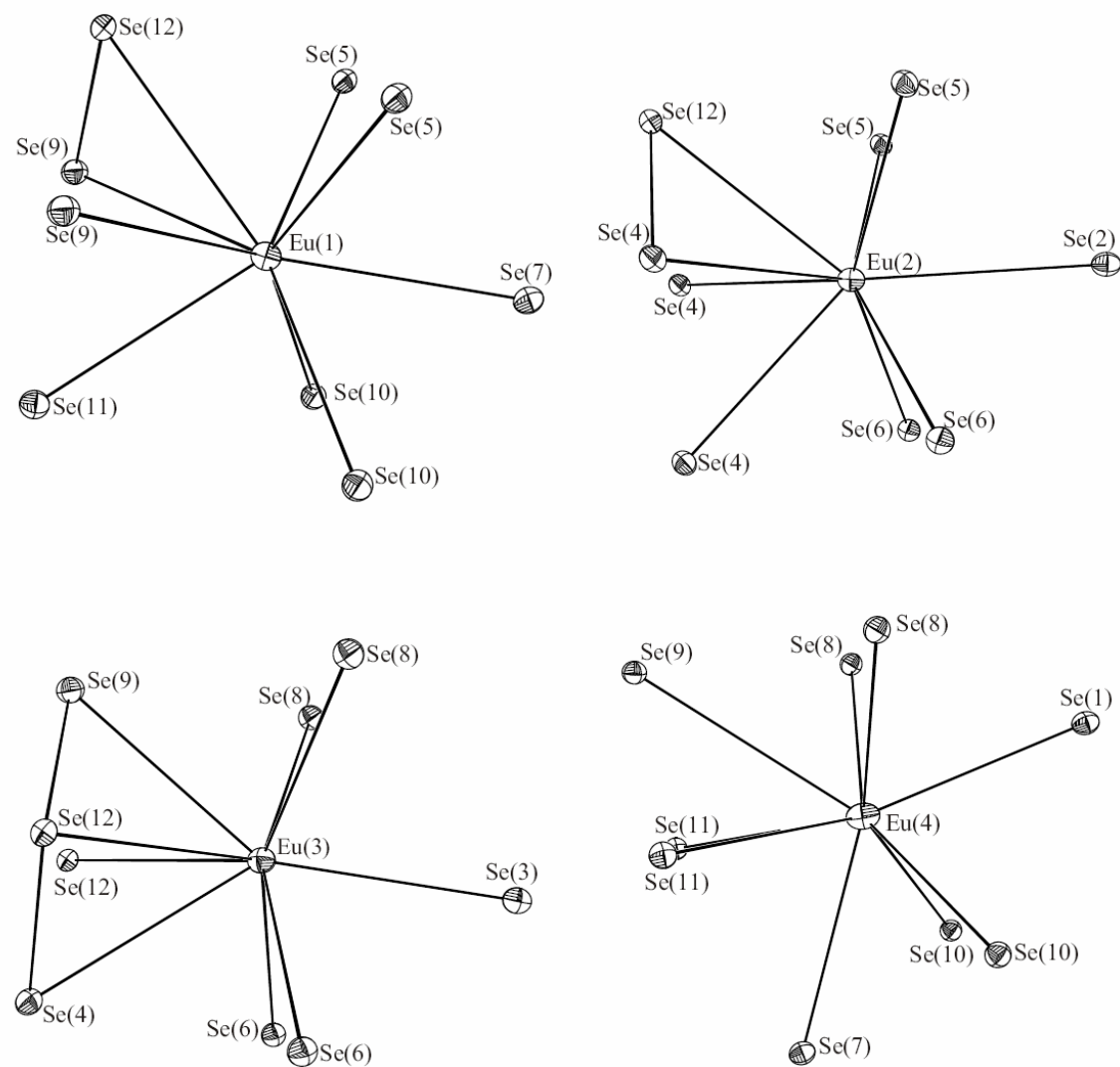


Figure 3.1. Illustrations of the nine-coordinate tricapped trigonal prismatic environments around the Eu centers in EuSbSe_3 .

Table 3.4. Selected Bond Distances (Å) for EuSbSe₃.

| Distances (Å) | | | |
|-----------------|------------|------------------|------------|
| Eu(1)–Se(5) | 3.0846(9) | Eu(4)–Se(8) #3 | 3.2083(9) |
| Eu(1)–Se(5) #1 | 3.1731(9) | Eu(4)–Se(9) #2 | 3.6567(8) |
| Eu(1)–Se(7) #4 | 3.2312(9) | Eu(4)–Se(10) #2 | 3.1183(9) |
| Eu(1)–Se(9) #2 | 3.2104(9) | Eu(4)–Se(10) #12 | 3.1850(9) |
| Eu(1)–Se(9) #3 | 3.2189(9) | Eu(4)–Se(11) #2 | 3.2911(10) |
| Eu(1)–Se(10) #1 | 3.0923(9) | Eu(4)–Se(11) #12 | 3.7031(10) |
| Eu(1)–Se(10) | 3.1848(9) | Sb(1)–Se(1) #14 | 2.8108(12) |
| Eu(1)–Se(11) #2 | 3.1940(9) | Sb(1)–Se(1) #15 | 2.9323(13) |
| Eu(1)–Se(12) #2 | 3.2950(9) | Sb(1)–Se(3) #5 | 2.9438(14) |
| Eu(2)–Se(2) #3 | 3.3496(9) | Sb(1)–Se(3) | 2.9829(13) |
| Eu(2)–Se(4) #8 | 3.1734(9) | Sb(1)–Se(8) #13 | 2.5834(10) |
| Eu(2)–Se(4) #6 | 3.2769(8) | Sb(2)–Se(2) | 2.7999(12) |
| Eu(2)–Se(4) #9 | 3.2936(9) | Sb(2)–Se(2) #5 | 2.9329(14) |
| Eu(2)–Se(5) #3 | 3.0927(9) | Sb(2)–Se(3) | 3.0442(15) |
| Eu(2)–Se(5) #2 | 3.0967(9) | Sb(2)–Se(3) #5 | 3.0804(13) |
| Eu(2)–Se(6) #6 | 3.0516(8) | Sb(2)–Se(6) #13 | 2.5562(9) |
| Eu(2)–Se(6) #7 | 3.1358(8) | Sb(3)–Se(1) #19 | 2.8974(12) |
| Eu(2)–Se(12) #9 | 3.3247(9) | Sb(3)–Se(1) #20 | 3.1257(11) |
| Eu(3)–Se(3) #10 | 3.2026(10) | Sb(3)–Se(7) #4 | 3.1414(9) |
| Eu(3)–Se(4) | 3.2740(8) | Sb(3)–Se(10) #18 | 2.6312(9) |
| Eu(3)–Se(6) #5 | 3.0419(8) | Sb(3)–Se(11) | 2.6621(10) |
| Eu(3)–Se(6) | 3.1505(8) | Sb(3)–Se(11) #1 | 2.9759(11) |

| | | | |
|-----------------|------------|-----------------|------------|
| Eu(3)–Se(8) #5 | 3.0606(8) | Sb(4)–Se(2) | 3.0969(12) |
| Eu(3)–Se(8) | 3.1604(9) | Sb(4)–Se(2) #5 | 3.2172(11) |
| Eu(3)–Se(9) | 3.1453(8) | Sb(4)–Se(5) | 2.5537(9) |
| Eu(3)–Se(12) #1 | 3.0575(9) | Sb(4)–Se(7) #4 | 2.6870(10) |
| Eu(3)–Se(12) | 3.5712(9) | Sb(4)–Se(7) #18 | 2.8272(11) |
| Eu(4)–Se(1) | 3.3727(10) | Se(4)–Se(12) #5 | 2.4359(11) |
| Eu(4)–Se(7) #5 | 3.4814(9) | Se(12)–Se(9) #5 | 2.4584(11) |
| Eu(4)–Se(8) #2 | 3.1052(9) | | |

Symmetry transformations used to generate equivalent atoms:

| | | |
|---------------------------|---------------------------|---------------------------|
| #1 $x, y, z-1$ | #2 $-x+1, y-1/2, -z+3/2$ | #3 $-x+1, y-1/2, -z+1/2$ |
| #4 $-x+1, y+1/2, -z+1/2$ | #5 $x, y, z+1$ | #6 $-x+1/2, -y+1, z-1/2$ |
| #7 $-x+1/2, -y+1, z+1/2$ | #8 $x, y-1, z$ | #9 $x, y-1, z-1$ |
| #10 $x-1/2, -y+3/2, -z+1$ | #11 $x-1/2, -y+3/2, -z+2$ | #12 $-x+1, y-1/2, -z+5/2$ |
| #13 $x+1/2, -y+3/2, -z+1$ | #14 $-x+3/2, -y+1, z+1/2$ | #15 $-x+3/2, -y+1, z-1/2$ |
| #16 $-x+3/2, -y+2, z+1/2$ | #17 $x+1/2, -y+3/2, -z+2$ | #18 $-x+1, y+1/2, -z+3/2$ |
| #19 $x, y+1, z$ | #20 $x, y+1, z-1$ | |

Table 3.5. Selected Bond Distances (Å) for EuBiSe₃.

| Distances (Å) | | | |
|-----------------|------------|------------------|------------|
| Eu(1)–Se(5) | 3.0907(12) | Eu(4)–Se(8) #3 | 3.1976(12) |
| Eu(1)–Se(5) #1 | 3.1714(12) | Eu(4)–Se(9) | 3.7447(10) |
| Eu(1)–Se(7) #4 | 3.2457(11) | Eu(4)–Se(10) #2 | 3.1339(12) |
| Eu(1)–Se(9) #2 | 3.2187(13) | Eu(4)–Se(10) #11 | 3.2010(12) |
| Eu(1)–Se(9) #3 | 3.2251(13) | Eu(4)–Se(11) #2 | 3.2991(12) |
| Eu(1)–Se(10) #1 | 3.1130(12) | Eu(4)–Se(11) #11 | 3.6472(12) |
| Eu(1)–Se(10) | 3.1901(12) | Bi(1)–Se(1) #13 | 2.8243(11) |
| Eu(1)–Se(11) #2 | 3.2177(11) | Bi(1)–Se(1) #14 | 3.0206(11) |
| Eu(1)–Se(12) #2 | 3.3240(11) | Bi(1)–Se(3) #5 | 2.8812(11) |
| Eu(2)–Se(2) #3 | 3.4417(11) | Bi(1)–Se(3) | 3.0652(12) |
| Eu(2)–Se(4) #8 | 3.1647(12) | Bi(1)–Se(8) #12 | 2.6890(10) |
| Eu(2)–Se(4) #6 | 3.2663(10) | Bi(2)–Se(2) #5 | 2.8118(12) |
| Eu(2)–Se(4) #9 | 3.2833(13) | Bi(2)–Se(2) | 2.9216(12) |
| Eu(2)–Se(5) #3 | 3.0889(12) | Bi(2)–Se(3) #5 | 2.9939(11) |
| Eu(2)–Se(5) #2 | 3.0988(12) | Bi(2)–Se(3) | 3.1573(11) |
| Eu(2)–Se(6) #6 | 3.0587(11) | Bi(2)–Se(6) #12 | 2.6592(10) |
| Eu(2)–Se(6) #7 | 3.1360(12) | Bi(3)–Se(1) #16 | 2.9641(11) |
| Eu(2)–Se(12) #9 | 3.3387(12) | Bi(3)–Se(1) #17 | 3.1589(11) |
| Eu(3)–Se(3) #10 | 3.2405(11) | Bi(3)–Se(7) #4 | 3.1246(10) |
| Eu(3)–Se(4) | 3.3164(10) | Bi(3)–Se(10) #15 | 2.7298(10) |
| Eu(3)–Se(6) #5 | 3.0449(11) | Bi(3)–Se(11) | 2.7387(11) |
| Eu(3)–Se(6) | 3.1459(11) | Bi(3)–Se(11) #1 | 2.9918(11) |

| | | | |
|-----------------|------------|-----------------|------------|
| Eu(3)–Se(8) #5 | 3.0657(12) | Bi(4)–Se(2) #5 | 3.1444(11) |
| Eu(3)–Se(8) | 3.1731(12) | Bi(4)–Se(2) | 3.2141(11) |
| Eu(3)–Se(9) | 3.1440(10) | Bi(4)–Se(5) | 2.6479(10) |
| Eu(3)–Se(12) #1 | 3.0725(12) | Bi(4)–Se(7) #15 | 2.7808(12) |
| Eu(3)–Se(12) | 3.5773(12) | Bi(4)–Se(7) #4 | 2.8069(12) |
| Eu(4)–Se(1) | 3.4053(11) | Se(4)–Se(12) #1 | 2.4400(14) |
| Eu(4)–Se(7) #5 | 3.4590(10) | Se(12)–Se(9) #1 | 2.4503(15) |
| Eu(4)–Se(8) #2 | 3.1042(12) | | |

Symmetry transformations used to generate equivalent atoms:

| | | |
|---------------------------|---------------------------|---------------------------|
| #1 $x, y, z+1$ | #2 $-x+1, y+1/2, -z+1/2$ | #3 $-x+1, y+1/2, -z+3/2$ |
| #4 $-x+1, y-1/2, -z+3/2$ | #5 $x, y, z-1$ | #6 $-x+3/2, -y+1, z+1/2$ |
| #7 $-x+3/2, -y+1, z-1/2$ | #8 $x, y+1, z$ | #9 $x, y+1, z+1$ |
| #10 $x+1/2, -y+1/2, -z+1$ | #11 $-x+1, y+1/2, -z-1/2$ | #12 $x-1/2, -y+1/2, -z+1$ |
| #13 $-x+1/2, -y+1, z-1/2$ | #14 $-x+1/2, -y+1, z+1/2$ | #15 $-x+1, y-1/2, -z+1/2$ |
| #16 $x, y-1, z$ | #17 $x, y-1, z+1$ | |

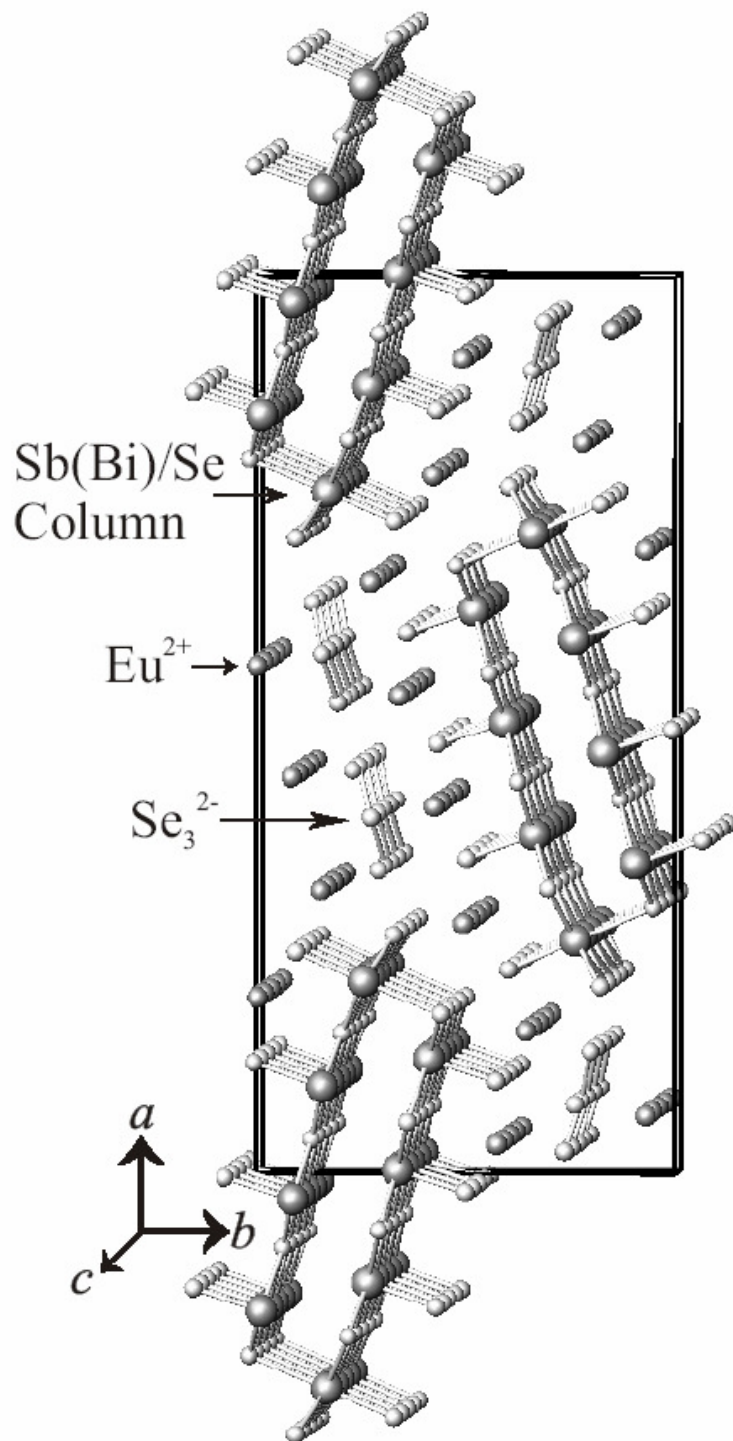


Figure 3.2. A view of the one-dimensional rectangular columns formed from Pn (Pn = Sb, Bi) and Se in EuPnSe_3 . These columns extend down the c axis and are separated by Eu^{2+} cations and Se_3^{2-} anions.

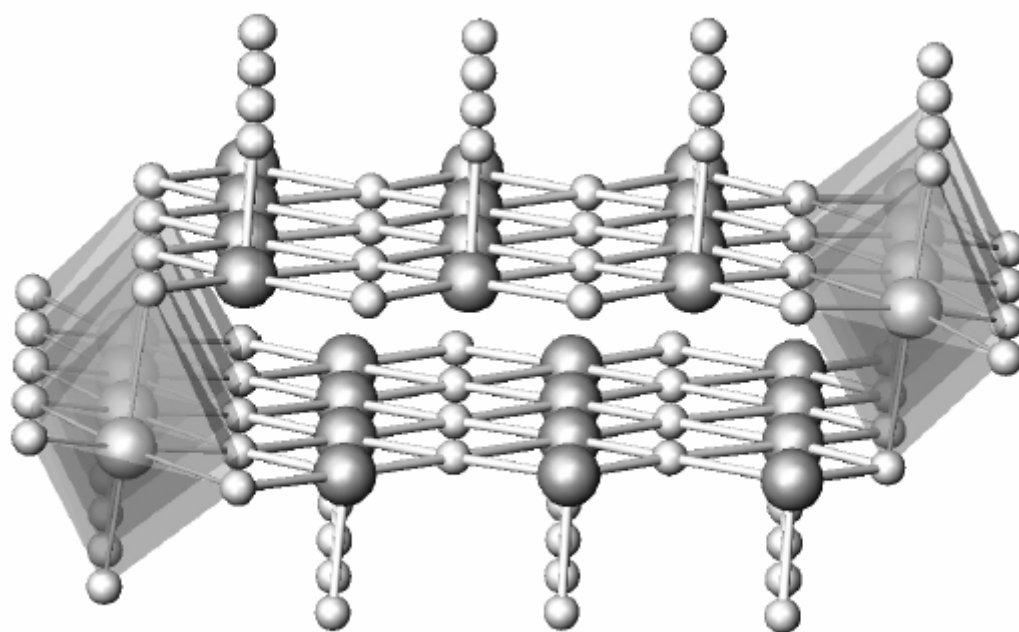


Figure 3.3. A depiction of the Pn/Se columns in EuPnSe_3 ($\text{Pn} = \text{Sb}, \text{Bi}$) that are formed from two opposing nets of square pyramidal PnSe_5 units that are linked by PnSe_6 octahedra.

In addition to the Sb(Bi)/Se columns, there are also triselenide units. These V-shaped Se_3^{2-} anions are also aligned along the c axis, and although they might be considered to be the most obvious source for the acentricity of EuPnSe_3 ($P2_12_12_1$ is chiral), groups of these units are aligned antiparallel with one another (see Figure 3.2). The Se...Se contacts, 2.4584(11) and 2.4359(11) Å, are typical of that expected for a single bond. For example, the Se–Se bonds the triselenide units in Sr_2SnSe_5 and Ba_2SnSe_5 range from 2.38 to 2.44 Å.^{21,22} In $\text{Eu}_8(\text{Sn}_4\text{Se}_{14})(\text{Se}_3)_2$ the Se–Se bonds in the triselenide units are 2.398(2) and 2.416(2).²³ EuSbSe_3 and EuBiSe_3 can then be formulated as $\text{Eu}^{2+}\times 4$ (for each crystallographically unique Eu center)/ $\text{Pn}^{3+}\times 4/\text{Se}^{2-}\times 9/\text{Se}_3^{2-}$.

Magnetic Susceptibility. Plots of the zero-field-cooled molar magnetic susceptibility and its inverse for EuSbSe_3 and EuBiSe_3 from 2 to 300 K at an applied field of 5 kOe are shown in Figure 3.4 and 3.5. Although the inverse susceptibility can be fit to the Curie-Weiss law, the Weiss constants are very small and close to zero (–0.5 to –1.0 K) for both compounds. The Curie constants are 7.0 emu K mol^{–1} for EuSbSe_3 and 6.9 emu K mol^{–1} for EuBiSe_3 , which correspond to an effective magnetic moment of 7.6 μ_B per europium in both cases. As this value is only slightly smaller than the theoretical free-ion magnetic moment for Eu^{2+} (7.9 μ_B),²⁴ the presence of divalent europium is essentially confirmed. There is an apparent transition below 5 K in the susceptibility curves, but whether it can be clearly attributed to a long-range antiferromagnetic ordering remains to be further investigated.

¹⁵¹Eu Mössbauer spectroscopy. The ¹⁵¹Eu Mössbauer spectra of EuSbSe_3 and EuBiSe_3 at 298, 77, and 4.2 K are presented in Figures 3.6 and 3.7 together with transmission integral fits. The corresponding fitting parameters are listed in Table 3.6.

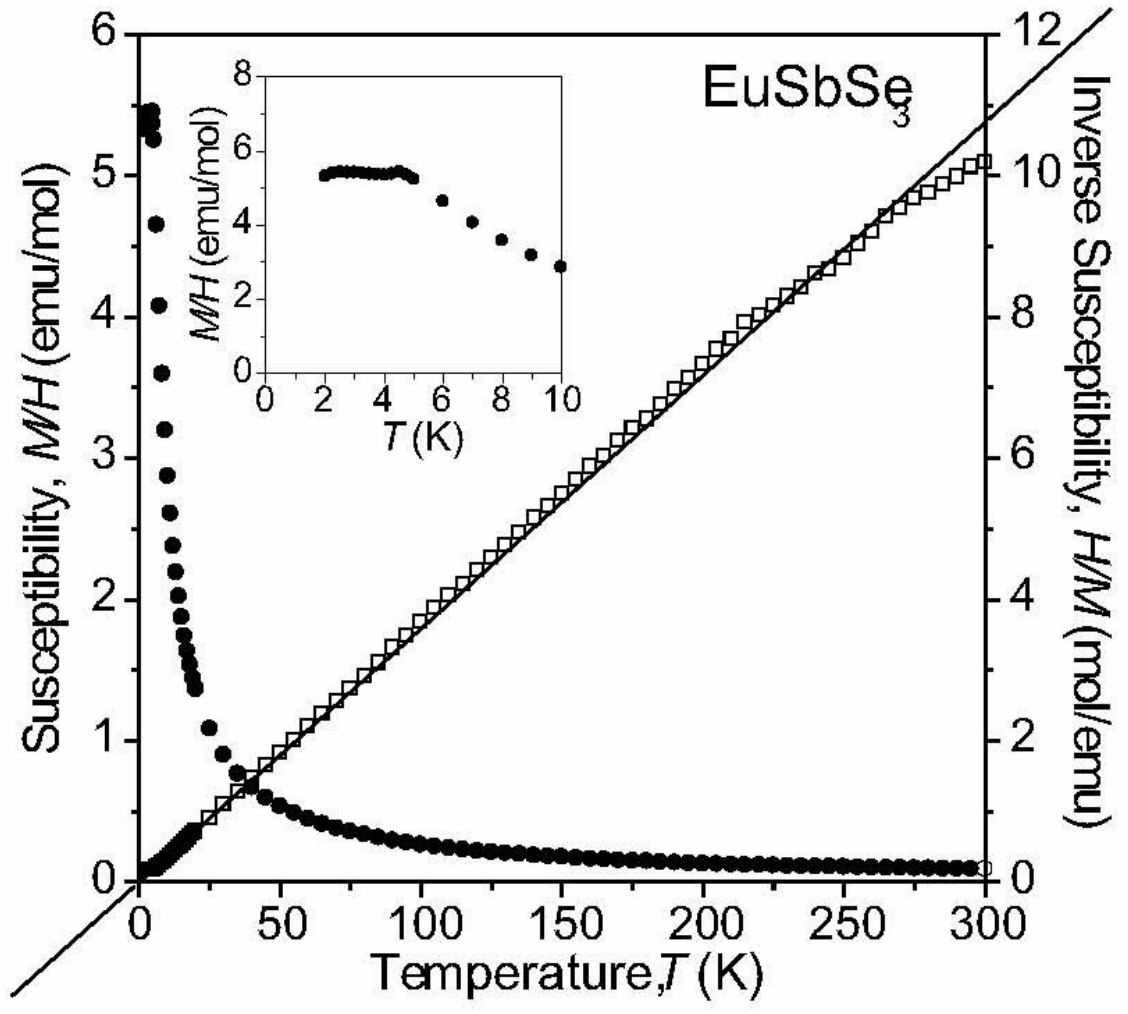


Figure 3.4. Plots of dc magnetic susceptibility (\bullet) and its inverse (\square) for EuSbSe_3 . The straight lines represent fits of the inverse susceptibility to the Curie-Weiss law. The inset shows the low-temperature behavior of the susceptibility.

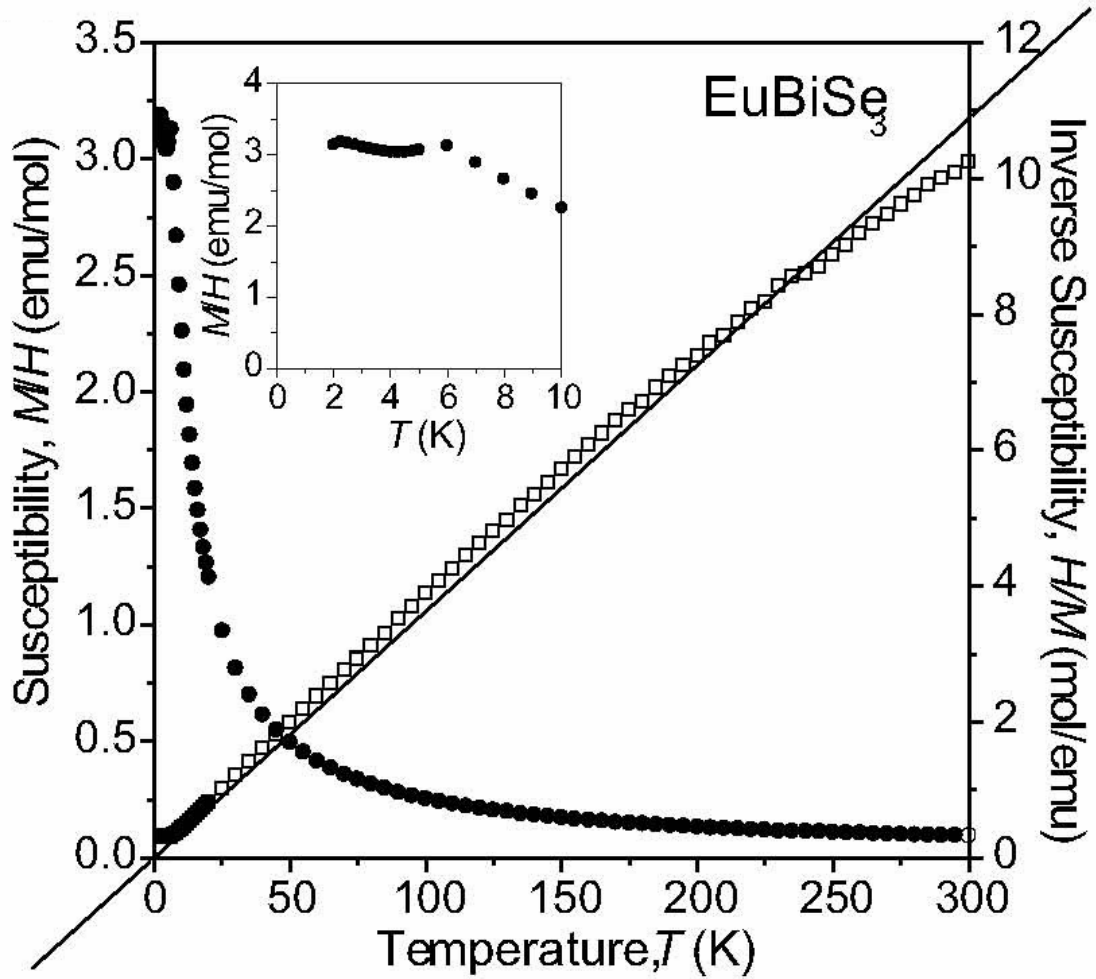


Figure 3.5. Plots of dc magnetic susceptibility (\bullet) and its inverse (\square) for EuBiSe_3 . The straight lines represent fits of the inverse susceptibility to the Curie-Weiss law. The inset shows the low-temperature behavior of the susceptibility.

Both samples show significant absorption, leading to medium signal-to-noise ratios. To give an example, the 4.2 K data of EuBiSe_3 were collected over a period of five days.

At room temperature EuBiSe_3 (Figure 3.7) shows a single signal at an isomer shift of $-12.18(2)$ mm/s, indicating purely divalent europium, in full agreement with the magnetic data. The largely negative value of the isomer shift is indicative for highly ionic bonding within EuBiSe_3 . Similar data have been observed at 7 K, slightly above the Néel temperature. The slightly higher line width (in comparison to the room temperature data) indicates already the onset of magnetic ordering.

The room temperature spectrum of EuSbSe_3 clearly shows two spectral contributions, a main signal at -12.10 mm/s, and a second one around 0 mm/s with an area ratio of 90/10. The minority contribution corresponds to a Eu^{III} impurity, most likely due to surface oxidation of the powdered sample.

Both compounds show magnetic hyperfine field splitting at 4.2 K. Since the Néel temperature of EuSbSe_3 is close to 4.2 K, we observe no full splitting. The detected hyperfine field at 4.2 K is 10.0 T. The area ratio of the Eu^{II} and Eu^{III} signals at 4.2 K is 94/6. For EuBiSe_3 with the higher Néel temperature of 6 K we observe the much higher hyperfine field of 21.2 T, a typical value for divalent europium compounds in the magnetically ordered state.²⁵ The magnetic hyperfine field splitting is associated with a reduction in the magnitude of the EFG parameter used to optimize the least-squares fits to the data (Table 3.6), indicating a change in the orientation of the EFG principal axis with respect to the magnetic hyperfine field direction. Similar behavior has recently also been observed for EuPdIn^{26} and $\text{Eu}_2\text{Si}_5\text{N}_8^{27}$.

The isomer shifts of EuSbSe_3 and EuBiSe_3 are slightly smaller than for the selenogermanates(IV) Eu_2GeSe_4 ($\delta = -12.43$ mm/s) and $\text{Eu}_2\text{Ge}_2\text{Se}_5$ ($\delta = -12.69$ mm/s),²⁸ indicating slightly higher ionicity in the selenogermanates with respect to the group (V) compounds. Comparable values of $\delta = -12.2(5)$ mm/s and $\delta = -12.08(10)$ mm/s have been observed for binary EuSe .^{29,30}

^{121}Sb Mössbauer spectroscopy. The ^{121}Sb resonance of EuSbSe_3 at 77 K is presented in Figure 3.8 together with a transmission integral fit. Although the structure contains four crystallographically independent antimony sites, the spectrum is well reproduced by a single signal at $\delta = -14.04(2)$ mm/s, an experimental line width of $\Gamma = 3.00(9)$ mm/s and a quadrupole splitting parameter of $\Delta E_Q = 1.66(6)$ mm/s. The latter is a consequence of the non-cubic site symmetry of the antimony sites. The four subspectra show superposition leading to a slightly enhanced line width.

The isomer shift is clearly indicative of trivalent antimony.³¹ It is in between the values for the sesquioxide Sb_2O_3 ($\delta = -11.3$ mm/s) and the sesquiselenide Sb_2Se_3 ($\delta = -15.0$ mm/s).^{31,32} We therefore observe slightly smaller electron density at the antimony nuclei in EuSbSe_3 with respect to Sb_2Se_3 . For EuSbSe_3 , the Sb(1), Sb(2), and Sb(4) sites are connected to five Se atoms and the Sb(3) positions are six-coordinate, if we only consider the $\text{Sb}\cdots\text{Se}$ contacts with bond distances less than 3.4 \AA . Bond-valence calculations show that the valence sum of Sb for all four Sb positions is 2.63 on average. In the case of Sb_2Se_3 , the Sb(1) positions are six-coordinate and the Sb(2) sites are in five-coordinate environments.³³ The average bond-valence sum of Sb is 2.70. This finding is not consistent with the above result from ^{121}Sb Mössbauer spectroscopy.

Longer Sb...Se contacts and the stereochemical activity of the long pair electrons of Sb³⁺ may affect the electron density at the antimony nuclei as well.

CONCLUSIONS

In this work we have demonstrated that two new ternary europium pnictogen selenides, namely EuSbSe₃ and EuBiSe₃, can be prepared via the reaction of Eu with Pn₂Se₃ (Pn = Sb, Bi) and Se. These compounds form as pure phases, and large single crystals exceeding 2 mm in length can be isolated. EuSbSe₃ and EuBiSe₃ possess complex structures containing one-dimensional antimony and bismuth selenide columns separated by Eu²⁺ cations and triselenide anions. Magnetic susceptibility measurements and ¹⁵¹Eu and ¹²¹Sb Mössbauer spectroscopy studies have revealed the presence of divalent europium and trivalent antimony. Both of these compounds have highly ionic bonding and magnetic hyperfine field splitting in ¹⁵¹Eu spectrum at 4.2 K. EuSbSe₃ has slightly smaller electron density at the antimony nuclei than Sb₂Se₃.

Table 3.6. Fitting parameters of ^{151}Eu Mössbauer measurements of EuBiSe_3 and EuSbSe_3 . Numbers in parentheses represent the statistical errors in the last digit. Parameters without standard deviation were kept fixed during the fitting procedure. (δ), isomer shift; (Γ), experimental line width; (B_{hf}), magnetic hyperfine field; ΔE_{Q} , electric quadrupole splitting parameter.

| T / K | δ / mms^{-1} | $\Delta E_{\text{Q}_1} / \text{mms}^{-1}$ | B_{hf} / T | Γ / mms^{-1} |
|---------------------------|----------------------------|---|----------------------------|----------------------------|
| EuBiSe₃ | | | | |
| 298 | -12.18(2) | 1.18(4) | – | 2.36(15) |
| 7 | -12.04(4) | 1.1(3) | – | 3.3(2) |
| 4.2 | -12.06(6) | -1.1 | 21.2(2) | 3.12(16) |
| EuSbSe₃ | | | | |
| 298 | -12.10(2) | 1.12(9) | – | 2.56(15) |
| 4.2 | -12.40(9) | -1.1 | 10.0(3) | 3.85 |

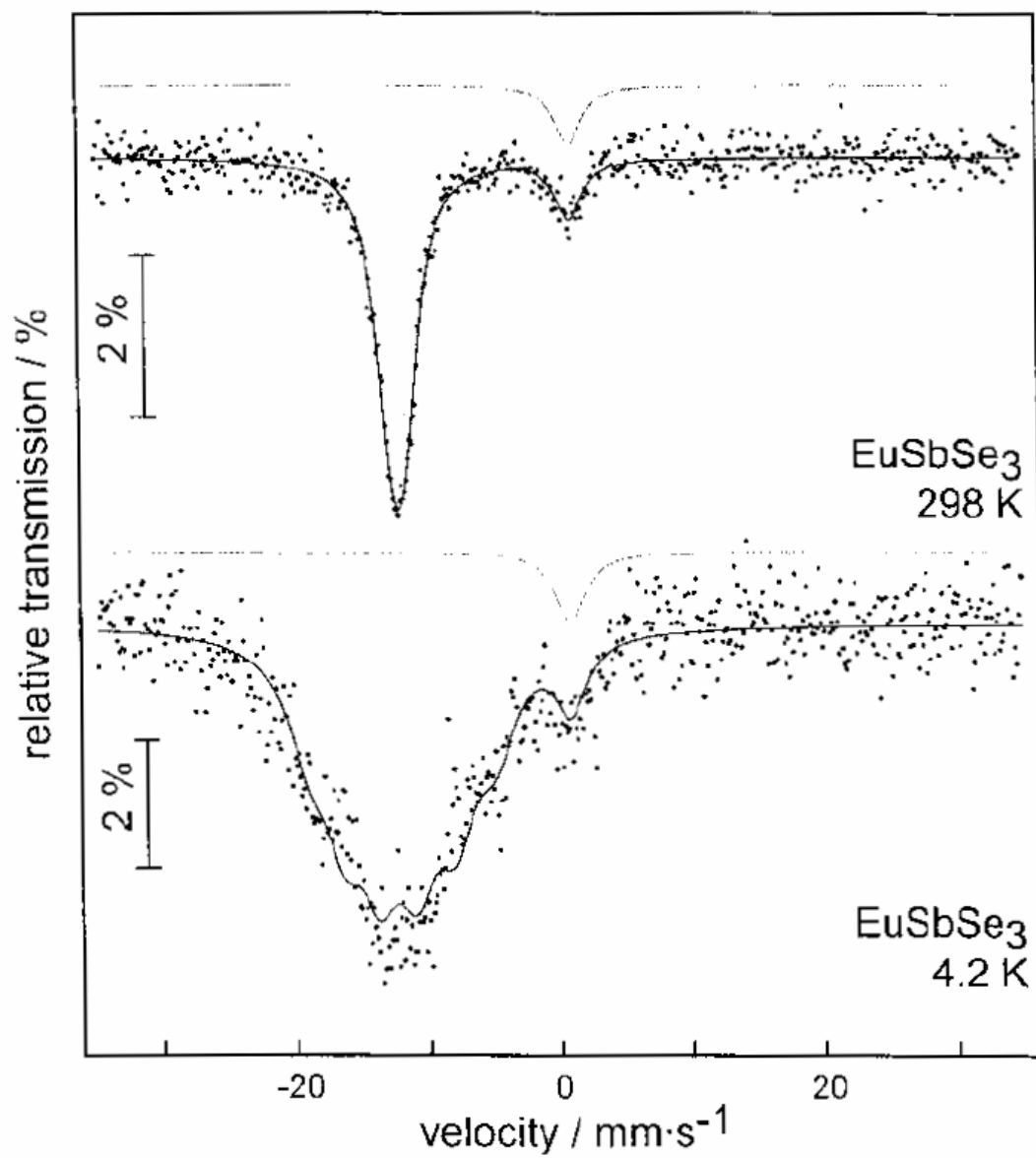


Figure 3.6. Experimental and simulated ¹⁵¹Eu Mössbauer spectra of EuSbSe₃ at various temperatures.

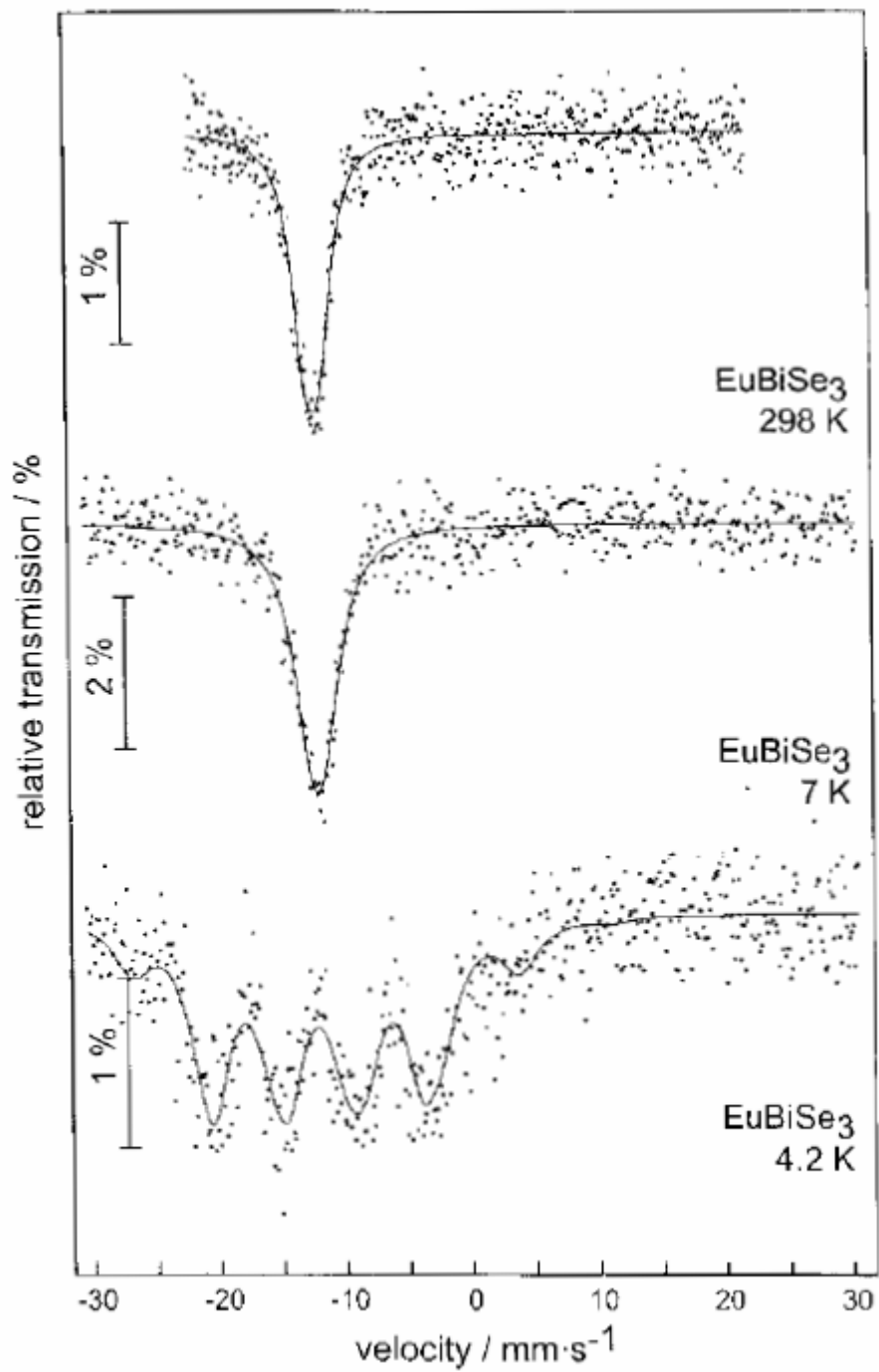


Figure 3.7. Experimental and simulated ¹⁵¹Eu Mössbauer spectra of EuBiSe₃ at various temperatures.

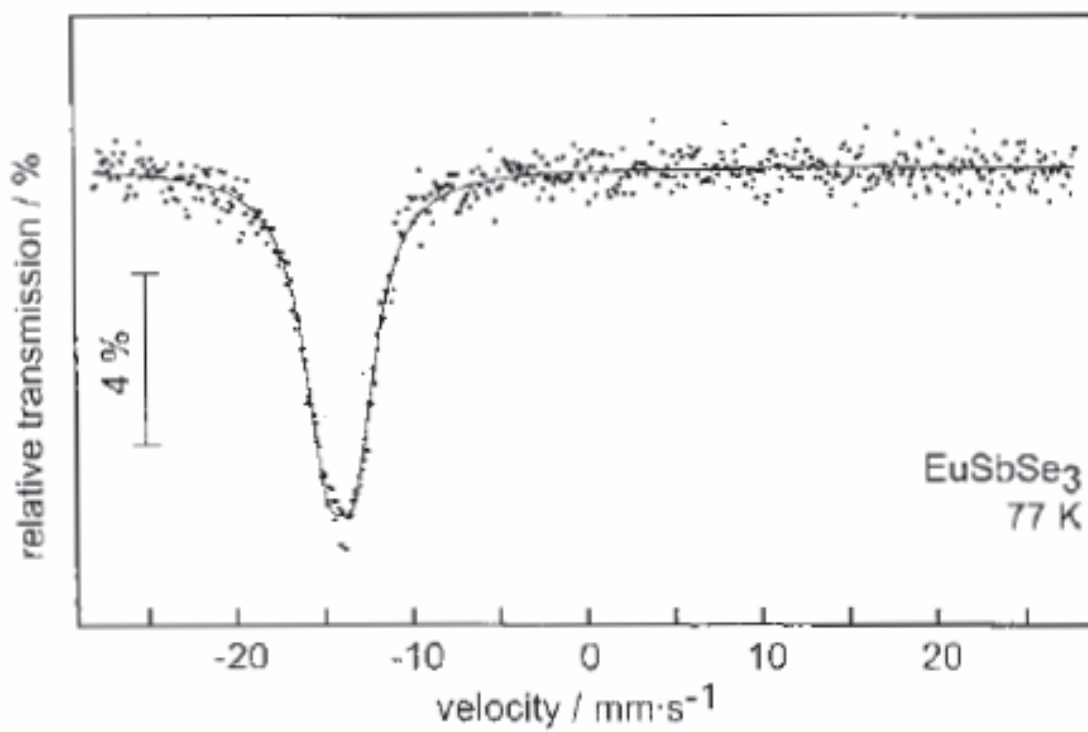


Figure 3.8. Experimental and simulated ¹²¹Sb Mössbauer spectrum of EuSbSe₃ at 77 K.

REFERENCES

1. Godzhaev, E. M.; Rustamov, P. G.; Guseinov, M. S.; Aliev, O. M. *Russ. J. Phys. Chem.* **1978**, *52*, 2424.
2. Aliev, O. M.; Rustamov, P. G.; Guseinov, G. G.; Guseinov, M. S. *Izvest. Akad. Nauk SSSR, Neorgan. Mater.* **1978**, *14*, 1346.
3. Lemoine, P.; Carré, D.; Guittard, M. *Acta Crystallogr.* **1981**, *B37*, 1281.
4. Lemoine, P.; Carré, D.; Guittard, M. *Acta Crystallogr.* **1986**, *C42*, 259.
5. Lemoine, P.; Carré, D.; Guittard, M. *Acta Crystallogr.* **1982**, *B38*, 727.
6. Aliev, O. M.; Maksudova, T. F.; Samsonova, N. D.; Finkel'shtein, L. D.; Rustamov, P. G. *Izvest. Akad. Nauk SSSR, Neorgan. Mater.* **1986**, *22*, 29.
7. Jin, G.; Wells, D. M.; Crerar, S. J.; Shehee, T. C.; Mar, A.; Albrecht-Schmitt, T. *E. Acta Crystallogr.* **2005**, *E61*, i116.
8. Hulliger, F. *Mater. Res. Bull.* **1979**, *14*, 259.
9. Carré, D.; Guittard, M.; Jaulmes, S.; Julien-Pouzul, M.; Lemoine, P.; Laurelle, P.; Flahaut, J. *J. Less-Common Met.* **1985**, *110*, 349.
10. Cook, R.; Schäfer, H. *Rev. Chim. Minér.* **1982**, *19*, 19.
11. Cook, R.; Schäfer, H. *Stud. Inorg. Chem.* **1982**, *3*, 757.
12. Jin, G. B.; Wells, D. M.; Crerar, Shane J.; Mar, A.; Albrecht-Schmitt, T. E. *J. Solid State Chem.* **2006**, *179*, 1596.
13. Schappacher, F. M.; Pöttgen, R.; Jin, G. B.; Albrecht-Schmitt, T. E. *J. Solid State Chem.* submitted.

14. Sheldrick, G. M. SHELXTL PC, Version 6.12, An Integrated System for Solving, Refining, and Displaying Crystal Structures from Diffraction Data; Siemens Analytical X-ray Instruments, Inc.: Madison, WI, 2001.
15. Sheldrick, G. M. *SADABS 2001, Program for absorption correction using SMART CCD based on the method of Blessing*; Blessing, R. H. *Acta Crystallogr.* **1995**, *A51*, 33.
16. Brown, I. D.; Altermatt, D. *Acta Crystallogr.* **1985**, *B41*, 244.
17. Brese, N. E.; O'Keeffe, M. *Acta Crystallogr.* **1991**, *B47*, 192.
18. Iordanidis, L.; Brazis, P. W.; Kyratsi, T.; Ireland, J.; Lane, M.; Kannewurf, C. R.; Chen, W.; Dyck, J. S.; Uher, C.; Ghelani, N. A.; Hogan, T.; Kanatzidis, M. G. *Chem. Mater.* **2001**, *13*, 622.
19. Cordier, G., Schäfer, H.; Schwidetzky, C. *Rev. Chim. Minér.* **1985**, *22*, 631.
20. Chung, D.-Y.; Iordanidis, L.; Choi, K.-S.; Kanatzidis, M. G. *Bull. Kor. Chem. Soc.* **1998**, *19*, 1281.
21. Assoud, A.; Soheilnia, N.; Kleinke, H. *J. Solid State Chem.* **2005**, *178*, 1087.
22. Assoud, A.; Soheilnia, N.; Kleinke, H. *Chem. Mater.* **2004**, *16*, 2215.
23. Evenson, C. R.; Dorhout, P. K. *Z. Anorg. Allg. Chem.* **2001**, *627*, 2178.
24. Kittel, C. *Introduction to Solid State Physics*; 6th Ed., Wiley, New York, 1986.
25. Pöttgen, R.; Johrendt, D. *Chem. Mater.* **2001**, *12*, 875.
26. Müllmann, R.; Mosel, B. D.; Eckert, H.; Kotzyba, G.; Pöttgen, R. *J. Solid State Chem.* **1998**, *137*, 174.
27. Höpfe, H. A.; Trill, H. B.; Mosel, D.; Eckert, H.; Kotzyba, G.; Pöttgen, R.; Schnick, W. *J. Phys. Chem. Solids* **2002**, *63*, 853.

28. Tampier, M.; Johrendt, D.; Pöttgen, R.; Kotzyba, G.; Rosenhahn, C.; Mosel, B. D. *Z. Naturforsch.* **2002**, *57b*, 133.
29. Hüfner, S.; Kienle, P.; Quitmann, D.; Brix, P. *Z. Phys.* **1965**, *187*, 67.
30. Streichele, E. *Z. Phys.* **1967**, *201*, 331.
31. Lippens, P. E. *Solid State Commun.* **2000**, *113*, 399.
32. Jumas, J.-C.; Olivier-Fourcade, J.; Ibanez, A.; Philippot, E. *Hyp. Int.* **1986**, *28*, 777.
33. Voutsas, G. P.; Papazoglou, A. G.; Rentzeperis, P. J. *Z. Kristallogr.* **1985**, *171*, 261.

CHAPTER 4

SYNTHESES, STRUCTURE, MAGNETISM, AND OPTICAL PROPERTIES OF THE ORDERED MIXED-LANTHANIDE SULFIDES, γ -LnLn'S₃ (Ln = La, Ce; Ln' = Er, Tm, Yb)

ABSTRACT

γ -LnLn'S₃ (Ln = La, Ce; Ln' = Er, Tm, Yb) have been prepared as dark red to black single crystals by the reaction of the respective lanthanides with sulfur in a Sb₂S₃ flux at 1000 °C. This isotypic series of compounds adopts a layered structure that consists of the smaller lanthanides (Er, Tm, and Yb) bound by sulfide in six- and seven-coordinate environments that are connected together by the larger lanthanides (La and Ce) in eight- and nine-coordinate environments. The layers can be broken down into three distinct one-dimensional substructures containing three crystallographically unique Ln' centers. The first of these is constructed from one-dimensional chains of edge-sharing [Ln'S₇] monocapped trigonal prisms that are joined to equivalent chains via edge-sharing to yield ribbons. There are parallel chains of [Ln'S₆] distorted octahedra that are linked to the first ribbons through corner-sharing. These latter units also share corners with a one-dimensional ribbon composed of parallel chains of [Ln'S₆] polyhedra that edge-share both in the direction of chain propagation and with adjacent identical chains.

Magnetic susceptibility measurements show Curie-Weiss behavior from 2 to 300 K with antiferromagnetic coupling, and no evidence for magnetic ordering. The θ_p values range from -0.4 to -37.5 K, and spin-frustration may be indicated for the Yb-containing compounds. All compounds show magnetic moments substantially reduced from those calculated for the free ions. The optical band gaps for γ -LaLn'S₃ (Ln' = Er, Tm, Yb) are approximately 1.6 eV, whereas γ -CeLn'S₃ (Ln' = Er, Tm, Yb) are approximately 1.3 eV.

INTRODUCTION

The structures and electronic properties of lanthanide chalcogenides are exquisitely tunable, allowing for the rational development of new optical¹⁻¹⁴ and magnetic materials.^{13,15-23} Even compositionally simple binary sesquisulfides of the trivalent lanthanides can have remarkably complex structures, and are found in at least seven different modifications ranging from A-type Ln₂S₃,²⁴ where the lanthanides are found in seven- and eight-coordinate geometries, to T-type²⁵ compounds that adopt the corundum structure with six-coordinate lanthanides.²⁴⁻³⁰ The structural complexity of the sesquisulfides is aptly illustrated by the F-type compounds that contain Ln³⁺ ions in three different environments as distorted octahedra and mono- and bicapped trigonal prisms.^{29,30} These structural features can be exploited for the development of potentially ordered ternary and quaternary mixed-lanthanide phases by systematically substituting smaller ions into lower coordination number sites and larger ions into higher coordination number sites (e.g. CeYb₃S₆).³¹⁻³³ However, disordering of the Ln³⁺ ions becomes increasingly problematic as the difference in the size of the ions becomes too small. While disorder of these ions can be advantageous from the perspective of doping (e.g. in

Ln:YAG),³⁴⁻³⁶ the preparation of materials where ordering of the lanthanide ions occurs allows for the exploration of structure-property relationships where different Ln³⁺ ions are structurally distinct.

In addition to disordered ternary mixed-lanthanide sesquisulfides adopting the F-Tm₃S₆ (e.g. ScEr₃S₆)^{29,33} and CeTmS₃³⁷ structures there are several known families of compounds where there is strong evidence for ordering of different Ln³⁺ ions. This is best known from α - and β -LnLn'S₃.³⁹⁻⁴³ α -LnLn'S₃ (Ln = Y, La, Ce, Nd; Ln' = Sc, Yb) adopts the ordered GdFeO₃³⁸ structure type.³⁹⁻⁴¹ Changes in bonding in ternary mixed-lanthanide sesquisulfides of a single composition can have dramatic effects on the electronic properties of these solids. For example, the band gap of β -LaYbS₃ is different than that of γ -LaYbS₃ (*vide infra*). Furthermore, there is also evidence supporting geometric spin-frustration in interlanthanide compounds.⁴³ In an effort to explore the possibility of spin-frustration and possible magnetic coupling between different lanthanide ions, we have prepared a series of new ordered mixed-lanthanide chalcogenides. Herein we disclose the syntheses, structure, magnetic susceptibility, and optical properties of the interlanthanide sulfides γ -LnLn'S₃ (Ln = La, Ce; Ln' = Er, Tm, Yb), and discuss the relationships between these details and those known for other materials in this class. The information in this chapter has been published as a full paper in *Chemistry of Materials*.⁴⁴

EXPERIMENTAL

Materials. La (99.9%, Alfa-Aesar), Ce (99.9%, Alfa-Aesar), Er (99.9%, Alfa-Aesar), Tm (99.9%, Alfa-Aesar), Yb (99.9%, Alfa-Aesar), S (99.5%, Alfa-Aesar), and Sb

(99.5%, Alfa-Aesar) were used as received. Sb_2S_3 was prepared from the direct reaction of the elements in sealed fused-silica ampoules at 850 °C.

Syntheses of $\gamma\text{-LnLn}'\text{S}_3$ (Ln = La, Ce; Ln' = Er, Tm, Yb). 200 mg of Ln, Ln', S, and Sb_2S_3 in a ratio of 1:1:3:0.5 were loaded into fused-silica ampoules in an argon-filled glovebox. The ampoules were sealed under vacuum and heated in a programmable tube furnace. The following heating profile was used: 2 °C/min to 500 °C (held for 1 h), 0.5 °C/min to 1000 °C (held for 5 d), 0.04 °C/min to 550 °C (held for 2 d), and 0.5 °C/min to 24 °C. In all cases high yields of dark red/black prisms of $\gamma\text{-LnLn}'\text{S}_3$ and unreacted Sb_2S_3 were obtained. The desired products can be separated from the flux during the cooling process by slightly tilting the furnace, which allows the flux to flow to the bottom of the tubes leaving crystals of $\gamma\text{-LnLn}'\text{S}_3$ behind, minimizing the need for manual separation of solids. Powder X-ray diffraction measurements were used to confirm phase purity by comparing the powder patterns calculated from the single crystal X-ray structures with the experimental data. Semi-quantitative SEM/EDX analyses were performed using JEOL 840/Link Isis or JEOL JSM-7000F instrument. Ln, Ln', and S percentages were calibrated against standards. Sb was not detected in the crystals. The Ln:Ln':S ratios were determined to be approximately 1:1:3 from EDX analyses.

Crystallographic Studies. Single crystals of $\gamma\text{-LnLn}'\text{S}_3$ (Ln = La, Ce; Ln' = Er, Tm, Yb) were mounted on glass fibers with epoxy and optically aligned on a Bruker APEX single crystal X-ray diffractometer using a digital camera. Initial intensity measurements were performed using graphite monochromated Mo $\text{K}\alpha$ ($\lambda = 0.71073 \text{ \AA}$) radiation from a sealed tube and monocapillary collimator. SMART (v 5.624) was used for preliminary determination of the cell constants and data-collection control. The

intensities of reflections of a sphere were collected by a combination of 3 sets of exposures (frames). Each set had a different ϕ angle for the crystal and each exposure covered a range of 0.3° in ω . A total of 1800 frames were collected with exposure times per frame of 10 or 20 seconds depending on the crystal.

For $\gamma\text{-LnLn}'\text{S}_3$ (Ln = La, Ce; Ln' = Er, Tm, Yb), determination of integrated intensities and global refinement were performed with the Bruker SAINT (v 6.02) software package using a narrow-frame integration algorithm. These data were treated first with a face-index numerical absorption correction using XPREP,⁴⁵ followed by a semi-empirical absorption correction using SADABS.⁴⁶ The program suite SHELXTL (v 6.12) was used for space group determination (XPREP), direct methods structure solution (XS), and least-squares refinement (XL).⁴⁵ The final refinements included anisotropic displacement parameters for all atoms and secondary extinction. Some crystallographic details are given in Table 4.1. As an example, atomic coordinates and equivalent isotropic displacement parameters for $\gamma\text{-LaYbS}_3$ are given in Table 4.2. It is important to note that we have expressed the formula of these compounds as $\gamma\text{-LnLn}'\text{S}_3$, which implies $Z = 12$. However, a more accurate description would be $\text{Ln}_3\text{Ln}'_3\text{S}_9$ with $Z = 4$, because there are three crystallographically unique sites for each type of lanthanide ion. We use $\gamma\text{-LnLn}'\text{S}_3$ here so that comparisons with other 1:1:3 interlanthanide compounds can be made more easily.

Powder X-ray Diffraction. Powder X-ray diffraction patterns were collected with a Rigaku Miniflex powder X-ray diffractometer using Cu $K\alpha$ ($\lambda = 1.54056 \text{ \AA}$) radiation.

Table 4.1. Crystallographic Data for γ -LnLn'S₃ (Ln = La, Ce; Ln' = Er, Tm, Yb).

| Formula | γ -LaErS ₃ | γ -LaTmS ₃ | γ -LaYbS ₃ | γ -CeErS ₃ | γ -CeTmS ₃ | γ -CeYbS ₃ |
|---|------------------------------|------------------------------|------------------------------|------------------------------|------------------------------|------------------------------|
| fw | 402.35 | 404.02 | 408.13 | 403.56 | 405.23 | 409.34 |
| Color | dark red | dark red | dark red | black | black | black |
| Crystal | orthorhombic | orthorhombic | orthorhombic | orthorhombic | orthorhombic | orthorhombic |
| Space | <i>Pnma</i> (No. | <i>Pnma</i> (No. | <i>Pnma</i> (No. | <i>Pnma</i> (No. | <i>Pnma</i> (No. | <i>Pnma</i> (No. |
| a (Å) | 16.510(1) | 16.4500(9) | 16.410 (1) | 16.4891(9) | 16.459(1) | 16.368(1) |
| b (Å) | 3.9963(2) | 3.9877(2) | 3.9847 (3) | 3.9705(2) | 3.9704(3) | 3.9562(2) |
| c (Å) | 21.260(1) | 21.215(1) | 21.202 (2) | 21.127(1) | 21.091(2) | 21.058(1) |
| V (Å ³) | 1402.7(2) | 1391.6(2) | 1386.4 (3) | 1383.1(2) | 1378.3(3) | 1363.6(2) |
| Z | 12 (4) | 12 (4) | 12 (4) | 12 (4) | 12 (4) | 12 (4) |
| T (K) | 193 | 193 | 193 | 193 | 193 | 193 |
| λ (Å) | 0.71073 | 0.71073 | 0.71073 | 0.71073 | 0.71073 | 0.71073 |
| ρ_{calcd} (g) | 5.716 | 5.785 | 5.866 | 5.814 | 5.859 | 5.982 |
| μ (cm ⁻¹) | 279.71 | 292.28 | 303.80 | 289.74 | 301.21 | 315.00 |
| R(F) ^a | 0.0297 | 0.0282 | 0.0328 | 0.0270 | 0.0300 | 0.0286 |
| R _w (F _o ²) | 0.0692 | 0.0744 | 0.0672 | 0.0675 | 0.0735 | 0.0803 |

$${}^a R(F) = \sum \left| |F_o| - |F_c| \right| / \sum |F_o| \text{ for } F_o^2 > 2\sigma(F_o^2). \quad {}^b R_w(F_o^2) = \left[\frac{\sum \left[w(F_o^2 - F_c^2)^2 \right]}{\sum wF_o^4} \right]^{1/2}.$$

Table 4.2. Atomic Coordinates and Equivalent Isotropic Displacement Parameters for γ -LaYbS₃.

| Atom (site) | x | y | z | $U_{\text{eq}} (\text{\AA}^2)^a$ |
|-------------|--------------|---------|--------------|----------------------------------|
| La(1) | 0.15941(4) | 0.2500 | 0.24448(3) | 0.00942(16) |
| La(2) | -0.16994(4) | 0.2500 | 0.41369(3) | 0.00593(15) |
| La(3) | -0.19293(4) | -0.2500 | 0.08024(3) | 0.00787(15) |
| Yb(1) | 0.06664(3) | 0.2500 | 0.42039(2) | 0.00756(13) |
| Yb(2) | -0.09466(3) | -0.2500 | 0.25016(3) | 0.01124(14) |
| Yb(3) | 0.05686(3) | -0.2500 | 0.06883(2) | 0.00886(13) |
| S(1) | -0.03553(18) | 0.2500 | 0.31730(14) | 0.0080(6) |
| S(2) | 0.20923(18) | 0.2500 | 0.48254(14) | 0.0083(6) |
| S(3) | 0.04299(18) | 0.2500 | 0.55274(14) | 0.0082(6) |
| S(4) | -0.1778(2) | -0.7500 | 0.18492(14) | 0.0124(6) |
| S(5) | 0.05953(18) | -0.2500 | -0.05774(14) | 0.0091(6) |
| S(6) | 0.15831(18) | -0.7500 | 0.06464(15) | 0.0104(6) |
| S(7) | -0.22911(18) | -0.2500 | 0.32202(14) | 0.0076(6) |
| S(8) | 0.14585(18) | -0.2500 | 0.35127(14) | 0.0087(6) |
| S(9) | 0.05085(19) | -0.2500 | 0.19232(14) | 0.0101(6) |

^a U_{eq} is defined as one-third of the trace of the orthogonalized U_{ij} tensor.

Magnetic Susceptibility Measurements. Magnetism data were measured on powders in gelcap sample holders with a Quantum Design MPMS 7T magnetometer/susceptometer between 2 and 300 K and in applied fields up to 7 T. DC temperature dependent susceptibility measurements were made under zero-field-cooled conditions with an applied field of 0.1 T. Susceptibility values were corrected for the sample diamagnetic contribution according to Pascal's constants⁴⁷ as well as for the sample holder diamagnetism. θ_p values were obtained from extrapolations from fits between 100 to 300 K. (Magnetic susceptibility measurements were performed by Eun Sang Choi and James S. Brooks at Florida State University)

UV-vis-NIR Diffuse Reflectance Spectroscopy. The diffuse reflectance spectra for γ -LnLn'S₃ (Ln = La, Ce; Ln' = Er, Tm, Yb) were measured from 200 to 1500 nm using a Shimadzu UV3100 spectrophotometer equipped with an integrating sphere attachment. The Kubelka-Monk function was used to convert diffuse reflectance data to absorption spectra.⁴⁸

RESULTS AND DISCUSSION

Effects of Synthetic Parameters on Product Composition and Structure. γ -LnLn'S₃ (Ln = La, Ce; Ln' = Er, Tm, Yb) were synthesized via the reaction of the respective lanthanides with elemental sulfur in a Sb₂S₃ flux at 1000 °C. Conveniently, when the reactions are maintained at a slight angle, on cooling, the majority of the flux moves to the bottom of the ampoules leaving isolated crystals of γ -LnLn'S₃ (Ln = La, Ce; Ln' = Er, Tm, Yb). In sharp contrast, in the absence of the flux, microcrystalline mixed-

lanthanide sulfides phases form, but the yield is very low, and the crystals are far too small to investigate using single crystal X-ray diffraction. Furthermore, because there are several recognized phases for mixed-lanthanide sulfides with compositions close to 1:1:3,^{37,41-43} the products of these direct reactions are also ambiguous. The choice of flux has proven to be critical in this system as demonstrated by the replacement of Sb_2S_3 with CsCl , which instead results in Cs^+ incorporation, and the formation of the quaternary phases $\text{Cs}_{0.14-0.17}\text{Ln}_{0.26-0.33}\text{YbS}_2$ ($\text{Ln} = \text{La} - \text{Yb}$).⁴⁹ A KI flux has been used in the preparation of $\beta\text{-LnYbQ}_3$ ($\text{Ln} = \text{La} - \text{Sm}$; $\text{Q} = \text{S}, \text{Se}$).⁴³ However, in contrast to the selenides, the yield of $\beta\text{-LaYbS}_3$ was very low, inhibiting detailed measurements of its electronic properties.⁴³ It has been previously noted even in binary sesquisulfides that preparative conditions play a dramatic role in the structure type adopted.²⁷⁻²⁹ For example, four different forms of Er_2S_3 can be synthesized by varying temperature, pressure, and crystal growth methods.³⁰

Product composition and structure were investigated as a function of the size of Ln , Ln' , and by the substitution of Se for S . When the size of Ln is decreased slightly (on the order of 0.02 \AA) on going from Ce to Pr , ternary phases with the CeYb_3S_6 ($\text{F-Tm}_2\text{S}_3$) structure-type²⁹ were found to form. It is important to note that the trivalent ions in this phase are highly disordered.^{31,33} For the La -containing phases, when Ln' is increased in size by transitioning from Er to Ho , mixtures of LaHo_3S_6 with the CeYb_3S_6 structure and $\gamma\text{-LaHo}'\text{S}_3$ crystallize. In contrast, for the Ce -containing phases, when the same substitution of Ho for Er is performed, the new phase $\delta\text{-CeHoS}_3$ (CeTmS_3 -type³⁷) is found. The structure and properties of $\delta\text{-CeHoS}_3$ are quite distinct from that of $\gamma\text{-LnLn}'\text{S}_3$

(Ln = La, Ce; Ln' = Er, Tm, Yb), and will be the subject of a subsequent report. In general, when Ln and Ln' become too close in size, we have found that for those reactions that occur in Sb₂S₃ fluxes, that the yield of the desired ternary phases becomes very low and crystals often do not form.

The substitution of Se for S results in a highly complex Ln_xLn'_ySe_z system. For the La/Yb/Se reaction in a Sb₂Se₃ flux, La₅Yb_{5-x}Se₇ with the Y₅S₇ structure-type forms.^{50,51} The lanthanide ions in this phase are highly disordered. In the (Ce – Nd)/Yb/Se series the β-LnYbS₃ phases are found instead.⁴³ When the size of Ln' is increased on substituting Tm for Yb the Ln_{1+x}Tm_{3-x}Se₆ (Ln = La – Sm) compounds form, which adopt the disordered CeYb₃S₆ structure.³¹ When the size of Ln' is increased again by replacing Tm with Er, in the La/Er/Se system, LaErSe₃ with the δ-CeHoS₃ structure crystallizes. As in the sulfide reactions, if the difference in the size of the two lanthanide ions becomes too small, as is the case in Nd/Er/Se, the disordered CeYb₃S₆ structure is adopted again (e.g. in Nd_{1+x}Er_{3-x}Se₆).

As can be gleaned from the above discussion, there can be sharp demarcations between neighboring lanthanide ions in ternary mixed-lanthanide sulfides and selenides. Notably we have yet to mention the Lu-containing phases in the above discussion. This is because our observations are that these reactions do not follow previously observed trends for mixed-lanthanide phases where there is substantial size mismatch. Instead, we have isolated (in low yield) LaLu₃S₆ with the CeYb₃S₆ structure, which would normally result from having lanthanides of more similar size, as well as δ-LnLuS₃ (Ln = Ce, Pr,

Nd). To reiterate, both of structure-types have lanthanide site positional disorder that is unexpected in this system because these trivalent ions differ by approximately 0.17 Å.

Structural Features of γ -LnLn'S₃ (Ln = La, Ce; Ln' = Er, Tm, Yb). The isotopic series, γ -LnLn'S₃ (Ln = La, Ce; Ln' = Er, Tm, Yb), crystallize in the centrosymmetric orthorhombic space group *Pnma*. While this structure is a dense layered network, we will describe it in terms of lower-dimensional substructures so that the subtleties of bonding in these complex materials can be better understood. It is important to note from the outset that the structure of γ -LnLn'S₃ is dramatically different from that of both α - and β -LnLn'S₃.⁴¹⁻⁴³ γ -LnLn'S₃ adopts the same space group as α -LnLn'S₃. However, there is only one distinct crystallographic site for each of the Ln and Ln' centers (two total sites). The same is also true for the layered structure of β -LnLn'S₃ (UFeS₃-type⁵²).⁴³ In contrast, γ -LnLn'S₃ can also be expressed as Ln₃Ln'₃S₉ because there are three crystallographically unique sites for both the Ln and Ln' atoms. Ordering of two different Ln³⁺ ions in a lattice is often difficult to achieve owing to the similarities in the structural chemistry of the trivalent lanthanide ions (*vide supra*). In α -, β -, and γ -LnLn'S₃, ordering of the Ln and Ln' sites is accomplished by choosing lanthanide ions at opposite ends of the series. Typically earlier, larger lanthanides favor higher coordination numbers than the later, smaller ions. In α -LnLn'S₃ the two different lanthanide ions are actually both six-coordinate; however the larger ions are found in trigonal prisms, whereas the small ones are found in octahedral environments. In contrast, the larger trivalent lanthanides in β -LnLn'S₃ have eight close neighbors, and the Yb³⁺ ions only have six. γ -LnLn'S₃ follows the same general trends as β -LnLn'S₃ by

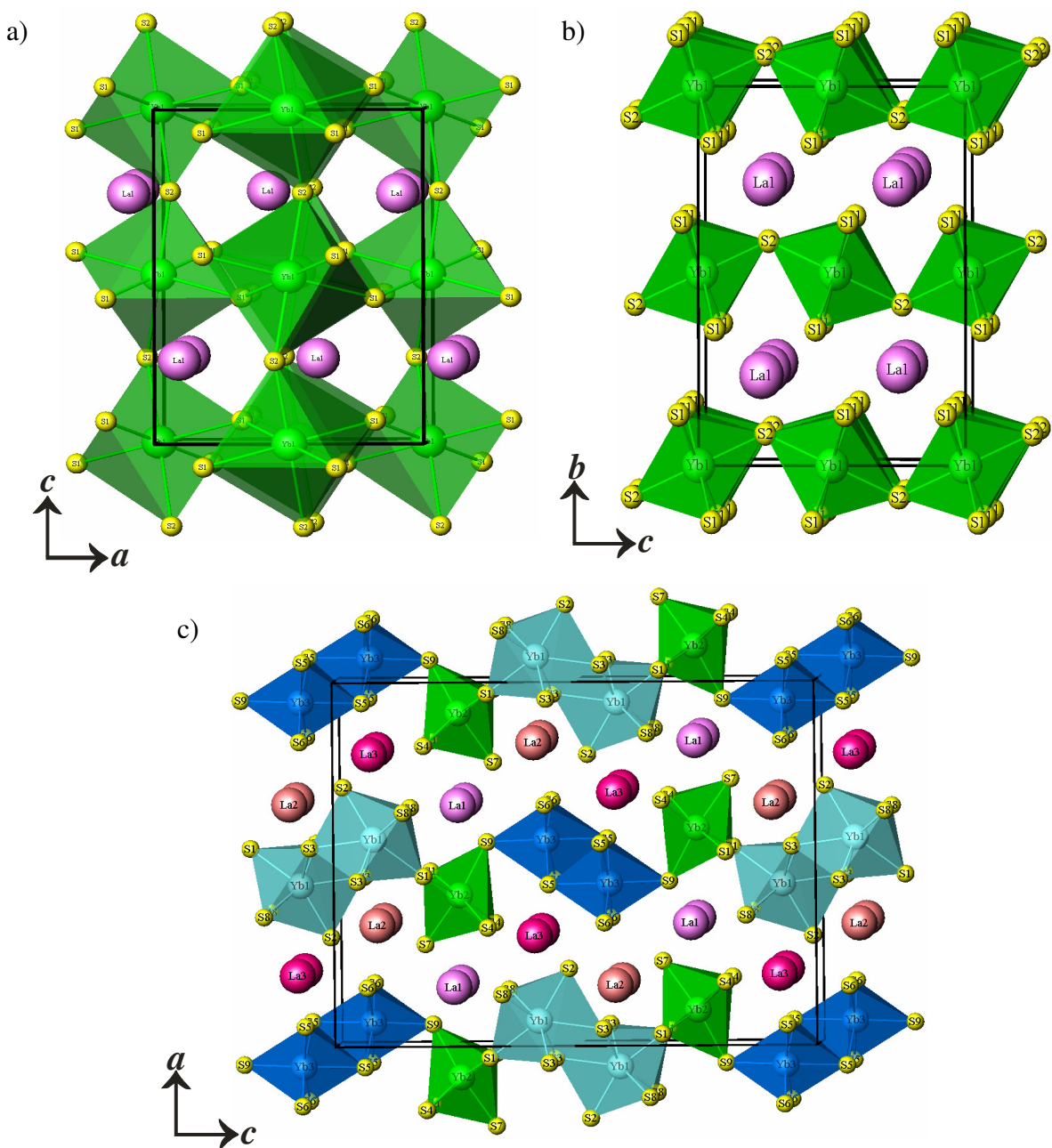


Figure 4.1. Views of the structures of a) α -LnLn'S₃, b) β -LnLn'S₃, and c) γ -LnLn'S₃ (Ln = La, Ce; Ln' = Er, Tm, Yb). γ -LnLn'S₃ adopts a layered structure with two-dimensional $[\text{Ln}'_3\text{S}_9]^{9-}$ (Ln' = Er, Tm, Yb) slabs that extend in the $[bc]$ plane that contain the smaller lanthanide ions that are separated by larger Ln³⁺ ions, La³⁺ and Ce³⁺, as is depicted in Figure 4.1c.

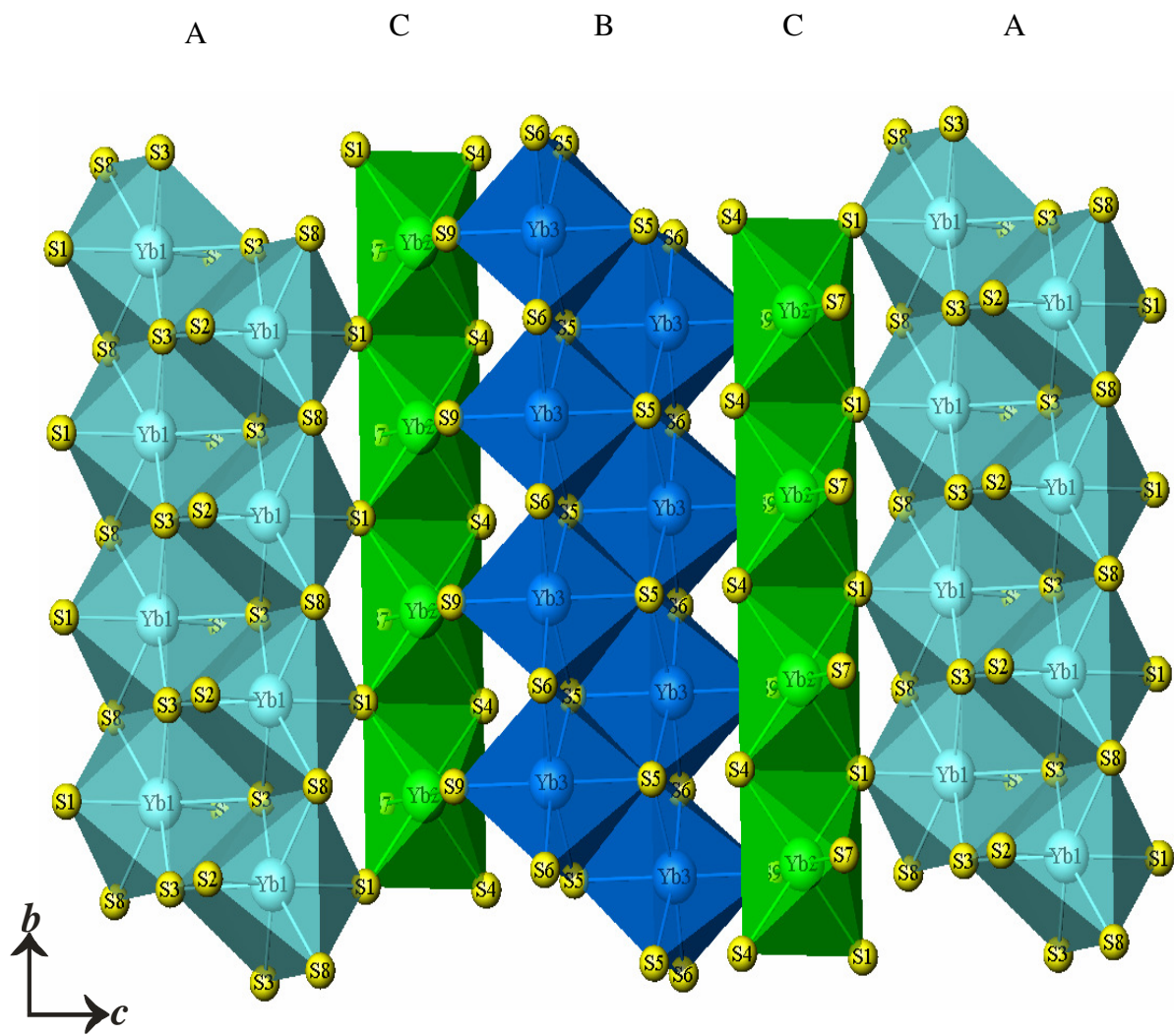


Figure 4.2. A depiction of an individual ${}^2[\text{Ln}'_3\text{S}_9]^{9-}$ ($\text{Ln}' = \text{Er}, \text{Tm}, \text{Yb}$) layer viewed down the a axis in $\gamma\text{-LnLn}'\text{S}_3$ ($\text{Ln} = \text{La}, \text{Ce}; \text{Ln}' = \text{Er}, \text{Tm}, \text{Yb}$). This layer is constructed from edge-sharing double chains of $[\text{Ln}'\text{S}_7]$ monocapped trigonal prisms (A) and double chains of $[\text{Ln}'\text{S}_6]$ octahedra (B) that are linked by single chains of $[\text{Ln}'\text{S}_6]$ octahedra (C) in the manner of ACBCA. The central C chains share corners with the A and B chains.

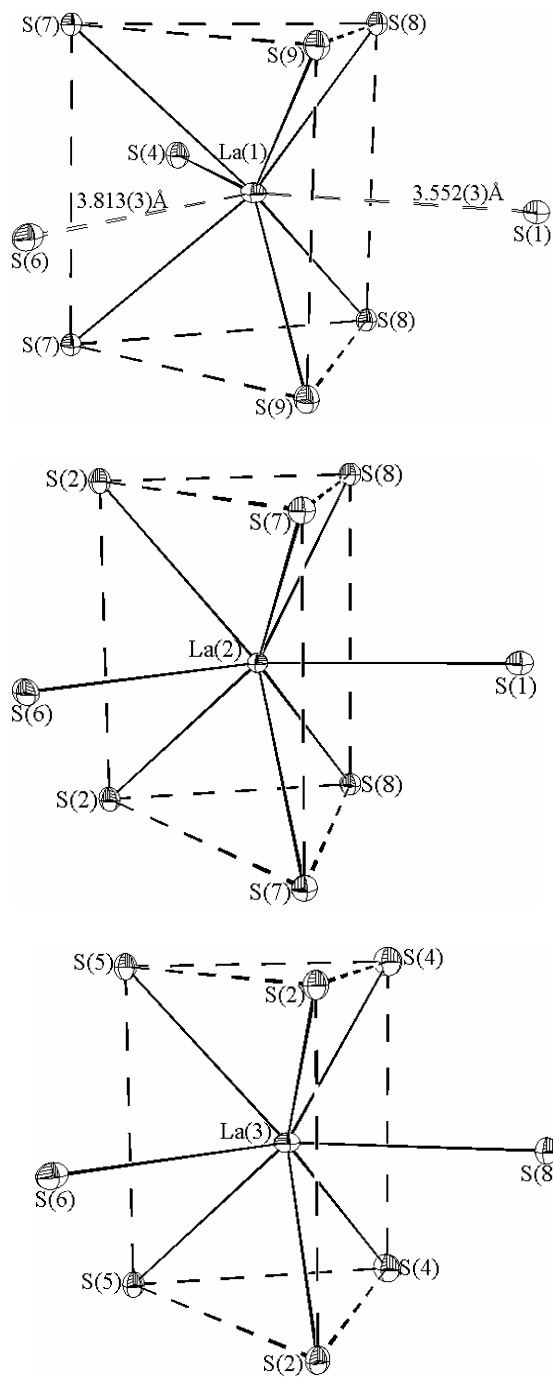


Figure 4.3. Illustrations of the coordination environments for the larger lanthanides, La^{3+} and Ce^{3+} , in $\gamma\text{-LnLn}'\text{S}_3$ ($\text{Ln} = \text{La}, \text{Ce}; \text{Ln}' = \text{Er}, \text{Tm}, \text{Yb}$). We use $\gamma\text{-LaYbS}_3$ to represent this family of compounds here.

placing the larger ions in eight- and nine-coordinate environments, and the smaller ions are seven- and six-coordinate geometries.

We choose here to adopt the same convention as used for β -LnLn'S₃ to describe the structure of γ -LnLn'S₃, which is as two-dimensional ${}^2_{\infty}[\text{Ln}'_3\text{S}_9]^{9-}$ (Ln' = Er, Tm, Yb) layers that extend in the $[bc]$ plane that contain the smaller lanthanide ions that are separated by larger Ln³⁺ ions, La³⁺ and Ce³⁺, as is depicted in Figure 4.1c. For comparison, α - and β -LnLn'S₃ are shown in Figures 4.1a and 4.1b. There are no S–S bonds in α -, β -, or γ -LnLn'S₃, and therefore the oxidation states in these compounds can be assigned as +3/+3/-2. This designation is confirmed by both bond-valence sum calculations^{53,54} and by magnetic susceptibility measurements (*vide infra*).

An individual ${}^2_{\infty}[\text{Ln}'_3\text{S}_9]^{9-}$ (Ln' = Er, Tm, Yb) layer viewed down the a axis is shown in Figure 4.2. As can be seen in this sketch, this layer is constructed from edge-sharing double chains of [Ln'S₇] monocapped trigonal prisms (A) and double chains of [Ln'S₆] octahedra (B) that are linked by single chains of [Ln'S₆] octahedra (C) in the manner ACBCA. The central C chains share corners with the A and B chains. The ${}^2_{\infty}[\text{Ln}'_3\text{S}_9]^{9-}$ layers in γ -LnLn'S₃ are more buckled than those in β -LnLn'S₃, because the chains of [Ln'S₆] octahedra (C) share both axial and equatorial corners with the double chains (A and B). In β -LnLn'S₃ only axial (trans) atoms are corner-sharing. For reference, in γ -LaYbS₃ the Yb–S bond distance for Yb(1), Yb(2), and Yb(3) range from 2.5979(19) to 2.783(2) Å, and are normal (see Table 4.3).

As shown in Figure 4.3, the larger lanthanides La³⁺ and Ce³⁺ (Ln(1), Ln(2), and Ln(3)) ions are found in coordination environments with more neighbors than the Er³⁺,

Table 4.3. Selected Bond Distances (Å) for γ -LnLn'S₃ (Ln = La, Ce; Ln' = Er, Tm, Yb).

| Formula | γ -LaErS ₃ | γ -LaTmS ₃ | γ -LaYbS ₃ | γ -CeErS ₃ | γ -CeTmS ₃ | γ -CeYbS ₃ |
|---------------|------------------------------|------------------------------|------------------------------|------------------------------|------------------------------|------------------------------|
| Ln(1)-S(1) | 3.613(3) | 3.579(3) | 3.552(3) | 3.661(3) | 3.647(3) | 3.591(3) |
| Ln(1)-S(4) | 3.039(3) | 3.048(3) | 3.062(3) | 2.988(3) | 2.995(3) | 3.003(3) |
| Ln(1)-S(6) | 3.825(3) | 3.814(3) | 3.813(3) | 3.803(3) | 3.781(3) | 3.801(3) |
| Ln(1)-S(7) ×2 | 3.058(2) | 3.051(2) | 3.050(2) | 3.0248(19) | 3.018(2) | 3.0145(19) |
| Ln(1)-S(8) ×2 | 3.035(2) | 3.028(2) | 3.024(2) | 3.0096(19) | 3.007(2) | 2.9967(19) |
| Ln(1)-S(9) ×2 | 2.884(2) | 2.885(2) | 2.892(2) | 2.8616(19) | 2.863(2) | 2.866(2) |
| Ln(2)-S(1) | 3.003(3) | 3.004(3) | 3.007(3) | 2.974(3) | 2.977(3) | 2.976(3) |
| Ln(2)-S(2) ×2 | 3.036(2) | 3.034(2) | 3.037(2) | 3.0145(18) | 3.013(2) | 3.0094(19) |
| Ln(2)-S(3) ×2 | 2.980(2) | 2.977(2) | 2.969(2) | 2.9580(18) | 2.956(2) | 2.9533(19) |
| Ln(2)-S(6) | 2.862(3) | 2.858(3) | 2.856(3) | 2.844(3) | 2.845(3) | 2.838(3) |
| Ln(2)-S(7) ×2 | 2.9450(19) | 2.944(2) | 2.948(2) | 2.9256(18) | 2.926(2) | 2.9274(19) |
| Ln(3)-S(2) ×2 | 2.8863(19) | 2.8855(19) | 2.884(2) | 2.8593(18) | 2.864(2) | 2.8586(18) |
| Ln(3)-S(4) ×2 | 2.989(2) | 2.989(2) | 2.993(2) | 2.9610(19) | 2.960(2) | 2.964(2) |
| Ln(3)-S(5) ×2 | 3.002(2) | 2.998(2) | 2.998(2) | 2.9858(19) | 2.984(2) | 2.9764(19) |

| | | | | | | |
|----------------|------------|------------|------------|------------|------------|------------|
| Ln(3)-S(6) | 3.128(3) | 3.128(3) | 3.124(3) | 3.098(3) | 3.107(3) | 3.082(3) |
| Ln(3)-S(8) | 3.024(3) | 3.019(3) | 3.018(3) | 3.008(2) | 3.012(3) | 2.996(3) |
| Ln'(1)-S(1) | 2.785(3) | 2.771(3) | 2.755(3) | 2.789(2) | 2.786(3) | 2.758(2) |
| Ln'(1)-S(2) | 2.716(3) | 2.697(3) | 2.685(3) | 2.720(2) | 2.713(3) | 2.683(3) |
| Ln'(1)-S(3) ×2 | 2.7594(18) | 2.7497(18) | 2.744(2) | 2.7613(17) | 2.7602(19) | 2.7367(18) |
| Ln'(1)-S(3) | 2.837(3) | 2.825(3) | 2.833(3) | 2.822(2) | 2.822(3) | 2.812(3) |
| Ln'(1)-S(8) ×2 | 2.8045(19) | 2.7976(19) | 2.794(2) | 2.7988(18) | 2.798(2) | 2.7854(18) |
| Ln'(2)-S(1) ×2 | 2.6429(17) | 2.6352(17) | 2.6339(19) | 2.6300(16) | 2.6239(18) | 2.6178(16) |
| Ln'(2)-S(4) ×2 | 2.815(2) | 2.797(2) | 2.783(2) | 2.8155(19) | 2.806(2) | 2.7852(19) |
| Ln'(2)-S(7) | 2.698(3) | 2.691(3) | 2.681(3) | 2.691(2) | 2.684(3) | 2.673(3) |
| Ln'(2)-S(9) | 2.705(3) | 2.689(3) | 2.684(3) | 2.720(3) | 2.705(3) | 2.685(3) |
| Ln'(3)-S(5) ×2 | 2.7946(18) | 2.7791(18) | 2.770(2) | 2.7869(18) | 2.779(2) | 2.7616(18) |
| Ln'(3)-S(5) | 2.720(3) | 2.702(3) | 2.684(3) | 2.725(3) | 2.708(3) | 2.691(3) |
| Ln'(3)-S(6) ×2 | 2.6149(17) | 2.6036(17) | 2.5979(19) | 2.6142(16) | 2.6056(18) | 2.5928(17) |
| Ln'(3)-S(9) | 2.656(3) | 2.640(3) | 2.620(3) | 2.650(3) | 2.644(3) | 2.627(3) |

Tm³⁺, and Yb³⁺ ions. There is some difficulty in precisely describing the coordination number of the Ln(1) centers. These Ln³⁺ cations are located within highly distorted tricapped trigonal prismatic environments. Two of the Ln···S capping contacts, however, are substantially longer than those that define the trigonal prism. For example, in γ -LaYbS₃ the short La–S bonds range from 2.892(2) to 3.062(3) Å, whereas the longer contacts are 3.552(3) and 3.813(3) Å (see Table 4.3). The longest contact should probably not be considered as important. The Ln(2) and Ln(3) atoms, however, are clearly eight-coordinate, and occur as bicapped trigonal prisms with La–S bonds ranging from 2.856(3) to 3.037(2) Å for La(2), and from 2.844(2) to 3.124(3) Å for La(3) in γ -LaYbS₃ (see Table 4.3). The transitions between α -LnLn'S₃, β -LnLn'S₃, and γ -LnLn'S₃ represent systematic increases in the average coordination numbers of the lanthanides, leading to more efficient packing and increased densities in this single compositional family.

Magnetic Properties of γ -LnLn'S₃ (Ln = La, Ce; Ln' = Er, Tm, Yb). At first glance the magnetic behavior of γ -LnLn'S₃ (Ln = La, Ce; Ln' = Er, Tm, Yb) seem relatively uninteresting as there is no indication of long-range magnetic ordering down to 2 K, as shown in Figure 4.4. However, the θ_p parameters are atypical for some of these compounds. The θ_p values are -0.4, -6.7, -32.1, -18.7, -14.6, -37.5 K, for γ -LaErS₃, γ -LaTmS₃, γ -LaYbS₃, γ -CeErS₃, γ -CeTmS₃, and γ -CeYbS₃, respectively. The θ_p parameters for γ -LaYbS₃ and γ -CeYbS₃ are quite negative, indicating relatively strong antiferromagnetic coupling between Ln³⁺ ions. In the case of γ -LaYbS₃, this interaction must be between Yb³⁺ centers. We observed similar phenomena in Cs_{0.14-0.17}Ln_{0.26-}

0.33YbS_2 ($\text{Ln} = \text{La} - \text{Yb}$).⁴⁹ Despite this strong coupling, short- and long-range order are apparently absent. This behavior is consistent with a geometrically spin-frustrated system. It should be noted that $\beta\text{-CeYbSe}_3$ and $\beta\text{-SmYbSe}_3$ have very large θ_p values of $-44.6(9)$ K and $-107.6(4)$ K without any indication of long-range order down to 5 K.⁴³

The origin of potential geometric spin-frustration may lie in the layered substructures found in $\beta\text{-LnLn}'\text{S}_3$ and $\gamma\text{-LnLn}'\text{S}_3$. The Sm network for $\beta\text{-SmYbSe}_3$ is shown in Figure 4.5a. This drawing shows a layer constructed from triangles. The asymmetry of these triangles is capable of preventing ordering in two dimensions. Figure 4.5b shows these layers rotated by 90° with the Yb^{3+} ions further connecting the network to create a system that might be frustrated in all three dimensions. In contrast, the source of geometric spin-frustration in $\gamma\text{-LnLn}'\text{S}_3$ is less obvious. In these phases, there are networks of both squares and triangles within the Yb layers as well as the potential for higher-order frustration via the interlayer Ce^{3+} ions as shown in Figures 4.6a and b, respectively. We propose that if spin-frustration is occurring in these compounds that it is within the Yb layers, because $\gamma\text{-LaYbS}_3$ and $\gamma\text{-CeYbS}_3$ have large θ_p values that are quite similar in magnitude, and the La^{3+} ions obviously can not contribute to this behavior. The Yb...Yb distances vary considerably between $\beta\text{-SmYbSe}_3$ and $\gamma\text{-LaYbS}_3$, and are different depending on the substructures that they are present in. In $\beta\text{-LaYbS}_3$ and $\gamma\text{-LaYbS}_3$, the shortest Yb...Yb distances of $3.9238(8)$ and $3.9847(3)$ Å, respectively, are similar.

In the absence of appropriate trigonal or hexagonal symmetry the triangular networks in $\beta\text{-LnLn}'\text{S}_3$ and $\gamma\text{-LnLn}'\text{S}_3$ are necessarily asymmetric. As such, one of the

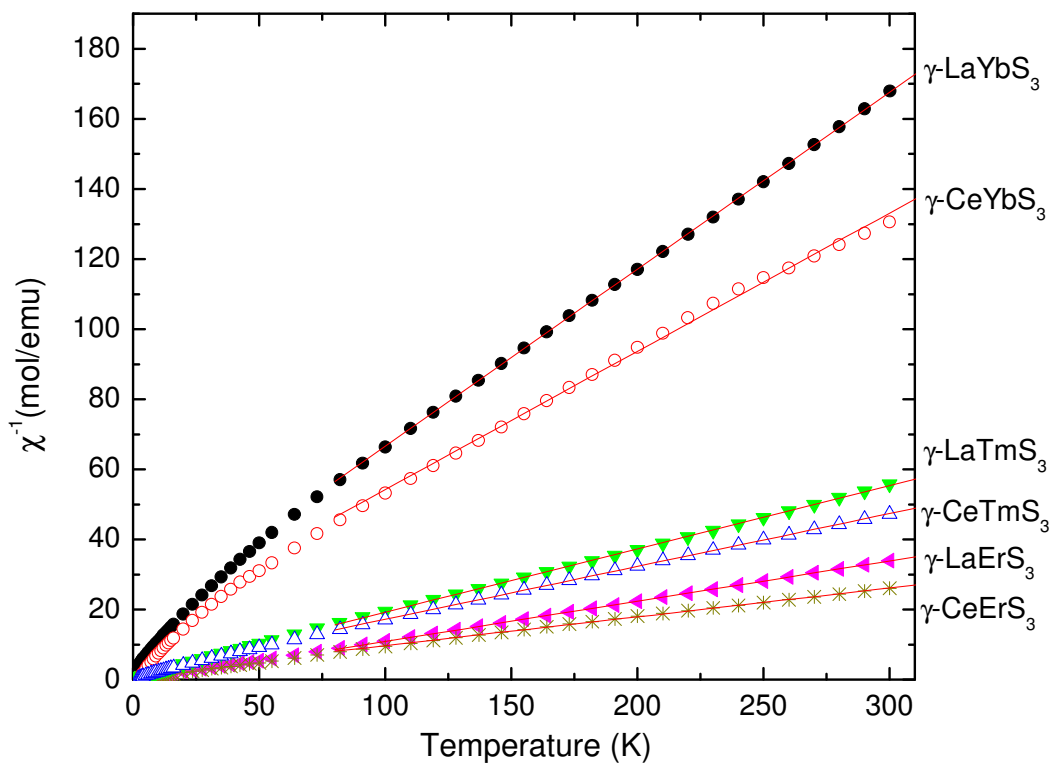


Figure 4.4. Temperature dependence of the reciprocal molar magnetic susceptibility for γ -LnLn'S₃ (Ln = La, Ce; Ln' = Er, Tm, Yb) under an applied magnetic field of 0.1 T.

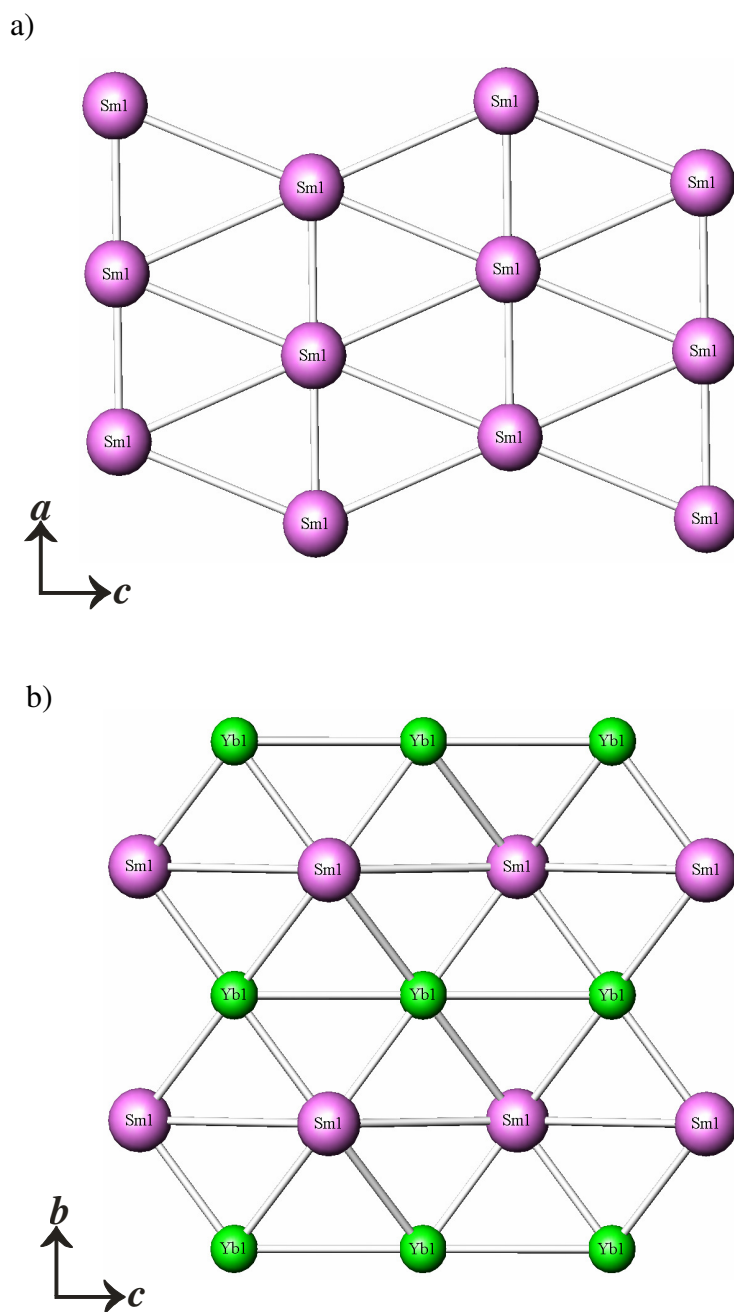
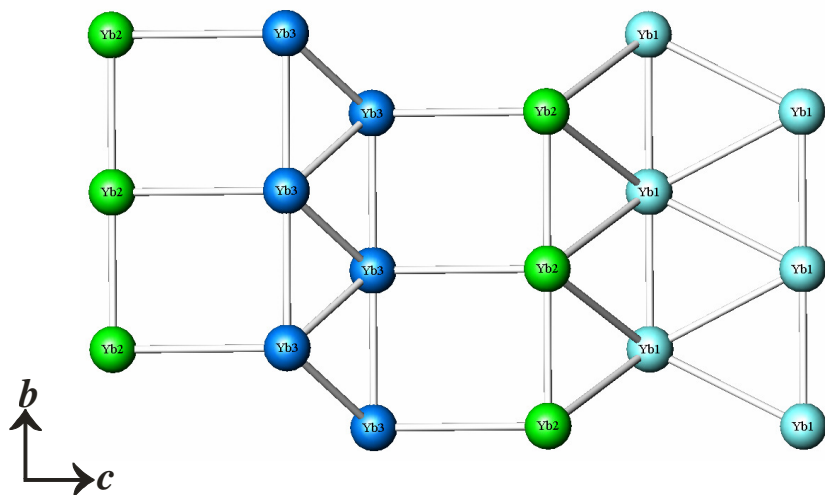


Figure 4.5. a) A view of the layers in Sm-based triangles in β -SmYbSe₃. b) A depiction of the interconnection of the Sm layers by Yb³⁺ ions. In both cases the chalcogenide ions have been omitted for clarity.

a)



b)

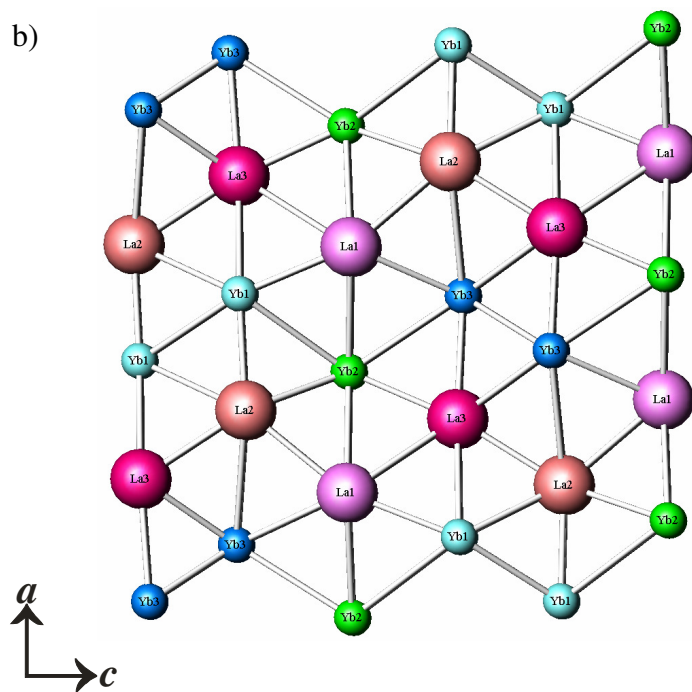


Figure 4.6. a) An illustration of the square and triangular networks in γ -CeYbS₃. b) A drawing of the complex three-dimension network in γ -CeYbS₃. In both cases the chalcogenide ions have been omitted for clarity.

requirements of spin-frustration may not be present, and there may be alternative mechanisms for explaining the large negative θ_p values. The first of these is that this might be an effect of crystal-field splitting of the ground state of the Yb^{3+} ions. A second, and much more complex, mechanism has also been proposed for the frustrated pyrochlore antiferromagnet, $\text{Tb}_2\text{Ti}_2\text{O}_7$.⁵⁵ In this compound there is strong evidence supporting extra perturbative exchange coupling beyond nearest neighbors as well as dipolar interactions that may be the cause of the lack of long-range ordering of the moments.⁵⁶

The calculated free-ion moments for $\gamma\text{-LaErS}_3$, $\gamma\text{-LaTmS}_3$, $\gamma\text{-LaYbS}_3$, $\gamma\text{-CeErS}_3$, $\gamma\text{-CeTmS}_3$, and $\gamma\text{-CeYbS}_3$ are 9.59, 7.57, 4.54, 9.92, 7.98, and 5.20 μ_B , respectively.⁵⁷ Not surprisingly the observed moments (8.35, 6.65, 3.98, 9.87, 7.28, and 4.50 μ_B) are notably smaller than the ideal values, most likely because of splitting of the ground state terms for these ions. It would require substantially larger fields than 7 T to obtain full moment values for these compounds. The above calculated values are only true if Ce is trivalent. The single 4f electron in Ce is tenuous at best, and tetravalent Ce carries no moment, in which case the Ce-based compounds would have the same effective moment as the La-based compounds. The isothermal magnetization measurements also show that the saturation moment is considerably less than the free-ion value. Isothermal magnetization measurements carried out to 7 T at 2 K support the conclusions of the effective moment measurements, i.e., that the moments are low.

Optical Properties of $\gamma\text{-LnLn}'\text{S}_3$ (Ln = La, Ce; Ln' = Er, Tm, Yb). The optical band gaps of ternary and quaternary chalcogenides have been shown to be tunable based

on the choice of lanthanide ion and chalcogen (e.g. CsLnZnSe₃ (Ln = Sm, Tb, Dy, Ho, Er, Tm, Yb, and Y)).^{9,11,13,14,58} Based on electronic structure calculations, CsLnZnSe₃ are thought to be direct band gap semiconductors.⁹ The band gaps for binary lanthanide sesquisulfides are generally indirect.⁵⁹ Therefore, both direct and indirect band gap semiconductors are recognized in lanthanide chalcogenides, and they are highly dependent on the structure adopted by the phase.^{13,14,56,59} The optical band gaps for γ -LnLn'S₃ (Ln = La, Ce; Ln' = Er, Tm, Yb) were measured using UV-vis-NIR spectroscopy (see Figure 4.7).

Unfortunately, the band gaps of α - and β -LnLn'S₃ materials have not been reported, although β -LaYbS₃ is reported to be yellow.⁴³ Qualitatively, the γ -LaLn'S₃ (Ln' = Er, Tm, Yb) compounds are dark red, whereas the γ -CeLn'S₃ (Ln' = Er, Tm, Yb) compounds are black. Congruent with these visual observations, the measured band gaps for γ -LaLn'S₃ (Ln' = Er, Tm, Yb) are all approximately 1.6 eV. The replacement of La by Ce results in a smaller gap for γ -CeLn'S₃ (Ln' = Er, Tm, Yb) of ~1.3 eV. The apparent fine-structure in these spectra are actually f-f transitions for the lanthanide ions. The band gaps observed for γ -LnLn'S₃ are comparable to the indirect band gaps reported for Nd³⁺:doped α -Gd₂S₃ (A-type), β -La₂S₃, and γ -Y₂S₃ (D-type).⁵⁹ The Ce compounds often show the smallest band gaps of the series owing the high energy of 4f¹ electron.^{60,61} The structural modification that occurs for γ -LnLn'S₃ clearly alters the band gap substantially from that observed for the binary phases.

CONCLUSIONS

The role of reaction conditions (pressure, temperature, flux, etc.) in determining composition and structure in both binary and ternary interlanthanide sesquichalcogenides cannot be overemphasized. We focus here on the use of the new flux, Sb_2S_3 , which has been used to prepare $\gamma\text{-LnLn}'\text{S}_3$ ($\text{Ln} = \text{La, Ce}$; $\text{Ln}' = \text{Er, Tm, Yb}$) in high yield. In contrast, when KI is employed as a flux, $\beta\text{-LaYbS}_3$ can only be prepared in low yield, and this medium is more amenable for the syntheses of selenide compounds. Some fluxes, such as CsCl, are in fact reactive, resulting in Cs^+ incorporation into the lanthanide chalcogenide phases, and the formation of quaternary compounds that are illustrated by $\text{Cs}_{0.14-0.17}\text{Ln}_{0.26-0.33}\text{YbS}_2$ ($\text{Ln} = \text{La} - \text{Yb}$).⁴⁹ The use of fluxes provides access to mixed-lanthanide compounds with novel structure types, and is a means of understanding structure-property relationships in these intricate materials.

The structure of $\gamma\text{-LnLn}'\text{S}_3$ diverges substantially from previously reported interlanthanide sesquisulfides in that there are three crystallographically unique Ln sites in the structure, whereas $\alpha\text{-}$ and $\beta\text{-LnLn}'\text{S}_3$ have one site for each type of lanthanide ion.⁴¹⁻⁴³ Ordering of the Ln^{3+} ions is achieved by placing the larger ions in eight- and nine-coordinate environments, and the smaller ions are seven- and six-coordinate geometries. Table 4.4 provides a listing of mixed-lanthanide sesquichalcogenides that form under the conditions described in this work, indicating whether ordering of the Ln^{3+} ions is achieved, and the coordination environments of the Ln^{3+} ions. These data apply to solids that form from a Sb_2Q_3 ($\text{Q} = \text{S, Se}$) flux at 1000 °C.

Currently, the most promising application of the mixed-lanthanide chalcogenides is the ability to change, and perhaps systematically vary, the band gap of these semiconductors. This can be accomplished by both changing the lanthanide, as we demonstrated in this report, and by changing the chalcogenide, whereby the band gap should decrease when heavier chalcogenides are substituted into the structure.⁵⁸ Doing this allows materials to be prepared that range from nearly colorless to black. This property is not unique to the present system, but rather applies to many lanthanide compounds. We suggest that the possibility exists for finding interesting electronic phenomena by preparing ordered quaternary interlanthanide sesquichalcogenides with three different lanthanides, which might be accomplished by exploiting structures with three different coordination environments for the Ln^{3+} ions.

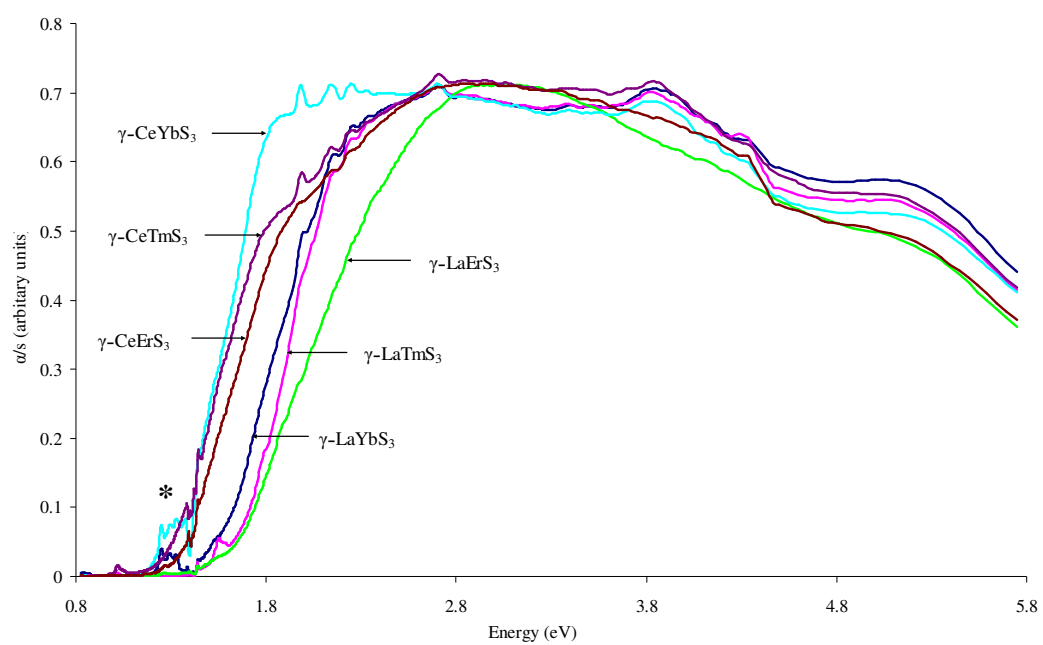


Figure 4.7. UV-vis diffuse reflectance spectra of $\gamma\text{-LnLn}'\text{S}_3$ (Ln = La, Ce; Ln' = Er, Tm, Yb). (*Denotes detector change.)

Table 4.4. Comparisons of Ternary Interlanthanide Sesquichalcogenides that Form in a Sb_2Q_3 (Q = S, Se) Flux at 1000 °C.

| Structure type | Compounds | Ordered/Disordered | Coordination |
|---|---|--------------------|-------------------------|
| β -LnLn'S ₃ (UFeS ₃ -type) | CeYbSe ₃ , PrYbSe ₃ , NdYbSe ₃ | Ordered | Ln – 8 Ln' – 6 |
| γ -LnLn'S ₃ | LnLn'S ₃ (Ln=La, Ce, Ln'=Er-Yb) | Ordered | Ln – 8, 9 Ln' – 6, 7 |
| δ -LnLn'S ₃ (CeTmS ₃ -type) | La _{5-x} Er _{3+x} Se ₁₂ , Ce _{5-x} Ho _{3+x} Se ₁₂ , Ln _{5-x} Lu _{3+x} S ₁₂ (Ln = Ce, Pr, Nd) | Disordered | Ln – 7, 8 Ln' – 6, 7 |
| F-Ln ₂ S ₃ | La _{1+x} Lu _{3-x} S ₆ , Pr _{1+x} Tm _{3-x} S ₆ Ln _{1+x} Yb _{3-x} S ₆ (Ln= Pr-Gd), Ln _{1+x} Yb _{3-x} Se ₆ (Ln= Sm, Gd) Ln _{1+x} Tm _{3-x} Se ₆ (Ln= La-Sm), Nd _{1+x} Er _{3-x} Se ₆ | Disordered | Ln – 7, 8 Ln' – 6, 7 |
| Y ₅ S ₇ | La ₅ Yb _{5-x} Se ₇ | Disordered | Ln – 7 Ln' – 6, 7 |

REFERENCES

1. Isaacs, T. J.; Hopkins, R. H.; Kramer, W. E. *J. Electron. Mater.* **1975**, *4*, 1181.
2. Hautala, J.; Taylor, P. C. *J. Non-Cryst. Solids* **1992**, *141*, 24.
3. Nadler, M. P.; Lowe-Ma, C. K.; Vanderah, T. A. *Mater. Res. Bull.* **1993**, *28*, 1345.
4. Kumta P. N.; Risbud, S. H. *J. Mater. Sci.* **1994**, *29*, 1135.
5. Lowe-Ma, C. K.; Vanderah, T. A.; Smith, T. E. *J. Solid State Chem.* **1995**, *117*, 363.
6. Ueda, K.; Inoue, S.; Hosono, H.; Sarukura, N.; Hirano, H. *Appl. Phys. Lett.* **2001**, *78*, 2333.
7. Inoue, S.; Ueda, K.; Hosono, H.; Hamada, N. *Phys. Rev. B* **2001**, *64*, 245211.
8. Huang, F. Q.; Mitchell, K.; Ibers, J. A. *Inorg. Chem.* **2001**, *40*, 5123.
9. Mitchell, K.; Haynes, C. L.; McFarland, A. D.; Van Duyne, R. P.; Ibers, J. A. *Inorg. Chem.* **2002**, *41*, 1199.
10. Mitchell, K.; Ibers, J. A. *Chem. Rev.* **2002**, *102*, 1929.
11. Mitchell, K.; Huang, F. Q.; McFarland, A. D.; Haynes, C. L.; Somers, R. C.; Van Duyne, R. P.; Ibers, J. A. *Inorg. Chem.* **2003**, *42*, 4109.
12. Ueda, K.; Takafuji, K.; Hiramatsu, H.; Ohta, H.; Kamiya, T.; Hirano, M.; Hosono, H. *Chem. Mater.* **2003**, *15*, 3692.
13. Mitchell, K.; Huang, F. Q.; Caspi, E. N.; McFarland, A. D.; Haynes, C. L.; Somers, R. C.; Jorgensen, J. D.; Van Duyne, R. P.; Ibers, J. A. *Inorg. Chem.* **2004**, *43*, 1082.

14. Yao, J.; Deng, B.; Sherry, L. J.; McFarland, A. D.; Ellis, D. E.; Van Duyne, R. P.; Ibers, J. A. *Inorg. Chem.* **2004**, *43*, 7735.
15. Bronger, W.; Miessen, H.-J.; Schmitz, D. *J. Less-Common Met.* **1983**, *95*, 275.
16. Sutorik, A. C.; Albritton-Thomas, J.; Hogan, T.; Kannewurf, C. R.; Kanatzidis, M. G. *Chem. Mater.* **1996**, *8*, 751.
17. Givord, D.; Courtois, D. *J. Magn. Magn. Mater.* **1999**, *196-197*, 684.
18. Wakeshima, M.; Hinatsu, Y. *J. Solid State Chem.* **2000**, *153*, 330.
19. Tougait, O.; Ibers, J. A. *Inorg. Chem.* **2000**, *39*, 1790.
20. Wakeshima, M.; Hinatsu, Y.; Oikawa, K.; Shimojo, Y.; Morii, Y. *J. Mater. Chem.* **2000**, *10*, 2183.
21. Meng, F.; Hughbanks, T. *Inorg. Chem.* **2001**, *40*, 2482.
22. Wakeshima, M.; Hinatsu, Y.; Ishii, Y.; Shimojo, Y.; Morii, Y. *J. Mater. Chem.* **2002**, *12*, 631.
23. Lau, G. C.; Ueland, B. G.; Freitas, R. S.; Dahlberg, M. L.; Schiffer, P.; Cava, R. J. *Phys. Rev. B* **2006**, *73*, 012413.
24. Sleight, A. W.; Prewitt, C. T. *Inorg. Chem.* **1968**, *7*, 2283.
25. Patrie, M. *Bull. Soc. Chim. Fr.* **1969**, *5*, 1600.
26. Bergman, H., Ed. *Gmelin Handbook of Inorganic Chemistry, Sc, Y, La-Lu (Rare Earth Elements), System Number 39, C7: Sulfides*; Springer: Berlin, 1983.
27. Flahaut, J.; Guittard, M.; Patrie, M.; Pardo, M. P.; Golabi, S. M.; Domange, L. *Acta Cryst.* **1965**, *19*, 14.
28. Range, K. J.; Leeb, R. *Z. Naturf. B.* **1975**, *30*, 889.
29. Schleid, T.; Lissner, F. *J. Alloys Compd.* **1992**, *189*, 69.

30. Fang, C. M.; Meetsma, A.; Wiegers, G. A. *J. Alloys Compd.* **1993**, *201*, 255.
31. Rodier, N.; Tien, V. C. *R. Seances Acad. Sci. Ser. C* **1974**, *279*, 817.
32. Rodier, N.; Firor, R. L.; Tien, V.; Guittard, M. *Mat. Res. Bull.* **1976**, *11*, 1209.
33. Rodier, N.; Laruelle, P. *Bull. Soc. fr. de Mineral. Cristallogr.* **1973**, *96*, 30.
34. Hamilton, D. S.; Gayen, S. K.; Pogatshnik, G. J.; Ghen, R. D. *Phys. Rev. B* **1989**, *39*, 8807.
35. Cheung, Y. M.; Gayen, S. K. *Phys. Rev. B* **1994**, *49*, 14827.
36. Schweizer, T.; Mobert, P. E.-A.; Hector, J. R.; Hewak, D. W.; Brocklesby, W. S.; Payne, D. N.; Huber, G. *Phys. Rev. Lett.* **1998**, *80*, 1537.
37. Rodier, N. *Bull. Soc. fr. de Mineral. Cristallogr.* **1973**, *96*, 350.
38. Marezio, M.; Remeika, J. P.; Dernier, P. D. *Acta Crystallogr. B* **1970**, *26*, 2008.
39. Rodier, N.; Laruelle, P. *C. R. Seances Acad. Sci. Ser. C* **1970**, *270*, 2127.
40. Ijdo, D. J. W. *Acta Crystallogr. B* **1980**, *36*, 2403.
41. Rodier, N.; Julien, R.; Tien, V. *Acta Crystallogr. C* **1983**, *39*, 670.
42. Carre, D.; Laruelle, P. *Acta Crystallogr. B* **1974**, *30*, 952.
43. Mitchell, K.; Somers, R. C.; Huang, F. Q.; Ibers, J. A. *J. Solid State Chem.* **2004**, *177*, 709.
44. Jin, G. B.; Choi, E. S.; Guertin, R. P.; Brooks, J. S.; Bray, T. H.; Booth, C. H.; Albrecht-Schmitt, T. E. *Chem. Mater.* **2007**, *19*, 567.
45. Sheldrick, G. M. *SHELXTL PC, Version 6.12, An Integrated System for Solving, Refining, and Displaying Crystal Structures from Diffraction Data*; Siemens Analytical X-Ray Instruments, Inc.: Madison, WI 2001.

46. Sheldrick, G. M. *SADABS 2001, Program for absorption correction using SMART CCD based on the method of Blessing*; Blessing, R. H. *Acta Crystallogr.* **1995**, *A51*, 33.
47. Mulay, L. N.; Boudreaux, E. A. *Theory and Applications of Molecular Diamagnetism*; Wiley–Interscience: New York, 1976.
48. Wendlandt, W. W.; Hecht, H. G.: *Reflectance Spectroscopy*; Interscience Publishers: New York, 1966.
49. Jin, G. B.; Booth, C. H.; Albrecht-Schmitt, T. E. *Phys. Rev. B* manuscript in preparation.
50. Adolphe, C. *C. R. Seances Acad. Sci.* **1961**, *252*, 3266.
51. Rodier, N.; Laruelle, P. *Bull. Soc. Fr. Mineral. Cristallogr.* **1972**, *95*, 548.
52. Noel, H.; Padiou, J. *Acta Crystallogr. B* **1976**, *32*, 1593.
53. Brown, I. D.; Altermatt, D. *Acta Crystallogr.* **1985**, *B41*, 244.
54. Brese, N. E.; O’Keeffe, M. *Acta Crystallogr.* **1991**, *B47*, 192.
55. Gardner, J. S.; Dunsinger, S. R.; Gaulin, B. D.; Gingras, M. J. P.; Greedan, J. E.; Kiefl, R. F.; Lumsden, M. D.; MacFarlane, W. A.; Raju, N. P.; Sonier, J. E.; Swainson, I.; Tun, Z. *Phys. Rev. Lett.* **1999**, *82*, 1012.
56. Gingras, M. J. P.; den Hertog, B. C.; Faucher, M.; Gardner, J. S.; Dunsinger, S. R.; Chang, L. J.; Gaulin, B. D.; Raju, N. P.; Greedan, J. E. *Phys. Rev. B* **2000**, *62*, 6496.
57. Kittel, C. *Introduction to Solid State Physics*; 6th Ed.; Wiley: New York, 1986.
58. Deng, B.; Ellis, D. E.; Ibers, J. A. *Inorg. Chem.* **2002**, *41*, 5716.
59. Leiss, M. *J. Phys. C: Solid St. Phys.* **1980**, *13*, 151.

60. Prokofiev, A. V.; Shelykh, A. I.; Golubkov, A. V.; Smirnov, I. A. *J. Alloys Compd.* **1995**, 219, 172.
61. Prokofiev, A. V.; Shelykh, A. I.; Melekh, B. T. *J. Alloys Compd.* **1996**, 242, 41.
62. Ito, K.; Tezuka, K.; Hinatsu, Y. *J. Solid State Chem.* **2001**, 157, 173.

CHAPTER 5

SYNTHESES, STRUCTURE, MAGNETISM, AND OPTICAL PROPERTIES OF THE INTERLANTHANIDE SULFIDES δ -Ln_{2-x}Lu_xS₃ (Ln = Ce, Pr, Nd)

ABSTRACT

δ -Ln_{2-x}Lu_xS₃ (Ln = Ce, Pr, Nd; $x = 0.67 - 0.71$) compounds have been synthesized through the reaction of elemental rare earth metals and S using Sb₂S₃ flux at 1000 °C. These compounds are isotypic with CeTmS₃, which has a complex three-dimensional structure. It includes four larger Ln³⁺ sites in eight- and nine-coordinate environments, two disordered seven-coordinate Ln³⁺/Lu³⁺ positions, and two six-coordinate Lu³⁺ ions. The structure is constructed from one-dimensional chains of LnS_n ($n = 6 - 9$) polyhedra that extend along the *b* axis. These polyhedra share faces or edges with two neighbors within the chains, while in the [*ac*] plane they share edges and corners with other chains. Least squares refinements gave rise to the formulas of δ -Ce_{1.30}Lu_{0.70}S₃, δ -Pr_{1.29}Lu_{0.71}S₃ and δ -Nd_{1.33}Lu_{0.67}S₃, which are consistent with the EDX analysis and magnetic susceptibility data. δ -Ln_{2-x}Lu_xS₃ (Ln = Ce, Pr, Nd; $x = 0.67 - 0.71$) show no evidence of magnetic ordering down to 5 K. Optical-property measurements show that the band gaps for δ -Ce_{1.30}Lu_{0.70}S₃, δ -Pr_{1.29}Lu_{0.71}S₃, and δ -Nd_{1.33}Lu_{0.67}S₃ are 1.25 eV, 1.38 eV, and 1.50 eV, respectively. Crystallographic data: δ -

Ce_{1.30}Lu_{0.70}S₃, monoclinic, space group $P2_1/m$, $a = 11.0186(7)$, $b = 3.9796(3)$, $c = 21.6562(15)$ Å, $\beta = 101.6860(10)$, $V = 929.93(11)$, $Z = 8$; δ -Pr_{1.29}Lu_{0.71}S₃, monoclinic, space group $P2_1/m$, $a = 10.9623(10)$, $b = 3.9497(4)$, $c = 21.5165(19)$ Å, $\beta = 101.579(2)$, $V = 912.66(15)$, $Z = 8$; δ -Nd_{1.33}Lu_{0.67}S₃, monoclinic, space group $P2_1/m$, $a = 10.9553(7)$, $b = 3.9419(3)$, $c = 21.4920(15)$ Å, $\beta = 101.5080(10)$, $V = 909.47(11)$, $Z = 8$.

INTRODUCTION

Ternary interlanthanide chalcogenides display a wide variety of structures that can possess both ordered and disordered Ln³⁺ sites.¹⁻¹⁴ The ordering of two different Ln³⁺ cations over two or more crystallographic sites can be achieved by maximizing the difference in the size of the Ln³⁺ ions. Typical examples of ordered phases include α -LnLn'S₃ (GdFeO₃-type)^{15, 14}, β -LnLn'Q₃ (Q = S, Se) (UFeS₃-type)^{16, 3,5,6} and γ -LnLn'S₃.⁷ In these compounds, there are sharp demarcations in coordination numbers and bond distances between the larger ions and smaller ions, which inhibit the disordering of two lanthanides. In contrast, mixed site occupancies are found in disordered structures, e.g. F-Ln₂S₃ (CeYb₃S₆)^{9, 17,18}, CeTmS₃,¹⁰ and Y₅S₇ (Sc₂Er₃S₇)^{11, 19}. When the difference in size between the two Ln³⁺ ions is too small, disorder is unavoidable owing to the strong similarities in the structural chemistry of lanthanides. This is best represented by F-Ln₂S₃ type compounds, which contain an eight-coordinate environment for larger Ln³⁺ ion (A), a seven-coordinate intermediate site (B), and two six-coordinate octahedral sites for the smaller Ln³⁺ ion (C). In case of F-GdLu₃S₆, the position B is occupied by both metal ions.⁹ For F-Er₃ScS₆, both C sites are disordered.⁸

In addition to the remarkable structural flexibility of mixed-lanthanide sulfides that gives rise to a myriad of structure types, these compounds also display important physical properties including tunable band gaps. In an effort to understand the structure-property relationships in interlanthanide chalcogenides, we present the preparation, structure determination, magnetism, and optical properties of the partially disordered δ - $\text{Ln}_{2-x}\text{Lu}_x\text{S}_3$ ($\text{Ln} = \text{Ce}, \text{Pr}, \text{Nd}; x = 0.67 - 0.71$) (CeTmS₃-type) compounds. The information in this chapter has been published as a full paper in *Journal of Solid-State Chemistry*.²⁰

EXPERIMENTAL

Starting Materials. Ce (99.9%, Alfa-Aesar), Pr (99.9%, Alfa-Aesar), Nd (99.9%, Alfa-Aesar), Lu (99.9%, Alfa-Aesar), S (99.5%, Alfa-Aesar), and Sb (99.5%, Alfa-Aesar) were used as received. The Sb₂S₃ flux was prepared from the direct reaction of the elements in sealed fused-silica ampoules at 850 °C.

Syntheses of δ - $\text{Ln}_{2-x}\text{Lu}_x\text{S}_3$ ($\text{Ln} = \text{Ce}, \text{Pr}, \text{Nd}; x = 0.67 - 0.71$). Reaction mixtures included 0.2000 g of Ln, Lu, S, and Sb₂S₃ in a ratio of 1:1:3:0.5 mmol. They were loaded into fused-silica ampoules in an argon-filled glovebox. The ampoules were sealed under vacuum and heated in the following profile using a programmable tube furnace.: 2 °C/min to 500 °C (held for 1 h), 0.5 °C/min to 1000 °C (held for 5 d), 0.04 °C/min to 550 °C (held for 2 d), and 0.5 °C/min to 24 °C. High yields of black crystals of δ -Ce_{1.30}Lu_{0.70}S₃ and dark red crystals of δ -Pr_{1.29}Lu_{0.71}S₃ and δ -Nd_{1.33}Lu_{0.67}S₃ were isolated manually. Powder X-ray diffraction measurements were used to confirm phase purity by comparing the powder patterns calculated from the single crystal X-ray

structures with the experimental data. Semi-quantitative SEM/EDX analyses were performed using JEOL 840/Link Isis or JEOL JSM-7000F instruments. Ln, Ln', and S percentages were calibrated against standards. Sb was not detected in the crystals. The Ln:Ln':S ratios were determined to be approximately 2:1:4.5 from EDX analyses.

Crystallographic Studies. Single crystals of δ -Ln_{2-x}Lu_xS₃ (Ln = Ce, Pr, Nd; x = 0.67 – 0.71) were mounted on glass fibers with epoxy and optically aligned on a Bruker APEX single crystal X-ray diffractometer using a digital camera. Initial intensity measurements were performed using graphite monochromated Mo K α (λ = 0.71073 Å) radiation from a sealed tube and monocapillary collimator. SMART (v 5.624) was used for preliminary determination of the cell constants and data-collection control. The intensities of reflections of a sphere were collected by a combination of 3 sets of exposures (frames). Each set had a different ϕ angle for the crystal and each exposure covered a range of 0.3° in ω . A total of 1800 frames were collected with exposure times per frame of 10 or 20 seconds depending on the crystal.

For δ -Ln_{2-x}Lu_xS₃ (Ln = Ce, Pr, Nd; x = 0.67 – 0.71), determination of integrated intensities and global refinement were performed with the Bruker SAINT (v 6.02) software package using a narrow-frame integration algorithm. These data were treated first with a face-indexed numerical absorption correction using XPREP,²¹ followed by a semi-empirical absorption correction using SADABS.²² The program suite SHELXTL (v 6.12) was used for space group determination (XPREP), direct methods structure solution (XS), and least-squares refinement (XL).²¹ The final refinements included anisotropic displacement parameters for all atoms and secondary extinction. Some crystallographic details are given in Table 5.1. Atomic coordinates and equivalent isotropic displacement

Table 5.1. Crystallographic Data for $\delta\text{-Ln}_{2-x}\text{Lu}_x\text{S}_3$ (Ln = Ce, Pr, Nd; x = 0.67 – 0.71).

| Formula | $\delta\text{-Ce}_{1.30}\text{Lu}_{0.70}\text{S}_3$ | $\delta\text{-Pr}_{1.29}\text{Lu}_{0.71}\text{S}_3$ | $\delta\text{-Nd}_{1.33}\text{Lu}_{0.67}\text{S}_3$ |
|---|---|---|---|
| Fw | 400.86 | 402.31 | 405.13 |
| Color | Black | Dark red | Dark red |
| Crystal system | monoclinic | monoclinic | monoclinic |
| Space group | $P2_1/m$ (No. 11) | $P2_1/m$ (No. 11) | $P2_1/m$ (No. 11) |
| a (Å) | 11.0186(7) | 10.9623(10) | 10.9553(7) |
| b (Å) | 3.9796(3) | 3.9497(4) | 3.9419(3) |
| c (Å) | 21.6562(15) | 21.5165(19) | 21.4920(15) |
| β | 101.6860(10) | 101.579(2) | 101.5080(10) |
| V (Å ³) | 929.93(11) | 912.66(15) | 909.47(11) |
| Z | 8 | 8 | 8 |
| T (K) | 193 | 193 | 193 |
| λ (Å) | 0.71073 | 0.71073 | 0.71073 |
| ρ_{calcd} (g cm ⁻³) | 5.726 | 5.856 | 5.918 |
| μ (cm ⁻¹) | 284.95 | 300.82 | 306.04 |
| $R(F)^a$ | 0.0288 | 0.0407 | 0.0300 |
| $R_w(F_o^2)^b$ | 0.0656 | 0.0987 | 0.0762 |

$$^a R(F) = \frac{\sum \|F_o\| - |F_c|}{\sum |F_o|} \text{ for } F_o^2 > 2\sigma(F_o^2).$$

$$^b R_w(F_o^2) = \left[\frac{\sum [w(F_o^2 - F_c^2)^2]}{\sum wF_o^4} \right]^{1/2}.$$

Table 5.2. Atomic Coordinates and Equivalent Isotropic Displacement Parameters for δ - $\text{Ce}_{1.30}\text{Lu}_{0.70}\text{S}_3$.

| Atom (site) | x | y | z | $U_{\text{eq}} (\text{\AA}^2)^a$ |
|-------------|-------------|------|-------------|----------------------------------|
| Ce1 | 0.19847(5) | 0.25 | 0.76193(3) | 0.00853(13) |
| Ce2 | 0.58871(5) | 0.25 | 0.86078(3) | 0.00753(13) |
| Ce3 | 0.80925(5) | 0.25 | 0.72906(3) | 0.00609(12) |
| Ce4 | 0.69987(5) | 0.25 | 0.53486(3) | 0.00697(13) |
| Ce5 | 0.02154(10) | 0.25 | 0.09339(5) | 0.0113(2) |
| Lu1 | 0.94671(4) | 0.25 | 0.41832(2) | 0.00977(11) |
| Lu2 | 0.52820(5) | 0.25 | 0.35266(3) | 0.00965(13) |
| Ce/Lu | 0.67261(5) | 0.25 | 0.04880(2) | 0.00988(18) |
| Lu4 | 0.0588(5) | 0.25 | 0.0804(2) | 0.0176(10) |
| S1 | 0.4135(2) | 0.25 | 0.03938(12) | 0.0088(5) |
| S2 | 0.2948(2) | 0.25 | 0.36659(11) | 0.0069(5) |
| S3 | 0.7532(2) | 0.25 | 0.32707(12) | 0.0094(5) |
| S4 | 0.8554(2) | 0.25 | 0.96392(12) | 0.0107(5) |
| S5 | 0.9936(2) | 0.25 | 0.22765(12) | 0.0089(5) |
| S6 | 0.2529(2) | 0.25 | 0.17836(12) | 0.0080(5) |
| S7 | 0.6208(2) | 0.25 | 0.16832(12) | 0.0080(5) |
| S8 | 0.1437(2) | 0.25 | 0.51372(12) | 0.0089(5) |
| S9 | 0.4433(2) | 0.25 | 0.55520(12) | 0.0109(5) |
| S10 | 0.5364(2) | 0.25 | 0.72589(12) | 0.0083(5) |
| S11 | 0.9553(2) | 0.25 | 0.63164(12) | 0.0104(5) |
| S12 | 0.1680(2) | 0.25 | 0.89765(12) | 0.0117(5) |

^a U_{eq} is defined as one-third of the trace of the orthogonalized U_{ij} tensor.

Table 5.3. Atomic Coordinates and Equivalent Isotropic Displacement Parameters for δ -Pr_{1.29}Lu_{0.71}S₃.

| Atom (site) | x | y | z | $U_{\text{eq}} (\text{\AA}^2)^a$ |
|-------------|------------|------|-------------|----------------------------------|
| Pr1 | 0.19691(8) | 0.25 | 0.76308(4) | 0.0084(2) |
| Pr2 | 0.58798(8) | 0.25 | 0.86070(4) | 0.0075(2) |
| Pr3 | 0.80815(8) | 0.25 | 0.72974(4) | 0.00628(19) |
| Pr4 | 0.69981(8) | 0.25 | 0.53557(4) | 0.00693(19) |
| Pr5 | 0.0220(4) | 0.25 | 0.09241(17) | 0.0087(4) |
| Lu1 | 0.94660(6) | 0.25 | 0.41786(3) | 0.00951(17) |
| Lu2 | 0.52939(6) | 0.25 | 0.35258(3) | 0.01012(18) |
| Pr/Lu | 0.67394(7) | 0.25 | 0.04788(3) | 0.0094(3) |
| Lu4 | 0.051(2) | 0.25 | 0.0793(9) | 0.015(3) |
| S1 | 0.4140(4) | 0.25 | 0.03935(19) | 0.0092(8) |
| S2 | 0.2947(3) | 0.25 | 0.36625(18) | 0.0071(7) |
| S3 | 0.7549(3) | 0.25 | 0.32577(19) | 0.0090(8) |
| S4 | 0.8567(4) | 0.25 | 0.96457(19) | 0.0113(8) |
| S5 | 0.9947(3) | 0.25 | 0.22627(19) | 0.0095(8) |
| S6 | 0.2531(3) | 0.25 | 0.17760(18) | 0.0076(7) |
| S7 | 0.6222(4) | 0.25 | 0.16747(19) | 0.0090(7) |
| S8 | 0.1442(3) | 0.25 | 0.51375(19) | 0.0086(7) |
| S9 | 0.4424(4) | 0.25 | 0.55476(19) | 0.0107(8) |
| S10 | 0.5369(4) | 0.25 | 0.72688(18) | 0.0092(7) |
| S11 | 0.9543(4) | 0.25 | 0.6323(2) | 0.0111(8) |
| S12 | 0.1657(4) | 0.25 | 0.89822(19) | 0.0112(8) |

^a U_{eq} is defined as one-third of the trace of the orthogonalized U_{ij} tensor.

Table 5.4. Atomic Coordinates and Equivalent Isotropic Displacement Parameters for δ -Nd_{1.33}Lu_{0.67}S₃.

| Atom (site) | <i>x</i> | <i>y</i> | <i>z</i> | $U_{\text{eq}} (\text{\AA}^2)^a$ |
|-------------|------------|----------|-------------|----------------------------------|
| Nd1 | 0.19518(5) | 0.25 | 0.76324(3) | 0.00894(14) |
| Nd2 | 0.58694(5) | 0.25 | 0.85947(3) | 0.00822(14) |
| Nd3 | 0.80693(5) | 0.25 | 0.72945(3) | 0.00681(13) |
| Nd4 | 0.70009(5) | 0.25 | 0.53580(3) | 0.00763(13) |
| Nd5 | 0.0234(3) | 0.25 | 0.09212(12) | 0.0082(3) |
| Lu1 | 0.94665(4) | 0.25 | 0.41779(2) | 0.01036(12) |
| Lu2 | 0.53089(4) | 0.25 | 0.35315(2) | 0.01107(13) |
| Nd/Lu | 0.67466(5) | 0.25 | 0.04720(2) | 0.00911(19) |
| Lu4 | 0.049(2) | 0.25 | 0.0816(10) | 0.013(3) |
| S1 | 0.4146(2) | 0.25 | 0.04108(12) | 0.0094(5) |
| S2 | 0.2955(2) | 0.25 | 0.36661(12) | 0.0069(5) |
| S3 | 0.7555(2) | 0.25 | 0.32486(13) | 0.0100(5) |
| S4 | 0.8566(3) | 0.25 | 0.96404(13) | 0.0110(5) |
| S5 | 0.9960(2) | 0.25 | 0.22621(13) | 0.0094(5) |
| S6 | 0.2545(2) | 0.25 | 0.17833(12) | 0.0087(5) |
| S7 | 0.6232(2) | 0.25 | 0.16816(12) | 0.0091(5) |
| S8 | 0.1452(2) | 0.25 | 0.51344(12) | 0.0091(5) |
| S9 | 0.4426(2) | 0.25 | 0.55385(13) | 0.0115(5) |
| S10 | 0.5367(2) | 0.25 | 0.72630(12) | 0.0090(5) |
| S11 | 0.9535(3) | 0.25 | 0.63255(13) | 0.0106(5) |
| S12 | 0.1628(2) | 0.25 | 0.89773(12) | 0.0103(5) |

^a U_{eq} is defined as one-third of the trace of the orthogonalized U_{ij} tensor.

parameters for $\delta\text{-Ln}_{2-x}\text{Lu}_x\text{S}_3$ (Ln = Ce, Pr, Nd; $x = 0.67 - 0.71$) are given in Tables 5.2-5.4. The structure of CeTmS_3 was previously determined to be ordered, with four eight-coordinate Ce^{3+} ions, two seven-coordinate Tm^{3+} and two six-coordinate Tm^{3+} ions.¹⁰ However, elemental analysis for $\delta\text{-Ln}_{2-x}\text{Lu}_x\text{S}_3$ (Ln = Ce, Pr, Nd; $x = 0.67 - 0.71$) indicated the ratio of $\text{Ln}^{3+}:\text{Lu}^{3+}$ is approximately 2:1. Considerable disordering of Ce/Lu in the Lu^{3+} positions should be present. Reexamining the Tm-S bond distances in CeTmS_3 , the average values of $\text{Tm}(3)\text{S}_7$ and $\text{Tm}(4)\text{S}_7$ are 2.77 and 2.86 Å respectively. Compared to Shannon's data,²³ in which TmS_7 and CeS_7 are 2.77 and 2.91 Å, $\text{Tm}(4)$ site is more likely disordered. For $\delta\text{-Ln}_{2-x}\text{Lu}_x\text{S}_3$ (Ln = Ce, Pr, Nd; $x = 0.67 - 0.71$), the four eight-coordinate positions were assigned as Ln^{3+} and the $\text{Tm}(1)$, $\text{Tm}(2)$ and $\text{Tm}(3)$ sites were assigned as Lu^{3+} at the beginning of the refinement cycles. Two large residual electron density peaks approximately 0.5 Å away from each other were found in the original place of $\text{Tm}(4)$. Each of these sites was assigned as a Ln^{3+} position. The one with longer Ln-S bond distances was named as $\text{Ln}(5)$ (Ln = Ce, Pr, or Nd), and the other one was assigned as $\text{Lu}(4)$. It has to be mentioned, switching the $\text{Ln}(5)$ and $\text{Lu}(4)$ positions as well as disordering of $\text{Ln}(5)/\text{Lu}(4)$ at one site were both tried, and gave poorer residuals. The refinement of occupancies of $\text{Ln}(5)$ and $\text{Lu}(4)$ showed 3:2 ratio of $\text{Ln}^{3+}:\text{Lu}^{3+}$, which requires more disordering in other Lu^{3+} sites. In the next step, Ln/Lu were both assigned at $\text{Lu}(3)$ positions. This lowered the R_1 value and the weighting scheme to an even greater extent. The final refinements gave rise to formulas of $\delta\text{-Ce}_{1.30}\text{Lu}_{0.70}\text{S}_3$, $\delta\text{-Pr}_{1.29}\text{Lu}_{0.71}\text{S}_3$, and $\delta\text{-Nd}_{1.33}\text{Lu}_{0.67}\text{S}_3$, which are consistent with the Ln:Lu ratios from calibrated EDX results. The standard deviation on the composition from the refinements is 0.01.

Powder X-ray Diffraction. Powder X-ray diffraction patterns were collected with a Rigaku Miniflex powder X-ray diffractometer using Cu K α ($\lambda = 1.54056 \text{ \AA}$) radiation.

Magnetic Susceptibility Measurements. Magnetism data were measured on powders in gelcap sample holders with a Quantum Design MPMS 7T magnetometer/susceptometer between 2 and 300 K and in applied fields up to 7 T. DC susceptibility measurements were made under zero-field-cooled conditions with an applied field of 0.1 T. Susceptibility values were corrected for the sample diamagnetic contribution according to Pascal's constants²⁴ as well as for the sample holder diamagnetism. θ_p values were obtained from extrapolations from fits between 100 and 300 K. In addition, ZFC and FC data were collected as follows: The samples were first zero field cooled from room temperature and the susceptibility was measured at 100 Oe to 300 K. Then the sample was field cooled at 100 Oe to 2 K and the same measurement was done by increasing with increasing temperatures. There are no differences between ZFC and FC data at the measured temperatures. (Magnetic susceptibility measurements were performed by Eun Sang Choi and James S. Brooks at Florida State University)

UV-vis-NIR Diffuse Reflectance Spectroscopy. The diffuse reflectance spectra for $\delta\text{-Ln}_{2-x}\text{Lu}_x\text{S}_3$ (Ln = Ce, Pr, Nd; $x = 0.67 - 0.71$) were measured from 200 to 1500 nm using a Shimadzu UV3100 spectrophotometer equipped with an integrating sphere attachment. The Kubelka-Munk function was used to convert diffuse reflectance data to absorption spectra.²⁵

RESULTS AND DISCUSSION

Structures of δ -Ln_{2-x}Lu_xS₃ (Ln = Ce, Pr, Nd; x = 0.67 – 0.71). The δ -Ln_{2-x}Lu_xS₃ (Ln = Ce, Pr, Nd; x = 0.67 – 0.71) series are isotypic with CeTmS₃,¹⁰ which crystallizes in *P2₁/m* space group with a very complex three-dimensional structure. A view of the unit cell is illustrated in Figure 5.1. There are nine crystallographically unique lanthanides sites and twelve sulfide positions. Ln(1) are coordinated to nine S atoms in a tricapped trigonal prismatic environment with two long capping Ln···S contacts. For instance, in δ -Ce_{1.30}Lu_{0.70}S₃ the short Ce-S bond distances range from 2.8940(19) Å to 3.025(3) Å, while the longer contacts are 3.476(3) Å and 3.957(3) Å. The longest of these can probably be disregarded. Ln(2), Ln(3), and Ln(4) have similar coordination geometries. All of them bond to eight S atoms and occur as bicapped trigonal prisms. Ln(5) and Ln/Lu sites are seven-coordinate in a monocapped trigonal prismatic arrangement. It is worth noting that Ln/LuS₇ has intermediate bond distances. For example, the average value of Ce/LuS₇ is 2.81 Å, which is between 2.91 Å for CeS₇ and 2.75 Å for LuS₇ according to the radii reported by Shannon.²³ Compared to larger lanthanides, Lu³⁺ ions have fewer S neighbors. Both Lu(1) and Lu(2) atoms are bound to six S atoms in octahedral environments. Seven-coordinate Lu(4) atoms are found to have a highly distorted monocapped trigonal prismatic geometry, with two short bonds and three long contacts. In case of δ -Ce_{1.30}Lu_{0.70}S₃, Lu(4)-S bond distances are 2.478(3) Å ×2, 2.690(6) Å, 3.016(6) Å, 3.304(4) Å ×2, and 3.408(5) Å. The selected bond distances are listed in Table 5.5.

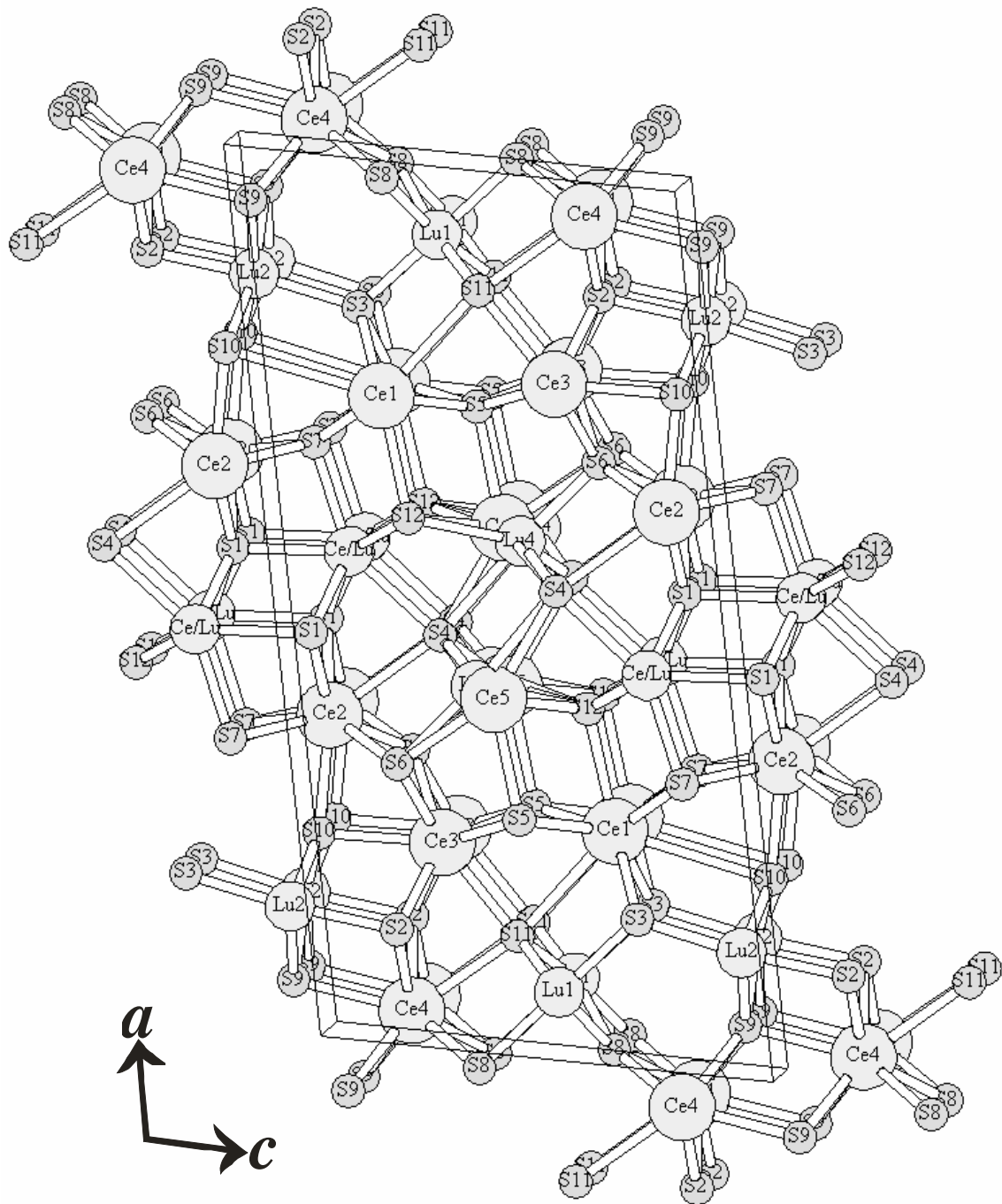


Figure 5.1. A view down the b axis shows the complex three-dimensional structure of δ - $\text{Ce}_{1.30}\text{Lu}_{0.70}\text{S}_3$.

Table 5.5. Selected Bond Distances (Å) for δ -Ln_{2-x}Lu_xS₃ (Ln = Ce, Pr, Nd; x = 0.67 – 0.71).

| Formula | δ -Ce _{1.30} Lu _{0.70} S ₃ | δ -Pr _{1.29} Lu _{0.71} S ₃ | δ -Nd _{1.33} Lu _{0.67} S ₃ |
|---------------|--|--|--|
| Ln(1)-S(3) ×2 | 2.8940(19) | 2.870(3) | 2.858(2) |
| Ln(1)-S(5) ×2 | 2.9466(19) | 2.925(3) | 2.918(2) |
| Ln(1)-S(7) ×2 | 2.9978(19) | 2.980(3) | 2.974(2) |
| Ln(1)-S(10) | 3.957(3) | 3.957(4) | 3.976(3) |
| Ln(1)-S(11) | 3.476(3) | 3.462(4) | 3.454(3) |
| Ln(1)-S(12) | 3.025(3) | 2.995(4) | 2.981(3) |
| Ln(2)-S(1) ×2 | 2.9421(19) | 2.923(3) | 2.910(2) |
| Ln(2)-S(4) | 3.312(3) | 3.321(4) | 3.336(3) |
| Ln(2)-S(6) ×2 | 2.8850(18) | 2.862(3) | 2.8507(19) |
| Ln(2)-S(7) ×2 | 3.0162(19) | 3.002(3) | 2.998(2) |
| Ln(2)-S(10) | 2.861(3) | 2.821(4) | 2.805(3) |
| Ln(3)-S(2) ×2 | 2.9331(18) | 2.916(3) | 2.9122(19) |
| Ln(3)-S(5) ×2 | 2.9551(19) | 2.941(3) | 2.938(2) |
| Ln(3)-S(6) ×2 | 3.0007(19) | 2.977(3) | 2.966(2) |
| Ln(3)-S(10) | 2.993(3) | 2.962(4) | 2.948(3) |
| Ln(3)-S(11) | 2.901(3) | 2.882(4) | 2.872(3) |
| Ln(4)-S(2) ×2 | 2.9098(18) | 2.884(3) | 2.8715(19) |
| Ln(4)-S(8) ×2 | 2.9615(19) | 2.946(3) | 2.932(2) |
| Ln(4)-S(9) ×2 | 3.001(2) | 2.982(3) | 2.973(2) |
| Ln(4)-S(9) | 2.948(3) | 2.933(4) | 2.923(3) |

| | | | |
|----------------|------------|-----------|------------|
| Ln(4)-S(11) | 3.150(3) | 3.128(4) | 3.119(3) |
| Ln(5)-S(4) ×2 | 2.832(2) | 2.798(5) | 2.776(3) |
| Ln(5)-S(4) | 3.022(3) | 2.975(5) | 2.985(4) |
| Ln(5)-S(5) | 2.985(3) | 2.955(6) | 2.957(4) |
| Ln(5)-S(6) | 2.825(3) | 2.813(4) | 2.823(4) |
| Ln(5)-S(12) ×2 | 2.920(2) | 2.888(4) | 2.876(3) |
| Lu(1)-S(3) | 2.597(3) | 2.583(4) | 2.590(3) |
| Lu(1)-S(8) ×2 | 2.7771(18) | 2.765(3) | 2.7702(19) |
| Lu(1)-S(8) | 2.677(3) | 2.675(4) | 2.678(3) |
| Lu(1)-S(11) ×2 | 2.6020(17) | 2.592(3) | 2.5933(17) |
| Lu(2)-S(2) | 2.649(2) | 2.647(4) | 2.652(3) |
| Lu(2)-S(3) | 2.647(3) | 2.649(4) | 2.649(3) |
| Lu(2)-S(9) ×2 | 2.7904(19) | 2.779(3) | 2.7808(19) |
| Lu(2)-S(10) ×2 | 2.6210(16) | 2.618(3) | 2.6160(17) |
| Ln/Lu-S(1) ×2 | 2.7880(18) | 2.762(3) | 2.7749(19) |
| Ln/Lu-S(1) | 2.820(3) | 2.819(4) | 2.826(3) |
| Ln/Lu-S(4) | 2.989(3) | 2.944(4) | 2.930(3) |
| Ln/Lu-S(7) | 2.761(3) | 2.744(4) | 2.768(3) |
| Ln/Lu-S(12) ×2 | 2.7500(18) | 2.742(3) | 2.7595(19) |
| Lu(4)-S(4) ×2 | 2.478(3) | 2.487(16) | 2.513(16) |
| Lu(4)-S(4) | 3.016(6) | 2.921(15) | 2.951(18) |
| Lu(4)-S(5) | 3.408(5) | 3.34(2) | 3.27(2) |
| Lu(4)-S(6) | 2.690(6) | 2.736(15) | 2.741(18) |
| Lu(4)-S(12) ×2 | 3.304(4) | 3.20(2) | 3.145(19) |

The complex three-dimensional structure of $\delta\text{-Ln}_{2-x}\text{Lu}_x\text{S}_3$ (Ln = Ce, Pr, Nd; $x = 0.67 - 0.71$) is constructed from one-dimensional chains of LnS_n ($n = 6 - 9$) polyhedra that extend along the b axis. Chains constructed from LnS_9 or LnS_8 polyhedra share opposite trigonal faces with two neighbors along the direction of chain propagation. The small six- and seven coordinate Ln^{3+} -containing units only share edges within the chains. Each LnS_x or LuS_y polyhedron shares edges and corners with others in the $[ac]$ plane. They are normal compared to Shannon's data.²³

Because there are no S-S bonds in $\delta\text{-Ln}_{2-x}\text{Lu}_x\text{S}_3$ (Ln = Ce, Pr, Nd; $x = 0.67 - 0.71$), the oxidation states in these compounds can be assigned as +3/+3/-2. This designation is confirmed by both bond-valence sum calculations^{27, 28} and by magnetic susceptibility measurements (*vide infra*).

Magnetic Susceptibility. The inverse molar Ln magnetic susceptibilities for $\delta\text{-Ln}_{2-x}\text{Lu}_x\text{S}_3$ (Ln = Ce, Pr, Nd; $x = 0.67 - 0.71$) in the range of 2-300 K are shown in Figures 5.2-5.4. All three compounds show a deviation from the Curie-Weiss law near 100 K. Magnetic parameters, which are presented in Table 5.6, were determined from the fit from the Curie-Weiss regions. These compounds do not show evidence of long-range magnetic ordering down to 5 K. $\delta\text{-Ce}_{1.30}\text{Lu}_{0.70}\text{S}_3$ has very similar magnetic behavior with $\beta\text{-LnLn}'\text{S}_3$ ⁶ and $\gamma\text{-LnLn}'\text{S}_3$ ⁷ with a large negative value of θ_p of -34(1) K.

The $1/\chi$ data for $\delta\text{-Pr}_{1.29}\text{Lu}_{0.71}\text{S}_3$ show a positive, rather than negative, deviation from Curie-Weiss behavior at 120 K. The gradual change in the slope and the negative value of θ_p (-6.0(5) K) may indicate short-range antiferromagnetic ordering. $\delta\text{-Nd}_{1.33}\text{Lu}_{0.67}\text{S}_3$ acts like an intermediate state of $\delta\text{-Ce}_{1.30}\text{Lu}_{0.70}\text{S}_3$ and $\delta\text{-Pr}_{1.29}\text{Lu}_{0.71}\text{S}_3$. The curvature of the plot starts as upward at 120 K. At lower temperature, it becomes

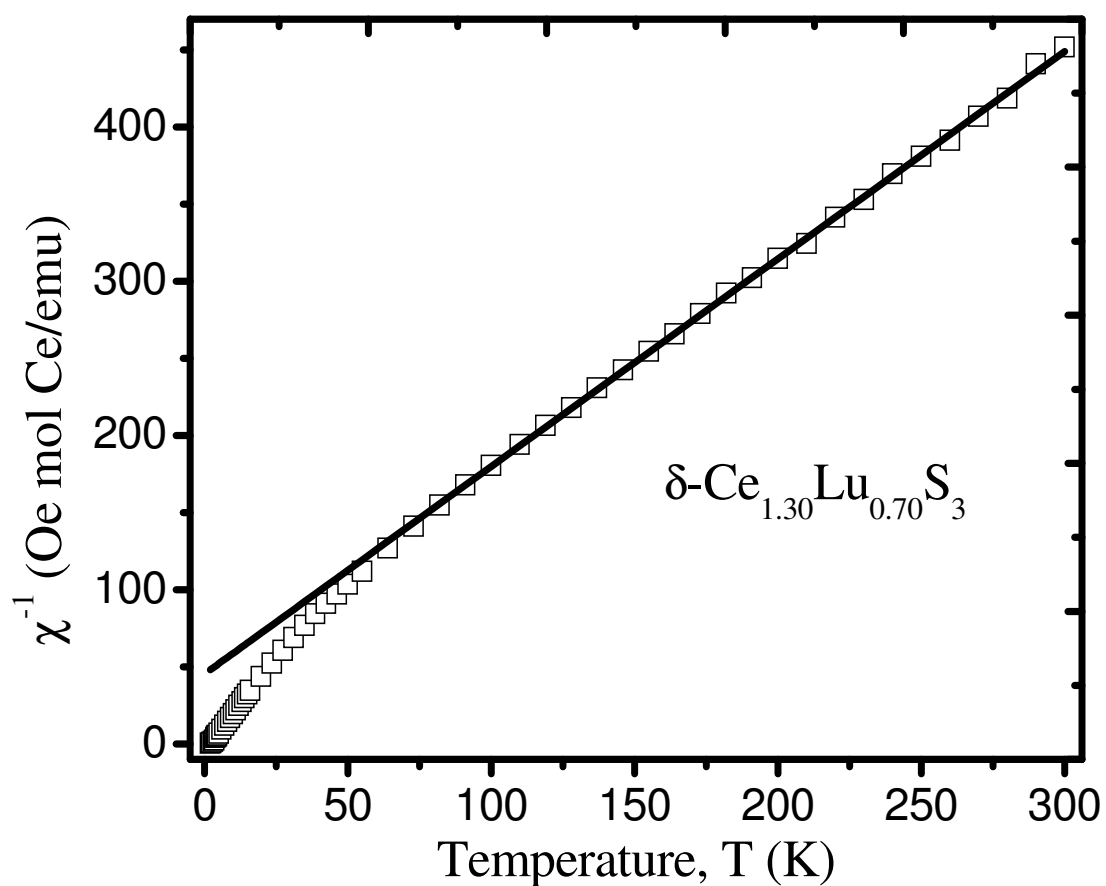


Figure 5.2. A plot of inverse molar cerium magnetic susceptibility for $\delta\text{-Ce}_{1.30}\text{Lu}_{0.70}\text{S}_3$ between 2 and 300 K. Data were taken under an applied magnetic field of 0.1 T. The straight line represents the fit to Curie-Weiss law in the range of 100-300 K.

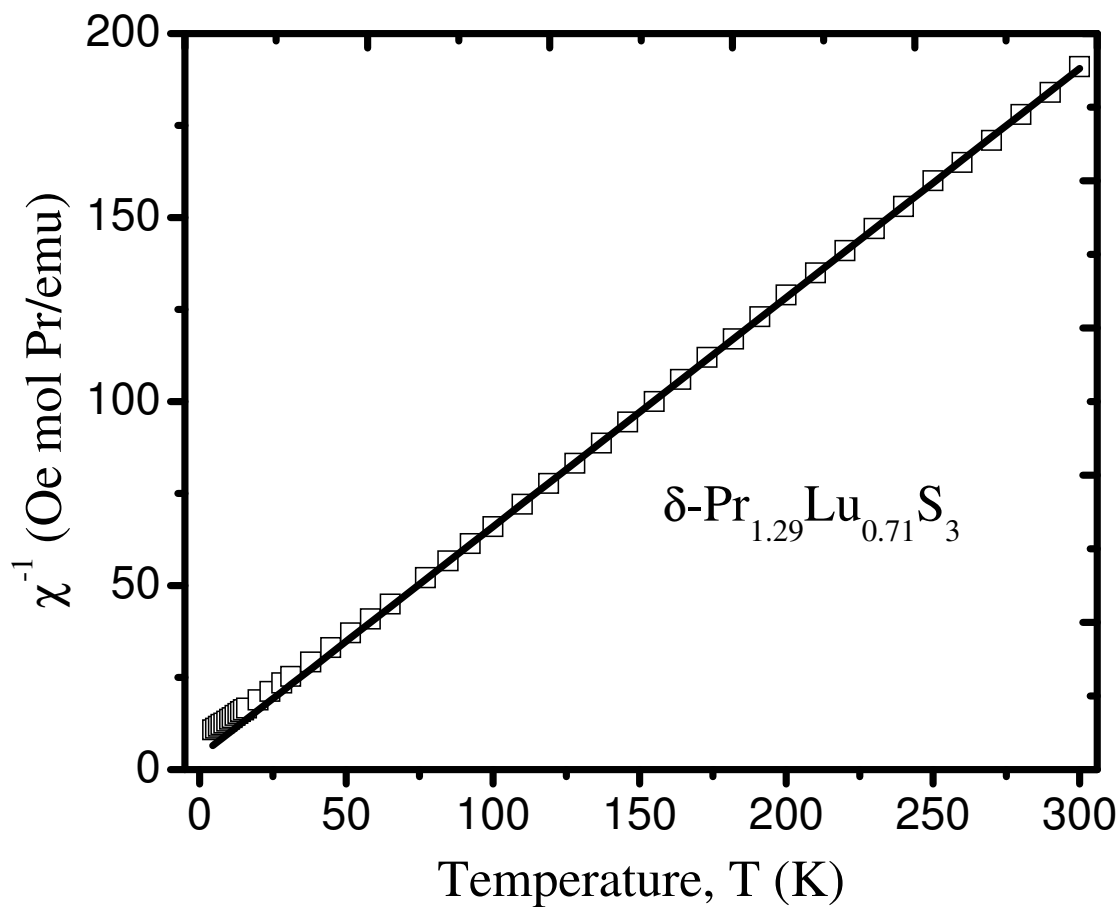


Figure 5.3. Temperature dependence of the reciprocal molar praseodymium magnetic susceptibility for $\delta\text{-Pr}_{1.29}\text{Lu}_{0.71}\text{S}_3$ under an applied magnetic field of 0.1 T between 2 and 300 K. The straight line represents the fit to Curie-Weiss law in the range of 100-300 K.

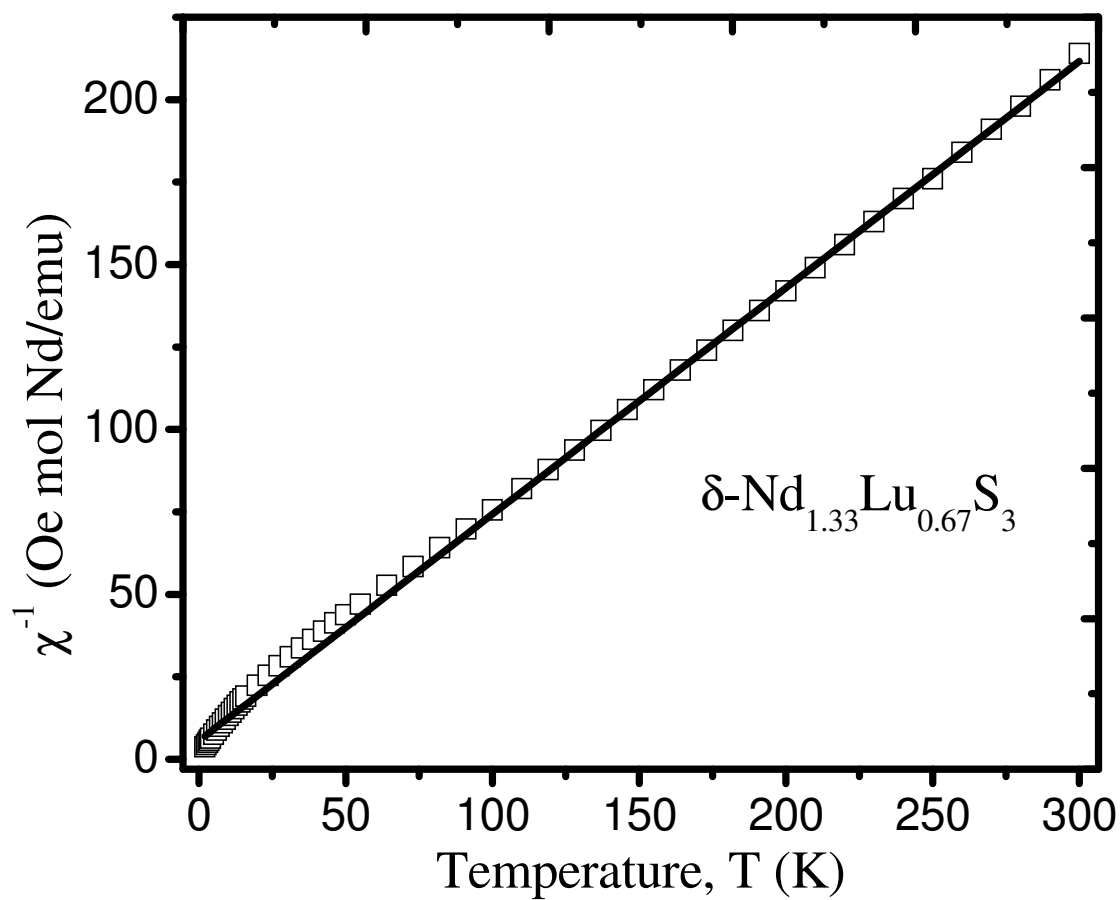


Figure 5.4. Inverse molar neodymium magnetic susceptibility vs. T for $\delta\text{-Nd}_{1.33}\text{Lu}_{0.67}\text{S}_3$ under an applied magnetic field of 0.1 T between 2 and 300 K. The straight line represents the fit to Curie-Weiss law in the range of 100-300 K.

Table 5.6. Magnetic Parameters for δ -Ln_{2-x}Lu_xS₃ (Ln = Ce, Pr, Nd; x = 0.67 – 0.71).

| Formula | P_{cal}/μ_B | P_{eff}/μ_B | θ_p/K | R^2 |
|--|------------------------|------------------------|---------------------|---------|
| δ -Ce _{1.30} Lu _{0.70} S ₃ | 2.54 | 2.438(5) | -34(1) | 0.99952 |
| δ -Pr _{1.29} Lu _{0.71} S ₃ | 3.58 | 3.583(4) | -6.0(5) | 0.99989 |
| δ -Nd _{1.33} Lu _{0.67} S ₃ | 3.62 | 3.413(8) | -8(1) | 0.99959 |

^a P_{cal} and P_{eff} : calculated²⁶ and experimental effective magnetic moments per Ln ion.

^b Weiss constant (θ_p) and goodness of fit (R^2) obtained from high temperature (100-300 K) data.

negative. Crystal-field effects and short-range ordering may both contribute to this behavior. The θ_p of $\delta\text{-Nd}_{1.33}\text{Lu}_{0.67}\text{S}_3$ is $-8(1)$ K. The experimental effective magnetic moments per Ln ion based on the formulas proposed are very close to the theoretical value of the free Ln^{3+} ions as shown in Table 5.6. As a reference, the experimental moments using the formulas as LnLuS_3 (Ln = Ce, Pr, Nd) are $2.82 \mu_B$ for CeLuS_3 , $4.05 \mu_B$ for PrLuS_3 , and $3.98 \mu_B$ for NdLuS_3 , which are larger than the accepted values.²⁶ This provides further supporting evidence for the disorder refinements.

Optical Properties. The UV-vis-NIR diffuse reflectance spectra are presented in Figure 5.5 for $\delta\text{-Ln}_{2-x}\text{Lu}_x\text{S}_3$ (Ln = Ce, Pr, Nd; $x = 0.67 - 0.71$). The measured band gaps for $\delta\text{-Ce}_{1.30}\text{Lu}_{0.70}\text{S}_3$, $\delta\text{-Pr}_{1.29}\text{Lu}_{0.71}\text{S}_3$, and $\delta\text{-Nd}_{1.33}\text{Lu}_{0.67}\text{S}_3$ are 1.25 eV, 1.38 eV, and 1.50 eV respectively. They are consistent with the observed colors. $\delta\text{-Ce}_{1.30}\text{Lu}_{0.70}\text{S}_3$ is black, while both $\delta\text{-Pr}_{1.29}\text{Lu}_{0.71}\text{S}_3$ and $\delta\text{-Nd}_{1.33}\text{Lu}_{0.67}\text{S}_3$ are dark red. In addition to the observed band gap for $\delta\text{-Nd}_{1.33}\text{Lu}_{0.67}\text{S}_3$, f-f transitions are also apparent in the spectrum of this compound. The band gap results are comparable to the value reported for $\gamma\text{-LnLn}'\text{S}_3$ (Ln = La, Ce; Ln' = Er, Tm, Yb).⁷ $\delta\text{-Ce}_{1.30}\text{Lu}_{0.70}\text{S}_3$ has smaller band gap due to the enhanced energy of the $4f^1$ electron. Much like other mixed-lanthanide chalcogenides, the electronic structures of $\delta\text{-LnLuS}_3$ are tunable based on the choice of lanthanide.

Conclusions

$\delta\text{-Ln}_{2-x}\text{Lu}_x\text{S}_3$ (Ln = Ce, Pr, Nd; $x = 0.67 - 0.71$) were prepared using a Sb_2S_3 flux and their structures determined by single crystal X-ray diffraction. These compounds crystallize in the disordered CeTmS_3 structure-type. EDX analyses and magnetic

measurements support the proposed formulas as $\delta\text{-Ce}_{1.30}\text{Lu}_{0.70}\text{S}_3$, $\delta\text{-Pr}_{1.29}\text{Lu}_{0.71}\text{S}_3$, and $\delta\text{-Nd}_{1.33}\text{Lu}_{0.67}\text{S}_3$. The UV-vis-NIR diffuse reflectance measurements show these compounds to be wide band-gap semiconductors.

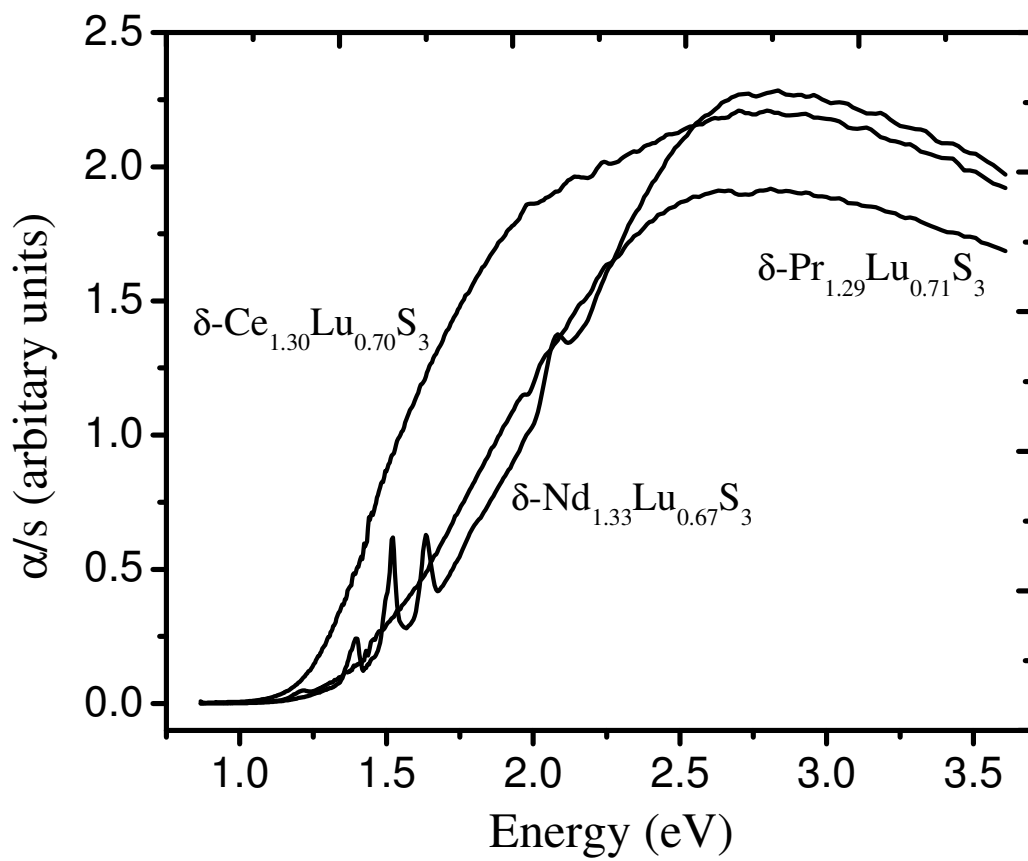


Figure 5.5. UV-vis diffuse reflectance spectra of $\delta\text{-Ln}_{2-x}\text{Lu}_x\text{S}_3$ (Ln = Ce, Pr, Nd; $x = 0.67 - 0.71$).

REFERENCES

1. Rodier, N.; Laruelle, P. *C. R. Seances Acad. Sci. Ser.* **1970**, C270, 2127.
2. Ijdo, D.J.W. *Acta Crystallogr.* **1980**, B36, 2403.
3. Rodier, N.; Julien, R.; Tien, V. *Acta Crystallogr.* **1983**, C39, 670.
4. Range, K.-J.; Gietl, A.; Klement, U. *Z. Kristallogr.* **1993**, 207, 147.
5. Carré, D.; Laruelle, P. *Acta Crystallogr.* **1974**, B30, 952.
6. Mitchell, K.; Somers, R. C.; Huang, F. Q.; Ibers, J. A. *J. Solid State Chem.* **2004**, 177, 709.
7. Jin, G. B.; Choi, E. S.; Guertin, R. P.; Brooks, J. S.; Bray, T. H.; Booth, C. H.; Albrecht-Schmitt, T. E. *Chem. Mater.* **2007**, 19, 567.
8. Rodier, N.; Laruelle, P. *Bull. Soc. fr. de Mineral. Cristallogr.* **1973**, 96, 30.
9. Rodier, N.; Firor, R. L.; Tien, V.; Guittard, M. *Mat. Res. Bull.* **1976**, 11, 1209.
10. Rodier, N. *Bull. Soc. fr. de Mineral. Cristallogr.* **1973**, 96, 350.
11. Rodier, N.; Laruelle, P. *Bull. Soc. fr. de Mineral. Cristallogr.* **1972**, 95, 548.
12. Carré, D.; Laruelle, P. *Acta Crystallogr.* **1973**, B29, 70.
13. Rodier, N.; Tien, V. *Bull. Soc. fr. de Mineral. Cristallogr.* **1975**, 98, 30.
14. Vovan, T.; Guittard, M.; Rodier, N. *Mat. Res. Bull.* **1979**, 14, 597.
15. Marezio, M.; Remeika, J.P.; Dernier, P.D. *Acta Crystallogr.* **1970**, B26, 2008.
16. Noël, H.; Padiou, J. *Acta Crystallogr.* **1976**, B32, 1593.
17. Schleid, T.; Lissner, F. *J. Alloys Compd.* **1992**, 189, 69.
18. Fang, C. M.; Meetsma, A.; Wiegers, G. A. *J. Alloys Compd.* **1993**, 201, 255.
19. Adolphe, C. *Annales de Chimie (Paris)* **1965**, 271.

20. Jin, G. B.; Choi, E. S.; Guertin, R. P.; Brooks, J. S.; Bray, T. H.; Booth, C. H.; Albrecht-Schmitt, T. E. *J. Solid State Chem.* in press.
21. Sheldrick, G. M. *SHELXTL PC, Version 6.12, An Integrated System for Solving, Refining, and Displaying Crystal Structures from Diffraction Data*; Siemens Analytical X-Ray Instruments, Inc.: Madison, WI 2001.
22. Sheldrick, G. M. *SADABS 2001, Program for absorption correction using SMART CCD based on the method of Blessing*; Blessing, R. H. *Acta Crystallogr.* **1995**, *A51*, 33.
23. Shannon, R. D. *Acta Crystallogr.* **1976**, *A32*, 751.
24. Mulay, L. N.; Boudreaux, E. A. *Theory and Applications of Molecular Diamagnetism*; Wiley-Interscience: New York, 1976.
25. Wendlandt, W. W.; Hecht, H. G. *Reflectance Spectroscopy*; Interscience Publishers: New York, 1966.
26. Kittel, C. *Introduction to Solid State Physics, 6th Edition*; Wiley: New York, 1986.
27. Brown, I. D.; Altermatt, D. *Acta Crystallogr.* **1985**, *B41*, 244.
28. Brese, N. E.; O’Keeffe, M. *Acta Crystallogr.* **1991**, *B47*, 192.

CHAPTER 6

SYNTHESES, STRUCTURE, MAGNETISM, AND OPTICAL PROPERTIES OF LUTETIUM-BASED INTERLANTHANIDE SELENIDES

ABSTRACT

Ln_3LuSe_6 (Ln = La, Ce), $\beta\text{-LnLuSe}_3$ (Ln = Pr, Nd), and $\text{Ln}_x\text{Lu}_{4-x}\text{Se}_6$ (Ln = Sm, Gd; x = 1.82, 1.87) have been synthesized using a Sb_2Se_3 flux at 1000 °C. Ln_3LuSe_6 (Ln = La, Ce) adopt the U_3ScS_6 -type three-dimensional structure, which is constructed from two-dimensional $\infty^2 [\text{Ln}_3\text{Se}_6]^{3-}$ slabs with the gaps between these slabs filled by octahedrally coordinated Lu^{3+} ions. The series of $\beta\text{-LnLuSe}_3$ (Ln = Pr, Nd) are isotypic with UFeS_3 . Their structures include layers formed from LuSe_6 octahedra that are separated by eight-coordinate larger Ln^{3+} ions in bicapped trigonal prismatic environments. $\text{Sm}_{1.82}\text{Lu}_{2.18}\text{Se}_6$ and $\text{Gd}_{1.87}\text{Lu}_{2.13}\text{Se}_6$ crystallize in the disordered F- Ln_2S_3 type structure with the eight-coordinate bicapped trigonal prismatic Ln(1) ions residing in the one-dimensional channels formed by three different double chains via edge and corner sharing. These double chains are constructed from Ln(2) Se_7 monocapped trigonal prisms, Ln(3) Se_6 octahedra, and Ln(4) S_6 octahedra, respectively. The magnetic susceptibilities of $\beta\text{-PrLuSe}_3$ and $\beta\text{-NdLuSe}_3$ follow the Curie-Weiss law. $\text{Sm}_{1.82}\text{Lu}_{2.18}\text{Se}_6$ shows van Vleck paramagnetism. Magnetic measurements show that

$\text{Gd}_{1.87}\text{Lu}_{2.13}\text{Se}_6$ undergoes an antiferromagnetic transition around 4 K. Ce_3LuSe_6 exhibits ferromagnetic ordering below 5 K. The optical band gaps for La_3LuSe_6 , Ce_3LuSe_6 , $\beta\text{-PrLuSe}_3$, $\beta\text{-NdLuSe}_3$, $\text{Sm}_{1.82}\text{Lu}_{2.18}\text{Se}_6$, and $\text{Gd}_{1.87}\text{Lu}_{2.13}\text{Se}_6$ are 1.26, 1.10, 1.56, 1.61, 1.51, and 1.56 eV, respectively.

INTRODUCTION

Interlanthanide chalcogenides have been the focus of intense interest owing to their remarkably complex structures, tunable band gaps, and in some cases atypical magnetism.¹⁻²¹ New developments in this area have been aided by the use of fluxes for the synthesis and crystal growth of new compounds. These fluxes have included a variety of alkali metal halides as well as Sb_2Q_3 (Q = S, Se).^{14,15,20-22}

Ternary interlanthanide chalcogenides usually include one large ion (Ln) and one small ion (Ln') from opposite ends of the lanthanide series with different coordination environments to avoid possible disordering. Ln/Yb/Q (Q = S, Se) phases have been extensively studied owing to the potential mixed-valency of Yb (II, III) ions, which might lead to interesting structures and electronic properties. The group of Ln/Yb/Q (Q = S, Se) is represented by $\alpha\text{-LaYbS}_3$ ¹² (GdFeO₃ type [19]),²³ $\beta\text{-LnYbQ}_3$ (Q = S, Se)¹²⁻¹⁴ (UFeS₃ type),²⁴ $\gamma\text{-LnYbS}_3$ (Ln = La, Ce),¹⁵ and LnYb_3S_6 ^{16,17} (F-Ln₂S₃ type).^{25,26} There are some Er or Tm containing ternary compounds prepared and characterized, including CeTmS_3 ,¹⁸ $\text{La}_{10}\text{Er}_9\text{S}_{27}$,¹⁹ $\gamma\text{-LnLn}'\text{S}_3$ (Ln = La, Ce; Ln' = Er, Tm),¹⁵ SmEr_3Q_6 (Q = S, Se)²⁰ (F-Ln₂S₃ type),^{25,26} and $\text{Sm}_{0.88}\text{Er}_{1.12}\text{Se}_3$ (U₂S₃ type).²⁷ Both Er³⁺ and Tm³⁺ ions are paramagnetic. Their substitutions in smaller Ln' sites may result in different magnetic performance from

the parent compounds. In contrast, Ln/Lu/Q phases are much simpler systems in term of magnetism and less investigated, because the Lu³⁺ ion is 4f¹⁴. The full 4f shell of the Lu³⁺ ion can be advantageous when the magnetic behavior of other Ln ions needs to be probed without the interference from the Ln' ions.

Recently, we reported the synthesis and characterization of interlanthanide sulfides δ -Ln_{2-x}Lu_xS₃ (Ln = Ce, Pr, Nd).²¹ These compounds crystallized in the disordered CeTmS₃ structure-type with tunable band gaps. The magnetic susceptibility of δ -Ce_{1.30}Lu_{0.70}S₃ deviates from the Curie-Weiss law at low temperature, due to the crystal-field effects. δ -Pr_{1.29}Lu_{0.71}S₃ shows some short-range antiferromagnetic ordering. While δ -Nd_{1.33}Lu_{0.67}S₃ acts like an intermediate state of δ -Ce_{1.30}Lu_{0.70}S₃ and δ -Pr_{1.29}Lu_{0.71}S₃. In the present study, we disclose the synthesis, structure, optical, and magnetic properties of Ln₃LuSe₆ (Ln = La, Ce), β -LnLuSe₃ (Ln = Pr, Nd), and Ln_xLu_{4-x}Se₆ (Ln = Sm, Gd; x = 1.82, 1.87). The information in this chapter has been submitted as a full paper in *Inorganic Chemistry*.²⁸

EXPERIMENTAL

Starting Materials. La (99.9%, Alfa-Aesar), Ce (99.9%, Alfa-Aesar), Pr (99.9%, Alfa-Aesar), Nd (99.9%, Alfa-Aesar), Sm (99.9%, Alfa-Aesar), Gd (99.9%, Alfa-Aesar), Lu (99.9%, Alfa-Aesar), Se (99.5%, Alfa-Aesar), and Sb (99.5%, Alfa-Aesar) were used as received. The Sb₂Se₃ flux was prepared from the direct reaction of the elements in sealed fused-silica ampoules at 850 °C.

Syntheses. Ln₃LuSe₆ (Ln = La, Ce) were synthesized from a reaction of 150 mg of stoichiometric Ln, Lu, and Se, and 100 mg of Sb₂Se₃. For β -LnLuSe₃ (Ln = Pr, Nd)

and $\text{Ln}_x\text{Lu}_{4-x}\text{Se}_6$ ($\text{Ln} = \text{Sm}, \text{Gd}; x = 1.82, 1.87$), the reaction mixtures include 150 mg of Ln, Lu, and Se in a molar ratio of 1:1:3, and 100 mg of Sb_2Se_3 . All these starting materials were loaded into fused-silica ampoules under argon atmosphere in a glovebox. The ampoules were flame sealed under vacuum and heated in programmable tube furnaces. The following heating profile was used for all reactions: 2 °C/min to 500 °C (held for 1 h), 0.5 °C/min to 1000 °C (held for 14 d), 0.04 °C/min to 550 °C (held for 2 d), and 0.5 °C/min to 24 °C. Major title products were found as large black chunks that were well separated from the Sb_2Se_3 flux. They were isolated and ground for powder X-ray diffraction measurements, which were used to confirm phase purity by comparing the powder patterns calculated from the single crystal X-ray structures with the experimental data. Semi-quantitative SEM/EDX analyses were performed on several single crystals for each compound using JEOL 840/Link Isis or JEOL JSM-7000F instruments. Ln, Lu, and Se percentages were calibrated against standards. Sb was not detected in the crystals. The Ln:Lu:Se ratios for Ln_3LuSe_6 ($\text{Ln} = \text{La}, \text{Ce}$) were determined to be approximately 3:1:6 from EDX analyses. While the ratios of Ln:Lu:Se were close to 1:1:3 for $\beta\text{-LnLuSe}_3$ ($\text{Ln} = \text{Pr}, \text{Nd}$) and $\text{Ln}_x\text{Lu}_{4-x}\text{Se}_6$ ($\text{Ln} = \text{Sm}, \text{Gd}; x = 1.82, 1.87$).

Crystallographic Studies. Single crystals of $\text{Ln}_x\text{Lu}_y\text{Se}_z$ ($\text{Ln} = \text{La}, \text{Ce}, \text{Pr}, \text{Nd}, \text{Sm}, \text{Gd}$) were mounted on glass fibers with epoxy and optically aligned on a Bruker APEX single crystal X-ray diffractometer using a digital camera. Initial intensity measurements were performed using graphite monochromated Mo $K\alpha$ ($\lambda = 0.71073 \text{ \AA}$) radiation from a sealed tube and monocapillary collimator. SMART (v 5.624) was used for preliminary determination of the cell constants and data collection control. The intensities of reflections of a sphere were collected by a combination of 3 sets of

exposures (frames). Each set had a different ϕ angle for the crystal and each exposure covered a range of 0.3° in ω . A total of 1800 frames were collected with exposure times per frame of 10 or 20 seconds depending on the crystal.

For $\text{Ln}_x\text{Lu}_y\text{Se}_z$ ($\text{Ln} = \text{La}, \text{Ce}, \text{Pr}, \text{Nd}, \text{Sm}, \text{Gd}$), determination of integrated intensities and global refinement were performed with the Bruker SAINT (v 6.02) software package using a narrow-frame integration algorithm. These data were treated first with a face-index numerical absorption correction using XPREP,²⁹ followed by a semi-empirical absorption correction using SADABS.³⁰ The program suite SHELXTL (v 6.12) was used for space group determination (XPREP), direct methods structure solution (XS), and least-squares refinement (XL).²⁹ The final refinements included anisotropic displacement parameters for all atoms and secondary extinction. Some crystallographic details are given in Table 6.1. Atomic coordinates and equivalent isotropic displacement parameters for La_3LuSe_6 , $\beta\text{-PrLuSe}_3$, and $\text{Sm}_{1.82}\text{Lu}_{2.18}\text{Se}_6$ are given in Tables 6.2-6.4.

The structures of Ln_3LuSe_6 ($\text{Ln} = \text{La}, \text{Ce}$) and $\beta\text{-LnLuSe}_3$ ($\text{Ln} = \text{Pr}, \text{Nd}$) are ordered. For these compounds, the assignments of cation positions were straightforward. $\text{Ln}_x\text{Lu}_{4-x}\text{Se}_6$ ($\text{Ln} = \text{Sm}, \text{Gd}$; $x = 1.82, 1.87$) compounds crystallize in the $\text{F-Ln}_2\text{S}_3$ ^{25,26} type structure, which is highly disordered. All four cation sites, including one eight-coordinate position (Ln (1)), one seven-coordinate position (Ln (2)), and two octahedral positions (Ln (3) and Ln (4)), were assumed to be occupied by both metals at the beginning of the refinements. The final refinements shown that the occupancies of Lu atoms in Ln (1), Ln (2), Ln (3), and Ln (4) positions are 0.02, 0.32, 0.88, and 0.95 respectively for the Sm-based compound and 0.04, 0.40, 0.84 and 0.86 for the Gd case.

Table 6.1. Crystallographic Data for $\text{Ln}_x\text{Lu}_y\text{Se}_z$ (Ln = La, Ce, Pr, Nd, Sm, Gd).

| Formula | La_3LuSe_6 | Ce_3LuSe_6 | $\beta\text{-PrLuSe}_3$ | $\beta\text{-NdLuSe}_3$ | $\text{Sm}_{1.82}\text{Lu}_{2.18}\text{Se}_6$ | $\text{Gd}_{1.87}\text{Lu}_{2.13}\text{Se}_6$ |
|---|----------------------------|----------------------------|-------------------------|-------------------------|---|---|
| fw | 1065.46 | 1069.09 | 552.76 | 556.09 | 1128.83 | 1140.50 |
| Color | black | black | black | black | black | black |
| Crystal System | orthorhombic | orthorhombic | orthorhombic | orthorhombic | monoclinic | monoclinic |
| Space group | <i>Pnmm</i> (No. 58) | <i>Pnmm</i> (No. 58) | <i>Cmcm</i> (No. 63) | <i>Cmcm</i> (No. 63) | <i>P2₁/m</i> (No. 11) | <i>P2₁/m</i> (No. 11) |
| a (Å) | 14.6195(10) | 14.5020(9) | 4.0052(10) | 3.9946(5) | 11.3925(13) | 11.4274(12) |
| b (Å) | 17.5736(12) | 17.4954(11) | 12.996(3) | 13.0015(17) | 4.0483(5) | 4.0542(4) |
| c (Å) | 4.1542(3) | 4.1129(3) | 9.865(3) | 9.8583(13) | 11.6844(14) | 11.7160(12) |
| β | / | / | / | / | 108.915(2) | 109.005(2) |
| V (Å ³) | 1067.29(13) | 1043.52(12) | 513.5(2) | 512.00(11) | 509.79(11) | 513.20(9) |
| Z | 4 | 4 | 4 | 4 | 2 | 2 |
| T (K) | 193 | 193 | 193 | 193 | 193 | 193 |
| λ (Å) | 0.71073 | 0.71073 | 0.71073 | 0.71073 | 0.71073 | 0.71073 |
| ρ_{calcd} (g cm ⁻³) | 6.631 | 6.805 | 7.150 | 7.214 | 7.354 | 7.381 |
| μ (cm ⁻¹) | 413.24 | 430.70 | 495.66 | 503.36 | 525.94 | 534.34 |
| $R(F)^a$ | 0.0273 | 0.0212 | 0.0429 | 0.0226 | 0.0300 | 0.0308 |
| $R_w(F_o^2)^b$ | 0.0645 | 0.0485 | 0.1049 | 0.0601 | 0.0822 | 0.0817 |

$$^a R(F) = \frac{\sum \|F_o\| - |F_c|}{\sum |F_o|} \text{ for } F_o^2 > 2\sigma(F_o^2). \quad ^b R_w(F_o^2) = \left[\frac{\sum [w(F_o^2 - F_c^2)^2]}{\sum wF_o^4} \right]^{1/2}.$$

Table 6.2. Atomic Coordinates and Equivalent Isotropic Displacement Parameters for La_3LuSe_6 .

| Atom (site) | x | y | z | $U_{\text{eq}} (\text{\AA}^2)^a$ |
|-------------|------------|------------|-----|----------------------------------|
| La1 | 0.04906(4) | 0.21859(3) | 0 | 0.00650(14) |
| La2 | 0.74828(4) | 0.59977(3) | 0 | 0.00737(14) |
| La3 | 0.18086(3) | 0.65120(3) | 0 | 0.00551(14) |
| Lu1 | 0.5 | 0.5 | 0 | 0.00765(14) |
| Lu2 | 0.5 | 0 | 0 | 0.00796(15) |
| Se1 | 0.09090(6) | 0.92147(5) | 0 | 0.0070(2) |
| Se2 | 0.37451(6) | 0.60983(5) | 0 | 0.0088(2) |
| Se3 | 0.39505(7) | 0.25435(5) | 0 | 0.0079(2) |
| Se4 | 0.31246(6) | 0.02363(5) | 0 | 0.0075(2) |
| Se5 | 0.02329(6) | 0.39487(5) | 0 | 0.0077(2) |

^a U_{eq} is defined as one-third of the trace of the orthogonalized U_{ij} tensor.

Table 6.3. Atomic Coordinates and Equivalent Isotropic Displacement Parameters for β -PrLuSe₃.

| Atom (site) | <i>x</i> | <i>y</i> | <i>Z</i> | $U_{\text{eq}} (\text{\AA}^2)^a$ |
|-------------|----------|-------------|-------------|----------------------------------|
| Pr1 | 0 | 0.74823(8) | 0.25 | 0.0104(4) |
| Lu1 | 0 | 0 | 0 | 0.0094(4) |
| Se1 | 0 | 0.35622(11) | 0.06234(15) | 0.0098(4) |
| Se2 | 0 | 0.08646(16) | 0.25 | 0.0103(5) |

^a U_{eq} is defined as one-third of the trace of the orthogonalized U_{ij} tensor.

Table 6.4. Atomic Coordinates and Equivalent Isotropic Displacement Parameters for $\text{Sm}_{1.82}\text{Lu}_{2.18}\text{Se}_6$.

| Atom (site) | x | y | Z | $U_{\text{eq}} (\text{\AA}^2)^a$ |
|-------------|-------------|------|-------------|----------------------------------|
| Sm1/Lu1 | 0.54854(5) | 0.25 | 0.19591(5) | 0.00802(16) |
| Sm2/Lu2 | 0.18189(5) | 0.25 | 0.00181(5) | 0.00928(16) |
| Sm3/Lu3 | 0.93774(4) | 0.25 | 0.33530(4) | 0.00899(15) |
| Sm4/Lu4 | 0.65835(4) | 0.25 | 0.58350(4) | 0.00947(15) |
| Se1 | 0.41771(9) | 0.25 | 0.59567(9) | 0.0079(2) |
| Se2 | 0.89302(10) | 0.25 | 0.56010(10) | 0.0095(2) |
| Se3 | 0.23926(9) | 0.25 | 0.77152(9) | 0.0074(2) |
| Se4 | 0.30802(10) | 0.25 | 0.25392(9) | 0.0093(2) |
| Se5 | 0.98403(10) | 0.25 | 0.11953(10) | 0.0104(2) |
| Se6 | 0.61334(9) | 0.25 | 0.96386(9) | 0.0070(2) |

^a U_{eq} is defined as one-third of the trace of the orthogonalized U_{ij} tensor.

These results gave rise to the formula of $\text{Sm}_{1.82}\text{Lu}_{2.18}\text{Se}_6$ and $\text{Gd}_{1.87}\text{Lu}_{2.13}\text{Se}_6$, which are consistent with the 1:1:3 ratios from EDX analysis. It is worth noting that $\text{Gd}_{1.87}\text{Lu}_{2.13}\text{Se}_6$ has a higher degree of disorder than $\text{Sm}_{1.82}\text{Lu}_{2.18}\text{Se}_6$ as the size of the cations get closer, even though they have similar Ln:Lu ratios.

Powder X-ray Diffraction. Powder X-ray diffraction patterns were collected with a Rigaku Miniflex powder X-ray diffractometer using Cu $K\alpha$ ($\lambda = 1.54056 \text{ \AA}$) radiation.

Magnetic Susceptibility Measurements. Magnetism data were measured on powders in gelcap sample holders with a Quantum Design MPMS 7T magnetometer/susceptometer between 2 and 300 K and in applied fields up to 7 T. DC susceptibility measurements were made under zero-field-cooled conditions with an applied field of 0.1 T. Magnetic susceptibility for Ce_3LuSe_6 under zero-field-cooled (ZFC) and field-cooled (FC) conditions were measured with 0.01 T applied field between 2 and 25 K. Susceptibility values were corrected for the sample diamagnetic contribution according to Pascal's constants³¹ as well as for the sample holder diamagnetism. Experimental effective magnetic moments and Weiss constants for Ce_3LuSe_6 , $\beta\text{-PrLuSe}_3$, $\beta\text{-NdLuSe}_3$, and $\text{Gd}_{1.87}\text{Lu}_{2.13}\text{Se}_6$ were obtained from extrapolations from fits between 100 and 300 K. (Magnetic susceptibility measurements were performed by Eun Sang Choi and James S. Brooks at Florida State University)

UV-vis-NIR Diffuse Reflectance Spectroscopy. The diffuse reflectance spectra for $\text{Ln}_x\text{Lu}_y\text{Se}_z$ (Ln = La, Ce, Pr, Nd, Sm, Gd) were measured from 200 to 2500 nm using a Shimadzu UV3100 spectrophotometer equipped with an integrating sphere attachment.

The Kubelka-Munk function was used to convert diffuse reflectance data to absorption spectra.³²

RESULTS AND DISCUSSION

Synthesis of Ln/Ln'/Q using Sb₂Q₃ fluxes (Q = S, Se). The proven method of using Sb₂Q₃ (Q = S, Se) fluxes to prepare ternary interlanthanide chalcogenides has been very effective in this present study. Eight different structure types have been identified for ternary interlanthanide chalcogenides prepared by employing these fluxes at 1000 °C. These compounds are given in Tables 6.5 and 6.6. The structures of Ln/Ln'/Q phases depend highly on the choices of Ln and Ln'. This is especially true for La/Ln'/Se, which can adopt five different structures with the variation of Ln'. It is important to note that the choices of flux and temperature could be critical as well; these will not be discussed here. Ordered phases can usually be found in bottom left corner of Tables 6.5 and 6.6, where Ln and Ln' ions have larger difference in size. When it reaches to the opposite corner, disordered compounds are often present owing to the similar structural chemistry of lanthanides. There are some exceptions, e.g. LaLu₃S₆ and La_xYb_{5-x}Se₇. The limitations of using Sb₂Q₃ (Q = S, Se) fluxes to prepare LnLn'Q include: 1) Attempts to prepare interlanthanide tellurides have not succeeded; 2) It is difficult to achieve high yield and high-quality single crystals when the ionic radii of the two Ln³⁺ ions approach equality; 3) Occasionally, distinguishing and separating products from Sb₂Q₃ (Q = S, Se) fluxes proves tricky.

Structures of Ln_xLu_ySe_z (Ln = La, Ce, Pr, Nd, Sm, Gd). The Ln₃LuSe₆ (Ln = La, Ce) compounds adopt U₃ScS₆³³ type structure. The unit cell of La₃LuSe₆, projected

Table 6.5. Ternary Interlanthanide Sulfides Prepared Using Sb_2S_3 flux at 1000 °C.

| | Eu^{2+} | La^{3+} | Ce^{3+} | Pr^{3+} | Nd^{3+} | Sm^{3+} | Gd^{3+} |
|------------------|------------------|------------------|------------------|------------------|------------------|------------------|------------------|
| Tb^{3+} | ● | | | | | | |
| Dy^{3+} | ● | ◐△ | | | | | |
| Ho^{3+} | ● | ◐△ | ◇ | | | | |
| Er^{3+} | ● | ◐ | ◐ | | | | |
| Tm^{3+} | ● | ◐ | ◐ | △ | | | |
| Yb^{3+} | ● | ◐ | ◐ | △ | △ | △ | △ |
| Lu^{3+} | ● | △ | ◇ | ◇ | ◇ | △ | |

Ordered structure types: ▲ $\beta\text{-LnLn}'\text{S}_3$,¹²⁻¹⁴ ◐ $\gamma\text{-LnLn}'\text{S}_3$,¹⁵ ■ U_3ScS_6 ,³³ ● CaFe_2O_4 .³⁴
 Disordered structure types: △ $\text{F-Ln}_2\text{S}_3$,^{25,26} ◇ $\delta\text{-LnLn}'\text{S}_3$,^{18,21} □ U_2S_3 ,²⁷ ○ Y_5S_7 .³⁵

Table 6.6. Ternary Interlanthanide Selenides Prepared Using Sb_2Se_3 flux at 1000 °C.

| | Eu^{2+} | La^{3+} | Ce^{3+} | Pr^{3+} | Nd^{3+} | Sm^{3+} | Gd^{3+} |
|------------------|------------------|------------------|------------------|------------------|------------------|------------------|------------------|
| Tb^{3+} | ● | □ | | | | | |
| Dy^{3+} | ● | | □ | | | | |
| Ho^{3+} | ● | | | | | | |
| Er^{3+} | ● | ◇ | | | △ | | |
| Tm^{3+} | ● | △ | △ | △ | △ | △ | △ |
| Yb^{3+} | ● | ○ | ▲ | ▲ | ▲ | △ | △ |
| Lu^{3+} | ● | ■ | ■ | ▲ | ▲ | △ | △ |

Ordered structure types: ▲ $\beta\text{-LnLn}'\text{S}_3$,¹²⁻¹⁴ ● $\gamma\text{-LnLn}'\text{S}_3$,¹⁵ ■ U_3ScS_6 ,³³ ● CaFe_2O_4 .³⁴
 Disordered structure types: △ F- Ln_2S_3 ,^{25,26} ◇ $\delta\text{-LnLn}'\text{S}_3$,^{18,21} □ U_2S_3 ,²⁷ ○ Y_5S_7 .³⁵

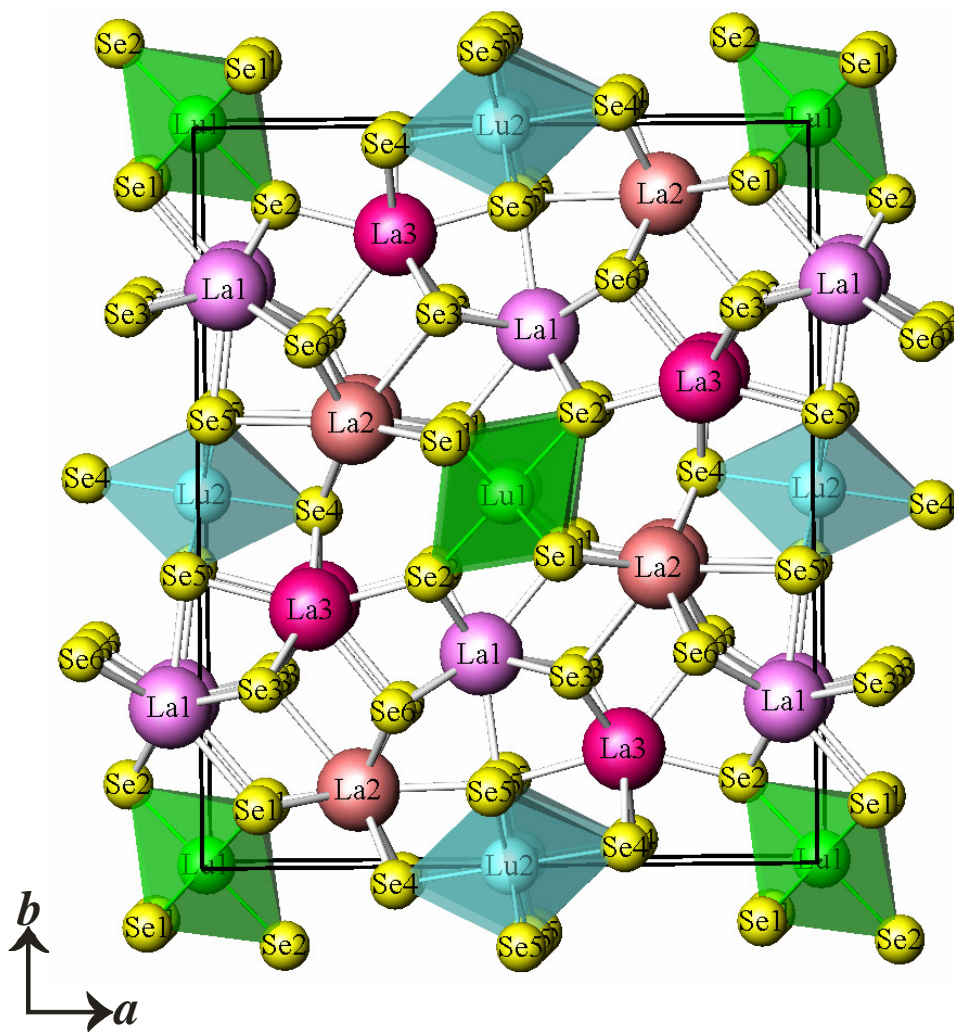


Figure 6.1. An illustration of the three-dimensional structure of La_3LuSe_6 down the c axis.

along the c axis, is shown in Figure 6.1. There are three crystallographically unique Ln sites ($4g$) and two octahedral Lu positions ($2d$, $2b$) in the structure. Both Ln(1) and Ln(2) atoms are surrounded by eight Se atoms and occur as bicapped trigonal prisms. Ln(3) sites are seven-coordinate in a monocapped trigonal prismatic environment. LnSe_8 and LnSe_7 polyhedra share faces or edges with each other to form two-dimensional slabs extending in the $[ac]$ plane. Furthermore these slabs connect at Se(4) positions to produce a three-dimensional structure. The gaps between these slabs are filled by isolated one-dimensional edge-sharing LuSe_6 octahedral chains running down the c axis. The bond distances for these two compounds, which can be found in Supporting Information, are normal compared to average values reported by Shannon.³⁶ In the case of La_3LuSe_6 , the bond distances for the LaSe_8 , LaSe_7 , and LuSe_6 polyhedra range from 2.9982(8) to 3.3408(11) Å, 2.9229(11) to 3.1116(11) Å, and 2.6629(9) to 2.8257(6) Å, respectively (see Table 6.7).

The series of β - LnLuSe_3 (Ln = Pr, Nd) are isotypic with UFeS_3 .²⁴ The structure, as shown in Figure 6.2, is constructed from two-dimensional LuSe_6 octahedra layers, which are separated by Ln^{3+} ions. The local environment of Ln^{3+} ions can be found in Figure 6.5. They coordinate to eight Se atoms with a bicapped trigonal prismatic geometry. The connectivities within LuSe_6 layers are illustrated in Figure 6.3. The LuSe_6 octahedral units are edge sharing along a axis and corner sharing along c axis. The bond lengths within these two compounds are regular. For example, Pr-Se and Lu-Se distances in compound β - PrLuSe_3 are in the range of 2.9035(18) and 3.3670(17) Å, and 2.7102(10) and 2.8072(11) Å, respectively (see Table 6.8).

Table 6.7. Selected Bond Distances (Å) for Ln₃LuSe₆ (Ln = La, Ce).

| Formula | La ₃ LuSe ₆ | Ce ₃ LuSe ₆ |
|----------------|-----------------------------------|-----------------------------------|
| Ln(1)-Se(1) | 3.2007(11) | 3.009(2) |
| Ln(1)-Se(2) ×2 | 3.0357(8) | 3.0044(7) |
| Ln(1)-Se(3) ×2 | 3.1001(8) | 3.0757(7) |
| Ln(1)-Se(5) | 3.1207(11) | 3.0818(9) |
| Ln(1)-Se(6) ×2 | 3.1500(8) | 3.1241(7) |
| Ln(2)-Se(1) ×2 | 3.1221(8) | 3.0924(6) |
| Ln(2)-Se(3) | 3.3110(11) | 3.2896(9) |
| Ln(2)-Se(4) ×2 | 3.1460(8) | 3.1239(7) |
| Ln(2)-Se(5) | 3.3408(11) | 3.3114(9) |
| Ln(2)-Se(6) ×2 | 2.9982(8) | 2.9678(6) |
| Ln(3)-Se(2) | 2.9229(11) | 2.8915(9) |
| Ln(3)-Se(3) ×2 | 2.9718(7) | 2.9415(6) |
| Ln(3)-Se(4) ×2 | 3.0578(8) | 3.0352(7) |
| Ln(3)-Se(5) | 3.0925(11) | 3.0650(9) |
| Ln(3)-Se(6) | 3.1116(11) | 3.0872(9) |
| Lu(1)-Se(1) ×4 | 2.8257(6) | 2.8169(5) |
| Lu(1)-Se(2) ×2 | 2.6629(9) | 2.6620(8) |
| Lu(2)-Se(4) ×2 | 2.7731(9) | 2.7684(8) |
| Lu(2)-Se(5) ×4 | 2.8007(6) | 2.7883(5) |

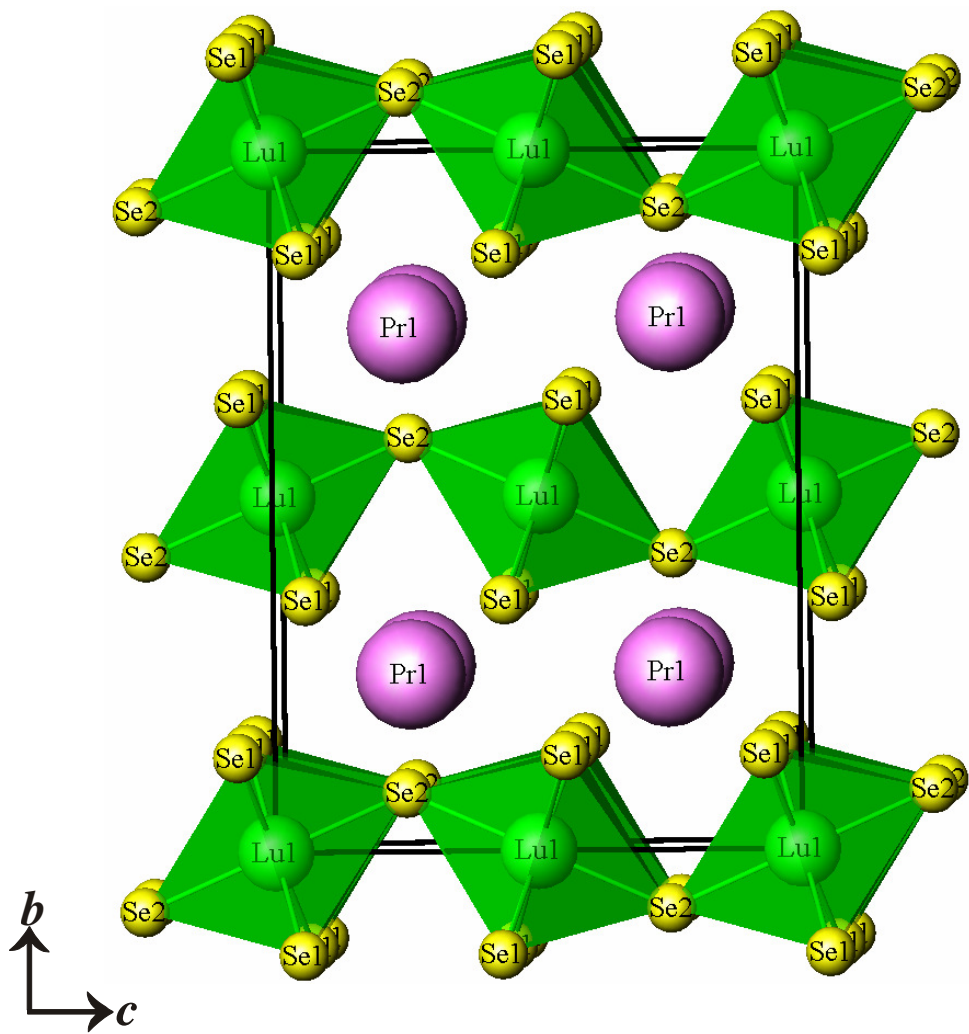


Figure 6.2. Unit cell of β -PrLuSe₃ viewed along the *a* axis. Pr-Se bonds have been omitted for clarity.

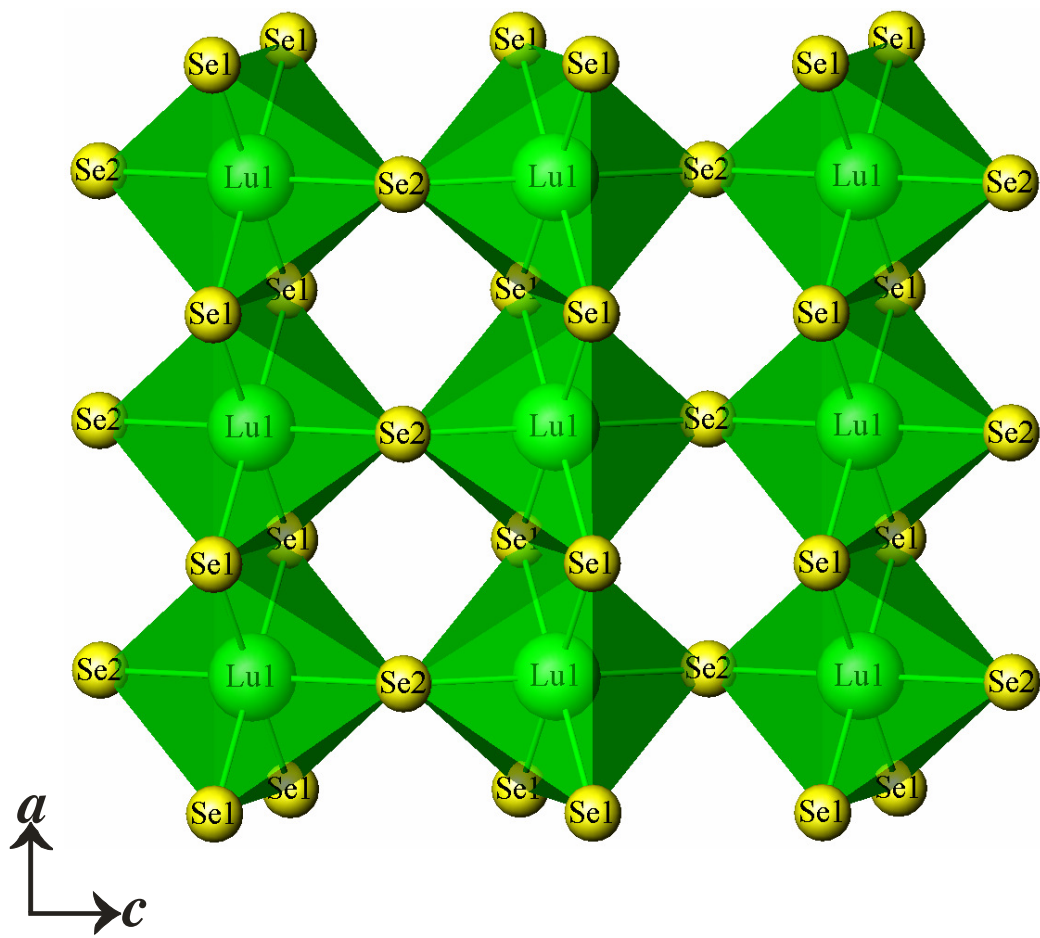


Figure 6.3. A depiction of an individual LuSe_6 octahedra layer viewed down the *b* axis in $\beta\text{-PrLuSe}_3$.

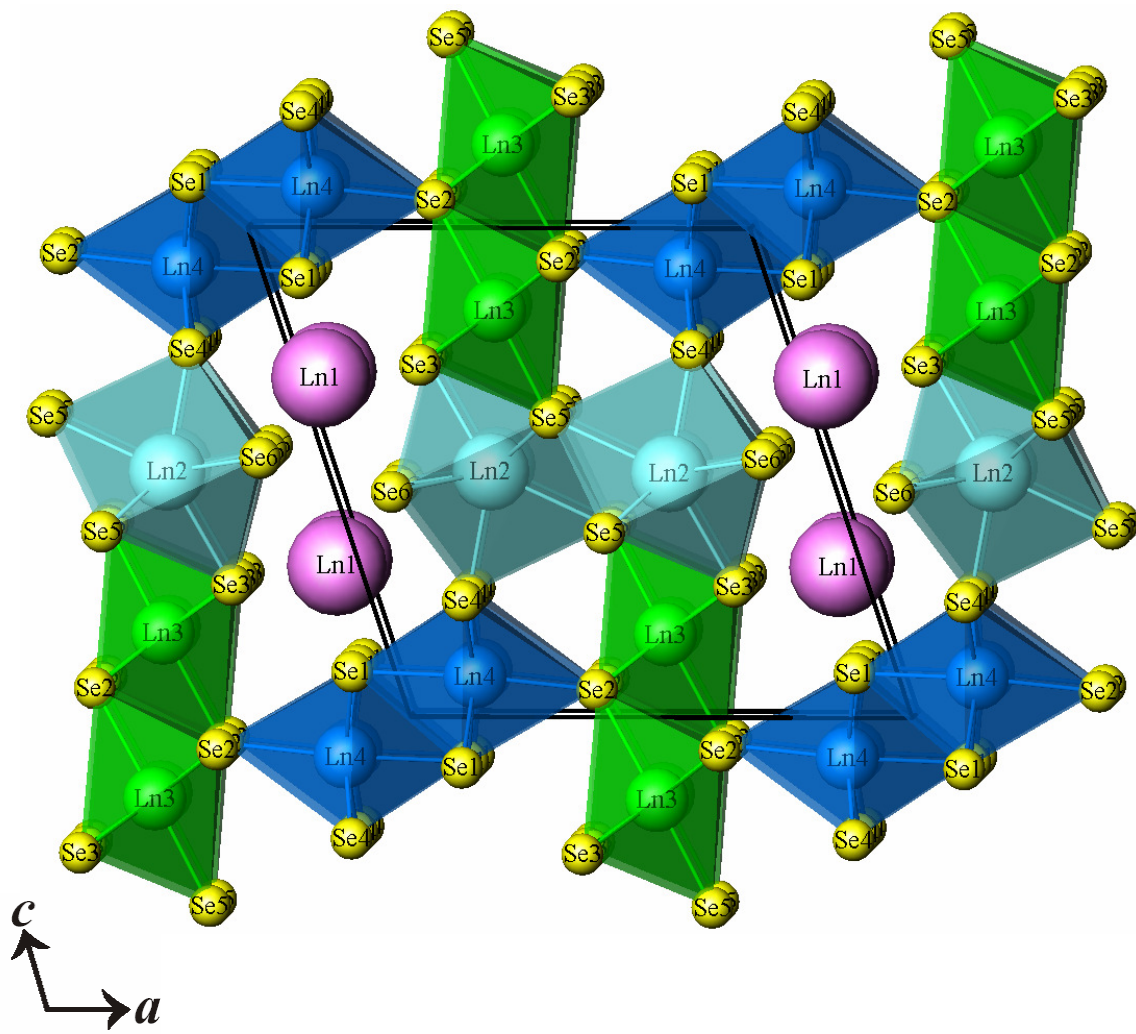


Figure 6.4. A view of the three-dimensional channel structure of $\text{Sm}_{1.82}\text{Lu}_{2.18}\text{Se}_6$ along the b axis.

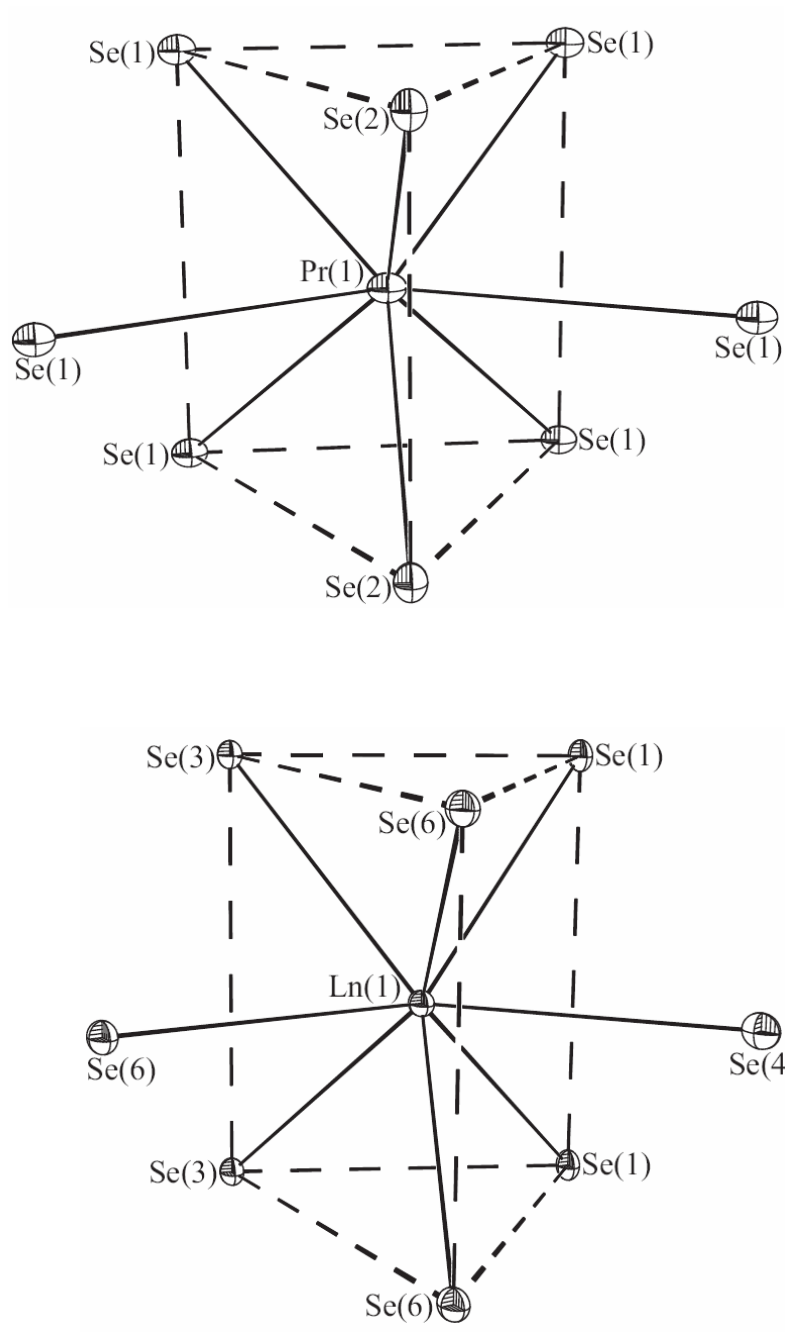


Figure 6.5. Illustrations of the coordination environments for Pr ions in β -PrLuSe₃ and Sm(1)/Lu(1) ions in Sm_{1.82}Lu_{2.18}Se.

Table 6.8. Selected Bond Distances (Å) for β -LnLuSe₃ (Ln = Pr, Nd).

| Formula | β -PrLuSe ₃ | β -NdLuSe ₃ |
|------------------------|------------------------------|------------------------------|
| Ln(1)-S(1) \times 4 | 3.0671(13) | 3.0577(6) |
| Ln(1)-S(1) \times 2 | 3.3670(17) | 3.3677(9) |
| Ln(1)-S(2) \times 2 | 2.9035(18) | 2.8935(9) |
| Lu(1)-Se(1) \times 4 | 2.8072(11) | 2.8078(6) |
| Lu(1)-Se(2) \times 2 | 2.7102(10) | 2.7138(5) |

$\text{Sm}_{1.82}\text{Lu}_{2.18}\text{Se}_6$ and $\text{Gd}_{1.87}\text{Lu}_{2.13}\text{Se}_6$ crystallize in $\text{F-Ln}_2\text{S}_3$ ^{25,26} type structure, which will be detailed in Chapter 7.²² As shown in Figure 6.4, the eight-coordinate bicapped trigonal prismatic Ln(1) ions (Figure 6.5) sit in the one-dimensional channels formed by three different double chains via edge- and corner- sharing. These double chains, all running down the *b* axis, are constructed from Ln(2)Se₇ monocapped trigonal prisms, Ln(3)Se₆ octahedra, and Ln(4)S₆ octahedra, respectively. Within each double chain, the building polyhedra share edges with each other both in the direction of chain propagation and with adjacent chains. For $\text{Sm}_{1.82}\text{Lu}_{2.18}\text{Se}_6$, as shown in Table 6.9, the average distances for Ln(1)S₈, Ln(2)Se₇, Ln(3)Se₆, and Ln(4)Se₆ polyhedra are 3.0406(10) Å, 2.9230(10) Å, 2.8064(10) Å, and 2.7791(9) Å, respectively, which are comparable to Shannon's data,³⁵ 3.05 Å for SmSe₈, 3.00 Å for SmSe₇, 2.90 Å for LuSe₇, and 2.84 Å for LuSe₆.

Magnetic Susceptibility. Figure 6.6 shows the temperature dependence of the inverse molar magnetic susceptibilities for $\beta\text{-LnLuSe}_3$ (Ln = Pr, Nd). Both compounds are paramagnetic and deviate from the Curie-Weiss law below 40 K. The effective magnetic moment and Weiss constant were obtained by fitting the high-temperature susceptibility data to the Curie-Weiss law. As shown in Table 6.10, the effective magnetic moments are close to calculated values for free Ln³⁺ ions. The negative θ_p values indicate antiferromagnetic coupling between magnetic ions.

The magnetic susceptibility of $\text{Sm}_{1.82}\text{Lu}_{2.18}\text{Se}_6$ shows a typical van Vleck paramagnetic behavior similar to Sm metal, which is displayed in Figure 6.7. There is no magnetic transition down to 2 K and susceptibility data do not follow the Curie-Weiss law. The difference between the ground state (⁶H_{5/2}) and the first excited state (⁶H_{7/2}) of

Table 6.9. Selected Bond Distances (Å) for Ln_xLu_{4-x}Se₆ (Ln = Sm, Gd; x = 1.82, 1.87).

| Formula | Sm _{1.82} Lu _{2.18} Se ₆ | Gd _{1.87} Lu _{2.13} Se ₆ |
|----------------|---|---|
| Ln(1)-S(1) ×2 | 3.0932(9) | 3.0955(9) |
| Ln(1)-S(3) ×2 | 3.0806(9) | 3.0803(9) |
| Ln(1)-S(4) | 3.0284(12) | 3.0191(12) |
| Ln(1)-S(6) ×2 | 2.9582(8) | 2.9472(8) |
| Ln(1)-S(6) | 3.0323(11) | 3.0326(11) |
| Ln(2)-S(3) | 2.9678(11) | 2.9666(11) |
| Ln(2)-S(4) | 2.8281(12) | 2.8227(11) |
| Ln(2)-S(5) ×2 | 2.8182(9) | 2.8152(9) |
| Ln(2)-S(5) | 2.9972(12) | 3.0112(12) |
| Ln(2)-S(6) ×2 | 3.0156(8) | 3.0269(9) |
| Ln(3)- S(2) ×2 | 2.7895(8) | 2.8027(8) |
| Ln(3)-S(2) | 2.8331(12) | 2.8460(12) |
| Ln(3)-S(3) ×2 | 2.8441(8) | 2.8582(8) |
| Ln(3)-S(5) | 2.7379(12) | 2.7544(11) |
| Ln(4)-S(1) ×2 | 2.8380(8) | 2.8505(8) |
| Ln(4)-S(1) | 2.7909(11) | 2.8071(11) |
| Ln(4)-S(2) | 2.7741(11) | 2.7827(11) |
| Ln(4)-S(4) ×2 | 2.7169(8) | 2.7308(8) |

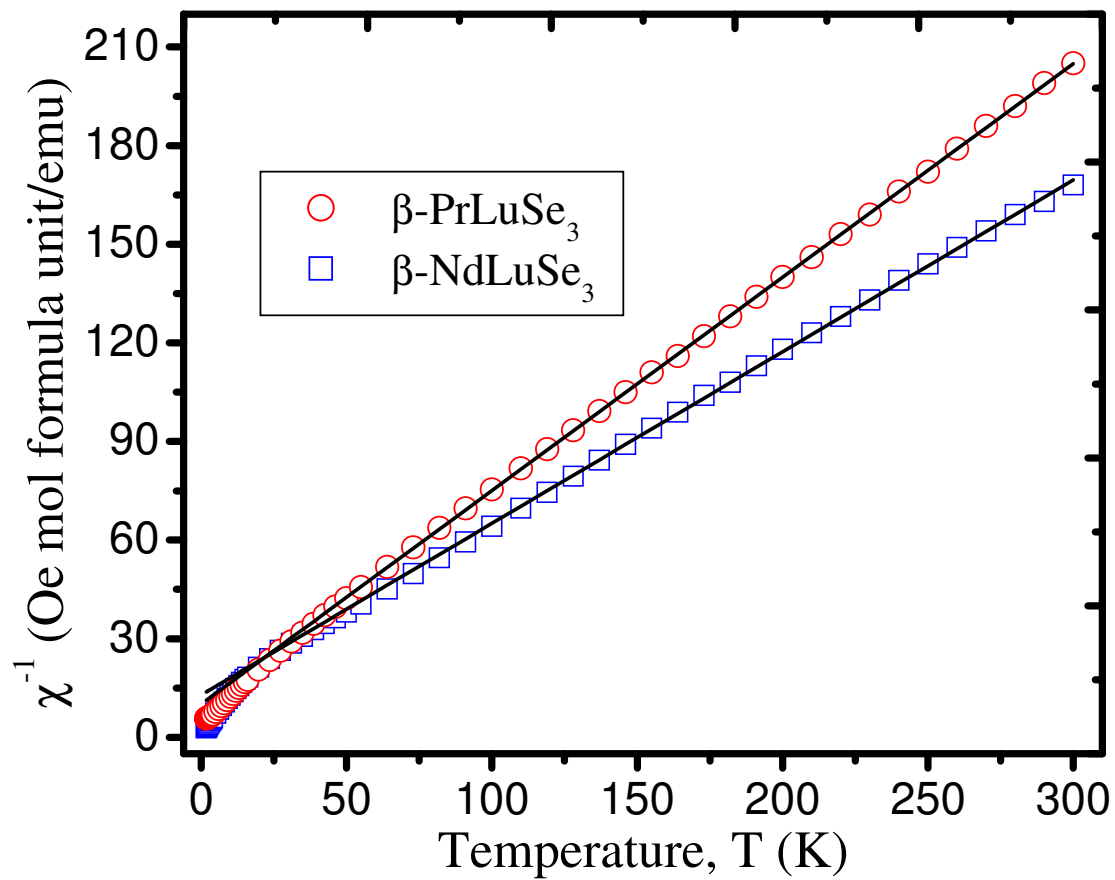


Figure 6.6. The temperature dependence of the reciprocal molar magnetic susceptibility for β -PrLuSe₃ and β -NdLuSe₃, under an applied magnetic field of 0.1 T between 2 and 300 K. The straight line represents the fit to Curie-Weiss law in the range of 100-300 K.

Table 6.10. Magnetic Parameters for Ce_3LuSe_6 , $\beta\text{-PrLuSe}_3$, $\beta\text{-NdLuSe}_3$, and $\text{Gd}_{1.87}\text{Lu}_{2.13}\text{Se}_6$.

| Formula | $P_{\text{cal}}/\mu_{\text{B}}$ | $P_{\text{eff}}/\mu_{\text{B}}$ | $\theta_{\text{p}}/\text{K}$ | R^2 |
|---|---------------------------------|---------------------------------|------------------------------|---------|
| Ce_3LuSe_6 | 4.40 | 4.56(1) | -20(1) | 0.99959 |
| $\beta\text{-PrLuSe}_3$ | 3.58 | 3.509(3) | -15.6(4) | 0.99993 |
| $\beta\text{-NdLuSe}_3$ | 3.62 | 3.913(9) | -25(1) | 0.99961 |
| $\text{Gd}_{1.87}\text{Lu}_{2.13}\text{Se}_6$ | 10.86 | 11.77(1) | -4.4(4) | 0.99991 |

^a P_{cal} and P_{eff} : calculated³⁷ and experimental effective magnetic moments per formula unit. ^b Weiss constant (θ_{p}) and goodness of fit (R^2) obtained from high temperature (100-300 K) data.

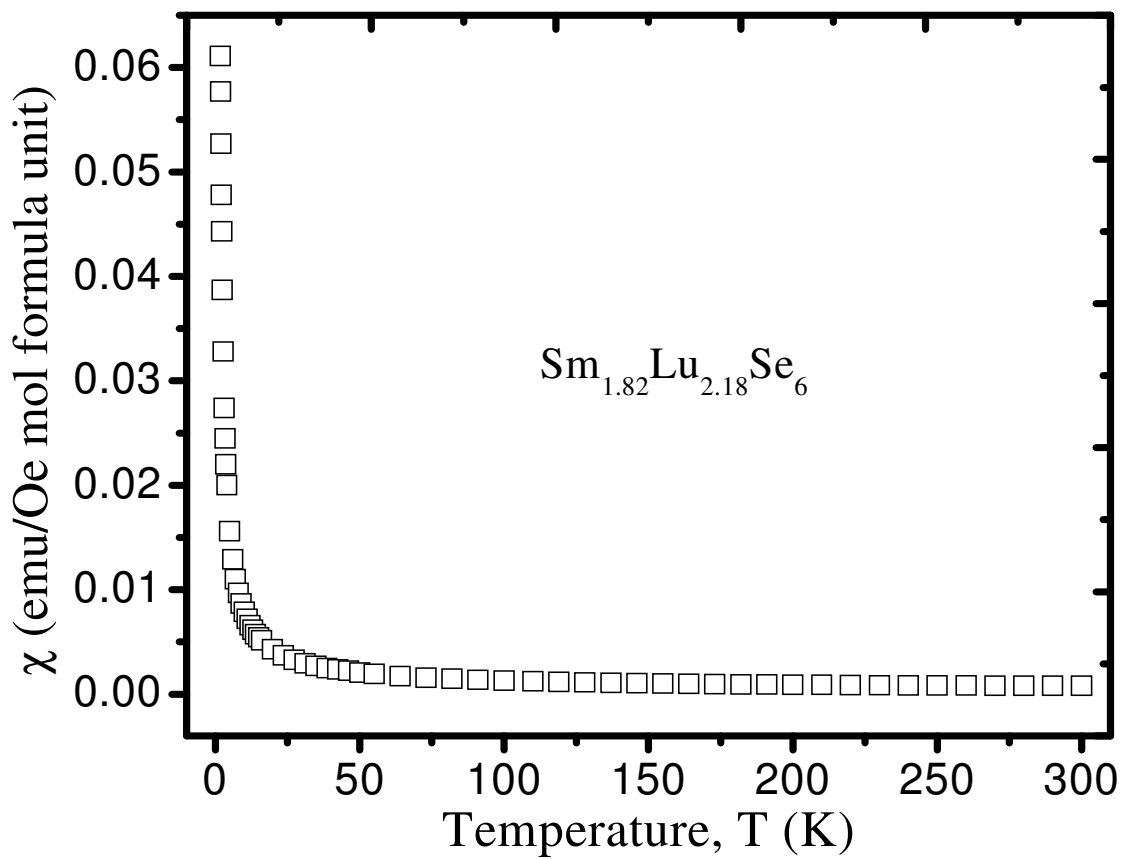


Figure 6.7. Molar magnetic susceptibility vs temperature between 2 and 300 K for $\text{Sm}_{1.82}\text{Lu}_{2.18}\text{Se}_6$. Data were taken under an applied magnetic field of 0.1 T.

Sm^{3+} is not large compared to thermal energy ($k_{\text{B}}T$). Therefore, the excited states make significant contributions to the magnetic susceptibility at high temperature.³⁸ The experimental effective magnetic moment of Sm^{3+} can be determined approximately using $\mu_{\text{eff}} = [3k_{\text{B}}\chi_{\text{m}}T/(L\mu_0\mu_{\text{B}}^2)]^{1/2}$, where k_{B} is Boltzmann constant, L is Avogadro's number, μ_0 is vacuum permeability, T is temperature in Kelvin, χ_{m} is molar susceptibility. At $T = 300$ K, $\mu_{\text{eff}} = 1.02 \mu_{\text{B}}$, which is smaller than the calculated value ($1.55 \mu_{\text{B}}$) for free Sm^{3+} ions using the van Vleck formula.³⁷ It is probably caused by crystal-field effects.

The magnetic susceptibility of $\text{Gd}_{1.87}\text{Lu}_{2.13}\text{Se}_6$ obeys the Curie-Weiss law above the temperature around 4 K where it undergoes a sharp antiferromagnetic transition, as shown in Figure 6.8. The effective magnetic moment and Weiss constant were obtained to be $11.77(1) \mu_{\text{B}}$ per formula unit and $-4.4(4)$ K. The magnetization measurement was performed at 2 K and the results are presented in Figure 6.9. The saturation moment per Gd^{3+} ion is $7.5 \mu_{\text{B}}$, which is close to the value for free Gd^{3+} ion ($7.94 \mu_{\text{B}}$) assuming $g = 2$. There is a weak spin reorientation transition at approximately $H = 0.5$ T.

Ce_3LuSe_6 shows a deviation from the Curie-Weiss law near 70 K owing to crystal-field effects. A magnetic transition was observed below 5 K, which is illustrated in Figure 6.10. A small divergence on the ZFC-FC measurements (Figure 6.11) below this temperature may indicate a ferromagnetic component of the transition or a small temperature difference. In order to investigate the magnetic transition in detail, the magnetization measurements at 2 K were conducted as well. Figure 6.12 shows the field-dependent magnetizations for Ce_3LuSe_6 . $M(H)$ increases abruptly at low field, which is consistent with ferromagnetic behavior. The saturation moment per Ce^{3+} ion ($1.13 \mu_{\text{B}}$) is

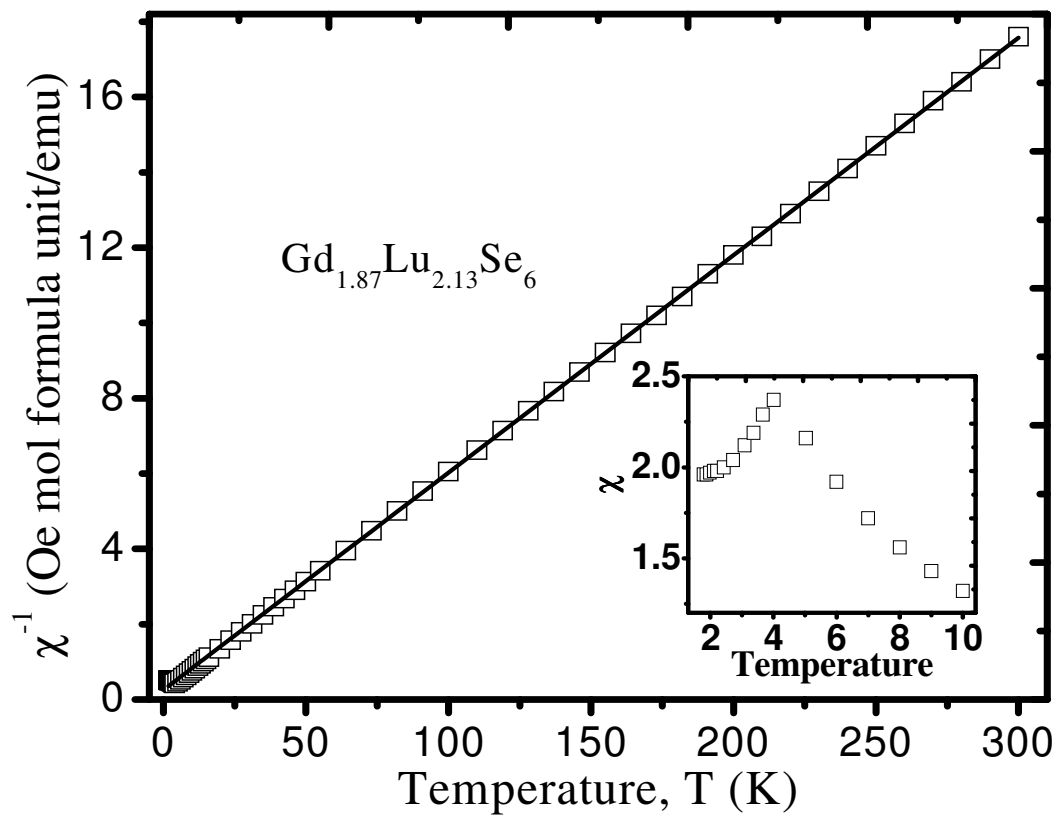


Figure 6.8. Inverse molar magnetic susceptibility vs temperature for $Gd_{1.87}Lu_{2.13}Se_6$ under an applied magnetic field of 0.1 T between 2 and 300 K. The solid line represents the fit to Curie-Weiss law in the range of 100-300 K. Inset shows the molar magnetic susceptibility at low temperature.

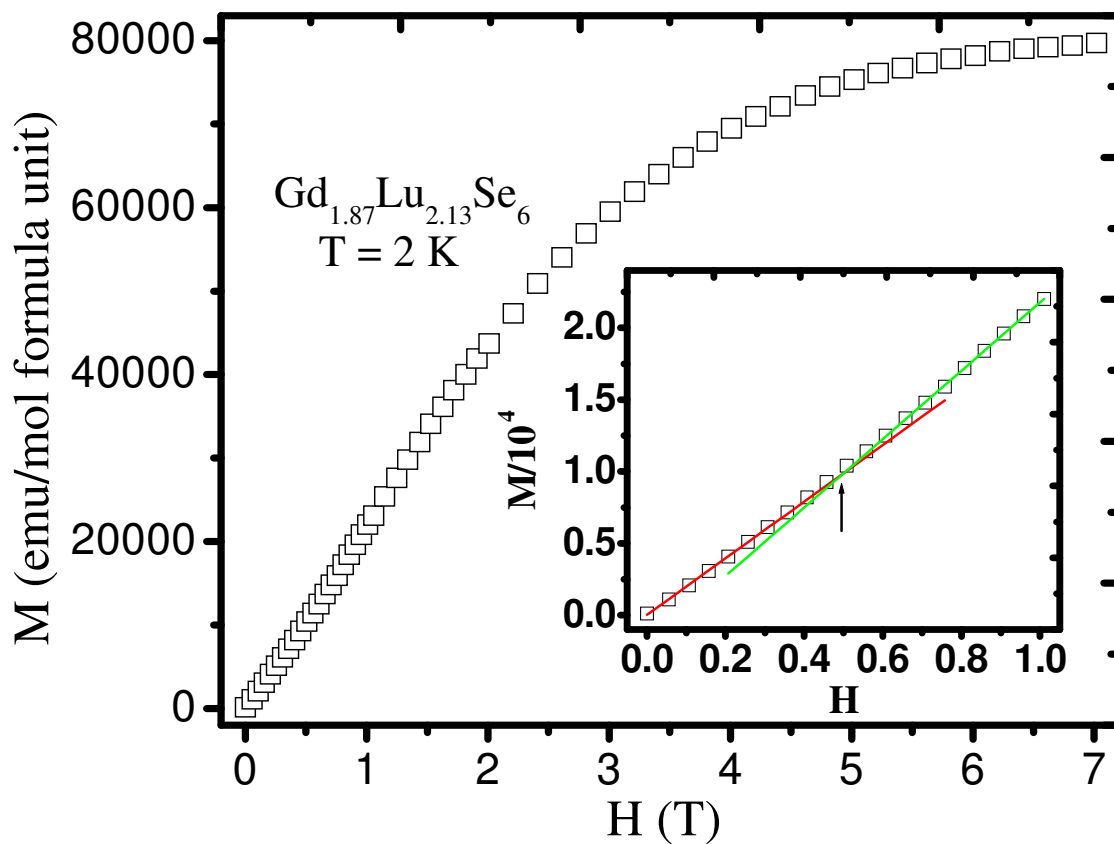


Figure 6.9. The magnetization for $\text{Gd}_{1.87}\text{Lu}_{2.13}\text{Se}_6$ as a function of applied field at 2 K. Inset shows the $M(H)$ curve between 0 and 1 T. Red and green lines are linear fits extended from zero field and from 1T, respectively. Slight increasing of the slope and the weak spin reorientation transition field at the junction (up arrow) can be observed.

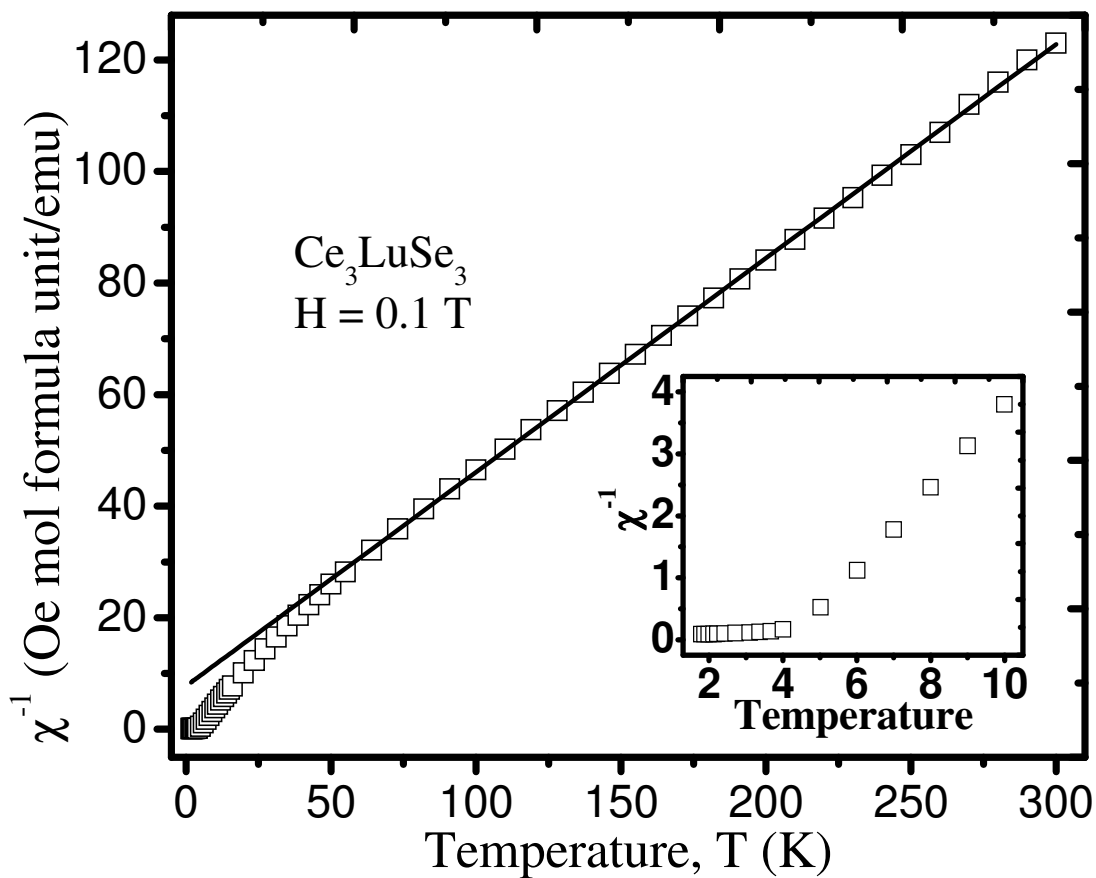


Figure 6.10. Inverse molar magnetic susceptibility as a function of temperature for Ce_3LuSe_6 under an applied magnetic field of 0.1 T between 2 and 300 K. The straight line represents the fit to Curie-Weiss law in the range of 100-300 K. Inset shows the inverse molar magnetic susceptibility at low temperature.

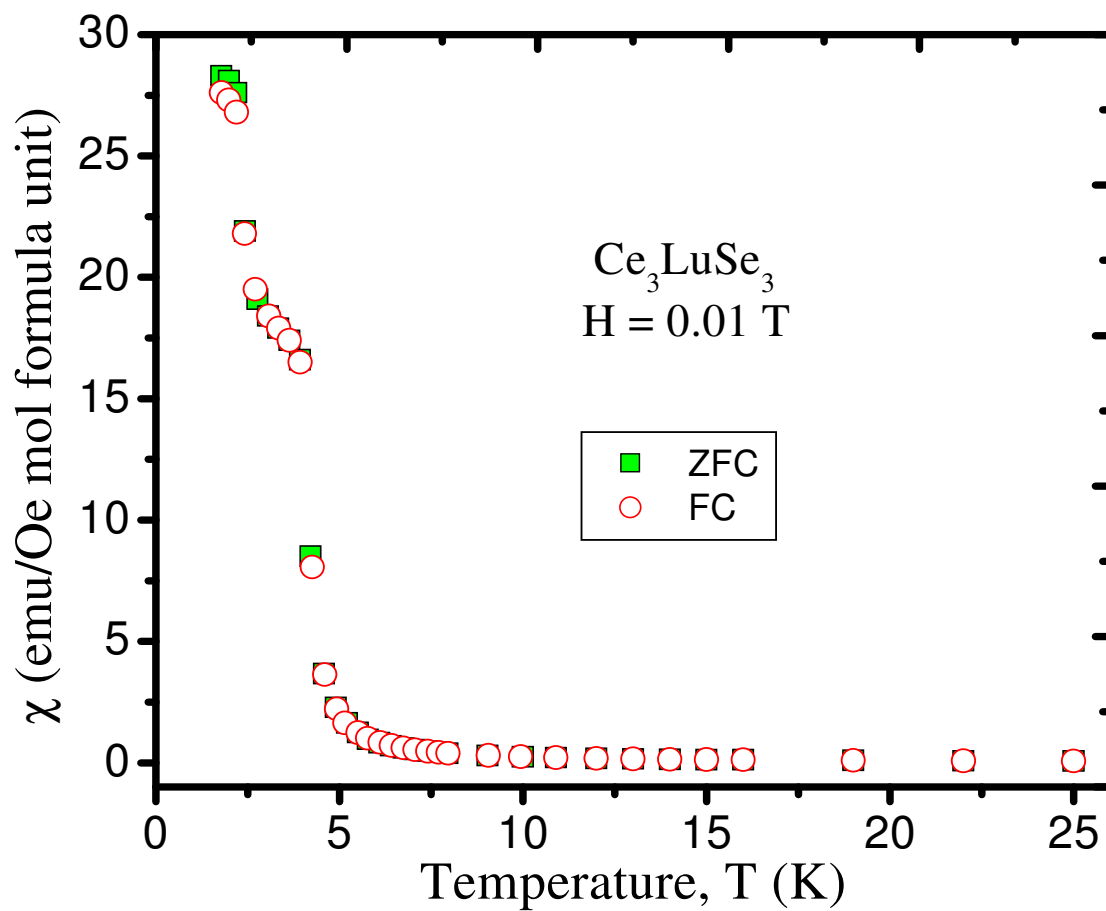


Figure 6.11. Molar magnetic susceptibility as a function of temperature for Ce_3LuSe_6 under ZFC and FC conditions with an applied magnetic field of 0.01 T between 2 and 25 K.

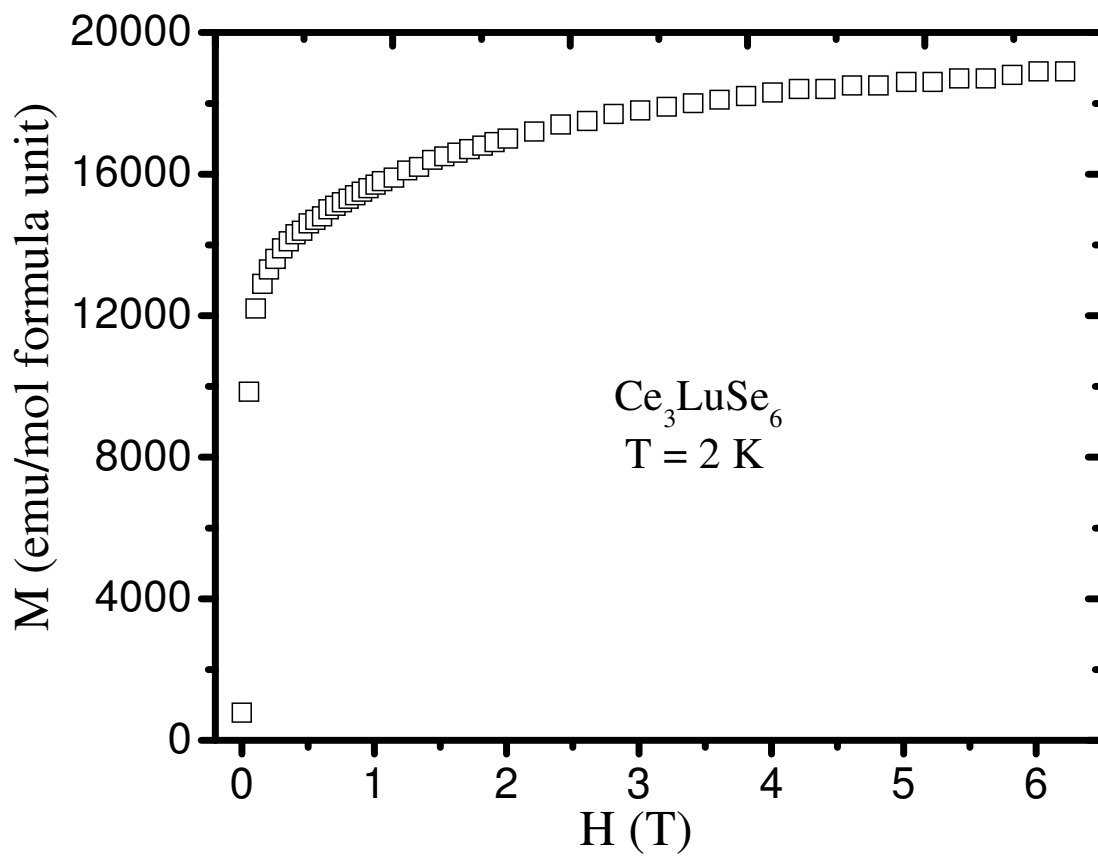


Figure 6.12. The magnetization for Ce_3LuSe_6 as a function of applied field at 2 K.

substantially smaller than the moment for free Ce^{3+} ion ($2.54 \mu_{\text{B}}$) assuming $g = 6/7$. It may be because of crystal-field splitting the ground state of Ce^{3+} ion ($^2\text{F}_{5/2}$). No magnetic hysteresis was found at 2 K, which is consistent with the behavior for a soft ferromagnet. In contrast, the Weiss constant for Ce_3LuSe_6 was determined to be $-20(1)$ K, indicating antiferromagnetic interactions between Ce^{3+} ions. It is worth noting that $|\theta_{\text{p}}|$ value may be enlarged due to the crystal-field splitting of the full $J=5/2$ multiplet for Ce^{3+} . To conclude, Ce_3LuSe_6 orders ferromagnetically with a weak antiferromagnetic component that might be due to canted spins of Ce^{3+} .

Optical Properties. There are few interlanthanide selenides reported in the literature. SmEr_3Se_6 , a red compound, was determined to be a wide direct semiconductor with a band gap of 2.0 eV.²⁰ The series of compounds, $\beta\text{-LnYbSe}_3$ ($\text{Ln} = \text{La}, \text{Ce}, \text{Pr}, \text{Nd}, \text{Sm}$), are black in color, as are the title compounds.¹⁴ The UV-vis-NIR diffuse reflectance spectra (Fig. 13) of $\text{Ln}_x\text{Lu}_y\text{Se}_z$ ($\text{Ln} = \text{La}, \text{Ce}, \text{Pr}, \text{Nd}, \text{Sm}, \text{Gd}$) reveal band gaps for La_3LuSe_6 , Ce_3LuSe_6 , $\beta\text{-PrLuSe}_3$, $\beta\text{-NdLuSe}_3$, $\text{Sm}_{1.82}\text{Lu}_{2.18}\text{Se}_6$, and $\text{Gd}_{1.87}\text{Lu}_{2.13}\text{Se}_6$ of 1.26, 1.10, 1.56, 1.61, 1.51, and 1.56 eV, respectively. The more condensed structure that Ln_3LuSe_6 ($\text{Ln} = \text{La}, \text{Ce}$) adopts may be the reason for their considerably smaller gaps compared to the Pr, Nd, Sm, and Gd containing phases. The smaller value for Ce_3LuSe_6 is due to the relatively low energy of the $4f^1 \rightarrow 4f^05d^1$ transition for cerium. The fine-structure observed in the spectra for $\beta\text{-PrLuSe}_3$, $\beta\text{-NdLuSe}_3$, and $\text{Sm}_{1.82}\text{Lu}_{2.18}\text{Se}_6$ is actually due to f-f transitions within the lanthanide ions.

CONCLUSIONS

Molten Sb_2Q_3 (Q = S, Se) fluxes have been valuable media to access ternary interlanthanide chalcogenides. The composition and structure of the products depends highly on the choices of lanthanides and chalcogenides. In this present study, we detailed the synthesis of lutetium-based interlanthanide selenides $\text{Ln}_x\text{Lu}_y\text{Se}_z$ (Ln = La, Ce, Pr, Nd, Sm, Gd) using a Sb_2Se_3 flux. All of these compounds show diverse structures and physical properties as a function of the Ln ions. They adopt three different structures types including U_3ScS_6 for Ln = La and Ce, UFoS_3 for Ln = Pr and Nd, and $\text{F-Ln}_2\text{S}_3$ for Ln = Sm and Gd. Ln_3LuSe_6 (Ln = La, Ce) have a very condensed three-dimensional structure that is constructed from two-dimensional ${}^2_{\infty}[\text{Ln}_3\text{Se}_6]^{3-}$ slabs with the gaps between these slabs filled by octahedral Lu^{3+} ions. The structure of $\beta\text{-LnLuSe}_3$ (Ln = Pr, Nd) includes two-dimensional LuSe_6 octahedra layers that are separated by eight-coordinate larger Ln^{3+} ions, whereas $\text{Sm}_{1.82}\text{Lu}_{2.18}\text{Se}_6$ and $\text{Gd}_{1.87}\text{Lu}_{2.13}\text{Se}_6$ have a three-dimensional channel structure. Magnetic measurements have shown that both $\beta\text{-PrLuSe}_3$ and $\beta\text{-NdLuSe}_3$ are Curie-Weiss type paramagnets. $\text{Sm}_{1.82}\text{Lu}_{2.18}\text{Se}_6$ exhibits van Vleck paramagnetism. $\text{Gd}_{1.87}\text{Lu}_{2.13}\text{Se}_6$ was found to have an antiferromagnetic transition around 4 K, whereas Ce_3LuSe_6 has ferromagnetic ordering with a weak antiferromagnetism below 5 K. $\text{Ln}_x\text{Lu}_y\text{Se}_z$ (Ln = La, Ce, Pr, Nd, Sm, Gd) are semiconductors with tunable band gaps.

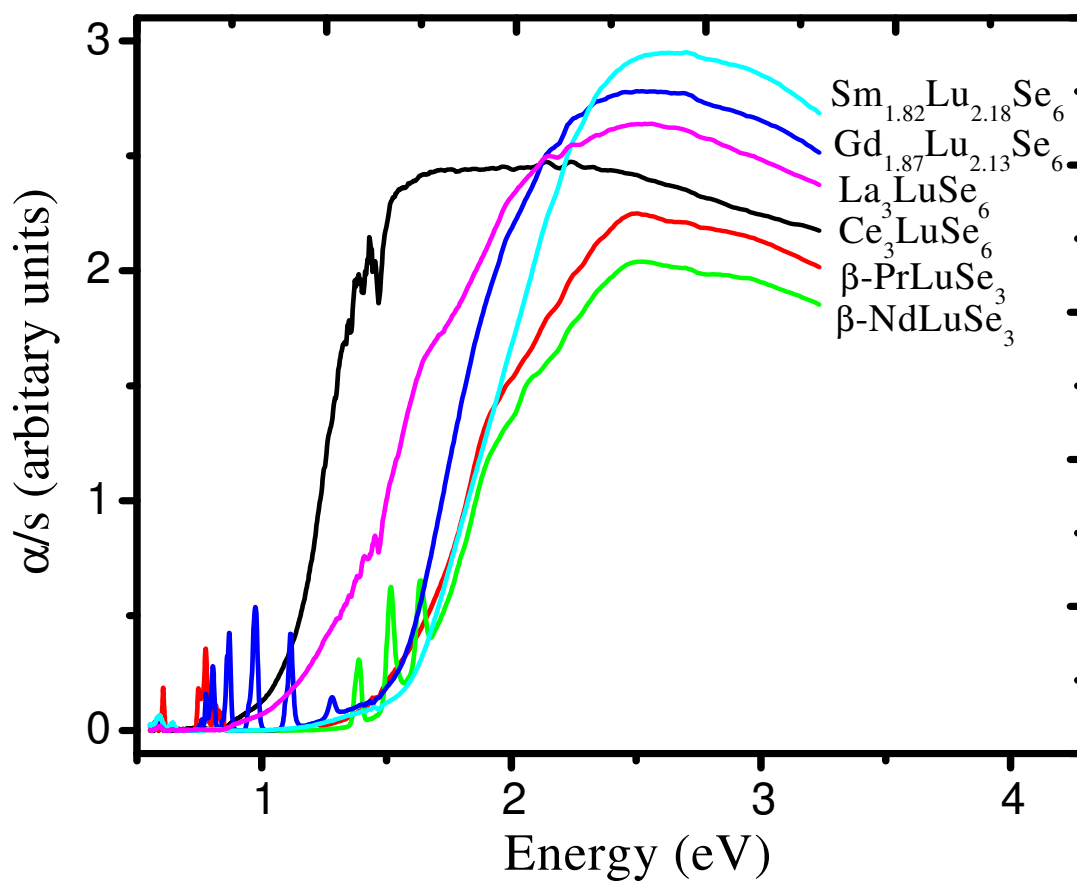


Figure 6.13. UV-vis diffuse reflectance spectra of $\text{Ln}_x\text{Lu}_y\text{Se}_z$ (Ln = La, Ce, Pr, Nd, Sm, Gd).

REFERENCES

1. Moreau, J. M. *Mater. Res. Bull.* **1968**, *3*, 427.
2. Moreau, J. M.; Mareschal, J.; Bertaut, E. F. *Solid State Commun.* **1968**, *6*, 751.
3. Mareschal, J.; Moreau, J. M.; Ollivier, G.; Pataud, P.; Sivardiere, J. *Solid State Commun.* **1969**, *7*, 669.
4. Rodier, N.; Laruelle, P. *C. R. Seances Acad. Sci. Ser. C* **1970**, *270*, 2127.
5. Coutures, J.; Coutures, J. P. *J. Solid State Chem.* **1976**, *19*, 29.
6. Müller-Buschbaum, H.; Graebner, P. -H. *Z. Anorg. Allg. Chem.* **1971**, *386*, 158.
7. Ijdo, D. J. W. *Acta Crystallogr. B* **1980**, *36*, 2403.
8. Ito, K.; Tezuka, K.; Hinatsu, Y. *J. Solid State Chem.* **2001**, *157*, 173.
9. Deepa, M.; Varadaraju, U. V. *Mater. Res. Soc. Symp. Proc.* **1998**, *527*, 507.
10. Berndt, U.; Maier, D.; Keller, C. *J. Solid State Chem.* **1976**, *16*, 189.
11. Ito, K.; Tezuka, K.; Hinatsu, Y. *J. Solid State Chem.* **2001**, *157*, 173.
12. Rodier, N.; Julien, R.; Tien, V. *Acta Crystallogr. C* **1983**, *39*, 670.
13. Carre, D.; Laruelle, P. *Acta Crystallogr. B* **1974**, *30*, 952.
14. Mitchell, K.; Somers, R. C.; Huang, F. Q.; Ibers, J. A. *J. Solid State Chem.* **2004**, *177*, 709.
15. Jin, G. B.; Choi, E. S.; Guertin, R. P.; Brooks, J. S.; Bray, T. H.; Booth, C. H.; Albrecht-Schmitt, T. E. *Chem. Mater.* **2007**, *19*, 567.
16. Rodier, N.; Tien, V. *C. R. Seances Acad. Sci. Ser. C* **1974**, *279*, 817.
17. Rodier, N.; Firor, R. L.; Tien, V.; Guittard, M. *Mater. Res. Bull.* **1976**, *11*, 1209.
18. Rodier, N. *Bull. Soc. Fr. Mineral. Cristallogr.* **1973**, *96*, 350.

19. Carré, D.; Laruelle, P. *Acta Cryst.* 1973, *B* 29, 70.
20. Gray, D. L.; Rodriguez, B. A.; Chan, G. H.; Van Duyne, R. P.; Ibers, J. A. *J. Solid State Chem.* in press.
21. Jin, G. B.; Choi, E. S.; Guertin, R. P.; Brooks, J. S.; Bray, T. H.; Booth, C. H.; Albrecht-Schmitt, T. E. *J. Solid State Chem.* in press.
22. Jin, G. B.; Choi, E. S.; Guertin, R. P.; Brooks, J. S.; Booth, C. H.; Albrecht-Schmitt, T. E. *PrLnYb₂S₆ (Ln = Tb, Dy)*; *J. Solid State Chem.* in press.
23. Marezio, M.; Remeika, J. P.; Dernier, P. D. *Acta Crystallogr. B* **1970**, 26, 2008.
24. Noel, H.; Padiou, J. *Acta Crystallogr. B* **1976**, 32, 1593.
25. Schleid, T.; Lissner, F. *J. Alloys Compd.* **1992**, 189, 69.
26. Fang, C. M.; Meetsma, A.; Wiegers, G. A. *J. Alloys Compd.* **1993**, 201, 255.
27. Zachariasen, W.H. *Acta Crystallogr.* **1949**, 2, 291.
28. Jin, G. B.; Choi, E. S.; Guertin, R. P.; Brooks, J. S.; Booth, C. H.; Albrecht-Schmitt, T. E. *Inorg. Chem.* submitted.
29. Sheldrick, G. M. *SHELXTL PC, Version 6.12, An Integrated System for Solving, Refining, and Displaying Crystal Structures from Diffraction Data*; Siemens Analytical X-Ray Instruments, Inc.: Madison, WI, 2001.
30. Sheldrick, G. M. *SADABS 2001, Program for absorption correction using SMART CCD based on the method of Blessing*; Blessing, R. H. *Acta Crystallogr.* **1995**, A51, 33.
31. Mulay, L. N.; Boudreaux, E. A. *Theory and Applications of Molecular Diamagnetism*; Wiley-Interscience: New York, 1976.

32. Wendlandt, W. W.; Hecht, H. G. *Reflectance Spectroscopy*; Interscience Publishers: New York, 1966.
33. Rodier, N.; Tien, V. *Acta Crystallogr.* **1976**, *32*, 2705.
34. Becker, D. F.; Kasper, J. S. *Acta Crystallogr.* **1957**, *10*, 332.
35. Adolphe, C. *Annales de Chimie (Paris)* **1965**, *10*, 271.
36. Shannon, R. D. *Acta Cryst.* **1976**, *A32*, 751.
37. Kittel, C. *Introduction to Solid State Physics*, 6th Ed., Wiley, New York, 1986.
38. Van Vleck, J. H. *The Theory of Electric and Magnetic Susceptibilities*; Oxford University Press: London, 1932.

CHAPTER 7

SYNTHESES, STRUCTURE, MAGNETISM, AND OPTICAL PROPERTIES OF THE PARTIALLY ORDERED QUATERNARY INTERLANTHANIDE SULFIDES $\text{PrLnYb}_2\text{S}_6$ ($\text{Ln} = \text{Tb, Dy}$)

ABSTRACT

Dark red single crystals of $\text{PrLnYb}_2\text{S}_6$ ($\text{Ln} = \text{Pr/Yb, Tb, Dy}$) have been synthesized through the reaction of elemental rare earth metals and S using a Sb_2S_3 flux at 1000 °C. These isotypic compounds adopt the $\text{F-Ln}_2\text{S}_3$ three-dimensional open channel structure type. Eight-coordinate Pr^{3+} ions sit in the channels that are constructed from three different edge-shared double chains running down the b axis that contain Yb(1)S_6 octahedra, Yb(2)S_6 , octahedral, and LnS_7 monocapped trigonal prisms, respectively. Each double chain connects to four other neighbors by sharing vertices and edges. Considerable disordering in Ln positions was observed in single X-ray diffraction experiments only in the case of Pr/Yb. Least square refinements gave rise to the formulas of $\text{Pr}_{1.34}\text{Yb}_{2.66}\text{S}_6$, $\text{PrTbYb}_2\text{S}_6$, and $\text{PrDyYb}_2\text{S}_6$ that were confirmed by elemental analysis and magnetic susceptibility measurements. $\text{Pr}_{1.34}\text{Yb}_{2.66}\text{S}_6$, $\text{PrTbYb}_2\text{S}_6$, and $\text{PrDyYb}_2\text{S}_6$ are paramagnetic down to 2 K without any indications of long-range magnetic ordering.

The optical transitions for $\text{Pr}_{1.34}\text{Yb}_{2.66}\text{S}_6$, $\text{PrTbYb}_2\text{S}_6$, and $\text{PrDyYb}_2\text{S}_6$ are at approximately 1.6 eV. Crystallographic data: $\text{Pr}_{1.34}\text{Yb}_{2.66}\text{S}_6$, monoclinic, space group $P2_1/m$, $a = 10.960(2)$, $b = 3.9501(8)$, $c = 11.220(2)$ Å, $\beta = 108.545(3)$, $V = 460.54(16)$, $Z = 2$; $\text{PrTbYb}_2\text{S}_6$, monoclinic, space group $P2_1/m$, $a = 10.9496(10)$, $b = 3.9429(4)$, $c = 11.2206(10)$ Å, $\beta = 108.525(2)$, $V = 459.33(7)$, $Z = 2$; $\text{PrDyYb}_2\text{S}_6$, monoclinic, space group $P2_1/m$, $a = 10.9384(10)$, $b = 3.9398(4)$, $c = 11.2037(10)$ Å, $\beta = 108.612(2)$, $V = 457.57(7)$, $Z = 2$.

INTRODUCTION

There have been numerous studies on ternary interlanthanide chalcogenides in terms of their diverse structural chemistry and interesting physical properties.¹⁻¹⁸ α - $\text{LnLn}'\text{S}_3$ (GdFeO_3 type)^{19, 1-4}, CeYb_3S_6 ($\text{F-Ln}_2\text{S}_3$ type)^{20,21, 5-6}, $\text{Sc}_2\text{Er}_3\text{S}_7$ (Y_5S_7 type)²² and EuLn_2Q_4 ⁸⁻¹⁰ (CaFe_2O_4 type)²³ possess three-dimensional open-channel structures, wherein the larger Ln^{3+} ions reside in channels formed by smaller lanthanide chalcogenides polyhedra. While β - $\text{LnLn}'\text{Q}_3$ ($\text{Q} = \text{S}, \text{Se}$) (UFeS_3 type)^{24, 3,11,12} and γ - $\text{LnLn}'\text{S}_3$ ($\text{Ln} = \text{La}, \text{Ce}$; $\text{Ln}' = \text{Er}, \text{Tm}, \text{Yb}$)¹³ have layers of $\text{Ln}'\text{Q}_x$ polyhedra, separated by larger Ln^{3+} ions. δ - LnLuS_3 ($\text{Ln} = \text{Ce}, \text{Pr}, \text{Nd}$)¹⁴ (CeTmS_3 type)¹⁵ have a very condensed three-dimensional structure. Recent work has shown that the electronic and magnetic properties of these materials highly depend on the structures they adopt and the choices of lanthanides. For example, the optical band gaps of γ - $\text{LnLn}'\text{S}_3$ ($\text{Ln} = \text{La}, \text{Ce}$; $\text{Ln}' = \text{Er}, \text{Tm}, \text{Yb}$) are approximately 1.3 – 1.6 eV,¹³ while SmEr_3S_6 is 2.4 – 2.6 eV.¹⁶ δ - LnLuS_3 ($\text{Ln} = \text{Pr}, \text{Nd}$) exhibit possible short-range antiferromagnetic ordering at low temperatures.¹⁴

In contrast, there are no existing ordered quaternary interlanthanide chalcogenides that possess three different lanthanide elements. Instead of making new ordered quaternary phases, they can be prepared using intermediate lanthanides to substitute in the disordered sites in already known ternary structures. F-Ln₂S₃ type ternary compounds are probably the best candidates to achieve this goal.^{17,18} This structure type has three different coordination environments for Ln³⁺ as octahedral, and mono- and bicapped trigonal prisms. The seven-coordinate sites are often disordered. By carefully choosing three different metals, ordered quaternary phases can be accessed. In this paper, we present the syntheses, structure, optical, and magnetic properties of the first two partially ordered quaternary interlanthanide chalcogenides, PrTbYb₂S₆ and PrDyYb₂S₆. As a reference, Pr_{1.34}Yb_{2.66}S₆ is also included in the discussion. The information in this chapter has been published as a full paper in *Journal of Solid-State Chemistry*.²⁵

EXPERIMENTAL

Starting Materials. Pr (99.9%, Alfa-Aesar), Tb (99.9%, Alfa-Aesar), Dy (99.9%, Alfa-Aesar), Yb (99.9%, Alfa-Aesar), S (99.5%, Alfa-Aesar), and Sb (99.5%, Alfa-Aesar) were used as received. The Sb₂S₃ flux was prepared from the direct reaction of the elements in sealed fused-silica ampoules at 850 °C.

Syntheses. PrLnYb₂S₆ (Ln = Tb, Dy) were prepared through the reaction of Pr (0.17 mmol), Ln (0.17 mmol), Yb (0.34 mmol), S (1.02 mmol), and Sb₂S₃ (0.17 mmol). For Pr_{1.34}Yb_{2.66}S₆, the reaction mixture consists of Pr (0.23 mmol), Yb (0.45 mmol), S (1.02 mmol), and Sb₂S₃ (0.17 mmol). All of the reactants were loaded into fused-silica ampoules under an argon atmosphere in a glovebox. The ampoules were sealed under

vacuum and heated in a programmable tube furnace. The following heating profile was used: 2 °C/min to 500 °C (held for 1 h), 0.5 °C/min to 1000 °C (held for 5 d), 0.04 °C/min to 550 °C (held for 2 d), and 0.5 °C/min to 24 °C. Powder X-ray diffraction measurements were used to confirm phase purity by comparing the powder patterns calculated from the single crystal X-ray structures with the experimental data. Semi-quantitative SEM/EDX analyses were performed using JEOL 840/Link Isis or JEOL JSM-7000F instruments. Pr, Ln, Yb, and S percentages were calibrated against standards. Sb was not detected in the crystals. Pr:Ln:Yb:S ratios of close to 1:1:2:6 were found for PrLnYb₂S₆ (Ln = Tb, Dy), while the Pr:Yb:S ratios in Pr_{1.34}Yb_{2.66}S₆ samples are approximately 1:2:4.5 from EDX analyses.

Crystallographic Studies. Single crystals of PrLnYb₂S₆ (Ln = Pr/Yb, Tb, Dy) were mounted on glass fibers with epoxy and optically aligned on a Bruker APEX single crystal X-ray diffractometer using a digital camera. Initial intensity measurements were performed using graphite monochromated Mo K α ($\lambda = 0.71073 \text{ \AA}$) radiation from a sealed tube and monocapillary collimator. SMART (v 5.624) was used for preliminary determination of the cell constants and data collection control. The intensities of reflections of a sphere were collected by a combination of 3 sets of exposures (frames). Each set had a different ϕ angle for the crystal and each exposure covered a range of 0.3° in ω . A total of 1800 frames were collected with exposure times per frame of 10 or 20 seconds depending on the crystal.

For PrLnYb₂S₆ (Ln = Pr/Yb, Tb, Dy), determination of integrated intensities and global refinement were performed with the Bruker SAINT (v 6.02) software package using a narrow-frame integration algorithm. These data were treated first with a face-

index numerical absorption correction using XPREP,²⁶ followed by a semi-empirical absorption correction using SADABS.²⁷ The program suite SHELXTL (v 6.12) was used for space group determination (XPREP), direct methods structure solution (XS), and least-squares refinement (XL).²⁶ The final refinements included anisotropic displacement parameters for all atoms and secondary extinction. Some crystallographic details are given in Table 7.1. Atomic coordinates and equivalent isotropic displacement parameters for PrLnYb₂S₆ (Ln = Pr/Yb, Tb, Dy) are given in Table 7.2-7.4.

The formula of F-Ln₂S₃ type compounds can be expressed as (A^{VIII})(B^{VII})(C^{VI})₂S₆. In the case of Pr_{1.34}Yb_{2.66}S₆, eight-coordinate A sites were assigned as Pr atoms and both seven-coordinate B and octahedral C positions were named as Yb at the beginning of the refinement. However the average bond distance of YbS₇ is longer than the accepted value, according to Shannon's radii data,²⁸ and its thermal parameter is larger than the other Yb atoms. The elemental analysis showed that the ratio of Pr:Yb is 1:2. This evidence suggests that there should be some disordering on the B sites. The refinement of occupancy lowered the residual and weighting scheme and gave rise to the final formula of Pr_{1.34(1)}Yb_{2.66(1)}S₆.

For PrLnYb₂S₆ (Ln = Tb, Dy), Pr, Ln, Yb atoms were put in A, B, and C positions respectively. This gave excellent residuals in the refinements, and the suggested formulas as PrLnYb₂S₆ (Ln = Tb, Dy) are consistent with the EDX results. Considering the similarity among Pr, Ln, and Yb, small amount of disordering on B and C, and even A sites can not be excluded.

Table 7.1. Crystallographic Data for PrLnYb₂S₆ (Ln = Pr/Yb, Tb, Dy).

| Formula | Pr _{1.34} Yb _{2.66} S ₆ | PrTbYb ₂ S ₆ | PrDyYb ₂ S ₆ |
|--|--|------------------------------------|------------------------------------|
| fw | 841.31 | 838.27 | 841.85 |
| Color | dark red | dark red | dark red |
| Crystal System | Monoclinic | monoclinic | monoclinic |
| Space group | <i>P2₁/m</i> (No. 11) | <i>P2₁/m</i> (No. 11) | <i>P2₁/m</i> (No. 11) |
| a (Å) | 10.960(2) | 10.9496(10) | 10.9384(10) |
| b (Å) | 3.9501(8) | 3.9429(4) | 3.9398(4) |
| c (Å) | 11.220(2) | 11.2206(10) | 11.2037(10) |
| β | 108.545(3) | 108.525(2) | 108.612(2) |
| V (Å ³) | 460.54(16) | 459.33(7) | 457.57(7) |
| Z | 2 | 2 | 2 |
| T (K) | 193 | 193 | 193 |
| λ (Å) | 0.71073 | 0.71073 | 0.71073 |
| ρ _{calcd} (g cm ⁻³) | 6.067 | 6.061 | 6.110 |
| μ (cm ⁻¹) | 349.71 | 342.64 | 348.32 |
| R(F) ^a | 0.0233 | 0.0330 | 0.0243 |
| R _w (F _o ²) ^b | 0.0657 | 0.1104 | 0.0597 |

$$^a R(F) = \frac{\sum \|F_o\| - |F_c|}{\sum |F_o|} \text{ for } F_o^2 > 2\sigma(F_o^2).$$

$$^b R_w(F_o^2) = \left[\frac{\sum [w(F_o^2 - F_c^2)^2]}{\sum wF_o^4} \right]^{1/2}.$$

Table 7.2. Atomic Coordinates and Equivalent Isotropic Displacement Parameters for $\text{Pr}_{1.34}\text{Yb}_{2.66}\text{S}_6$.

| Atom (site) | x | y | z | $U_{\text{eq}} (\text{\AA}^2)^a$ |
|-------------|-------------|------|-------------|----------------------------------|
| Pr1 | 0.55123(4) | 0.25 | 0.19606(4) | 0.00843(13) |
| Pr/Yb | 0.18137(4) | 0.25 | 0.00138(4) | 0.01093(16) |
| Yb1 | 0.94227(3) | 0.25 | 0.33496(3) | 0.00997(13) |
| Yb2 | 0.65971(3) | 0.25 | 0.58575(3) | 0.01011(13) |
| S1 | 0.41859(19) | 0.25 | 0.59374(19) | 0.0086(4) |
| S2 | 0.8937(2) | 0.25 | 0.5587(2) | 0.0100(4) |
| S3 | 0.23343(19) | 0.25 | 0.76947(19) | 0.0090(4) |
| S4 | 0.3064(2) | 0.25 | 0.25444(19) | 0.0098(4) |
| S5 | 0.9805(2) | 0.25 | 0.1160(2) | 0.0121(4) |
| S6 | 0.61659(19) | 0.25 | 0.96234(19) | 0.0084(4) |

^a U_{eq} is defined as one-third of the trace of the orthogonalized U_{ij} tensor.

Table 7.3. Atomic Coordinates and Equivalent Isotropic Displacement Parameters for PrTbYb₂S₆.

| Atom (site) | <i>x</i> | <i>y</i> | <i>z</i> | $U_{\text{eq}} (\text{\AA}^2)^a$ |
|-------------|------------|----------|------------|----------------------------------|
| Pr1 | 0.55027(7) | 0.25 | 0.19511(7) | 0.0064(2) |
| Tb1 | 0.18125(6) | 0.25 | 0.00196(6) | 0.0075(2) |
| Yb1 | 0.94104(5) | 0.25 | 0.33390(5) | 0.0098(2) |
| Yb2 | 0.65988(5) | 0.25 | 0.58556(5) | 0.0096(2) |
| S1 | 0.4185(3) | 0.25 | 0.5947(3) | 0.0073(6) |
| S2 | 0.8943(3) | 0.25 | 0.5591(3) | 0.0085(6) |
| S3 | 0.2357(3) | 0.25 | 0.7711(3) | 0.0071(6) |
| S4 | 0.3064(3) | 0.25 | 0.2532(3) | 0.0095(6) |
| S5 | 0.9800(3) | 0.25 | 0.1144(3) | 0.0101(7) |
| S6 | 0.6159(3) | 0.25 | 0.9625(3) | 0.0081(6) |

^a U_{eq} is defined as one-third of the trace of the orthogonalized U_{ij} tensor.

Table 7.4. Atomic Coordinates and Equivalent Isotropic Displacement Parameters for PrDyYb₂S₆.

| Atom (site) | <i>x</i> | <i>y</i> | <i>z</i> | $U_{\text{eq}} (\text{\AA}^2)^a$ |
|-------------|------------|----------|------------|----------------------------------|
| Pr1 | 0.54996(5) | 0.25 | 0.19506(5) | 0.00797(13) |
| Dy1 | 0.18100(4) | 0.25 | 0.00156(4) | 0.00847(13) |
| Yb1 | 0.94108(4) | 0.25 | 0.33369(4) | 0.01048(13) |
| Yb2 | 0.66021(4) | 0.25 | 0.58597(4) | 0.01040(13) |
| S1 | 0.4181(2) | 0.25 | 0.5945(2) | 0.0087(5) |
| S2 | 0.8943(2) | 0.25 | 0.5590(2) | 0.0098(5) |
| S3 | 0.2348(2) | 0.25 | 0.7715(2) | 0.0088(4) |
| S4 | 0.3051(2) | 0.25 | 0.2525(2) | 0.0100(5) |
| S5 | 0.9799(2) | 0.25 | 0.1140(2) | 0.0101(5) |
| S6 | 0.6165(2) | 0.25 | 0.9628(2) | 0.0095(5) |

^a U_{eq} is defined as one-third of the trace of the orthogonalized U_{ij} tensor.

Powder X-ray Diffraction. Powder X-ray diffraction patterns were collected with a Rigaku Miniflex powder X-ray diffractometer using Cu K α ($\lambda = 1.54056 \text{ \AA}$) radiation.

Magnetic Susceptibility Measurements. Magnetism data were measured on powders in gelcap sample holders with a Quantum Design MPMS 7T magnetometer/susceptometer between 2 and 300 K and in applied fields up to 7 T. DC susceptibility measurements were made under zero-field-cooled conditions with an applied field of 0.1 T. Susceptibility values were corrected for the sample diamagnetic contribution according to Pascal's constants²⁹ as well as for the sample holder diamagnetism. θ_p values were obtained from extrapolations from fits between 100 and 300 K. (Magnetic susceptibility measurements were performed by Eun Sang Choi and James S. Brooks at Florida State University)

UV-vis-NIR Diffuse Reflectance Spectroscopy. The diffuse reflectance spectra PrLnYb₂S₆ (Ln = Pr/Yb, Tb, Dy) were measured from 200 to 1500 nm using a Shimadzu UV3100 spectrophotometer equipped with an integrating sphere attachment. The Kubelka-Munk function was used to convert diffuse reflectance data to absorption spectra.³⁰

RESULTS AND DISCUSSION

Structures of PrLnYb₂S₆ (Ln = Pr/Yb, Tb, Dy). The isotypic series of PrLnYb₂S₆ (Ln = Pr/Yb, Tb, Dy) have the F-Ln₂S₃ type structure with Pr³⁺ ions sitting on eight-coordinate positions, Ln³⁺ ions in seven-coordinate positions, and Yb³⁺ ions occupying two octahedral sites. As shown in Figure 7.1, the structure of these

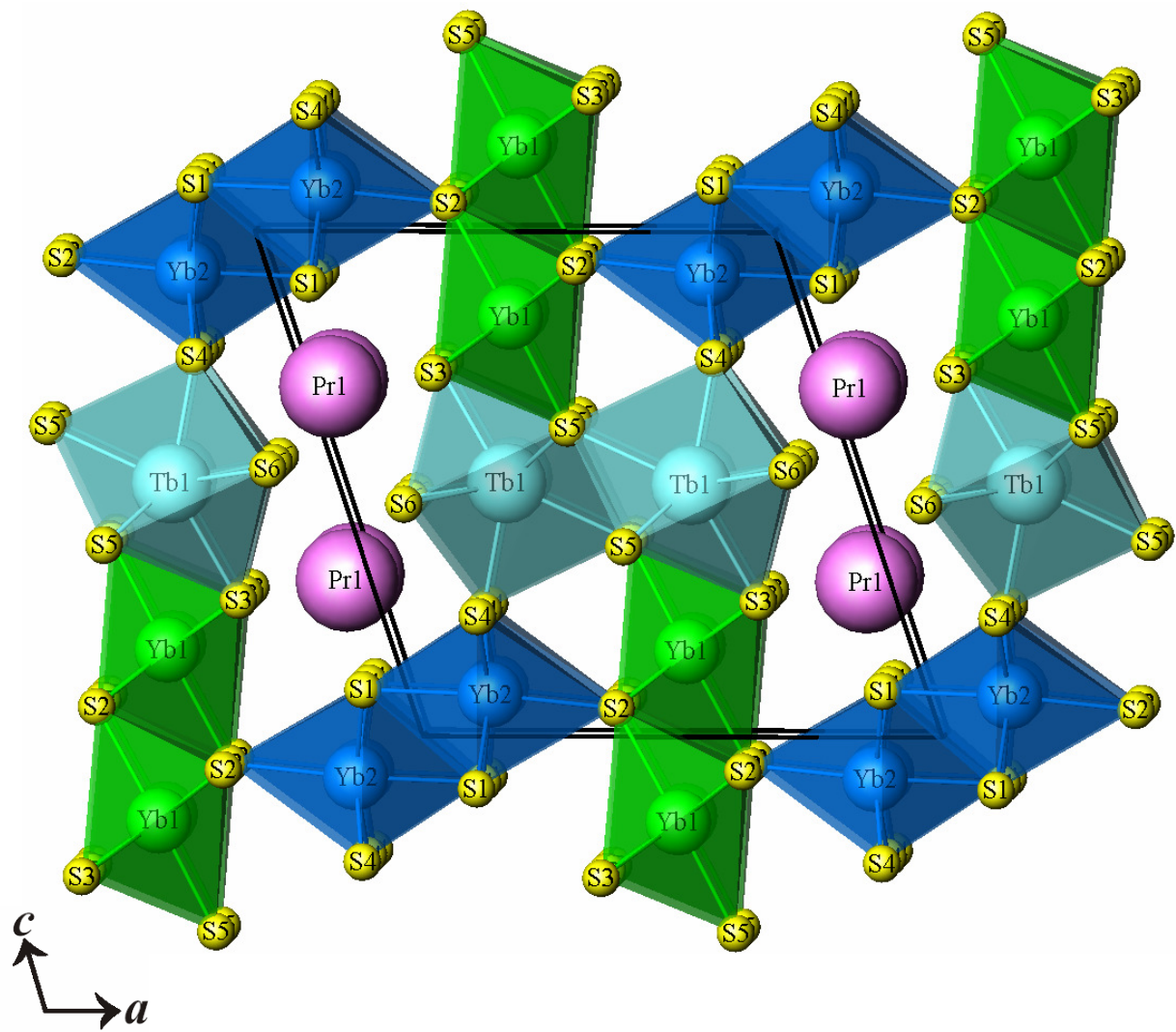


Figure 7.1. An illustration of the three-dimensional structure of PrTbYb₂S₆ along the *b* axis.

compounds is constructed from three different edge-shared double chains running down the b axis, which contain Yb(1)S₆ octahedra, Yb(2)S₆ octahedra, and LnS₇ monocapped trigonal prisms, respectively. Each double chain connects to four other neighbors by sharing vertices and edges to form the channels where Pr³⁺ ions reside. For example, Yb(1)S₆ double chains are bound to two Yb(2)S₆ double chains via corner-sharing and two LnS₇ double chains via edge-sharing. The PrS₈ polyhedra can be viewed as a bicapped trigonal prism, which is shown in Figure 7.2.

Selected bond distances for PrLnYb₂S₆ (Ln = Pr/Yb, Tb, Dy) are listed in Table 7.5. Pr-S bond distances range from 2.8755(19) Å to 3.0127 Å, which are comparable to Shannon's radii data of 2.966 Å.²⁸ The average bond distances for Pr/YbS₇, TbS₇, and DyS₇ are 2.807(2) Å, 2.800(2) Å, and 2.792(2) Å respectively. Compared to the accepted values for PrS₇ (2.89 Å), YbS₇ (2.765 Å), TbS₇ (2.82 Å), and DyS₇ (2.81 Å), they are all reasonable.²⁸ The bond distances for YbS₆ octahedra are in the range of 2.6134(14) Å and 2.759(2) Å.

Magnetic Susceptibility. The magnetic susceptibilities for PrLnYb₂S₆ (Ln = Pr/Yb, Tb, Dy), in the range of 2-300 K, are presented in Figures 7.3-7.5. There are no indications of long-range magnetic orderings down to 2 K. Pr_{1.34}Yb_{2.66}S₆ deviates from the ideal Curie-Weiss law below 70 K due to crystal-field splitting of lanthanide ions. PrTbYb₂S₆ shows a pure Curie-Weiss paramagnetic behavior in the whole temperature range, while the 1/χ plot for PrDyYb₂S₆ exhibits a deviation from the Curie-Weiss law and the onset of upward curvature at low temperature. This may indicate a short-range antiferromagnetic ordering, which has also been observed in δ-Pr_{1.29}Lu_{0.71}S₃.¹⁴ Table 7.6 shows the magnetic parameters for PrLnYb₂S₆ (Ln = Pr/Yb, Tb, Dy), which were

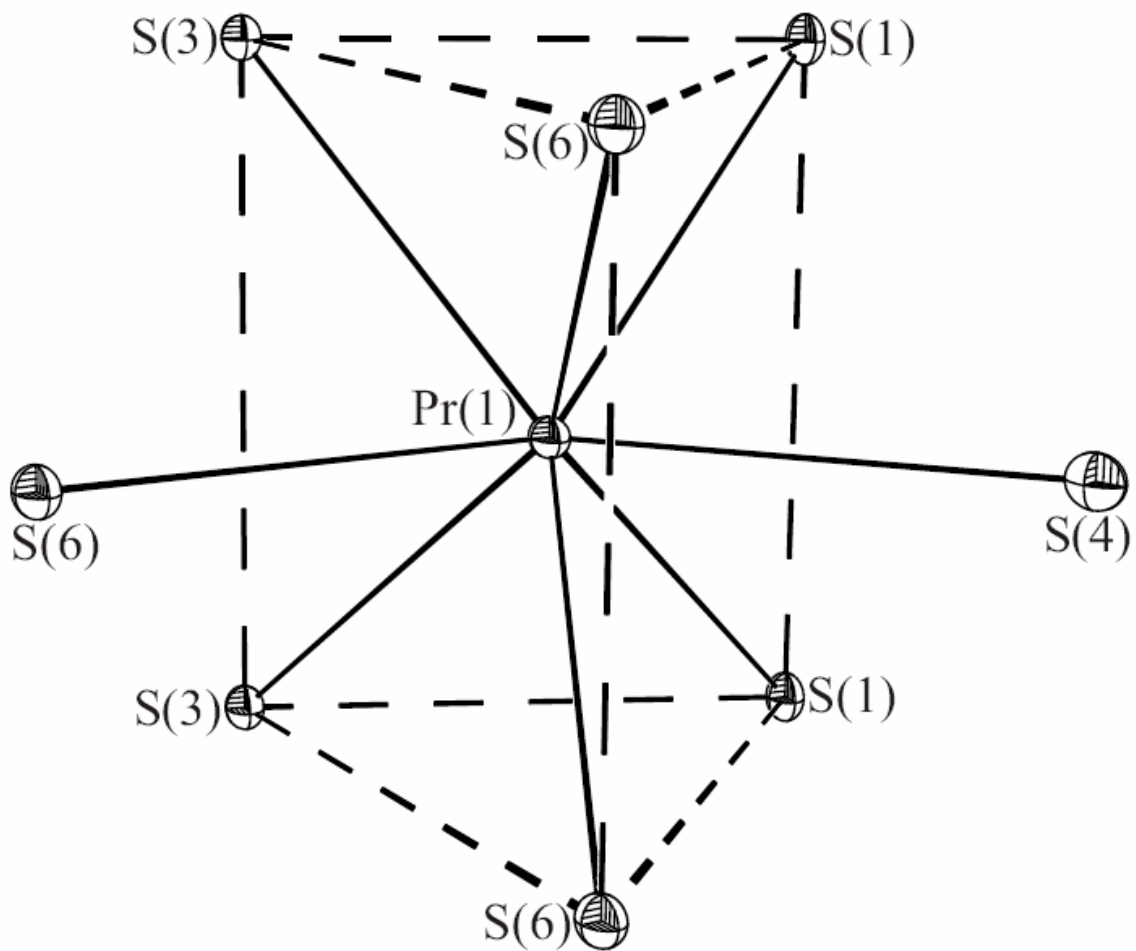


Figure 7.2. Bicapped trigonal prismatic coordination environment of the Pr ions in $\text{PrTbYb}_2\text{S}_6$.

Table 7.5. Selected Bond Distances (Å) for PrLnYb₂S₆ (Ln = Pr/Yb, Tb, Dy).

| Formula | Pr _{1.34} Yb _{2.66} S ₆ | PrTbYb ₂ S ₆ | PrDyYb ₂ S ₆ |
|---------------|--|------------------------------------|------------------------------------|
| Pr(1)-S(1) ×2 | 3.0127(16) | 3.009(2) | 3.0058(19) |
| Pr(1)-S(3) ×2 | 3.0068(16) | 2.993(2) | 3.0004(19) |
| Pr(1)-S(4) | 2.958(2) | 2.943(3) | 2.947(3) |
| Pr(1)-S(6) ×2 | 2.8919(16) | 2.877(2) | 2.8755(19) |
| Pr(1)-S(6) | 2.930(2) | 2.919(3) | 2.918(2) |
| Ln-S(3) | 2.836(2) | 2.837(3) | 2.821(2) |
| Ln-S(4) | 2.732(2) | 2.715(3) | 2.704(3) |
| Ln-S(5) ×2 | 2.7012(16) | 2.692(2) | 2.6832(18) |
| Ln-S(5) | 2.881(2) | 2.865(3) | 2.863(2) |
| Ln-S(6) ×2 | 2.8977(15) | 2.901(2) | 2.8947(18) |
| Yb(1)-S(2) ×2 | 2.6819(15) | 2.684(2) | 2.6810(18) |
| Yb(1)-S(2) | 2.726(2) | 2.734(3) | 2.731(2) |
| Yb(1)-S(3) ×2 | 2.7471(15) | 2.752(2) | 2.7426(18) |
| Yb(1)-S(5) | 2.620(2) | 2.630(3) | 2.628(2) |
| Yb(2)-S(1) ×2 | 2.7557(15) | 2.759(2) | 2.7565(17) |
| Yb(2)-S(1) | 2.673(2) | 2.678(3) | 2.680(2) |
| Yb(2)-S(2) | 2.677(2) | 2.675(3) | 2.672(2) |
| Yb(2)-S(4) ×2 | 2.6134(14) | 2.621(2) | 2.6194(16) |

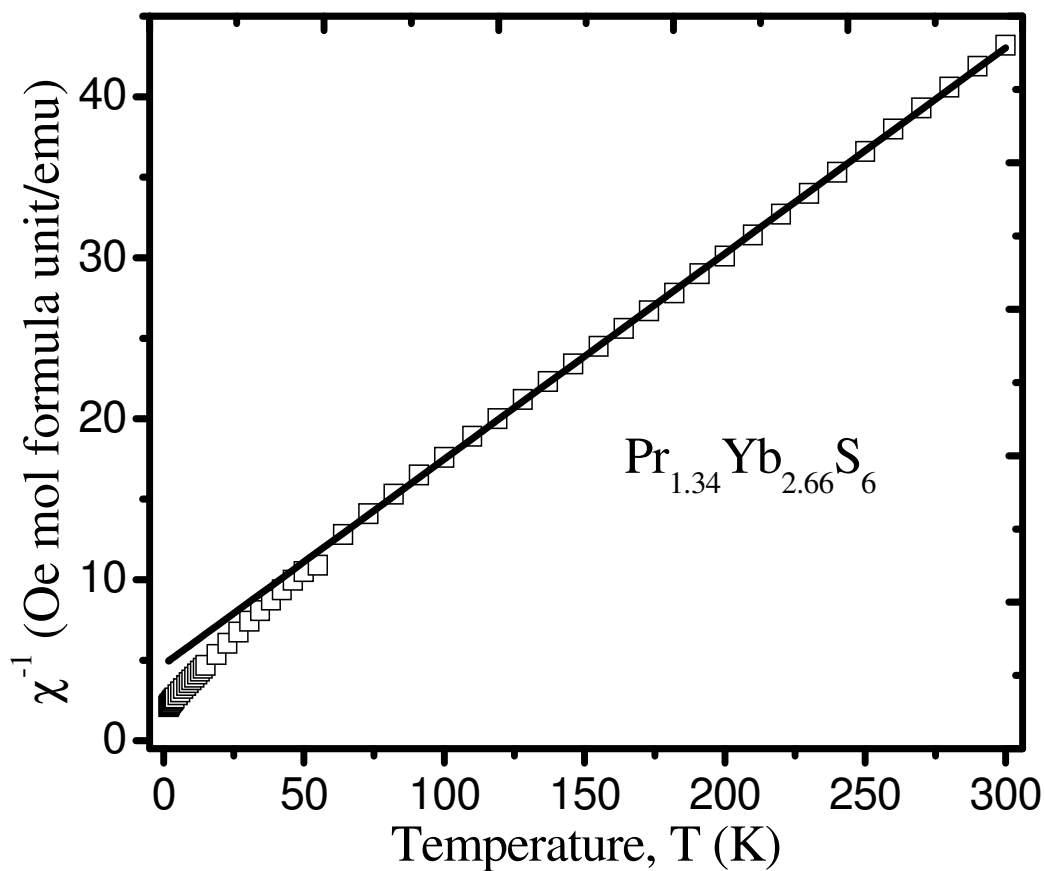


Figure 7.3. Inverse molar magnetic susceptibility plotted against temperature between 2 and 300 K for $\text{Pr}_{1.34}\text{Yb}_{2.66}\text{S}_6$. Data were taken under an applied magnetic field of 0.1 T. The straight line represents the fit to Curie-Weiss law in the range of 100-300 K.

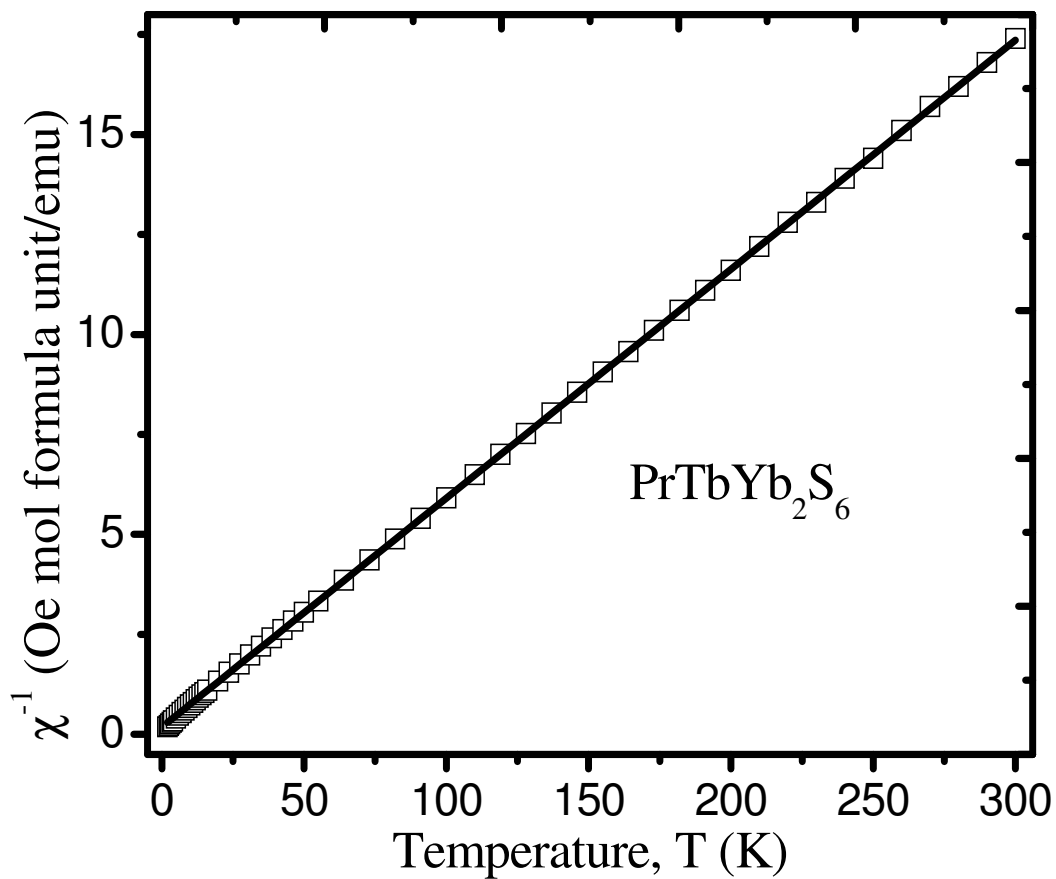


Figure 7.4. The plot of the inverse molar magnetic susceptibility vs T for $\text{PrTbYb}_2\text{S}_6$ under an applied magnetic field of 0.1 T between 2 and 300 K. The straight line represents the fit to Curie-Weiss law in the range of 100-300 K.

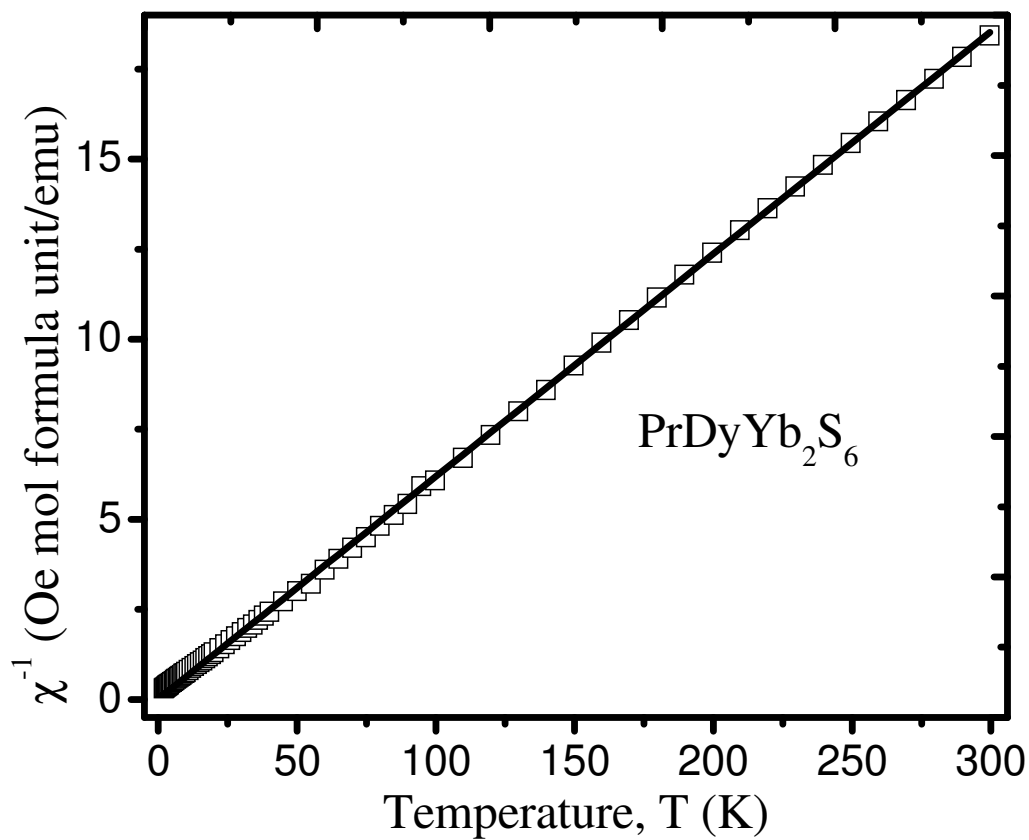


Figure 7.5. The temperature dependence of the reciprocal molar magnetic susceptibility for $\text{PrDyYb}_2\text{S}_6$ under an applied magnetic field of 0.1 T between 2 and 300 K. The straight line represents the fit to Curie-Weiss law in the range of 100-300 K.

Table 7.6. Magnetic Parameters for PrLnYb₂S₆ (Ln = Pr/Yb, Tb, Dy).

| Formula | P _{cal} /μ _B | P _{eff} /μ _B | θ _p /K | R ² |
|--|----------------------------------|----------------------------------|-------------------|----------------|
| Pr _{1.34} Yb _{2.66} S ₆ | 8.48 | 7.91(1) | -36.9(8) | 0.99979 |
| PrTbYb ₂ S ₆ | 12.19 | 11.82(1) | -3.1(4) | 0.99992 |
| PrDyYb ₂ S ₆ | 12.92 | 11.38(2) | -0.2(7) | 0.99979 |

^a P_{cal} and P_{eff} : calculated³¹ and experimental effective magnetic moments per formula unit. ^b Weiss constant (θ_p) and goodness of fit (R²) obtained from high temperature (100-300 K) data.

obtained from fitting the data in the range of 100 K and 300 K into the Curie-Weiss law. All of compounds have negative value of θ_p , which indicates antiferromagnetic interactions between cations. The experimental effective magnetic moments for these compounds are close to the accepted values.³¹ This provides further supporting evidence for the proposed formula from the single crystal X-ray experiments.

Optical Properties. The UV-vis-NIR diffuse reflectance spectra of $\text{PrLnYb}_2\text{S}_6$ (Ln = Pr/Yb, Tb, Dy) are shown in Figure 7.6. They are very similar to each other. This suggests that the substitutions using different lanthanides ions in seven-coordinate Ln positions causes only small changes in the band structures near the Fermi level for $\text{PrLnYb}_2\text{S}_6$ (Ln = Pr/Yb, Tb, Dy). The optical transition mainly results from the interactions among eight-coordinate Pr^{3+} cations, six-coordinate Yb^{3+} cations, and S^{2-} anions. It is also possible that the 4f-band of Pr, Yb, Tb, and Dy lie deep in the valence band. So the optical transitions are determined by the same gap between the [S]3p valence band and 5d(6s) conduction band.^{31,32} The band gaps of $\text{PrLnYb}_2\text{S}_6$ (Ln = Pr/Yb, Tb, Dy) are approximately 1.6 eV, which are consistent with the dark red color they possess. They are also close to the values we reported for $\gamma\text{-LnLn}'\text{S}_3$ (Ln = La, Ce; Ln' = Er, Tm, Yb)¹³ and $\delta\text{-Ln}_{2-x}\text{Lu}_x\text{S}_3$ (Ln = Ce, Pr, Nd; $x = 0.67\text{-}0.71$).¹⁴

CONCLUSIONS

The first two partially ordered quaternary interlanthanide sulfides $\text{PrLnYb}_2\text{S}_6$ (Ln = Tb, Dy) were prepared and characterized. They adopt the same $\text{F-Ln}_2\text{S}_3$ type structure as the parent disordered $\text{Pr}_{1.34}\text{Yb}_{2.66}\text{S}_6$ phase. All three compounds are paramagnetic on the range from 2 to 300 K. The UV-vis-NIR diffuse reflectance spectra show that these

compounds have very similar electronic structures near the Fermi level with wide band gaps. The elemental analysis and magnetic susceptibility measurements are consistent with the proposed formula.

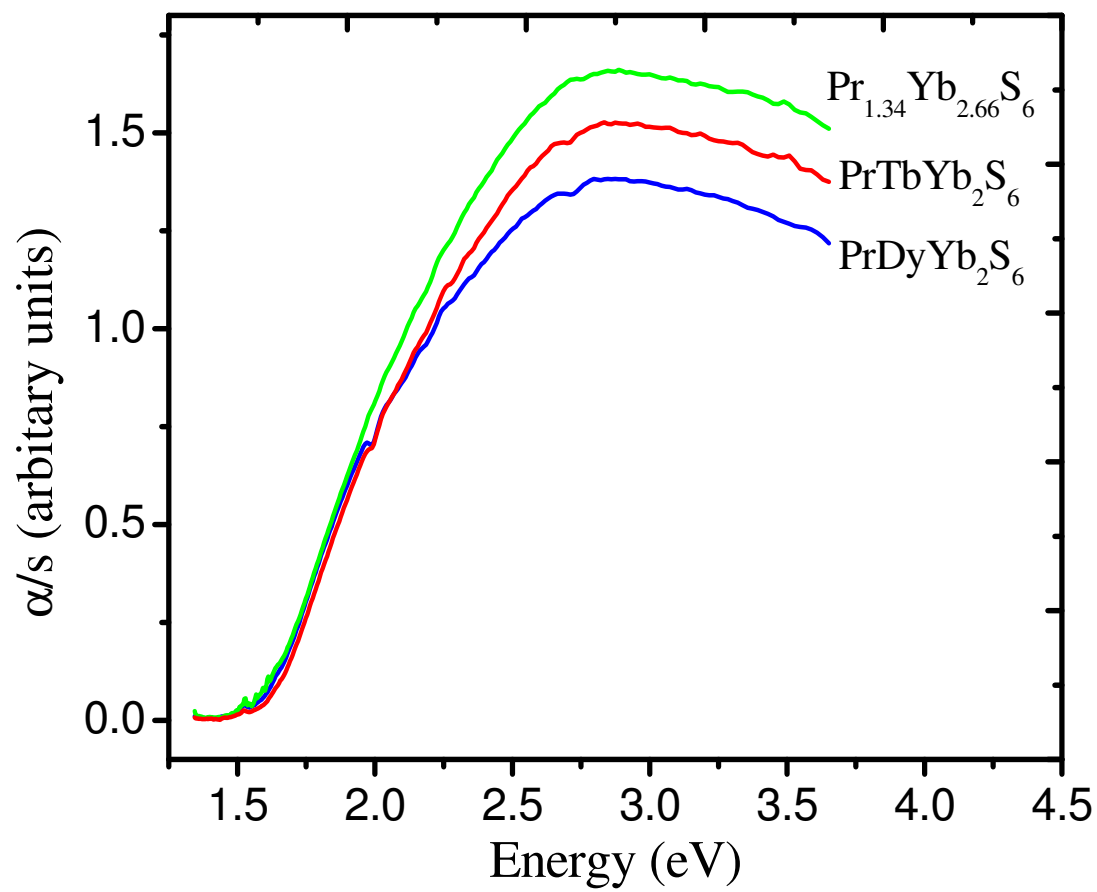


Figure 7.6. UV-vis diffuse reflectance spectra of $\text{PrLnYb}_2\text{S}_6$ (Ln = Pr/Yb, Tb, Dy).

REFERENCES

1. Rodier, N.; Laruelle, P.; Seances, C. R. *Acad. Sci. Ser.* **1970**, C 270, 2127.
2. Ijdo, D. J. W. *Acta Crystallogr.* **1980**, B36, 2403.
3. Rodier, N.; Julien, R.; Tien, V. *Acta Crystallogr.* **1983**, C39, 670.
4. Range, K.-J.; Gietl, A.; Klement, U. *Z. Kristallogr.* **1993**, 207, 147.
5. Rodier, N.; Firor, R. L.; Tien, V.; Guittard, M. *Mat. Res. Bull.* **1976**, 11, 1209.
6. Rodier, N.; Tien, V. *C. R. Acad. Sc. Paris Serie* **1974**, C279, 817.
7. Rodier, N.; Laruelle, P. *Bull. Soc. fr. de Mineral. Cristallogr.* **1972**, 95, 548.
8. Hulliger, F.; Vogt, O. *Phys. Lett.* **1966**, 21, 138.
9. Lugscheider, W.; Pink, H.; Weber, K.; Zinn, W. *Zeitschrift fuer Angewandte Physik* **1970**, 30, 36.
10. Lemoine, P.; Carre, D.; Guittard, M. *Acta Crystallogr.* **1985**, C41, 667.
11. Carré, D.; Laruelle, P. *Acta Crystallogr.* **1974**, B30, 952.
12. Mitchell, K.; Somers, R. C.; Huang, F. Q.; Ibers, J. A. *J. Solid State Chem.* **2004**, 177, 709.
13. Jin, G. B.; Choi, E. S.; Guertin, R. P.; Brooks, J. S.; Bray, T. H.; Booth, C. H.; Albrecht-Schmitt, T. E. *Chem. Mater.* **2007**, 19, 567.
14. Jin, G. B.; Choi, E. S.; Guertin, R. P.; Brooks, J. S.; Bray, T. H.; Booth, C. H.; Albrecht-Schmitt, T. E. *J. Solid State Chem.* **2007**, in press.
15. Rodier, N. *Bull. Soc. fr. de Mineral. Cristallogr.* **1973**, 96, 350.
16. Gray, D. L.; Rodriguez, B. A.; Chan, G. H.; Van Duyne, R. P.; Ibers, J. A. *J. Solid State Chem.* **2007**, in press.
17. Carré, D.; Laruelle, P. *Acta Crystallogr.* **1973**, B29, 70.

18. Rodier, N.; Tien, V. *Bull. Soc. fr. de Mineral. Cristallogr.* **1975**, 98, 30.
19. Marezio, M.; Remeika, J. P.; Dernier, P. D. *Acta Crystallogr.* **1970**, B26, 2008.
20. Schleid, T.; Lissner, F. *J. Alloys Compd.* **1992**, 189, 69.
21. Fang, C. M.; Meetsma, A.; Wiegers, G. A. *J. Alloys Compd.* **1993**, 201, 255.
22. Adolphe, C. *Annales de Chimie (Paris)*, **1965**, 271.
23. Becker, D. F.; Kasper, J. S. *Acta Crystallogr.* **1957**, 10, 332.
24. Noël, H.; Padiou, J. *Acta Crystallogr.* **1976**, B32, 1593.
25. Jin, G. B.; Choi, E. S.; Guertin, R. P.; Brooks, J. S.; Booth, C. H.; Albrecht-Schmitt, T. E. *J. Solid State Chem.* in press.
26. Sheldrick, G. M. *SHELXTL PC, Version 6.12, An Integrated System for Solving, Refining, and Displaying Crystal Structures from Diffraction Data*; Siemens Analytical X-Ray Instruments, Inc.: Madison, WI 2001.
27. Sheldrick, G. M. *SADABS 2001, Program for absorption correction using SMART CCD based on the method of Blessing*; Blessing, R. H. *Acta Crystallogr.* **1995**, A51, 33.
28. Shannon, R. D. *Acta Crystallogr.* **1976**, A32, 751.
29. Mulay, L. N.; Boudreaux, E. A. *Theory and Applications of Molecular Diamagnetism*; Wiley-Interscience: New York, 1976.
30. Wendlandt, W. W.; Hecht, H. G. *Reflectance Spectroscopy*; Interscience Publishers: New York, 1966.
31. Kittel, C. *Introduction to Solid State Physics*, 6th Edition; Wiley: New York, 1986.

32. Prokofiev, A. V.; Shelykh, A. I.; Golubkov, A. V.; Smirnov, I. A. *J. Alloys Compd.* **1995**, 219, 172.
33. Prokofiev, A. V.; Shelykh, A. I.; Melekh, B. T. *J. Alloys Compd.* **1996**, 242, 41.

CHAPTER 8

SYNTHESES, STRUCTURE, MAGNETISM, AND OPTICAL PROPERTIES OF THE ORDERED INTERLANTHANIDE COPPER CHALCOGENIDES



ABSTRACT

$\text{Ln}_2\text{YbCuQ}_5$ (Ln = La, Ce, Pr, Nd, Sm; Q = S, Se) were prepared using Sb_2Q_3 (Q = S, Se) fluxes at 900 °C. The structure of $\text{Ln}_2\text{YbCuQ}_5$ (Ln = La, Ce, Pr, Nd, Sm; Q = S, Se) consists of one-dimensional $[\text{YbCuQ}_5]^{6-}$ ribbons extending along the b axis that are separated by larger Ln^{3+} ions. Each one-dimensional $[\text{YbCuQ}_5]^{6-}$ ribbon is constructed from two single $[\text{YbQ}_6]$ octahedral chains with one double $[\text{CuQ}_5]$ trigonal bipyramidal chain in the middle. All three chains connect with each other via edge sharing. Two crystallographically unique eight-coordinate Ln atoms, one octahedral Yb site, and two disordered Cu positions are found in the structure. These two Cu sites reside in the trigonal bipyramidal cavities formed by Q^{2-} anions. $\text{Ce}_2\text{YbCuSe}_5$, $\text{La}_2\text{YbCuS}_5$, $\text{Ce}_2\text{YbCuS}_5$, and $\text{Pr}_2\text{YbCuS}_5$ are Curie-Weiss paramagnets. $\text{La}_2\text{YbCuSe}_5$ and $\text{Nd}_2\text{YbCuS}_5$ have short-range antiferromagnetic ordering at low temperature. The band gaps of $\text{La}_2\text{YbCuSe}_5$, $\text{Ce}_2\text{YbCuSe}_5$, $\text{La}_2\text{YbCuS}_5$, $\text{Ce}_2\text{YbCuS}_5$, $\text{Pr}_2\text{YbCuS}_5$, $\text{Nd}_2\text{YbCuS}_5$, and

$\text{Sm}_2\text{YbCuS}_5$ are 1.15 eV, 1.05 eV, 1.45 eV, 1.37 eV, 1.25 eV, 1.35 eV, and 1.28 eV, respectively.

INTRODUCTION

Rare-earth copper chalcogenides have been the source of considerable interest not only because of their tunable structures and electronic properties, but also because of some unusual coordination geometries and oxidation states of copper that they exhibit.^{1-11, 19-39} High-temperature solid-state syntheses often produce thermodynamic products, in which there are no Q-Q (Q = S, Se, Te) bonds. They include LnCuQ_2 (Ln = rare-earth element, Sc, Y; Q = S, Se, Te),¹⁻¹¹ $\text{Ln}_{0.66}\text{Cu}_2\text{S}_2$ (Ln = Gd, Er),¹²⁻¹⁵ and Eu_2CuQ_3 (Q = S, Se).¹⁶⁻¹⁸ LnCuQ_2 compounds adopt at least three different structures (monoclinic, orthorhombic, and trigonal) depend on the relative size of Ln ions. Mixed-valence Eu_2CuQ_3 phases have Eu^{2+} and Eu^{3+} ions occupying two crystallographically independent sites and Eu_2CuS_3 ¹⁷ shows a ferromagnetic transition at 3.4K owing to the coupling of Eu^{2+} ions. Kinetic products, in which polychalcogenides can exist, can be prepared using alkali-metal/lanthanide halide fluxes or reactive fluxes, thereby allowing for lower reaction temperatures. Examples include La_2CuS_4 ,²⁰ Sm_3CuSe_6 ,^{21,22} $\text{EuCu}_{0.66}\text{Te}_2$,²³ $\text{Gd}_3\text{Cu}_2\text{Te}_7$,²⁴ $\text{LaCu}_{0.28}\text{Te}_2$,²⁵ and LnCu_xTe_2 (Ln = La, Nd, Sm, Gd and Dy).²⁶ La_2CuS_4 features unusual discrete $[\text{S}_3\text{Cu}\cdots\text{S}-\text{S}\cdots\text{CuS}_3]$ ¹²⁻ units, which contain two nearly planar $[\text{CuS}_3]$ ⁵⁻ triangles bridged by a disulfide anions. $\text{EuCu}_{0.66}\text{Te}_2$ contains a flat square net of Te atoms, while all the latter three have linear Te chains.

Partial substitutions of chalcogenides have been tried to access new phases with different physical properties from the parent ternary phase LnCuQ_2 , e.g. LaCuSTe ²⁷ and

SmCuSTe.²⁷ Lanthanide copper oxychalcogenides including LnCuOQ (Ln = La, Ce, Pr, Nd; Q = S, Se, Te),²⁸⁻³⁸ La₅Cu₆O₄S₇,³⁹ and La₃CuO₂S₃⁴⁰ have been extensively studied. LnCuOQ adopt a structure with alternately stacking PbO-like [Cu₂Q₂]²⁻ layers and anti-PbO-like [Ln₂O₂]²⁺ layers, which is similar to that of copper-based high-T_c superconducting oxides. LaCuOQ are wide band gap *p*-type semiconductors, and are considered as potential transparent conductive materials. In contrast, La₅Cu₆O₄S₇ is metallic and the average oxidation state of the Cu atoms is +7/6.

To our knowledge, EuLnCuS₃ (Ln = Y, Gd-Lu)¹⁹ are the only known examples of interlanthanide copper chalcogenides, which were made by replacing the Eu³⁺ ions in Eu₂CuS₃ compound using other trivalent Ln atoms. The purpose of this study is to prepare new ordered quaternary interlanthanide copper chalcogenides phases by including two Ln atoms from opposite ends of lanthanide series, which tend to have different coordination geometries. Here we present the syntheses, structure, optical, and magnetic properties of new quaternary interlanthanide copper chalcogenides, Ln₂YbCuQ₅ (Ln = La, Ce, Pr, Nd, Sm; Q = S, Se).

EXPERIMENTAL

Starting Materials. La (99.9%, Alfa-Aesar), Ce (99.9%, Alfa-Aesar), Pr (99.9%, Alfa-Aesar), Nd (99.9%, Alfa-Aesar), Sm (99.9%, Alfa-Aesar), Yb (99.9%, Alfa-Aesar), Se (99.5%, Alfa-Aesar), S (99.5%, Alfa-Aesar), and Sb (99.5%, Alfa-Aesar) were used as received. The Sb₂Q₃ (Q = S, Se) fluxes were prepared from the direct reaction of the elements in sealed fused-silica ampoules at 850 °C.

Syntheses. Ln₂YbCuQ₅ (Ln = La, Ce, Pr, Nd, Sm; Q = S, Se) were prepared

using Sb_2Q_3 (Q = S, Se) fluxes. 150 mg of Ln, Yb, Cu, and S were stoichiometrically mixed with 0.075 mg Sb_2Q_3 into fused-silica ampoules in an Ar-filled glovebox. The ampoules were sealed under vacuum and placed in a programmable tube furnace. The following heating profile was used: 2 °C/min to 500 °C (held for 1 h), 0.5 °C/min to 900 °C (held for 7 d), 0.04 °C/min to 500 °C (held for 2 d), and 0.5 °C/min to 24 °C. In each reaction the major phases included high yields of black crystals of desired products and unreacted Sb_2Q_3 lying in the bottom of the tubes. Powder X-ray diffraction measurements were used to confirm phase purity by comparing the powder patterns calculated from the single-crystal X-ray structures with the experimental data. Semi-quantitative SEM/EDX analyses were performed using JEOL 840/Link Isis or JEOL JSM-7000F instruments. Ln, Yb, Cu, and Q percentages were calibrated against standards. Sb was not detected in the crystals. The Ln:Yb:Cu:S ratios were determined to be approximately 2:1:1:5 from EDX analyses.

Crystallographic Studies. Single crystals of $\text{Ln}_2\text{YbCuQ}_5$ (Ln = La, Ce, Pr, Nd, Sm; Q = S, Se) were mounted on glass fibers with epoxy and optically aligned on a Bruker APEX single crystal X-ray diffractometer using a digital camera. Initial intensity measurements were performed using graphite-monochromated Mo $\text{K}\alpha$ ($\lambda = 0.71073 \text{ \AA}$) radiation from a sealed tube and monocapillary collimator. SMART (v 5.624) was used for preliminary determination of the cell constants and data collection control. The intensities of reflections of a sphere were collected by a combination of 3 sets of exposures (frames). Each set had a different ϕ angle for the crystal and each exposure covered a range of 0.3° in ω . A total of 1800 frames were collected with exposure times per frame of 10 or 20 seconds depending on the crystal.

For $\text{Ln}_2\text{YbCuQ}_5$ ($\text{Ln} = \text{La, Ce, Pr, Nd, Sm}$; $\text{Q} = \text{S, Se}$), determination of integrated intensities and global refinement were performed with the Bruker SAINT (v 6.02) software package using a narrow-frame integration algorithm. These data were treated first with a face-indexed numerical absorption correction using XPREP,⁴¹ followed by a semi-empirical absorption correction using SADABS.⁴² The program suite SHELXTL (v 6.12) was used for space group determination (XPREP), direct methods structure solution (XS), and least-squares refinement (XL).⁴¹ The final refinements included anisotropic displacement parameters for all atoms and secondary extinction. Some crystallographic details are given in Table 8.1. As an example, atomic coordinates and equivalent isotropic displacement parameters for $\text{La}_2\text{YbCuS}_5$ are given in Table 8.2.

Powder X-ray Diffraction. Powder X-ray diffraction patterns were collected with a Rigaku Miniflex powder X-ray diffractometer using $\text{Cu K}\alpha$ ($\lambda = 1.54056 \text{ \AA}$) radiation.

Magnetic Susceptibility Measurements. Magnetic data were measured on powders in gelcap sample holders with a Quantum Design MPMS 7T magnetometer/susceptometer between 2 and 300 K and in applied fields up to 7 T. DC susceptibility measurements were made under zero-field-cooled conditions with an applied field of 0.1 T. Susceptibility values were corrected for the sample diamagnetic contribution according to Pascal's constants⁴³ as well as for the sample holder diamagnetism. θ_p values were obtained from extrapolations from fits between 100 to 300 K. (Magnetic susceptibility measurements were performed by Eun Sang Choi and James S. Brooks at Florida State University)

Table 8.1. Crystallographic Data for Ln₂YbCuQ₅ (Ln = La, Ce, Pr, Nd, Sm; Q = S, Se).

| Formula | La ₂ YbCuSe ₅ | Ce ₂ YbCuSe ₅ | La ₂ YbCuS ₅ | Ce ₂ YbCuS ₅ | Pr ₂ YbCuS ₅ | Nd ₂ YbCuS ₅ | Sm ₂ YbCuS ₅ |
|--|-------------------------------------|-------------------------------------|------------------------------------|------------------------------------|------------------------------------|------------------------------------|------------------------------------|
| fw | 909.20 | 911.62 | 674.70 | 677.12 | 678.70 | 685.36 | 697.58 |
| Color | black | black | black | black | black | black | black |
| Crystal System | orthorhombic | orthorhombic | orthorhombic | orthorhombic | orthorhombic | orthorhombic | orthorhombic |
| Space group | <i>Pnma</i> (No. 62) | <i>Pnma</i> (No. 62) | <i>Pnma</i> (No. 62) | <i>Pnma</i> (No. 62) | <i>Pnma</i> (No. 62) | <i>Pnma</i> (No. 62) | <i>Pnma</i> (No. 62) |
| a (Å) | 12.1326(11) | 12.1113(7) | 11.615(4) | 11.5616(13) | 11.547(2) | 11.5466(8) | 11.5323(8) |
| b (Å) | 4.1119(4) | 4.0780(3) | 3.9662(13) | 3.9304(4) | 3.9071(8) | 3.8927(3) | 3.8531(3) |
| c (Å) | 17.6653(16) | 17.5714(11) | 16.923(6) | 16.8423(18) | 16.795(3) | 16.7597(11) | 16.6470(12) |
| V (Å ³) | 881.29(14) | 867.85(10) | 779.6(5) | 765.34(14) | 757.7(3) | 753.31(9) | 739.71(9) |
| Z | 4 | 4 | 4 | 4 | 4 | 4 | 4 |
| T (K) | 193 | 193 | 193 | 193 | 193 | 193 | 193 |
| λ (Å) | 0.71073 | 0.71073 | 0.71073 | 0.71073 | 0.71073 | 0.71073 | 0.71073 |
| ρ _{calcd} (g cm ⁻³) | 6.853 | 6.977 | 5.748 | 5.877 | 5.950 | 6.043 | 6.264 |
| μ (cm ⁻¹) | 429.51 | 442.61 | 265.47 | 277.73 | 28.8.98 | 299.16 | 323.04 |
| R(F) ^a | 0.0369 | 0.0290 | 0.0261 | 0.0242 | 0.0317 | 0.0250 | 0.0263 |
| R _w (F _o ²) ^b | 0.0966 | 0.0757 | 0.0628 | 0.0588 | 0.0736 | 0.0566 | 0.0665 |

$$^a R(F) = \frac{\sum \|F_o\| - |F_c|}{\sum \|F_o\|} \text{ for } F_o^2 > 2\sigma(F_o^2). \quad ^b R_w(F_o^2) = \left[\frac{\sum [w(F_o^2 - F_c^2)^2]}{\sum wF_o^4} \right]^{1/2}.$$

Table 8.2. Atomic Coordinates and Equivalent Isotropic Displacement Parameters for $\text{La}_2\text{YbCuS}_5$.

| Atom (site) | x | y | z | $U_{\text{eq}} (\text{\AA}^2)^a$ |
|-------------|-------------|-------|-------------|----------------------------------|
| La(1) | 0.97977(4) | -0.25 | 0.82545(3) | 0.00691(14) |
| La(2) | 0.86754(4) | 0.25 | 0.40038(3) | 0.00686(14) |
| Yb(1) | 0.80240(3) | 0.25 | 0.63683(2) | 0.01060(13) |
| Cu(1) | 0.6657(2) | -0.25 | 0.51632(13) | 0.0144(4) |
| Cu(2) | 0.5960(3) | -0.25 | 0.50288(17) | 0.0177(6) |
| S(1) | 1.01210(17) | 0.25 | 0.69895(13) | 0.0066(4) |
| S(2) | 0.81356(17) | -0.75 | 0.88370(13) | 0.0072(4) |
| S(3) | 0.88403(18) | -0.25 | 0.53444(13) | 0.0104(4) |
| S(4) | 0.59555(18) | 0.25 | 0.57265(13) | 0.0084(4) |
| S(5) | 0.73861(18) | -0.25 | 0.72916(13) | 0.0076(4) |

^a U_{eq} is defined as one-third of the trace of the orthogonalized U_{ij} tensor.

UV-vis-NIR Diffuse Reflectance Spectroscopy. The diffuse reflectance spectra for $\text{Ln}_2\text{YbCuQ}_5$ ($\text{Ln} = \text{La, Ce, Pr, Nd, Sm}$; $\text{Q} = \text{S, Se}$) were measured from 200 to 2500 nm using a Shimadzu UV3100 spectrophotometer equipped with an integrating sphere attachment. The Kubelka-Munk function was used to convert diffuse reflectance data to absorption spectra.⁴⁴

RESULTS AND DISCUSSION

Structures of $\text{Ln}_2\text{YbCuQ}_5$ ($\text{Ln} = \text{La, Ce, Pr, Nd, Sm}$; $\text{Q} = \text{S, Se}$). The compounds $\text{Ln}_2\text{YbCuQ}_5$ ($\text{Ln} = \text{La, Ce, Pr, Nd, Sm}$; $\text{Q} = \text{S, Se}$) are isotypic and crystallize in the centrosymmetric orthorhombic space group $Pnma$. As illustrated in Figure 8.1, the structure can be described as composed of one-dimensional $[\text{YbCuQ}_5]^{6-}$ ribbons running down the $[010]$ direction and are separated by Ln^{3+} ions. It includes two crystallographically unique Ln atoms, one octahedral Yb site, and two Cu positions. The polyhedra of Ln and Cu atoms are shown in Figure 8.2 and 8.3. Both Ln^{3+} are eight-coordinate and occur as bicapped trigonal prisms. Two Cu atoms are very close to each other with the Cu(1)-Cu(2) distance being 0.841(3) Å in case of $\text{La}_2\text{YbCuS}_5$ (see Table 8.3). Obviously, these two sites cannot be occupied simultaneously. The occupancy of Cu(1) ranges from 0.19 to 0.54. Each Cu has a highly distorted tetrahedral environment. For example, the four Cu(1)-S distances for $\text{La}_2\text{YbCuS}_5$ are 2.257(3) Å, 2.3464(18) Å, 2.3464(18) Å, and 2.544(4) Å, and S-Cu(1)-S angles are in the range 90.78(11)-116.16(8)° (see Table 8.3). These bond distances are closer to the average values for Cu with triangular coordination (e.g. 2.33 Å in $\text{Cu}_2\text{S}^{45,46}$) than the ones for Cu with tetrahedral coordination (2.44 Å, according to Shannon⁴⁷). This similar

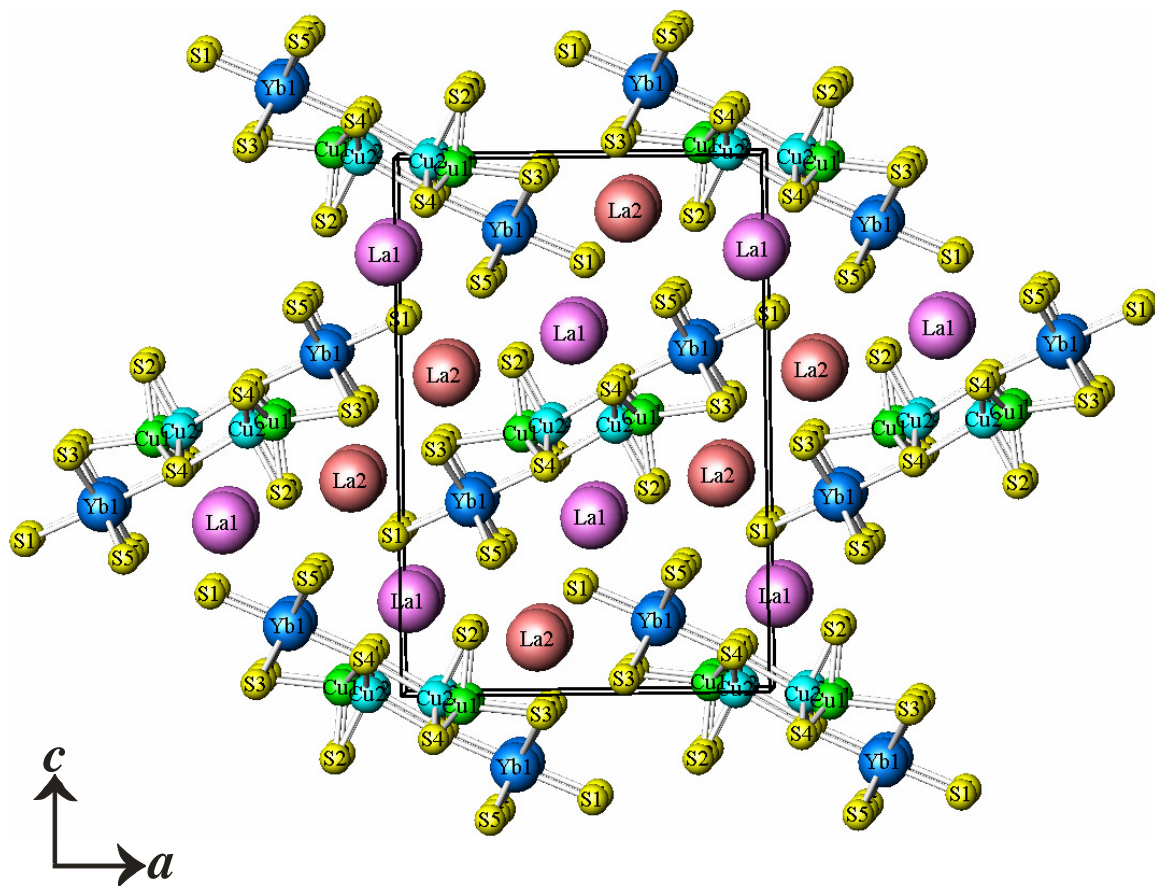


Figure 8.1. A view the three-dimensional structure of $\text{La}_2\text{YbCuS}_5$ along the b axis. La-S bonds have been omitted for clarity.

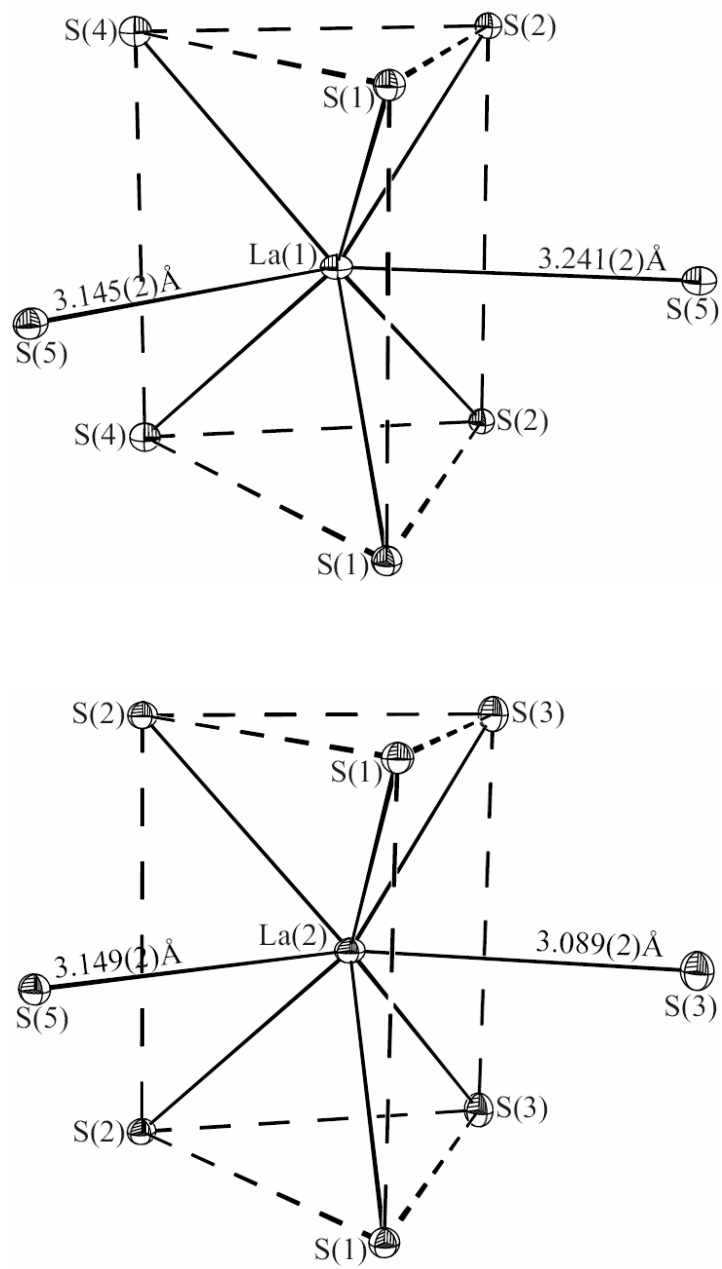


Figure 8.2. Illustrations of the coordination environments for La ions in $\text{La}_2\text{YbCuS}_5$.

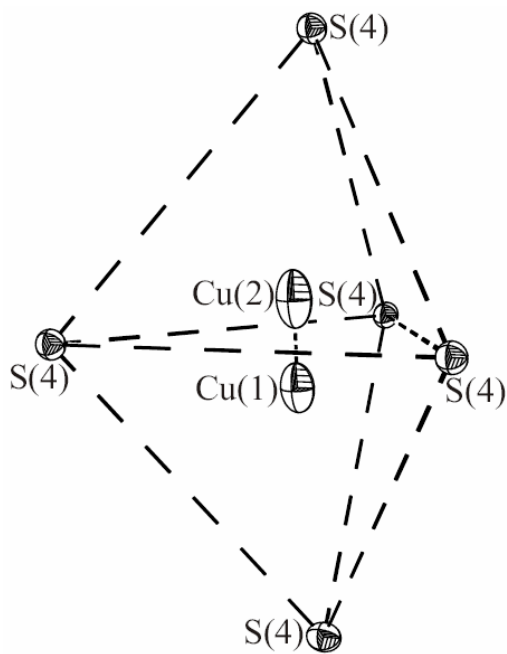
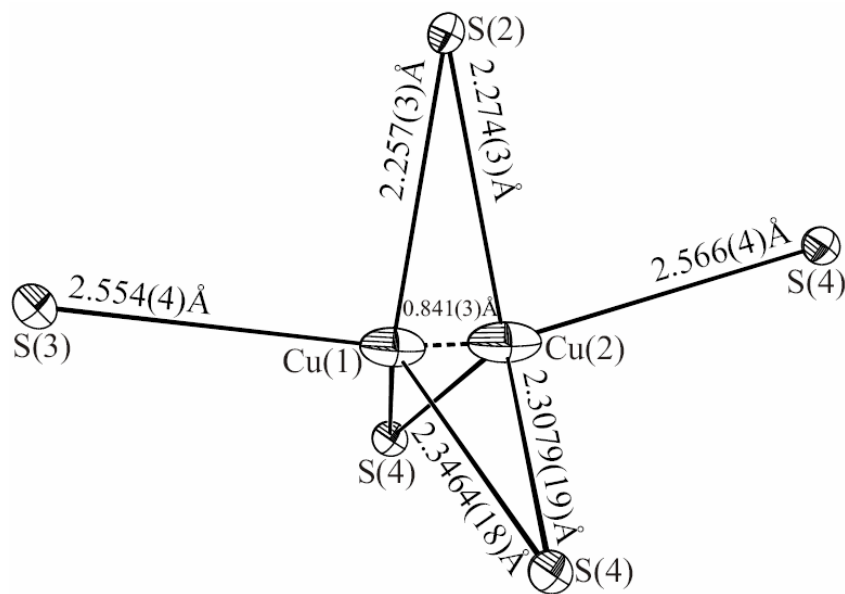


Figure 8.3. Illustrations of the coordination environments for Cu ions in $\text{La}_2\text{YbCuS}_5$.

Table 8.3. Selected Bond Distances (Å) and angles (deg) for Ln₂YbCuQ₅ (Ln = La, Ce, Pr, Nd, Sm; Q = S, Se).

| Formula | La ₂ YbCuSe ₅ | Ce ₂ YbCuSe ₅ | La ₂ YbCuS ₅ | Ce ₂ YbCuS ₅ | Pr ₂ YbCuS ₅ | Nd ₂ YbCuS ₅ | Sm ₂ YbCuS ₅ |
|---------------|-------------------------------------|-------------------------------------|------------------------------------|------------------------------------|------------------------------------|------------------------------------|------------------------------------|
| Ln(1)-Q(1) ×2 | 3.0560(12) | 3.0293(8) | 2.9421(18) | 2.9108(15) | 2.894(2) | 2.8834(16) | 2.8574(17) |
| Ln(1)-Q(2) ×2 | 3.0613(12) | 3.0428(9) | 2.9380(17) | 2.9185(16) | 2.899(2) | 2.8959(16) | 2.8691(18) |
| Ln(1)-Q(4) ×2 | 3.0701(13) | 3.0462(9) | 2.9522(18) | 2.9280(16) | 2.908(2) | 2.8969(17) | 2.8689(18) |
| Ln(1)-Q(5) | 3.2994(18) | 3.2871(12) | 3.145(2) | 3.150(2) | 3.150(3) | 3.110(2) | 3.017(2) |
| Ln(1)-Q(5) | 3.3571(18) | 3.3352(12) | 3.241(2) | 3.188(2) | 3.171(3) | 3.201(2) | 3.268(2) |
| Ln(2)-Q(1) ×2 | 3.0678(12) | 3.0368(8) | 2.9518(17) | 2.9234(15) | 2.909(2) | 2.8954(16) | 2.8620(17) |
| Ln(2)-Q(2) ×2 | 3.0231(12) | 3.0037(8) | 2.9046(16) | 2.8820(16) | 2.872(2) | 2.8597(16) | 2.8373(17) |
| Ln(2)-Q(3) ×2 | 3.1265(13) | 3.1107(9) | 3.0193(19) | 2.9998(17) | 2.975(2) | 2.9587(18) | 2.9345(19) |
| Ln(2)-Q(3) | 3.2154(17) | 3.1962(12) | 3.089(2) | 3.064(2) | 3.050(3) | 3.046(2) | 3.023(2) |
| Ln(2)-Q(5) | 3.2789(17) | 3.2486(12) | 3.149(2) | 3.116(2) | 3.104(3) | 3.096(2) | 3.067(2) |
| Yb(1)-Q(1) | 2.7830(16) | 2.7696(11) | 2.653(2) | 2.644(2) | 2.646(3) | 2.648(2) | 2.645(2) |
| Yb(1)-Q(3) ×2 | 2.9185(12) | 2.8951(8) | 2.7989(17) | 2.7824(16) | 2.780(2) | 2.7769(17) | 2.7543(18) |
| Yb(1)-Q(4) | 2.7597(16) | 2.7547(11) | 2.637(2) | 2.630(2) | 2.631(3) | 2.633(2) | 2.632(2) |

| | | | | | | | |
|-----------------|------------|------------|------------|------------|------------|------------|------------|
| Yb(1)-Q(5) ×2 | 2.7572(11) | 2.7538(7) | 2.6311(16) | 2.6274(14) | 2.625(2) | 2.6240(15) | 2.6193(16) |
| Cu(1)-Q(2) | 2.380(4) | 2.360(4) | 2.257(3) | 2.244(3) | 2.238(5) | 2.226(4) | 2.205(7) |
| Cu(1)-Q(3) | 2.583(4) | 2.591(4) | 2.554(4) | 2.556(4) | 2.567(6) | 2.610(6) | 2.656(11) |
| Cu(1)-Q(4) ×2 | 2.466(2) | 2.468(2) | 2.3464(18) | 2.3459(18) | 2.351(3) | 2.347(3) | 2.345(5) |
| Cu(2)-Q(2) | 2.404(4) | 2.404(2) | 2.274(3) | 2.277(3) | 2.278(4) | 2.287(3) | 2.281(3) |
| Cu(2)-Q(4) ×2 | 2.405(2) | 2.4142(13) | 2.3079(19) | 2.3018(16) | 2.302(2) | 2.3043(16) | 2.3081(16) |
| Cu(2)-Q(4) | 2.590(5) | 2.564(3) | 2.566(4) | 2.526(4) | 2.516(5) | 2.502(3) | 2.497(3) |
| Q(2)-Cu(1)-Q(3) | 92.51(13) | 91.59(13) | 90.78(11) | 90.12(12) | 89.30(19) | 87.47(17) | 85.4(3) |
| Q(2)-Cu(1)-Q(4) | 114.14(10) | 115.09(10) | 116.16(8) | 116.85(9) | 117.52(14) | 118.66(12) | 120.2(2) |
| Q(3)-Cu(1)-Q(4) | 110.67(11) | 111.07(11) | 107.23(9) | 107.82(10) | 108.37(16) | 107.91(15) | 107.9(3) |
| Q(4)-Cu(1)-Q(4) | 112.93(15) | 111.39(15) | 115.38(13) | 113.80(14) | 112.4(2) | 112.06(18) | 110.5(3) |
| Q(2)-Cu(2)-Q(4) | 88.36(14) | 87.97(8) | 87.63(13) | 87.19(11) | 86.47(14) | 86.25(10) | 85.45(10) |
| Q(2)-Cu(2)-Q(4) | 115.55(11) | 115.49(6) | 117.06(9) | 117.29(8) | 117.88(10) | 117.92(8) | 118.57(7) |
| Q(4)-Cu(2)-Q(4) | 107.53(13) | 109.48(7) | 104.63(11) | 105.60(10) | 106.04(12) | 106.82(9) | 108.07(8) |
| Q(4)-Cu(1)-Q(4) | 117.45(19) | 115.26(10) | 118.47(16) | 117.24(13) | 116.09(18) | 115.27(13) | 113.16(12) |

feature of Cu atoms have been found in other lanthanide copper chalcogenides including Sm_3CuSe_6 ,^{21,22} $\text{Gd}_3\text{Cu}_2\text{Te}_7$,²⁴ $\text{LaCu}_{0.28}\text{Te}_2$,²⁵ and LnCu_xTe_2 ($\text{Ln} = \text{La}, \text{Nd}, \text{Sm}, \text{Gd}$ and Dy),²⁶ in which two disordered Cu sites are equivalent and the tetrahedra are less distorted. In order to better describe the connectivity among the polyhedra, Cu(1) and Cu(2) atoms are considered as one average Cu site sitting in the cavities of a distorted trigonal bipyramid, as shown in Figure 8.3. Then the one-dimensional $[\text{YbCuQ}_5]^{6-}$ ribbons, which are shown Figure 8.4a, consist of two single $[\text{YbQ}_6]$ octahedral chains with one double $[\text{CuQ}_5]$ trigonal bipyramidal chain in the middle. All three chains connect with each other via edge sharing. Within the $[\text{YbQ}_6]$ octahedral chain, each unit shares edges with two neighbors along the chain direction, while each $[\text{CuQ}_5]$ trigonal bipyramid shares corner along the *b* axis and shares edge with adjacent identical chains. The connectivity of $[\text{CuQ}_5]$ trigonal bipyramids in these compounds is quite different from other known examples. For $\text{Gd}_3\text{Cu}_2\text{Te}_7$,²⁴ the $[\text{CuTe}_5]$ trigonal bipyramids share corners with four $[\text{CuTe}_4]$ tetrahedra within two-dimensional $[\text{Cu}_2\text{Te}_5]$ layers (Figure 8.4b). In Figure 8.4c, $[\text{CuSe}_5]$ trigonal bipyramids in compound Sm_3CuSe_6 ²¹ shares edges to form one-dimensional single chains along the $[010]$ direction, while Figure 8.4d shows a two-dimensional $[\text{Cu}_x\text{Te}_2]$ layer of $\text{LaCu}_{0.28}\text{Te}_2$ ²⁵ or LnCu_xTe_2 ($\text{Ln} = \text{La}, \text{Nd}, \text{Sm}, \text{Gd}$ and Dy)²⁶, constructed from $[\text{CuTe}_5]$ trigonal bipyramids sharing edges with four close neighbors and sharing corners with other four bipyramidal units.

It is noted that $\text{La}_3\text{CuO}_2\text{S}_3$ ⁴⁰ adopts similar formula, condensed three-dimensional structure, and space group as $\text{Ln}_2\text{YbCuQ}_5$ ($\text{Ln} = \text{La}, \text{Ce}, \text{Pr}, \text{Nd}, \text{Sm}$; $\text{Q} = \text{S}, \text{Se}$). But the structure of $\text{La}_3\text{CuO}_2\text{S}_3$, which is illustrated in Figure 8.5, has three eight-coordinate La^{3+} ions with bicapped trigonal prismatic geometry and one ordered tetrahedral

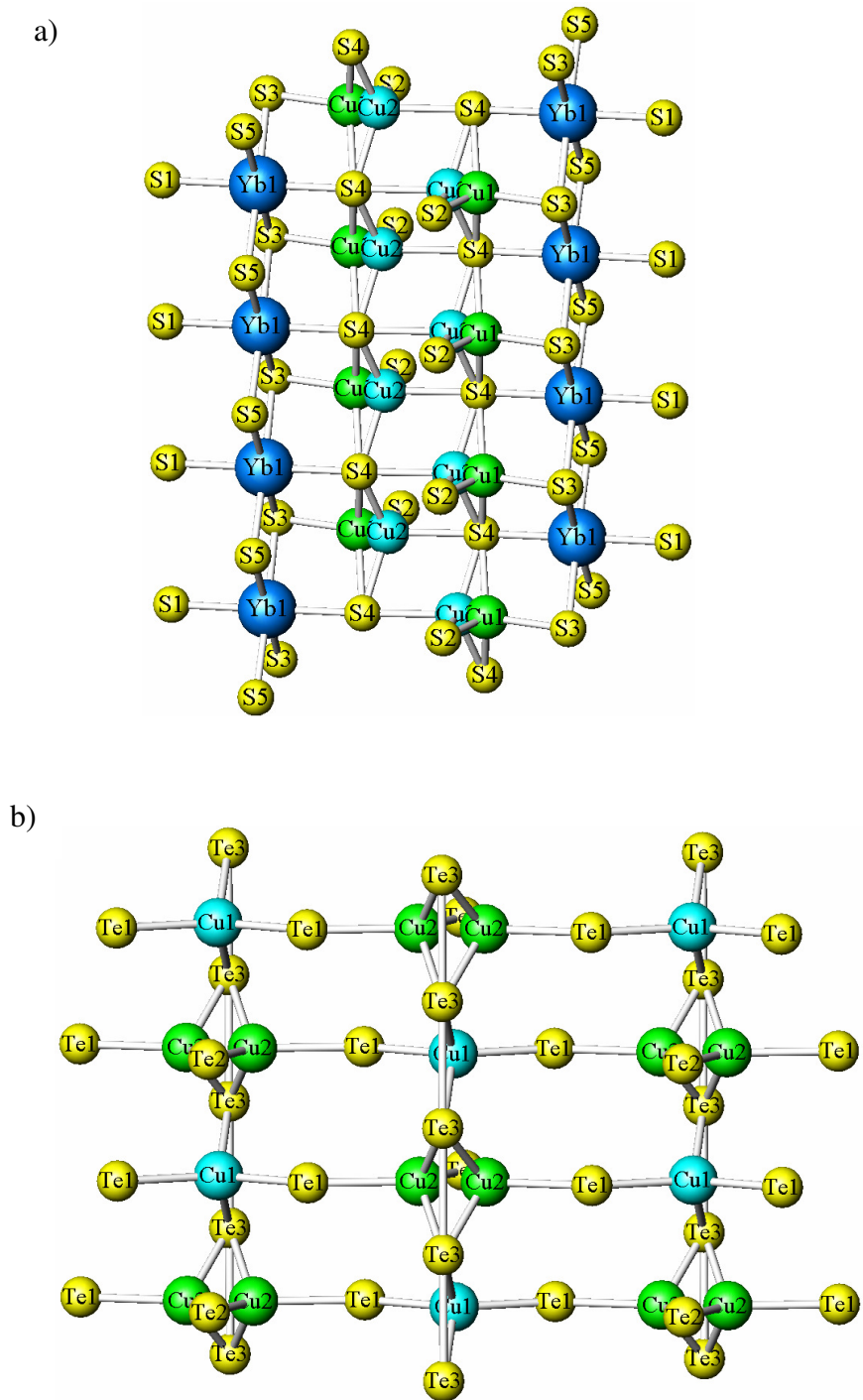


Figure 8.4. Depictions of various connectivities of $[\text{CuQ}_5]$ ($\text{Q} = \text{S}, \text{Se}, \text{Te}$) trigonal bipyramids in different compounds: a) $\text{La}_2\text{YbCuS}_5$; b) $\text{Gd}_3\text{Cu}_2\text{Te}_7$ ²⁴; c) Sm_3CuSe_6 ²¹; d) $\text{LaCu}_{0.28}\text{Te}_2$ ²⁵.

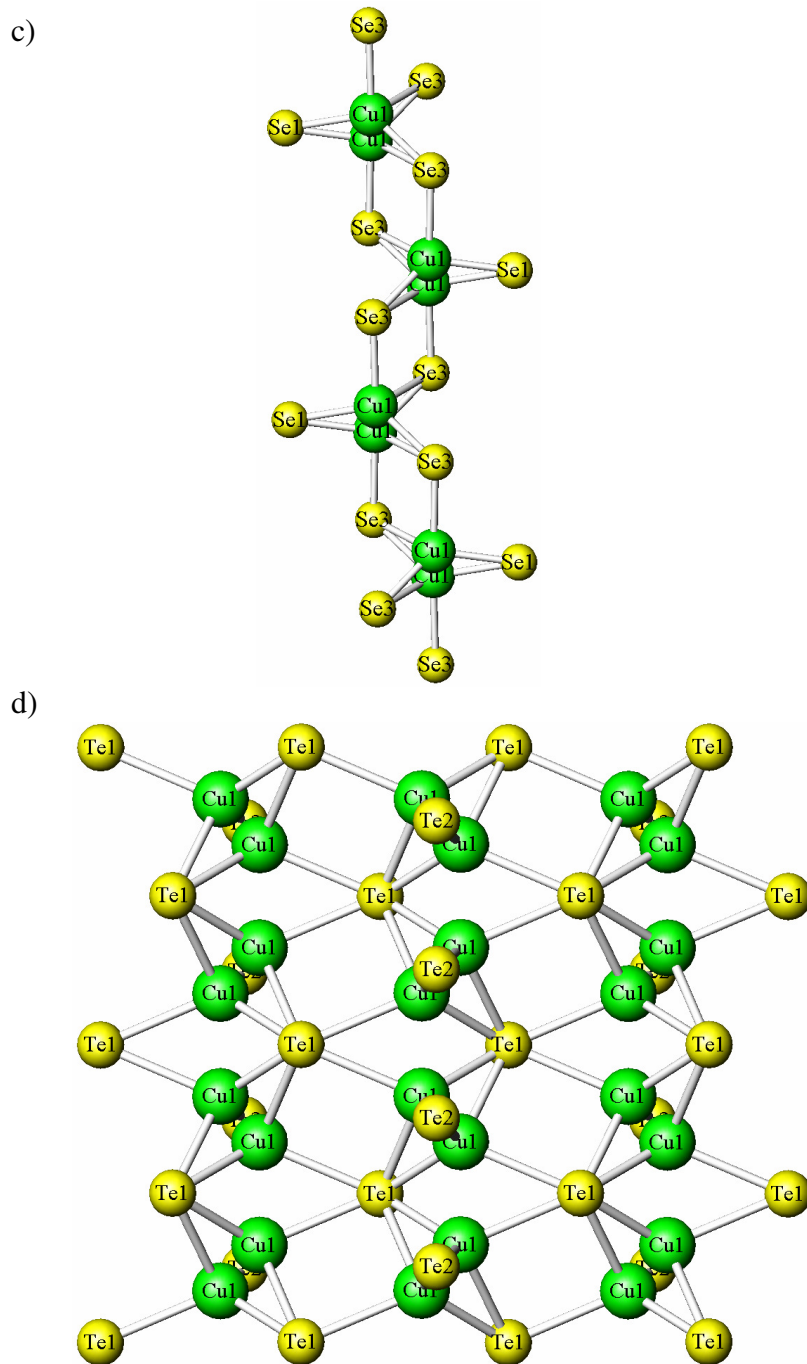


Figure 8.4. Depictions of various connectivities of $[\text{CuQ}_5]$ ($\text{Q} = \text{S}, \text{Se}, \text{Te}$) trigonal bipyramids in different compounds: a) $\text{La}_2\text{YbCuS}_5$; b) $\text{Gd}_3\text{Cu}_2\text{Te}_7$ ²⁴; c) Sm_3CuSe_6 ²¹; d) $\text{LaCu}_{0.28}\text{Te}_2$ ²⁵.

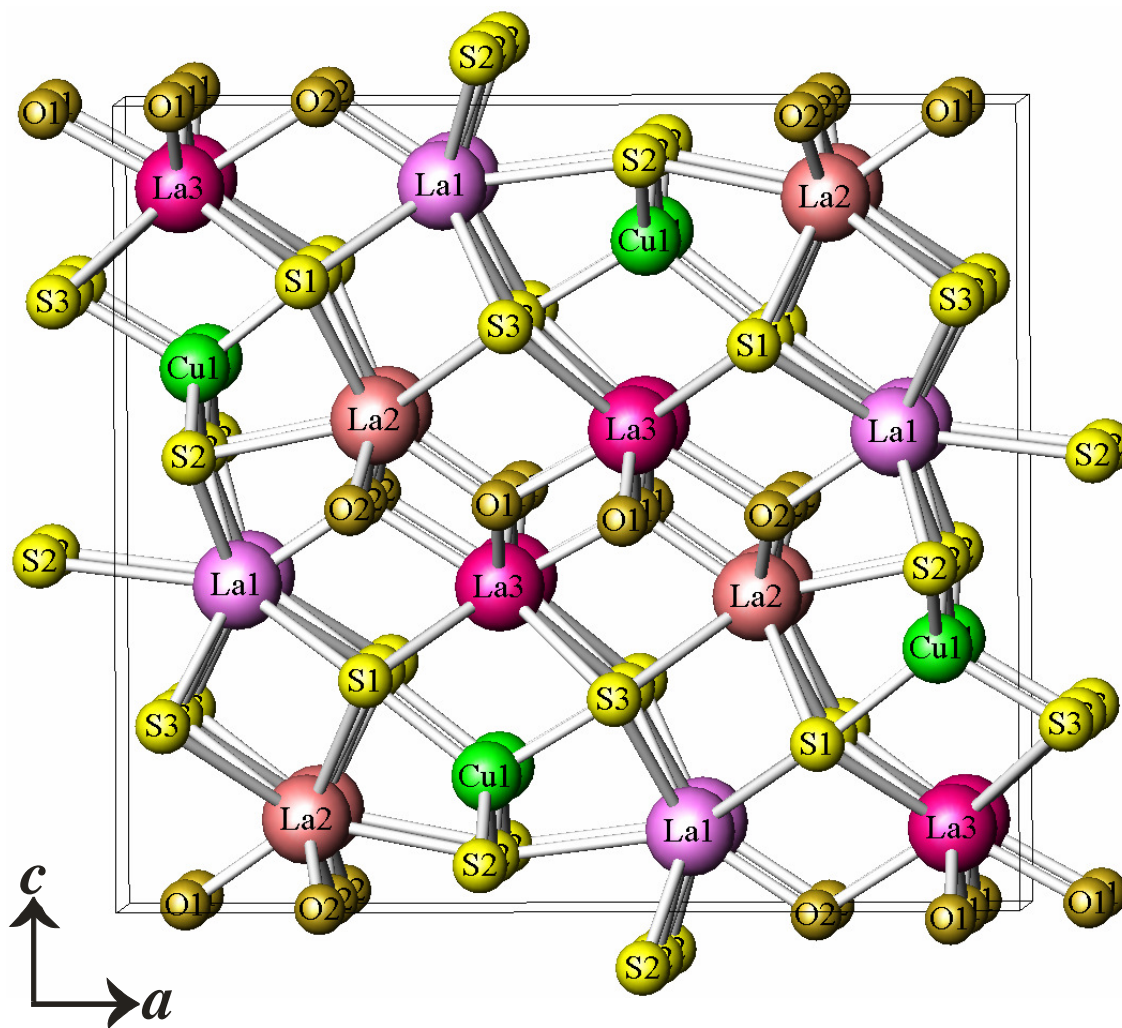


Figure 8.5. Unit cell of $\text{La}_3\text{CuO}_2\text{S}_3$ ⁴⁰ viewed along the b axis.

Cu⁺ site. It has higher symmetry in terms of [CuS₄] tetrahedra. The bond distances of LnQ₈ and YbQ₆ for Ln₂YbCuQ₅ (Ln = La, Ce, Pr, Nd, Sm; Q = S, Se) are normal, shown in Table 8.3. For example, in case of La₂YbCuS₅, La-S distances range from 2.9046(16) Å to 3.241(2) Å and Yb-S distances are in the range of 2.6311(16) Å to 2.7989(17) Å. They are comparable to Shannon's data,⁴⁷ 3.00 Å for LaS₈ and 2.70 Å for YbS₆. Since there are no Q-Q bonds and Cu-Cu interactions, the oxidation states of Ln₂YbCuQ₅ can be assigned as +3/+3/+1/-2.

Magnetic Susceptibility. The inverse molar Ln magnetic susceptibilities for Ln₂YbCuQ₅ (Ln = La, Ce, Pr, Nd; Q = S, Se) in the range of 2-300 K are shown in Figure 8.6-8.8. All of three compounds show deviation from the Curie-Weiss law around 70 K. This could be due to the crystal-field splitting of the ground state of magnetic ions. There is no evidence of magnetic ordering for Ce₂YbCuSe₅, La₂YbCuS₅, Ce₂YbCuS₅, and Pr₂YbCuS₅. In contrast, the magnetic susceptibilities for La₂YbCuSe₅ and Nd₂YbCuS₅ show gradual changes in the slope at low temperature, which may indicate the short-range antiferromagnetic ordering. Magnetic measurements have shown that Sm₂YbCuS₅ exhibits spin glass behavior below 7 K. In order to draw a conclusion, further investigations, e.g. heat capacity measurements, are underway. Therefore the magnetic properties of Sm₂YbCuS₅ will not be discussed here. Table 8.4 presents the magnetic parameters that were determined from the fit from the Curie-Weiss regions. The Weiss constants for these compounds are all quite negative; that might be due to the crystal field effect as well. The experimental effective magnetic moments per formula unit are very close to the theoretical values based on the free Ln³⁺ ions.⁵²

Optical Properties. The electronic structures of interlanthanide copper

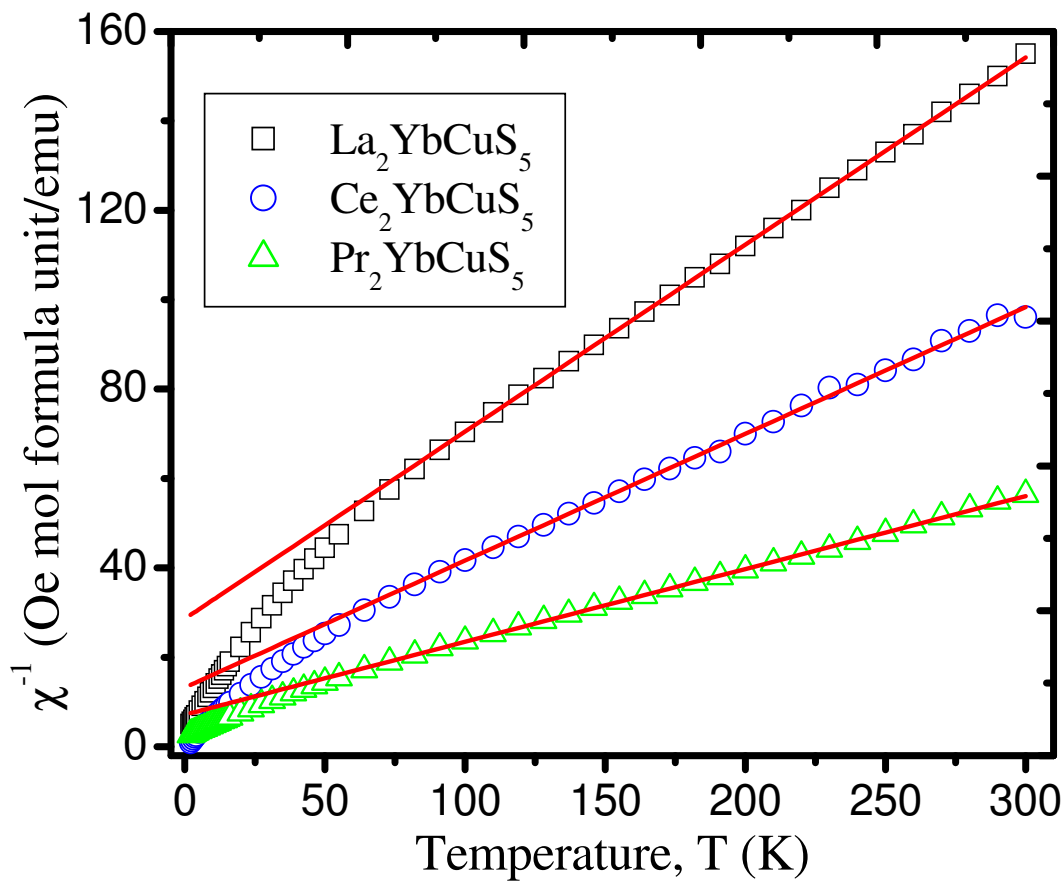


Figure 8.6. Molar magnetic susceptibility vs temperature between 2 and 300 K for $\text{La}_2\text{YbCuS}_5$, $\text{Ce}_2\text{YbCuS}_5$, and $\text{Pr}_2\text{YbCuS}_5$. Data were taken under an applied magnetic field of 0.1 T. The straight line represents the fit to Curie-Weiss law in the range of 100-300 K.

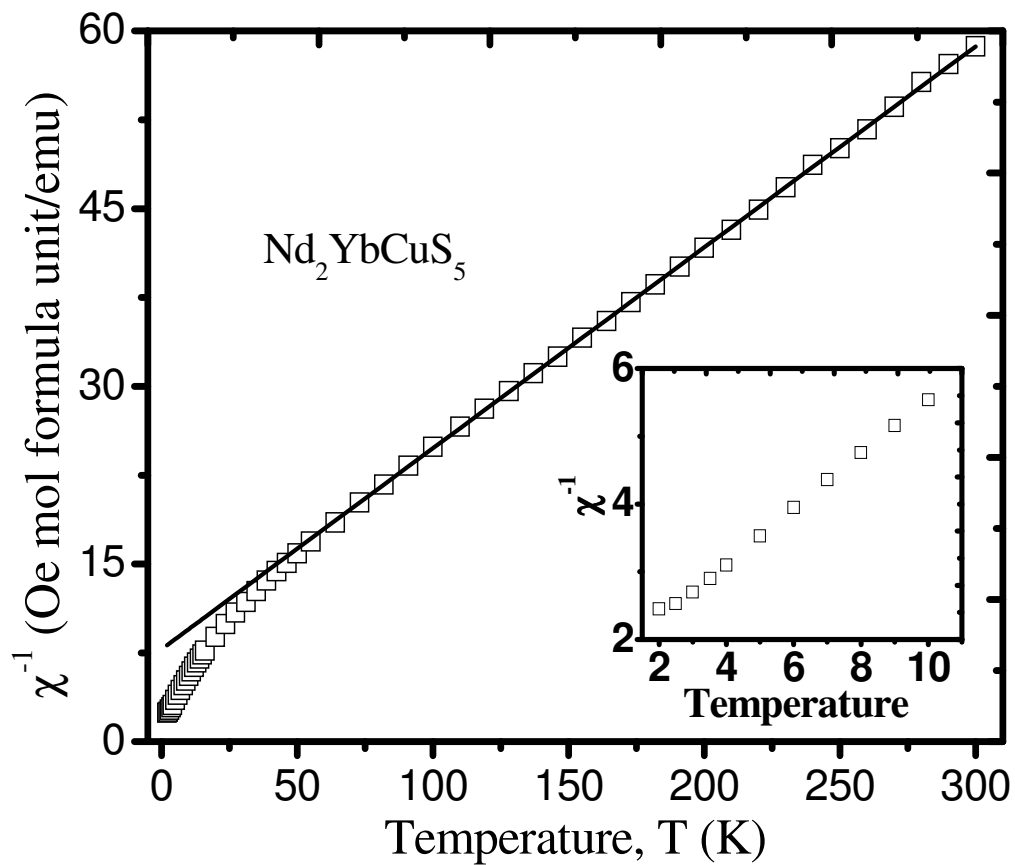


Figure 8.7. The temperature dependence of the reciprocal molar magnetic susceptibility for $\text{Nd}_2\text{YbCuS}_5$ under an applied magnetic field of 0.1 T between 2 and 300 K. Inset shows the molar magnetic susceptibility at low temperature.

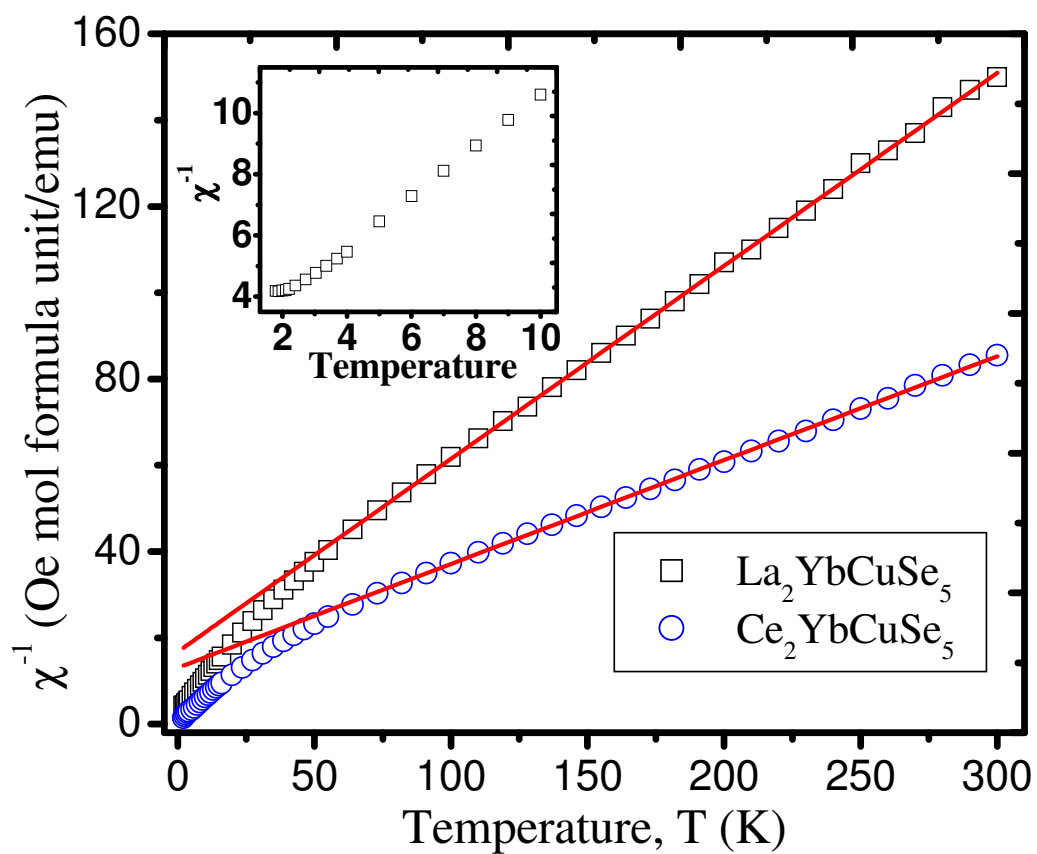


Figure 8.8. Molar magnetic susceptibility as a function of temperature for $\text{La}_2\text{YbCuSe}_5$ and $\text{Ce}_2\text{YbCuSe}_5$ under an applied magnetic field of 0.1 T between 2 and 300 K. Inset shows the molar magnetic susceptibility for $\text{La}_2\text{YbCuSe}_5$ at low temperature.

Table 8.4. Magnetic Parameters for $\text{Ln}_2\text{YbCuQ}_5$ ($\text{Ln} = \text{La, Ce, Pr, Nd, Sm}$; $\text{Q} = \text{S, Se}$).

| Formula | $P_{\text{cal}}/\mu_{\text{B}}$ | $P_{\text{eff}}/\mu_{\text{B}}$ | θ_{p} | R^2 |
|------------------------------|---------------------------------|---------------------------------|---------------------|---------|
| $\text{La}_2\text{YbCuSe}_5$ | 4.54 | 4.229(9) | -38(1) | 0.99959 |
| $\text{Ce}_2\text{YbCuSe}_5$ | 5.79 | 5.76(1) | -54(1) | 0.99962 |
| $\text{La}_2\text{YbCuS}_5$ | 4.54 | 4.372(6) | -68.4(8) | 0.99981 |
| $\text{Ce}_2\text{YbCuS}_5$ | 5.79 | 5.31(3) | -47(2) | 0.99794 |
| $\text{Pr}_2\text{YbCuS}_5$ | 6.80 | 7.00(2) | -44(2) | 0.99926 |
| $\text{Nd}_2\text{YbCuS}_5$ | 6.84 | 6.87(1) | -46.0(8) | 0.99979 |

^a P_{cal} and P_{eff} : calculated⁵² and experimental effective magnetic moments per formula unit. ^b Weiss constant (θ_{p}) and goodness of fit (R^2) obtained from high temperature (100-300 K) data

chalcogenides are expected to be different from the parent interlanthanide chalcogenides after introducing more soft and electronegative Cu^+ ions into the system. Cu^+ ions prefer to bind larger chalcogenides to form more covalent bonds. This is best exhibited by the LnCuOQ ($\text{Ln} = \text{La, Ce, Pr, Nd}$; $\text{Q} = \text{S, Se, Te}$)²⁸⁻³⁸ series that consists of alternately stacked $[\text{Cu}_2\text{Q}_2]^{2-}$ layers and $[\text{Ln}_2\text{O}_2]^{2+}$ layers. The optical properties of LnCuOQ ($\text{Ln} = \text{La, Pr, Nd}$; $\text{Q} = \text{S, Se, Te}$) are mainly determined by $[\text{Cu}_2\text{Q}_2]^{2-}$ layers, e.g. the valence band of LaCuOTe ³⁸ is filled with $\text{Cu } 3d$ and $\text{Te } 5p$ states and the conduction band is composed of $\text{Cu } 4s$, $\text{Te } 5p$ and $\text{La } 5d$ states; $\text{La } 4f$ states are well above the Fermi energy. LnCuOQ ($\text{Ln} = \text{La, Pr, Nd}$; $\text{Q} = \text{S, Se}$) are determined to be direct allowed p-type semiconductors with wide band gaps, while corresponding tellurides have indirect-type gaps.^{35,38} In contrast, recent studies have shown that $\text{Ce } 4f$ states in CeCuOS and $\text{CeCu}_{0.75}\text{OS}$ compounds are fully spin-polarized and delocalized result in black colors and much smaller band gaps.³⁶ Another series compounds with layered structures, LnCuS_2 ($\text{Ln} = \text{La, Nd, Sm, Gd, Dy, Ho, Yb, Lu, Y}$), are wide band gap p-type semiconductors too.² Substitution of larger chalcogenides narrows the band gaps by increasing the covalency in the Cu-Q bonds to lift the Fermi levels.^{27,35}

The optical properties for $\text{Ln}_2\text{YbCuQ}_5$ ($\text{Ln} = \text{La, Ce, Pr, Nd, Sm}$; $\text{Q} = \text{S, Se}$) were measured by UV-vis-NIR diffuse reflectance spectroscopy. The spectra are presented in Figure 8.9. The band gaps of $\text{La}_2\text{YbCuSe}_5$, $\text{Ce}_2\text{YbCuSe}_5$, $\text{La}_2\text{YbCuS}_5$, $\text{Ce}_2\text{YbCuS}_5$, $\text{Pr}_2\text{YbCuS}_5$, $\text{Nd}_2\text{YbCuS}_5$, and $\text{Sm}_2\text{YbCuS}_5$ are 1.15 eV, 1.05 eV, 1.45 eV, 1.37 eV, 1.25 eV, 1.35 eV, and 1.28 eV respectively. Apparently selenides have smaller band gaps than sulfides due to the higher energy of $\text{Se } 4p$ orbitals. The two lanthanum compounds have somewhat larger values than the rest. This means $4f$ states of other lanthanides

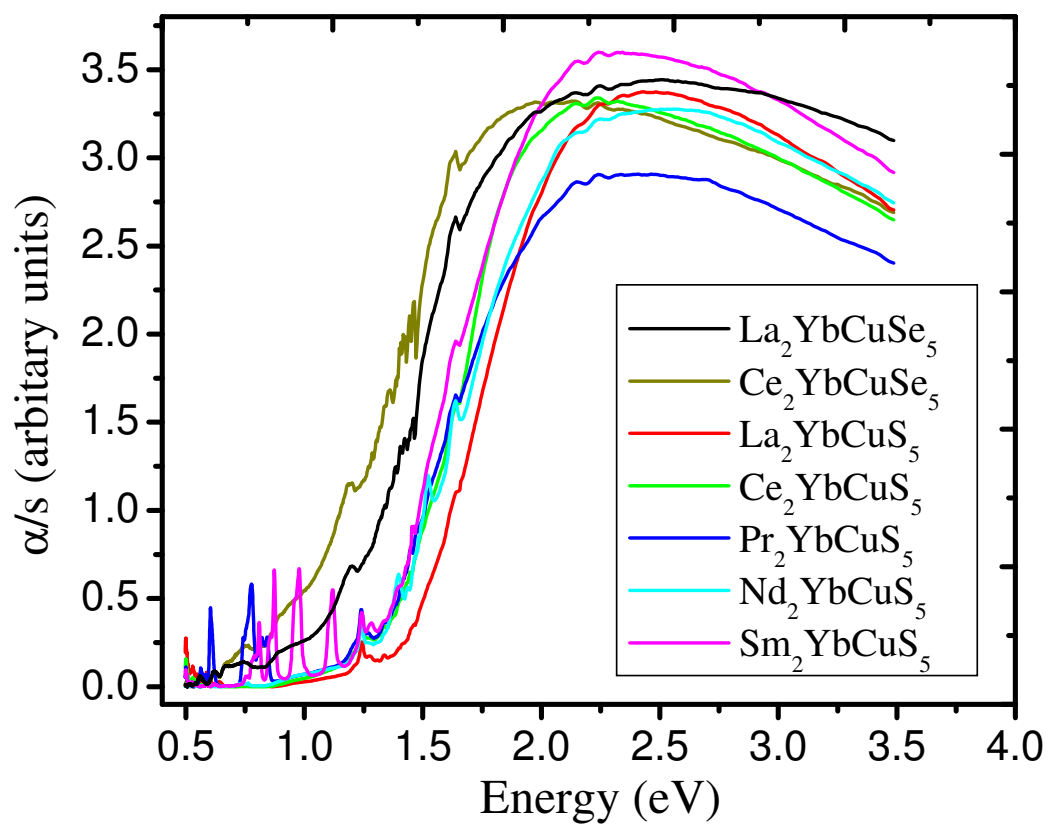


Figure 8.9. UV-vis diffuse reflectance spectra of $\text{Ln}_2\text{YbCuQ}_5$ ($\text{Ln} = \text{La, Ce, Pr, Nd, Sm}$; $\text{Q} = \text{S, Se}$).

besides La have some contribution to the electronic structures around the Fermi levels. Unlike most lanthanide and interlanthanide chalcogenides, among which cerium compounds have the smallest band gaps due to the high energy of $4f^1$ electron,⁴⁸⁻⁵¹ Ce_2YbCuS_5 has slight larger values than the Pr, Nd, and Sm cases. This indicates that the band structures of Ln_2YbCuS_5 are more controlled by Cu energy levels as expected, because of the more covalent Cu-S bonds.

The band gaps of Ln_2YbCuQ_5 ($Ln = La, Ce, Pr, Nd, Sm; Q = S, Se$) are consistent with the observed black colors and are reasonable compared to $SmCuS_2$ (2.1 eV)⁶ and $La_3CuO_2S_3$ (2.01 eV)⁴⁰, which have less condensed structure and lower energy O $2p$ orbitals respectively. Overall, the electronic structures of Ln_2YbCuQ_5 ($Ln = La, Ce, Pr, Nd, Sm; Q = S, Se$) are tunable based on the choices of Ln and Q.

CONCLUSIONS

A new series of ordered quaternary interlanthanide copper chalcogenides, Ln_2YbCuQ_5 ($Ln = La, Ce, Pr, Nd, Sm; Q = S, Se$), have been synthesized using Sb_2O_3 ($Q = S, Se$) fluxes at 900 °C. Compared to other known lanthanide copper chalcogenides, these compounds crystallize in a new structure type that is realized by including two different lanthanides with large size difference, which tend to have distinct coordination environments. The three-dimensional complex structure of Ln_2YbCuQ_5 ($Ln = La, Ce, Pr, Nd, Sm; Q = S, Se$) include two crystallographically unique eight-coordinate Ln atoms, one octahedral Yb site, and two Cu positions. These two Cu sites closely reside in the trigonal bipyramidal cavities formed by Q^{2-} anions that cannot be occupied simultaneously. The structure includes one-dimensional $[YbCuQ_5]^{6-}$ ribbons along the b

axis that are separated by larger Ln^{3+} ions. $\text{Ce}_2\text{YbCuSe}_5$, $\text{La}_2\text{YbCuS}_5$, $\text{Ce}_2\text{YbCuS}_5$, and $\text{Pr}_2\text{YbCuS}_5$ are Curie-Weiss paramagnets. $\text{La}_2\text{YbCuSe}_5$ and $\text{Nd}_2\text{YbCuS}_5$ have short range antiferromagnetic ordering at low temperature. The UV-vis-NIR diffuse reflectance measurements show these compounds to be wide band-gap semiconductors.

REFERENCES

1. Julien-Pouzol, M.; Jaulmes, S.; Mazurier, A.; Guittard, M. *Acta Crystallogr., Sect. B: Struct. Crystallogr. Cryst. Chem.* **1981**, *37*, 1901.
2. Murugesan, T.; Gopalakrishnan, J. *Indian J. Chem.* **1983**, *22A*, 469.
3. Guseinov, G. G.; Amirov, A. S.; Mamedov, K. S. *Dokl. Akad. Nauk Az. SSR* **1984**, *40*, 62.
4. Gschneidner, K. A., Jr., Eyring, L. R., Eds. *Handbook on the Physics and Chemistry of Rare Earths*; North-Holland Physics Publishing: New York, 1984; Vol. 6.
5. Wang, Yarong; Sato, Nobuaki; Fujino, Takeo *Mater. Res. Bull.* **2001**, *36*, 1029.
6. Llanos, Jaime; Mujica, Carlos; Sanchez, Victor; Schnelle, Walter; Cardoso-Gil, Raul. *J. Solid State Chem.* **2004**, *177*, 1388.
7. Ijjaali, I.; Mitchell, K.; Ibers, J. A. *J. Solid State Chem.* **2004**, *177*, 760.
8. Julien-Pouzol, M.; Guittard, M.; Mazurier, A. *C. R. Acad. Sci.* **1970**, *271*, 1317.
9. Julien-Pouzol, M.; Guittard, M. *Ann. Chim. (Paris)* **1972**, *7*, 253.
10. Lauxmann, Petra; Schleid, Thomas. *Z. Anorg. Allg. Chem.* **2000**, *626*, 1608.
11. Dismukes, J. P.; Smith, R. T.; White, J. G. *J. Phys. Chem. Solids* **1971**, *32*, 913.
12. Ballestracci, R.; Bertaut, E. F. *C. R. Acad. Sci. Paris* **1965**, *261*, 5064.
13. Ballestracci, R.; Bertaut, E. F. *Bull. Soc. Miner. Crystallogr.* **1965**, *88*, 575.
14. Guymont, M.; Thomas, A.; Julien-Pouzol, M.; Jaulmes, S.; Guittard, M. *Phys. Status Solidi A* **1990**, *121*, 21.
15. Onoda, M.; Chen, X. A.; Sato, A.; Wada, H. *J. Solid State Chem.* **2000**, *152*, 332.
16. Lemoine, P.; Carré, D.; Guittard, M. *Acta Cryst.* **1986**, *C42*, 390.

17. Furuuchi, F.; Wakeshima, M.; Hinatsu, Y. *J. Solid State Chem.* **2004**, *177*, 3853.
18. Eu₂CuSe₃, isostructure to Eu₂CuS₃, unpublished results.
19. Wakeshima, M.; Furuuchi, F. Hinatsu, Y. *J. Phys.: Condens. Matter* **2004**, *16* 5503.
20. Strobel, S.; Schleid, T. *Angew. Chem. Int. Ed.* **2003**, *42*, 4911.
21. Strobel, S.; Schleid, T. *J. Solid State Chem.* **2003**, *171*, 424.
22. Ijjaali, I.; Ibers, J. A. *Acta Cryst.***2004**, *E39*, i89.
23. Patschke, R.; Brazis, P.; Kannewurf, C. R.; Kanatzidis, M. G. *J. Mater. Chem.* **1999**, *9*, 2293.
24. Huang, F. Q.; Ibers, J. A. *J. Solid State Chem.* **2001**, *159*, 186.
25. Dung, N.-H.; Pardo, M.-P.; Boy, P. *Acta Cryst.***1983**, *C39*, 668.
26. Huang, F. Q.; Brazis, P.; Kannewurf, C. R.; Ibers, J. A. *J. Am. Chem. Soc.* **2000**, *122*, 80.
27. Huang, F. Q.; Ibers, J. A. *Inorg. Chem.* **1999**, *38*, 5978.
28. Popovkin, B. A.; Kusainova, A. M.; Dolgikh, V. A.; Aksel'rud, L. G. *Russ. J. Inorg. Chem. (Transl. of Zh. Neorg. Khim.)* **1998**, *43*, 1471.
29. Charkin, D. O.; Akopyan, A. V.; Dolgikh, V. A. *Russ. J. Inorg. Chem. (Transl. of Zh. Neorg. Khim.)* **1999**, *44*, 833.
30. Ueda, K.; Inoue, S.; Hirose, S.; Kawazoe, H.; Hosono, H. *Appl. Phys. Lett.* **2000**, *77*, 2701.
31. Ueda, K.; Inoue, S.; Hosono, H.; Sarukura, N.; Hirano, H. *Appl. Phys. Lett.* **2001**, *78*, 2333.
32. Inoue, S.; Ueda, K.; Hosono, H.; Hamada, N. *Phys. Rev. B* **2001**, *64*, 245211.

33. Ueda, K.; Takafuji, K.; Hiramatsu, H.; Ohta, H.; Kamiya, T.; Hirano, M.; Hosono, H. *Chem. Mater.* **2003**, *15*, 3692.
34. Ueda, K.; Takafuji, K.; Hosono, H. *J. Solid State Chem.* **2003**, *170*, 182.
35. Ueda, K.; Hosono, H.; Hamada, N. *J. Phys.: Condens. Matter* **2004**, *16*, 5179.
36. Chan, G. H.; Deng, B.; Bertoni, M.; Ireland, J. R.; Hersam, M. C.; Mason, T. O.; Van Duyne, R. P.; Ibers, J. A. *Inorg. Chem.* **2006**, *45*, 8264.
37. Ueda, K.; Hiramatsu, H.; Hirano, M.; Kamiya, T.; Hosono, H. *Thin Solid Films* **2006**, *496*, 8.
38. Liu, M. L.; Wu, L. B.; Huang, F. Q.; Chen, L. D.; Ibers, J. A. *J. Solid State Chem.* **2007**, *180*, 62.
39. Huang, F. Q.; Brazis, P.; Kannewurf, C. R.; Ibers, J. A. *J. Solid State Chem.* **2000**, *155*, 366.
40. Ijjaali, I.; Haynes, C. L.; Mcfarland, A. D.; Van Duyne, R. P.; Ibers, J. A. *J. Solid State Chem.* **2003**, *172*, 257.
41. Sheldrick, G. M. *SHELXTL PC, Version 6.12, An Integrated System for Solving, Refining, and Displaying Crystal Structures from Diffraction Data*; Siemens Analytical X-Ray Instruments, Inc.: Madison, WI 2001.
42. Sheldrick, G. M. *SADABS 2001, Program for absorption correction using SMART CCD based on the method of Blessing*; Blessing, R. H. *Acta Crystallogr.* **1995**, *A51*, 33.
43. Mulay, L. N.; Boudreaux, E. A. *Theory and Applications of Molecular Diamagnetism*; Wiley–Interscience: New York, 1976.

44. Wendlandt, W. W.; Hecht, H. G.: *Reflectance Spectroscopy*; Interscience Publishers: New York, 1966.
45. Evans, H. T., Jr. *Nature* **1971**, 232, 69.
46. Evans, H. T., Jr. *Z. Kristallogr.* **1979**, 150, 299.
47. Shannon, R. D. *Acta Cryst.* **1976**, A32, 751.
48. Prokofiev, A. V.; Shelykh, A. I.; Golubkov, A. V.; Smirnov, I. A. *J. Alloys Compd.* **1995**, 219, 172.
49. Prokofiev, A. V.; Shelykh, A. I.; Melekh, B. T. *J. Alloys Compd.* **1996**, 242, 41.
50. Jin, G. B.; Choi, E. S.; Guertin, R. P.; Brooks, J. S.; Bray, T. H.; Booth, C. H.; Albrecht-Schmitt, T. E. *Chem. Mater.* **2007**, 19, 567.
51. Jin, G. B.; Choi, E. S.; Guertin, R. P.; Brooks, J. S.; Bray, T. H.; Booth, C. H.; Albrecht-Schmitt, T. E. *J. Solid State Chem.* in press.
52. Kittel, C. *Introduction to Solid State Physics*, 6th Edition; Wiley: New York, 1986.

CHAPTER 9

PARTIALLY-FILLED MIXED-LANTHANIDE VARIANTS OF THE $K_2Tm_{23.33}S_{36}$

STRUCTURE-TYPE: STRUCTURE AND PROPERTIES OF

$Cs_xLn_yYbS_2$ ($x = 0.14 - 0.16$; $Ln = La-Nd, Sm-Yb$; $y = 0.26 - 0.33$)

ABSTRACT

The mixed-lanthanide sulfides, $Cs_xLn_yYbS_2$ ($x = 0.14 - 0.16$; $Ln = La, Ce, Pr, Nd, Sm, Eu, Gd, Tb, Dy, Ho, Er, Tm, Yb$; $y = 0.26 - 0.33$), have been grown as single crystals from a CsCl reactive flux at 900°C. Single-crystal X-ray diffraction experiments on all of these compounds reveal that they crystallize in the hexagonal space group $P6_3/m$ with a structure similar to that found for $K_2Tm_{23.33}S_{36}$. $Cs_xLn_yYbS_2$ adopts a three-dimensional channel structure with two different hexagonal channels. One of these channels is nearly filled with Cs^+ cations while the other is only partially filled. The Ln^{3+} cations are bound by bridging S^{2-} anions to create two distinct local environments: one where the smaller Yb^{3+} cations preferentially reside in six-coordinate distorted octahedral sites, and a second where the larger Ln^{3+} are located in a nine-coordinate tricapped trigonal prismatic site. Owing to the hexagonal lattice that is adopted by these compounds, spin-frustration was investigated by means of magnetic susceptibility measurements on polycrystalline samples. The θ_W values, some of which are large, are

all negative except for Tb, and range from -14.2(3) to -45(2) K. For $\text{Cs}_{0.15}\text{Tb}_{0.29}\text{YbS}_2$, ferromagnetic interactions are found with $\theta = 3.4(4)$ K. XANES measurements for $\text{Cs}_{0.14}\text{Ce}_{0.30}\text{YbS}_2$, $\text{Cs}_{0.14}\text{Nd}_{0.29}\text{YbS}_2$, and $\text{Cs}_{0.15}\text{Sm}_{0.29}\text{YbS}_2$ have shown that all lanthanides in these samples are trivalent. The optical band gaps for $\text{Cs}_x\text{Ln}_y\text{YbS}_2$ ($x = 0.14 - 0.16$; Ln = La, Ce, Pr, Nd, Sm, Eu, Gd, Tb, Dy, Ho, Er, Tm, Yb; $y = 0.26 - 0.33$) are in the range of 2.1 and 2.4 eV.

INTRODUCTION

The arrangement of paramagnetic ions in triangular arrays gives rise to the possibility of geometric spin-frustration, where long-range magnetic ordering is not predicted to occur.^{1,2} Spin-frustration is particularly well-known for systems with kagomé lattices, but is also well recognized in other high-symmetry structure types containing triangular moieties such as spinels³⁻¹⁴ and pyrochlores.¹⁵⁻³⁶ In the partially zinc-substituted paratacamite, $\text{Zn}_{0.33}\text{Cu}_{3.67}(\text{OH})_6\text{Cl}_2$, which possesses kagomé-type layers, spin-frustration is exceedingly large with a spin-frustration parameter $f > 157$ ($f = |\theta_{\text{CW}}|/T_c$).^{37-39,40} Despite well-established predictions to the contrary, long-range magnetic ordering is known to occur in certain phases with triangular sublattices, such as Fe-jarosites, $\text{AFe}_3(\text{OH})_6(\text{SO}_4)_2$ ($A = \text{Na}, \text{K}, \text{Rb}, \text{NH}_4^+, \text{H}_3\text{O}^+, \text{Ag}^+, \text{Tl}^+, \text{and Pb}^{2+}$), where the Dzyaloshinsky-Moriya (DM)⁴¹⁻⁴³ interaction allows for weak in-plane ferromagnetism and long-range ordering.⁴⁴⁻⁴⁸ These compounds are of particular interest because they can be prepared as large single crystals that have allowed for the discernment of spin chirality via neutron scattering measurements.⁴⁵ More recently, materials with one-

dimensional arrays of triangular units have been investigated such as the rare-earth olivines, ZnLn_2S_4 ($\text{Ln} = \text{Er}, \text{Tm}, \text{Yb}$), and these too show evidence for spin-frustration.⁴⁹

The $\text{K}_2\text{Tm}_{23.33}\text{S}_{36}$ structure type represents an unusual case for investigating spin-frustration in that there are two different interpenetrating honeycomb layers formed from Tm^{3+} in two different environments.⁵⁰ In this structure, one of the rare-earth ions resides in a site with seven close sulfide neighbors, and the second in a site with six surrounding sulfide anions. This allows for the possibility of using two different rare-earth ions of different sizes to preferentially occupy the two different sites, with larger rare-earth ions potentially favoring the site with higher coordination. In addition, this allows for the investigation of the electronic properties in systems where there are different numbers of f electrons on the metal centers. To this end we have synthesized the partially-filled mixed-lanthanide variants of the $\text{K}_2\text{Tm}_{23.33}\text{S}_{36}$ structure-type, $\text{Cs}_x\text{Ln}_y\text{YbS}_2$ ($x = 0.14 - 0.16$; $\text{Ln} = \text{La}, \text{Ce}, \text{Pr}, \text{Nd}, \text{Sm}, \text{Eu}, \text{Gd}, \text{Tb}, \text{Dy}, \text{Ho}, \text{Er}, \text{Tm}, \text{Yb}$; $y = 0.26 - 0.33$). We provide structural, magnetic susceptibility, XANES and optical data for these compounds.

EXPERIMENT

Starting Materials. La (99.9%, Alfa-Aesar), Ce (99.9%, Alfa-Aesar), Pr (99.9%, Alfa-Aesar), Nd (99.9%, Alfa-Aesar), Sm (99.9%, Alfa-Aesar), Eu (99.9%, Cerac), Gd (99.9%, Alfa-Aesar), Tb (99.9%, Alfa-Aesar), Dy (99.9%, Alfa-Aesar), Ho (99.9%, Alfa-Aesar), Er (99.9%, Alfa-Aesar), Tm (99.9%, Alfa-Aesar), Yb (99.9%, Alfa-Aesar), CsCl (99.9%, Alfa-Aesar), and S (99.5%, Alfa-Aesar) were used as received.

Cs_{0.14-0.17}Ln_{0.26-0.33}YbS₂ (Ln = La, Ce, Pr, Nd, Sm, Eu, Gd). Ln, Yb, and S in a ratio of 1:3:6 with a total mass of 0.0750 g was mixed together with 0.1500 g of CsCl and then loaded into fused-silica ampoules in an Ar-filled glovebox. The tubes were sealed under vacuum and heated using the following profiles: 2 °C/min to 500 °C (1 h), 0.5 °C/min to 900 °C (5 d), 0.04 °C/min to 400 °C (2 d), and 0.5 °C/min to 24 °C. The acicular crystals were isolated from the excess CsCl flux by washing with water and methanol. The yields are close to 100% based on Yb except for Eu which is Cs_{0.16}Eu_{0.33}YbS₂. The products are yellow (Ln= La, Pr, Nd, Sm), red (Ln= Ce, Eu), or brown (Ln= Gd) respectively.

Cs_{0.14-0.17}Ln_{0.26-0.33}YbS₂ (Ln = Tb, Dy, Ho, Er, Tm, Yb). The same procedure as above was used to prepare Cs_{0.14-0.17}Ln_{0.26-0.33}YbS₂ (Ln = Tb, Dy, Ho, Er, Tm, Yb) except that the Ln, Yb, S/Yb, and S ratio of 1:2:5/1:2 was used, and the total mass of these reactants was 0.0500 g. These starting materials were mixed with 0.1500 g of CsCl. The following heating profile was followed: 2 °C/min to 500 °C (1 h), 0.5 °C/min to 900 °C (7 d), 0.02 °C/min to 400 °C (2 d), and 0.5 °C/min to 24 °C. The desired products are obtained as brown needles.

All the compounds are stable in moist air for more than one year. Powder X-ray diffraction measurements confirmed the phase purity of Cs_xLn_yYbS₂ (x = 0.14 – 0.16; Ln = La, Ce, Pr, Nd, Sm, Gd, Tb, Dy, Ho, Er, Tm, Yb; y = 0.26 – 0.33) by comparison with powder patterns calculated from the single crystal X-ray structures. The major product of the reaction with Eu is EuYb₂S₄,⁵³ and Cs_{0.16}Eu_{0.33}YbS₂ is only isolated as a minor product. Semi-quantitative SEM/EDX analyses were performed using a JEOL 840/Link Isis instrument. Cs, Ln, Yb and S percentages were calibrated against standards.

Crystallographic Studies. Single crystals of $Cs_xLn_yYbS_2$ ($x = 0.14 - 0.16$; $Ln = La, Ce, Pr, Nd, Sm, Eu, Gd, Tb, Dy, Ho, Er, Tm, Yb$; $y = 0.26 - 0.33$) were mounted on glass fibers using epoxy, and optically aligned on a Bruker SMART APEX CCD X-ray diffractometer. The diffraction data were collected at 193 K using an Oxford Cryostat. Intensity measurements were performed using graphite-monochromated Mo $K\alpha$ radiation from a sealed tube and monocapillary collimator. SMART (v 5.624) was used for preliminary determination of the cell constants and data collection control. The intensities of reflections of a sphere were collected by a combination of 3 sets of exposures (frames). Each set had a different ϕ angle for the crystal and each exposure covered a range of 0.3° in ω . A total of 1800 frames were collected with an exposure time per frame of 30 s for all compounds.

Determination of integrated intensities and global refinement were performed with the Bruker SAINT (v 6.02) software package using a narrow-frame integration algorithm. A face-indexed numerical absorption correction was initially applied using XPREP.⁵¹ These files were subsequently treated with a multiscan absorption correction by SADABS.⁵² The program suite SHELXTL (v 6.12) was used for space group determination (XPREP), direct methods structure solution (XS), and least-squares refinement (XL).⁵¹ The final refinements included anisotropic displacement parameters for all atoms and secondary extinction.

The formulae for these compounds were arrived at by refinement of the occupancy of each site, yielding the following: $Cs_{0.14}La_{0.30}YbS_2$, $Cs_{0.14}Ce_{0.30}YbS_2$, $Cs_{0.14}Pr_{0.30}YbS_2$, $Cs_{0.14}Nd_{0.29}YbS_2$, $Cs_{0.15}Sm_{0.29}YbS_2$, $Cs_{0.16}Eu_{0.33}YbS_2$, $Cs_{0.15}Gd_{0.29}YbS_2$, $Cs_{0.15}Tb_{0.29}YbS_2$, $Cs_{0.16}Dy_{0.28}YbS_2$, $Cs_{0.16}Ho_{0.30}YbS_2$, $Cs_{0.17}Er_{0.32}YbS_2$, $Cs_{0.15}Tm_{0.26}YbS_2$,

and $\text{Cs}_{0.15}\text{Yb}_{0.26}\text{YbS}_2$. The cell reported herein represents a sub-cell of the $\text{K}_2\text{Tm}_{23.33}\text{S}_{36}$ structure-type.⁵⁰ This sub-cell can be inscribed within the larger cell by a 30° rotation and division of the a and b axes by $\sqrt{2}$. Some, but not all of the above compounds can be indexed to the $\text{K}_2\text{Tm}_{23.33}\text{S}_{36}$ cell. For the sake of consistency we have used the same cell to describe all compounds.

These compounds suffer from the classic problems of disorder in hexagonal systems along the c axis that is most evident from the elongation of the C_s thermal parameter along this axis. It is important to note that while we have modeled these structures with the two different lanthanide sites each containing only one lanthanide element, the chance that there is partial occupancy of both lanthanide elements at both sites is significant, particularly as the size of the two different lanthanides becomes more similar. We have refined models with this type of disorder, and they do not result in improvements in the structures, all of which are already of high resolution. Some crystallographic details are given in Table 9.1a and Table 9.1b. Atomic coordinates and equivalent isotropic displacement parameters for these compounds can be found in Table 9.2.

Powder X-ray Diffraction. Powder X-ray diffraction patterns were collected with a Rigaku Miniflex powder X-ray diffractometer using $\text{Cu K}\alpha$ ($\lambda = 1.54056 \text{ \AA}$) radiation.

Magnetism. Magnetic susceptibility measurements were made between 2 and 300 K under field-cooled conditions in an applied field of 5 kG on a Quantum Design 7T-MPMS SQUID magnetometer. θ_p values were obtained from extrapolations from

Table 9.1a. Crystallographic Data for Cs_{0.14-0.17}Ln_{0.26-0.33}YbS₂ (Ln = La, Ce, Pr, Nd, Sm, Eu, Gd).

| Formula | Cs _{0.14} La _{0.30} YbS ₂ | Cs _{0.14} Ce _{0.30} YbS ₂ | Cs _{0.14} Pr _{0.30} YbS ₂ | Cs _{0.14} Nd _{0.29} YbS ₂ | Cs _{0.15} Sm _{0.29} YbS ₂ | Cs _{0.16} Eu _{0.33} YbS ₂ | Cs _{0.15} Gd _{0.29} YbS ₂ |
|---|--|--|--|--|--|--|--|
| fw | 297.43 | 298.01 | 299.17 | 298.04 | 300.76 | 308.64 | 303.40 |
| Color | Yellow | Red | Yellow | Yellow | Yellow | Red | Brown |
| Crystal System | Hexagonal | Hexagonal | Hexagonal | Hexagonal | Hexagonal | Hexagonal | Hexagonal |
| Space group | <i>P6₃/m</i> (No. 176) | <i>P6₃/m</i> (No. 176) | <i>P6₃/m</i> (No. 176) | <i>P6₃/m</i> (No. 176) | <i>P6₃/m</i> (No. 176) | <i>P6₃/m</i> (No. 176) | <i>P6₃/m</i> (No. 176) |
| <i>a</i> (Å) | 12.2455(7) | 12.2147(14) | 12.2177(8) | 12.2119(8) | 12.1909(9) | 12.2483(13) | 12.1906(13) |
| <i>c</i> (Å) | 3.9393(3) | 3.9216(6) | 3.9223(4) | 3.9140(4) | 3.9085(4) | 3.9218(6) | 3.8976(6) |
| <i>V</i> (Å ³) | 511.57(6) | 506.71(11) | 507.05(7) | 505.50(7) | 503.05(7) | 509.53(11) | 501.62(11) |
| Z | 6 | 6 | 6 | 6 | 6 | 6 | 6 |
| T (K) | 193 | 193 | 193 | 193 | 193 | 193 | 193 |
| λ (Å) | 0.71073 | 0.71073 | 0.71073 | 0.71073 | 0.71073 | 0.71073 | 0.71073 |
| ρ_{calcd} (g cm ⁻³) | 5.793 | 5.860 | 5.879 | 5.874 | 5.957 | 6.035 | 6.026 |
| μ (cm ⁻¹) | 334.72 | 340.58 | 344.06 | 345.81 | 354.30 | 361.56 | 362.36 |
| $R(F)^a$ | 0.0204 | 0.0216 | 0.0235 | 0.0229 | 0.0315 | 0.0355 | 0.0384 |
| $R_w(F_o^2)^b$ | 0.0471 | 0.0545 | 0.0550 | 0.0581 | 0.0759 | 0.0907 | 0.0933 |

^a $R(F) = \frac{\sum \|F_o\| - |F_c|}{\sum \|F_o\|}$. ^b $R_w(F_o^2) = \left[\frac{\sum [w(F_o^2 - F_c^2)^2]}{\sum wF_o^4} \right]^{1/2}$.

Table 9.1b. Crystallographic Data for Cs_{0.14-0.17}Ln_{0.26-0.33}YbS₂ (Ln = Tb, Dy, Ho, Er, Tm, Yb).

| Formula | Cs _{0.15} Tb _{0.29} YbS ₂ | Cs _{0.16} Dy _{0.28} YbS ₂ | Cs _{0.16} Ho _{0.30} YbS ₂ | Cs _{0.17} Er _{0.32} YbS ₂ | Cs _{0.15} Tm _{0.26} YbS ₂ | Cs _{0.15} Yb _{0.26} YbS ₂ |
|---|--|--|--|--|--|--|
| fw | 303.36 | 304.07 | 307.52 | 312.89 | 300.29 | 302.09 |
| Color | Brown | Brown | Brown | Brown | Brown | Brown |
| Crystal System | Hexagonal | Hexagonal | Hexagonal | Hexagonal | Hexagonal | Hexagonal |
| Space group | <i>P6₃/m</i> (No. 176) | <i>P6₃/m</i> (No. 176) | <i>P6₃/m</i> (No. 176) | <i>P6₃/m</i> (No. 176) | <i>P6₃/m</i> (No. 176) | <i>P6₃/m</i> (No. 176) |
| <i>a</i> (Å) | 12.1558(13) | 12.1882(15) | 12.2006(16) | 12.2329(8) | 12.1944(11) | 12.1818(11) |
| <i>c</i> (Å) | 3.8894(6) | 3.8926(7) | 3.8976(7) | 3.9038(4) | 3.9026(5) | 3.8932(5) |
| <i>V</i> (Å ³) | 497.71(11) | 500.78(13) | 502.45(13) | 505.91(7) | 502.58(9) | 500.33(9) |
| Z | 6 | 6 | 6 | 6 | 6 | 6 |
| T (K) | 193 | 193 | 193 | 193 | 193 | 193 |
| λ (Å) | 0.71073 | 0.71073 | 0.71073 | 0.71073 | 0.71073 | 0.71073 |
| ρ _{calcd} (g cm ⁻³) | 6.073 | 6.050 | 6.098 | 6.162 | 5.953 | 6.016 |
| μ (cm ⁻¹) | 368.38 | 369.02 | 374.76 | 383.12 | 371.74 | 377.95 |
| <i>R</i> (<i>F</i>) ^a | 0.0379 | 0.0325 | 0.0279 | 0.0284 | 0.0280 | 0.0253 |
| <i>R</i> _w (<i>F</i> _o ²) ^b | 0.0910 | 0.0781 | 0.0631 | 0.0577 | 0.0706 | 0.0616 |

$$^a R(F) = \frac{\sum \|F_o\| - |F_c|}{\sum |F_o|}, \quad ^b R_w(F_o^2) = \left[\frac{\sum [w(F_o^2 - F_c^2)^2]}{\sum wF_o^4} \right]^{1/2}.$$

Table 9.2. Positional and Thermo parameters for Cs_{0.14}La_{0.30}YbS₂ and Cs_{0.16}Eu_{0.33}YbS₂

| Atom (site) | x | Y | z | U _{eq} (Å ²) ^a | Wychoff positon |
|--|-------------|-------------|------|--|--------------------|
| Cs _{0.14} La _{0.30} YbS ₂ | | | | | |
| Cs1 | 0 | 0 | 1/4 | 0.0798(14) | 2a |
| La1 | 2/3 | 1/3 | 1/4 | 0.0285(3) | 2d |
| Yb1 | 0.34938(3) | -0.00448(3) | 3/4 | 0.01486(14) | 6h |
| S1 | 0.60244(16) | 0.13376(17) | -1/4 | 0.0154(4) | 6h |
| S2 | 0.1314(7) | -0.2140(7) | -1/4 | 0.0119(11) | 6h |
| S3 | 0.1084(7) | -0.1907(8) | -1/4 | 0.0221(14) | 6h |
| Cs _{0.16} Eu _{0.33} YbS ₂ | | | | | |
| Cs1 | 0 | 0 | 1/4 | 0.0278(8) | 2a |
| Eu1 | 0.687(2) | 0.333(6) | 1/4 | 0.024(2) | 6h |
| Yb1 | 0.34926(6) | -0.00529(6) | 3/4 | 0.0193(3) | 6h |
| S1 | 0.6029(4) | 0.1351(4) | -1/4 | 0.0246(9) | 6h |
| S2 | 0.1270(13) | -0.2166(11) | -1/4 | 0.017(2) | 6h |
| S3 | 0.1081(13) | -0.1848(12) | -1/4 | 0.019(2) | 6h |

^a U_{eq} is defined as one-third of the trace of the orthogonalized U_{ij} tensor.

fits between 100 and 300 K. (Magnetic susceptibility measurements were performed by Corwin H. Booth at Lawrence Berkeley National Laboratory)

X-ray Absorption Near Edge Spectroscopy (XANES). Samples were ground and passed through a 20 μm sieve, then brushed onto adhesive tape. The tape was cut into strips and stacked to achieve an edge step at the Yb L_{III} edge corresponding to a change of one absorption length. X-ray absorption spectra were collected at room temperature at the Stanford Synchrotron Radiation Laboratory (SSRL) on beamline 2-3 using a double Si(111) crystal monochromator. The monochromator was detuned by 50% to reduce harmonic contamination of the beam. Contributions to the absorption from other processes than the L_{III} -edge excitation are removed using a standard procedure⁷¹ by extrapolating the pre-edge absorption such that the subtracted data follow a Victoreen formula. (XANES measurements were performed by Corwin H. Booth from Lawrence Berkeley National Laboratory)

UV-vis-NIR Diffuse Reflectance Spectroscopy. The diffuse reflectance spectra for $\text{Cs}_{0.14-0.17}\text{Ln}_{0.26-0.33}\text{YbS}_2$ (Ln = La, Ce, Pr, Nd, Sm, Gd, Tb, Dy, Ho, Er, Tm) were measured from 200 to 1500 nm using a Shimadzu UV3100 spectrophotometer equipped with an integrating sphere attachment. The Kubelka-Munk function was used to convert diffuse reflectance data to absorption spectra.⁵⁶

RESULTS AND DISCUSSION

Crystal Structures. The $\text{Cs}_x\text{Ln}_y\text{YbS}_2$ ($x = 0.14 - 0.16$; Ln = La, Ce, Pr, Nd, Sm, Eu, Gd, Tb, Dy, Ho, Er, Tm, Yb; $y = 0.26 - 0.33$) series are essentially isotypic, with the largest deviation being found when Ln = La. A view of part of the structure of

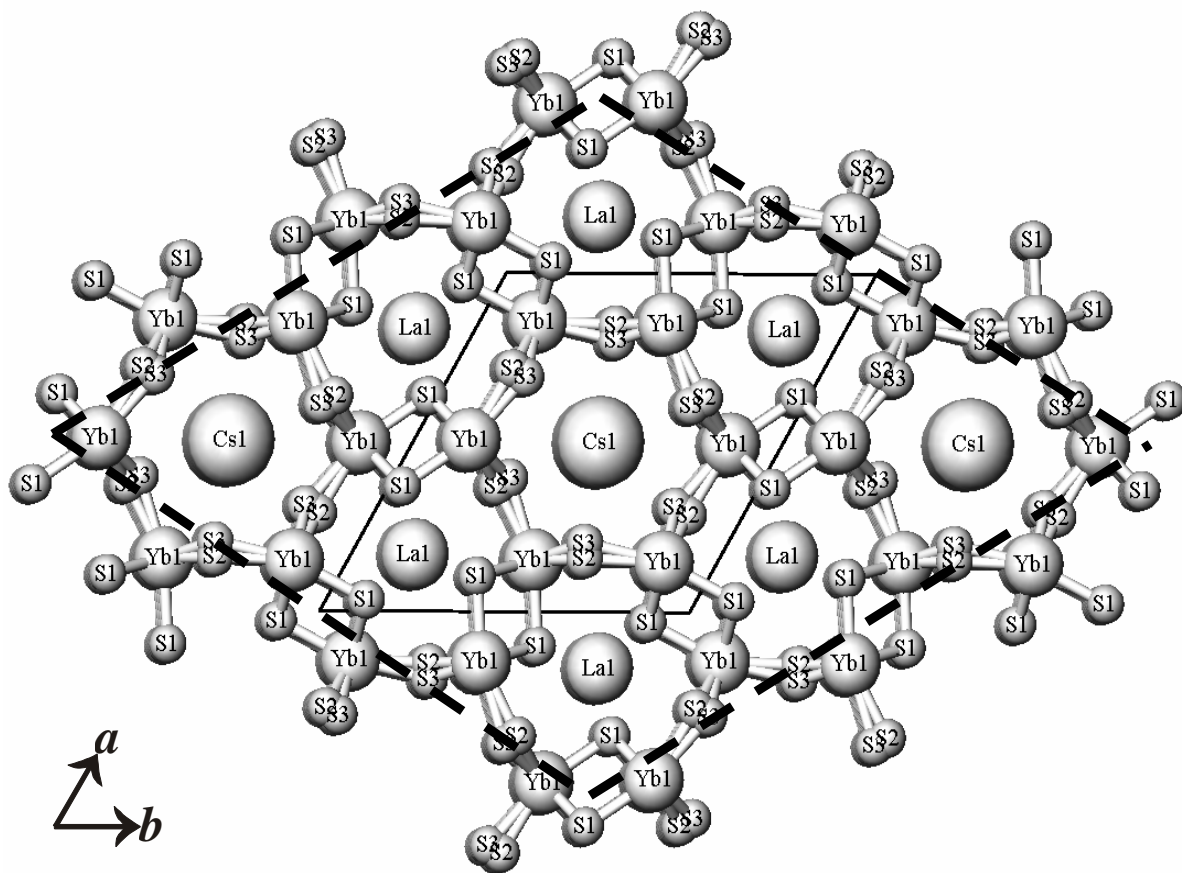


Figure 9.1. A view down the c axis shows the three-dimensional channel structure of $\text{Cs}_{0.14}\text{La}_{0.30}\text{YbS}_2$. Cs-S and La-S bonds have been omitted for clarity. The black solid rhombohedron is the unit cell of $\text{Cs}_{0.14}\text{La}_{0.30}\text{YbS}_2$ and the dashed one is the unit cell of $\text{K}_2\text{Tm}_{23.33}\text{S}_{36}$.

$\text{Cs}_x\text{Ln}_y\text{YbS}_2$ is shown in Figure 9.1. These compounds are partially-filled mixed-lanthanide variants of the $\text{K}_2\text{Tm}_{23,33}\text{S}_{36}$ structure type.⁵⁰ The structure of these compounds consists of edge-shared double rutile chains of $[\text{YbS}_6]$ octahedra. The double-octahedra unit is quite common in other ytterbium sulfide compounds, and is known from EuYb_2S_4 (CaFe_2O_4 structure-type).⁵³ Polyhedral representations of $\text{Cs}_x\text{Ln}_y\text{YbS}_2$ and EuYb_2S_4 are shown in Figure 9.2. In both cases, the basic framework is constructed from these double-octahedra. Each $[\text{YbS}_6]$ unit is joined at the vertices to four other units to form open channels of capped trigonal prismatic sites. Differing connectivity between neighboring units results in tunnels of different shapes. $\text{Cs}_x\text{Ln}_y\text{YbS}_2$ has hexagonal and pseudo-triangular channels containing Cs^+ ions and lanthanide ions respectively, while the Eu^{2+} ions reside in the slightly larger pseudo-triangular channels in EuYb_2S_4 . They are consistent with the size of the cations ($\text{Cs}^+ > \text{Eu}^{2+} > \text{Ln}^{3+}$).

The Cs^+ cations are nine-coordinate and occur as tricapped trigonal prisms. Cs-S bond distances range from 3.648(7) Å to 3.745(6) Å, which are comparable to the crystal radii sum, 3.62 Å, of nine-coordinated Cs^+ (1.92 Å) and six-coordinated S^{2-} (1.70 Å), according to Shannon.⁵⁴ This polyhedron is shown in Figure 9.3. Selected bond distances can be found in Table 9.3a and 9.3b. The structure is compressed along [100]. Three capping S(2) atoms adopt comparable or even shorter Cs-S distances in cases of Ln = La, Ce, and Eu, which is quite unusual. Cs^+ cations sit on (0,0,1/4) and have abnormally large thermal parameters associated with disorder for the early examples in the series; the largest residual electron density is always found at (0,0,1/2). It is suspected that the Cs^+ cations rattle along the channels. There could be some ionic conductivity along the *c* axis, but further measurements are required for confirmation.

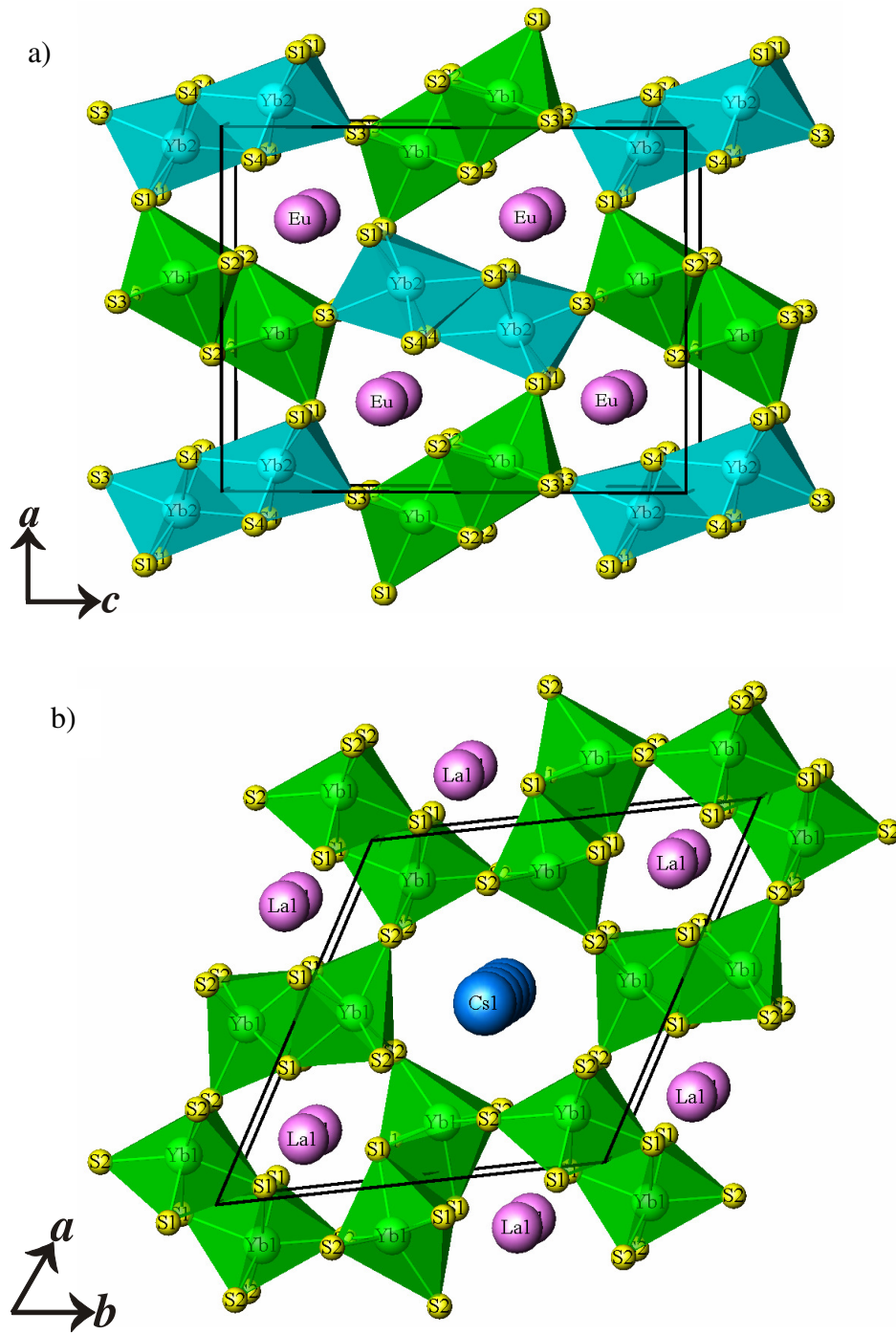


Figure 9.2. a) A polyhedral representation of EuYb_2S_4 structure projected along the b axis; b) A polyhedral view of $\text{Cs}_{0.14}\text{La}_{0.30}\text{YbS}_2$ structure projected along the c axis. $\text{S}(3)$ atoms have been removed for clarity.

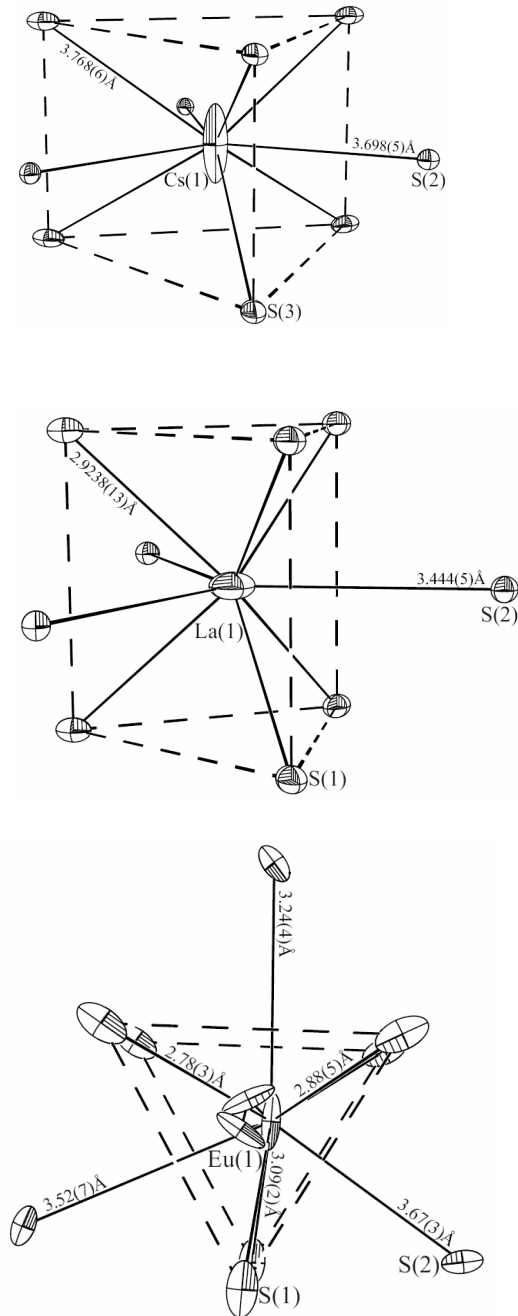


Figure 9.3. Depictions of the CsS₉ and LaS₉ tricapped trigonal prismatic geometries in Cs_{0.14}La_{0.30}YbS₂ and distorted EuS₉ tricapped trigonal prismatic environment in Cs_{0.16}Eu_{0.33}YbS₂.

Table 9.3a. Selected Bond Distances (Å) for Cs_{0.14-0.17}Ln_{0.26-0.33}YbS₂ (Ln = La, Ce, Pr, Nd, Sm, Eu, Gd).

| Formula | Cs _{0.14} La _{0.30} YbS ₂ | Cs _{0.14} Ce _{0.30} YbS ₂ | Cs _{0.14} Pr _{0.30} YbS ₂ | Cs _{0.14} Nd _{0.29} YbS ₂ | Cs _{0.15} Sm _{0.29} YbS ₂ | Cs _{0.16} Eu _{0.33} YbS ₂ | Cs _{0.15} Gd _{0.29} YbS ₂ |
|------------|--|--|--|--|--|--|--|
| Cs-S2×3 | 3.698(5) | 3.665(5) | 3.661(5) | 3.694(5) | 3.723(6) | 3.686(9) | 3.705(13) |
| Cs-S3×6 | 3.768(6) | 3.689(5) | 3.654(5) | 3.669(5) | 3.656(6) | 3.704(9) | 3.630(10) |
| Ln-S1×2 | 2.9238(13) | 2.749(19) | 2.724(13) | 2.707(10) | 2.662(7) | 2.78(3) | 2.636(10) |
| Ln-S1×2 | 2.9238(13) | 2.92(3) | 2.92(3) | 2.910(19) | 2.902(12) | 2.88(5) | 2.90(2) |
| Ln-S1×2 | 2.9238(13) | 3.061(15) | 3.062(13) | 3.065(9) | 3.079(6) | 3.09(2) | 3.064(12) |
| Ln -S2 | 3.444(5) | 3.25(2) | 3.246(19) | 3.193(14) | 3.117(11) | 3.24(4) | 3.14(2) |
| Ln -S2 | 3.444(5) | 3.48(5) | 3.47(4) | 3.44(3) | 3.404(18) | 3.52(7) | 3.40(3) |
| Ln -S2 | 3.444(5) | 3.67(3) | 3.707(18) | 3.681(15) | 3.687(11) | 3.67(3) | 3.721(17) |
| Yb-S1×2 | 2.7690(12) | 2.7632(13) | 2.7678(15) | 2.7677(15) | 2.768(2) | 2.765(3) | 2.770(4) |
| Yb-S1 | 2.6875(17) | 2.6886(17) | 2.6983(19) | 2.7007(19) | 2.708(2) | 2.696(4) | 2.716(5) |
| Yb-S2(3)×2 | 2.622(6) | 2.626(4) | 2.634(4) | 2.627(4) | 2.626(4) | 2.626(9) | 2.627(8) |
| Yb-S2(3) | 2.649(8) | 2.647(6) | 2.648(6) | 2.646(5) | 2.640(6) | 2.658(14) | 2.642(11) |
| Yb ~ Yb | 3.9393(3) | 3.9216(6) | 3.9223(4) | 3.9140(4) | 3.9085(4) | 3.9218(6) | 3.8976(6) |
| Ln ~ Yb | 3.9323(4) | 3.673(14) | 3.647(8) | 3.627(7) | 3.565(5) | 3.80(5) | 3.545(4) |
| Ln ~ Ln | 3.9393(3) | 3.9216(6) | 3.9223(4) | 3.9140(4) | 3.9085(4) | 3.9218(6) | 3.8976(6) |

Table 9.3b. Selected Bond Distances (Å) for Cs_{0.14-0.17}Ln_{0.26-0.33}YbS₂ (Ln = Tb, Dy, Ho, Er, Tm, Yb).

| Formula | Cs _{0.15} Tb _{0.29} YbS ₂ | Cs _{0.16} Dy _{0.28} YbS ₂ | Cs _{0.16} Ho _{0.30} YbS ₂ | Cs _{0.17} Er _{0.32} YbS ₂ | Cs _{0.15} Tm _{0.26} YbS ₂ | Cs _{0.15} Yb _{0.26} YbS ₂ |
|------------|--|--|--|--|--|--|
| Cs-S2×3 | 3.711(8) | 3.74(2) | 3.73(2) | 3.70(4) | 3.703(6) | 3.685(6) |
| Cs-S3×6 | 3.616(7) | 3.646(19) | 3.64(2) | 3.67(3) | 3.670(6) | 3.659(5) |
| Ln-S1×2 | 2.639(8) | 2.633(6) | 2.637(5) | 2.686(7) | 2.682(9) | 2.667(5) |
| Ln-S1×2 | 2.859(12) | 2.877(10) | 2.886(9) | 2.892(13) | 2.908(19) | 2.918(16) |
| Ln-S1×2 | 3.073(5) | 3.076(5) | 3.079(5) | 3.095(6) | 3.063(11) | 3.054(11) |
| Ln -S2 | 3.086(10) | 3.08(2) | 3.10(2) | 3.16(4) | 3.166(16) | 3.186(17) |
| Ln -S2 | 3.427(17) | 3.40(3) | 3.41(3) | 3.48(4) | 3.42(3) | 3.41(2) |
| Ln -S2 | 3.684(12) | 3.68(2) | 3.71(2) | 3.72(4) | 3.686(13) | 3.710(9) |
| Yb-S1×2 | 2.764(2) | 2.770(2) | 2.772(2) | 2.768(2) | 2.7634(18) | 2.7587(18) |
| Yb-S1 | 2.710(3) | 2.714(3) | 2.717(3) | 2.706(3) | 2.699(2) | 2.694(2) |
| Yb-S2(3)×2 | 2.621(4) | 2.622(7) | 2.625(7) | 2.625(10) | 2.620(4) | 2.618(4) |
| Yb-S2(3) | 2.636(6) | 2.641(6) | 2.648(6) | 2.656(8) | 2.643(4) | 2.640(7) |
| Yb ~ Yb | 3.8894(6) | 3.8926(7) | 3.8976(7) | 3.9038(4) | 3.9026(5) | 3.8932(5) |
| Ln ~ Yb | 3.535(6) | 3.534(4) | 3.540(3) | 3.596(4) | 3.595(5) | 3.5819(15) |
| Ln ~ Ln | 3.8894(6) | 3.8926(7) | 3.8976(7) | 3.9038(4) | 3.9026(5) | 3.8932(5) |

When $\text{Ln} = \text{La}$, the cations reside in the center of the pseudo-triangular channel (or 2d site), and are coordinated to nine S atoms in a tricapped trigonal prism arrangement. However, the atoms are disordered over three 6h sites in a triangular shape for $\text{Ln} = \text{Ce} - \text{Yb}$ in order to fit into the channel, which is illustrated in Figure 9.3. This results in large distortions of the polyhedra. The Ln–S distances range from 3.097(3) Å ($\text{Ln} = \text{La}$) to 3.04(1) Å ($\text{Ln} = \text{Dy}$). These distances are longer than Shannon's values especially for the later cases, 3.06 Å ($X = \text{La}$) to 2.88 Å ($X = \text{Yb}$), using Ln^{3+} in nine-coordinate S environments.⁵⁴ The Yb(1) sites have distorted octahedral geometries with normal Yb–S distances ranging from 2.693(5) Å to 2.681(4) Å.

The unit cell volume and Yb(1)–Yb(1) distances are plotted in Figure 9.4 to identify standard systematic changes associated with the lanthanide contraction. It is worth noting that the minor percentage of Ln in the compound and the confinement of the channel framework remarkably limit the effect of the lanthanide contraction on these parameters, so the experimental errors are considerable. Both plots are quite consistent with each other. For the early lanthanides, the data follow the trends of lanthanide contraction except Eu. In the later cases, large deviations are found. The large deviation at Eu can be ascribed to divalent or mixed-valent +2/+3 character, an occurrence that is common in chalcogenides, and consistent with the bond-valence sum of 2.50.⁵⁵ Yb(2) could be divalent also, with a bond-valence sum of 2.19. However, it is much less likely for $\text{Ln} = \text{Dy} - \text{Tm}$ to be anything other than +3, even though their valence sums were calculated to be 2.65, 2.68, 2.31, and 2.28, respectively. For these cases, disorder of Ln into the Yb(1) sites might be one of the reasons for the deviation, considering their similar sizes. It is far better to interpret the oxidation state of Ln from magnetic

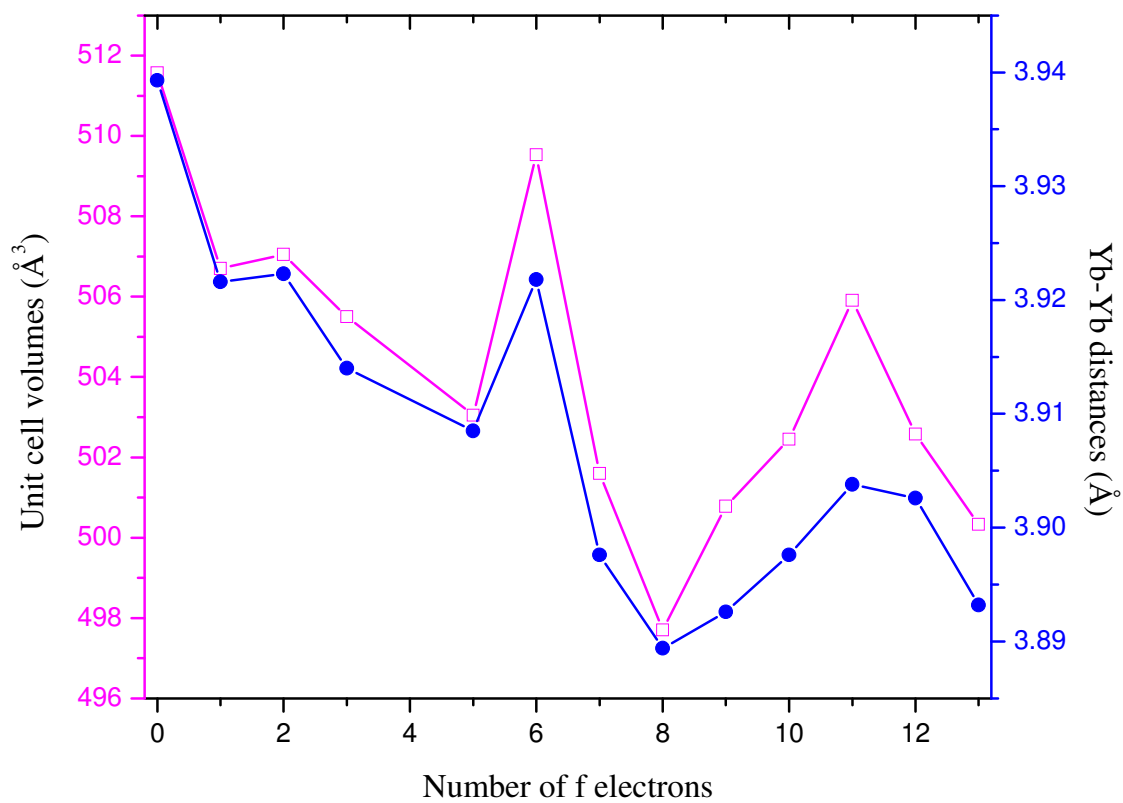


Figure 9.4. Unit cell volumes (Å³) and Yb~Yb distances (Å) vs the number of f electrons for Cs_{0.14-0.17}Ln_{0.26-0.33}YbS₂ (Ln = La, Ce, Pr, Nd, Sm, Eu, Gd, Tb, Dy, Ho, Er, Tm).

susceptibility and XANES measurements described in this work. S–S bonds are absent in the structure of $\text{Cs}_x\text{Ln}_y\text{YbS}_2$, and therefore the formal oxidation states of Cs/X/Yb/S are ideally +1/+3/+3/–2, except when $\text{Ln} = \text{Eu}$.

Magnetic Properties. Recently, $\text{A}^{\text{II}}\text{Ln}^{\text{III}}_2\text{O}_4$ ($\text{A} = \text{Sr}, \text{Ba}$), which crystallize in CaFe_2O_4 structure-type, were recognized as potentially geometrically frustrated systems because of their triangular Ln^{3+} sublattice and lack of long-range magnetic ordering at low temperatures.^{57,58} As previously mentioned, $\text{Cs}_x\text{Ln}_y\text{YbS}_2$ and EuYb_2S_4 (CaFe_2O_4 structure-type) are structurally related. Both structures have similar three-dimensional Yb^{3+} triangles, as shown in Figure 9.5. In contrast to EuYb_2S_4 , which contains two different double-octahedra chains, $\text{Cs}_x\text{Ln}_y\text{YbS}_2$ has one double chain even though the Yb–Yb distances are comparable in these two systems. Another factor that may soften the geometric frustration is that the triangular coordination is not perfect: there is a distribution of Yb–Yb bond lengths and other asymmetries that will at least partially remove the requirement of equal magnetic interactions for frustration to occur. In any case, Yb–Yb distances vary with the size of cations in the channels in the series $\text{Cs}_x\text{Ln}_y\text{YbS}_2$. The shortest Yb–Yb distances within the triangles range from 3.9393(3) Å ($\text{Cs}_{0.14}\text{La}_{0.30}\text{YbS}_2$) to 3.8994(6) Å ($\text{Cs}_{0.15}\text{Tb}_{0.29}\text{YbS}_2$). These distances can be reduced by using smaller alkali metal cations. For $\text{Cs}_{0.14}\text{La}_{0.30}\text{YbS}_2$, the Yb–Yb distances along the spines of the chains are 0.2 Å shorter than that between Yb^{3+} in parallel spines. This may allow for one-dimensional magnetic interactions. The interchain Yb–Yb distances are approximately 0.6 Å longer than the intrachain ones. Magnetic coupling across the double-octahedra chains should be weaker. In addition to the $\text{Yb}(1)^{3+}$ lattice, the larger Ln cations (except La) are also paramagnetic. There are potentially some Ln–Ln and Ln–

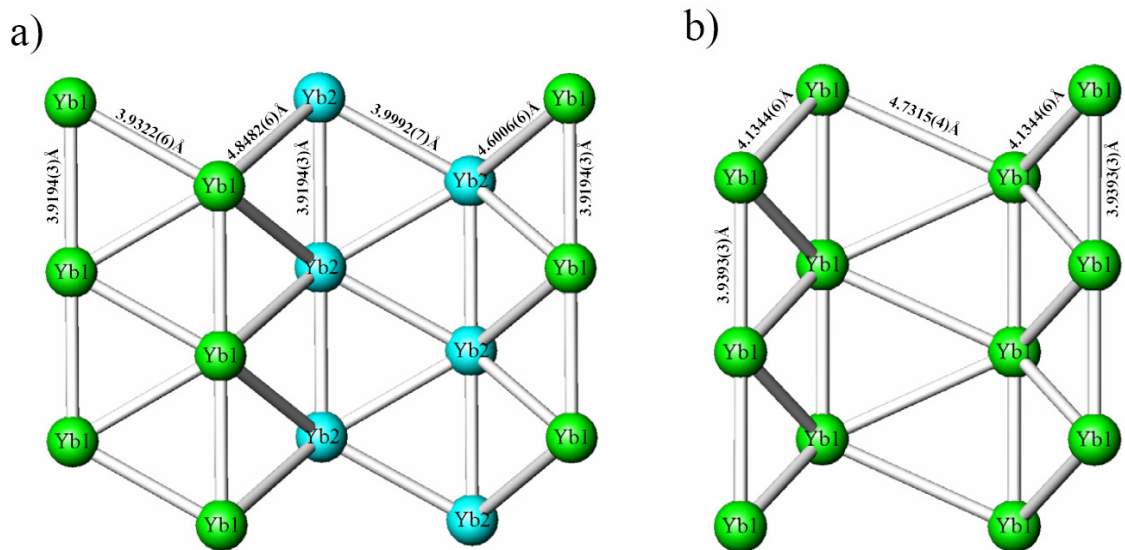


Figure 9.5. a) An illustration of the Yb^{3+} cations net work along the b axis with Yb-Yb distances labeled for EuYb_2S_4 . b) An drawing of the Yb^{3+} cations network along the c axis with Yb-Yb distances labeled for $\text{Cs}_{0.14}\text{La}_{0.30}\text{YbS}_2$.

Yb(1) interactions within the small channels too, which makes the $\text{Cs}_x\text{Ln}_y\text{YbS}_2$ system more complicated than $\text{A}^{\text{II}}\text{Ln}^{\text{III}}_2\text{O}_4$ ($\text{A} = \text{Sr}, \text{Ba}$)^{57,58}. The Ln–Ln distances range from 3.9223(4) Å (in $\text{Cs}_{0.14}\text{Pr}_{0.30}\text{YbS}_2$) to 3.8894(6) Å (in $\text{Cs}_{0.15}\text{Tb}_{0.29}\text{YbS}_2$), while Ln–Yb distances are in the range of 3.80(5) Å (in $\text{Cs}_{0.16}\text{Eu}_{0.33}\text{YbS}_2$) to 3.534(4) Å (in $\text{Cs}_{0.16}\text{Dy}_{0.28}\text{YbS}_2$). The magnetic coupling in $\text{Cs}_x\text{Ln}_y\text{YbS}_2$ compounds within the three-dimensional triangular Yb^{3+} lattice is potentially weakly frustrated.

Magnetic susceptibility data were all collected at 5 kG applied field after verifying linearity of M vs. H . There is a decrease in slope at higher fields due to a Brillouin-type saturation of the paramagnetic moments. All the data show a deviation from Curie-Weiss behavior around 50 K, as shown in Figure 9.6. Except for the $\text{Cs}_{0.15}\text{Tb}_{0.29}\text{YbS}_2$ data, all can be described as starting at RT from a full-moment state with a negative Weiss temperature, cooling through a state near 50 K where the moment and the Weiss temperature decrease. Table 9.4 shows the magnetic parameters for $\text{Cs}_x\text{Ln}_y\text{YbS}_2$, which were obtained from fitting the data in the range of 100 K and 300 K to the Curie-Weiss law. The θ_p values range from -14.2(3) K (for $\text{Cs}_{0.15}\text{Gd}_{0.29}\text{YbS}_2$) to -45(2) K (for $\text{Cs}_{0.15}\text{Yb}_{0.26}\text{YbS}_2$) without any indication of long-rang magnetic ordering down to 2 K. This suppression is consistent with a geometrically spin-frustrated system. As a cautionary note the observed $|\theta_p|$ value may be large due to the deviations from the Curie-Weiss law caused by a crystal-field splitting of the full $J=7/2$ multiplet for the Yb^{3+} , and possibly the other magnetic atoms. The experimental effective magnetic moments are all close to that expected for full moment Yb and the Ln-atom, except for some deviations were observed for $\text{Cs}_{0.15}\text{Gd}_{0.29}\text{YbS}_2$, $\text{Cs}_{0.16}\text{Dy}_{0.28}\text{YbS}_2$ and

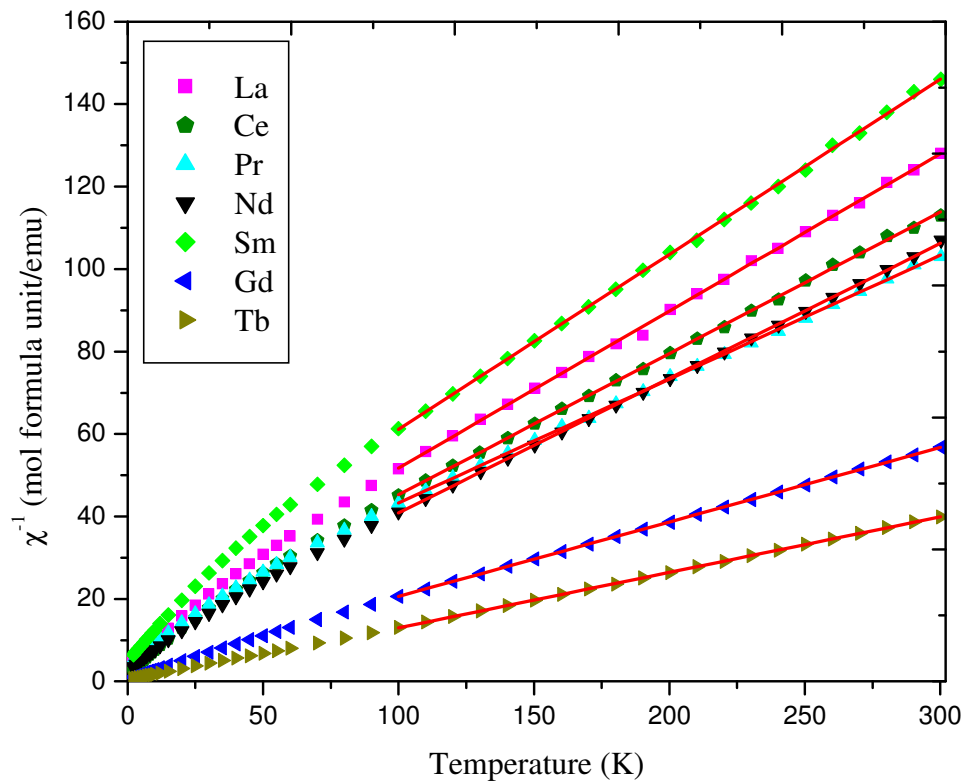


Figure 9.6. a) Plots of dc inverse molar magnetic susceptibility for $\text{Cs}_{0.14-0.17}\text{Ln}_{0.26-0.33}\text{YbS}_2$ ($\text{Ln} = \text{La}, \text{Ce}, \text{Pr}, \text{Nd}, \text{Sm}, \text{Gd}, \text{Tb}$) under an applied field of 0.5 T. The straight lines represent fits of the inverse susceptibility to the Curie-Weiss law in the high temperature rang of 100-300 K.

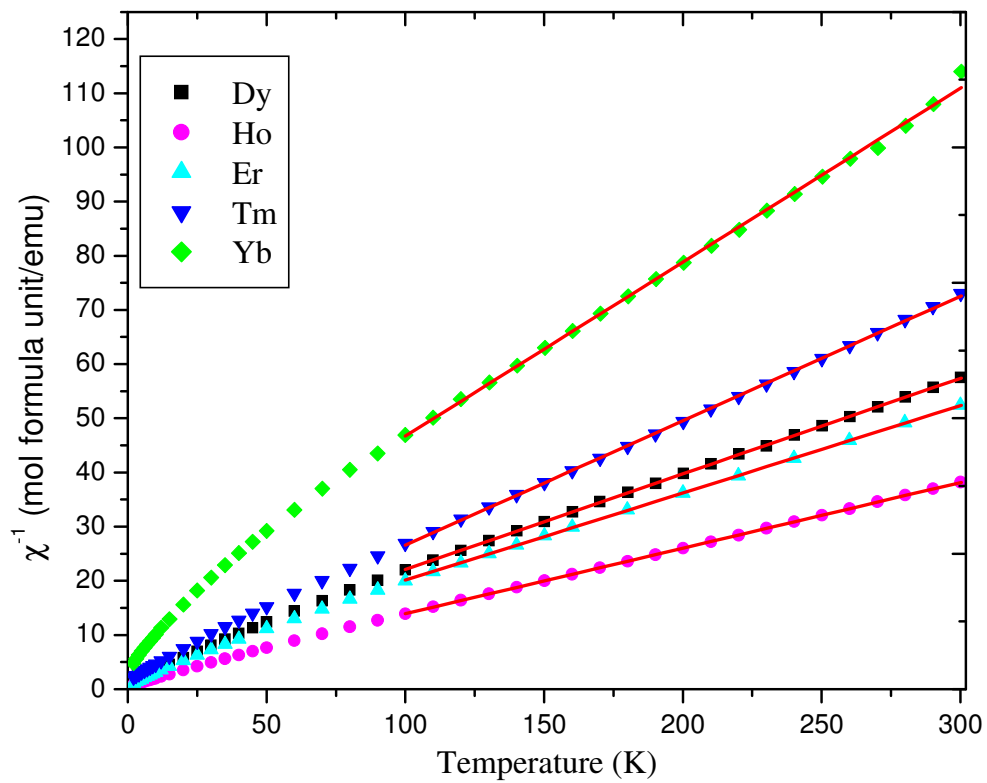


Figure 9.6. b) Plots of dc inversed molar magnetic susceptibility for $\text{Cs}_{0.14-0.17}\text{Ln}_{0.26-0.33}\text{YbS}_2$ (Ln = Dy, Ho, Er, Tm, Yb) under an applied field of 0.5 T. The straight lines represent fits of the inverse susceptibility to the Curie-Weiss law in the high temperature rang of 100-300 K.

Table 9.4. Magnetic Parameters for $\text{Cs}_{0.14-0.17}\text{Ln}_{0.26-0.33}\text{YbS}_2$ (Ln = La, Ce, Pr, Nd, Sm, Gd, Tb, Dy, Ho, Er, Tm, Yb).

| Formula | $P_{\text{cal}}/\mu_{\text{B}}$ | $P_{\text{eff}}/\mu_{\text{B}}$ | θ_{p} | R^2 |
|--|---------------------------------|---------------------------------|---------------------|---------|
| $\text{Cs}_{0.14}\text{La}_{0.30}\text{YbS}_2$ | 4.54 | 4.59(2) | -36(1) | 0.99938 |
| $\text{Cs}_{0.14}\text{Ce}_{0.30}\text{YbS}_2$ | 4.75 | 4.832(8) | -32(1) | 0.99955 |
| $\text{Cs}_{0.14}\text{Pr}_{0.30}\text{YbS}_2$ | 4.94 | 5.161(8) | -44.2(9) | 0.99974 |
| $\text{Cs}_{0.14}\text{Nd}_{0.29}\text{YbS}_2$ | 4.94 | 4.950(6) | -25.2(6) | 0.99986 |
| $\text{Cs}_{0.15}\text{Sm}_{0.29}\text{YbS}_2$ | 4.56 | 4.344(9) | -44(1) | 0.99966 |
| $\text{Cs}_{0.15}\text{Gd}_{0.29}\text{YbS}_2$ | 6.24 | 6.657(4) | -14.2(3) | 0.99997 |
| $\text{Cs}_{0.15}\text{Tb}_{0.29}\text{YbS}_2$ | 6.93 | 7.708(5) | 3.4(4) | 0.99993 |
| $\text{Cs}_{0.16}\text{Dy}_{0.28}\text{YbS}_2$ | 7.23 | 6.726(5) | -24.8(3) | 0.99996 |
| $\text{Cs}_{0.16}\text{Ho}_{0.30}\text{YbS}_2$ | 7.37 | 8.123(5) | -14.9(3) | 0.99997 |
| $\text{Cs}_{0.17}\text{Er}_{0.32}\text{YbS}_2$ | 7.07 | 7.042(6) | -24.6(4) | 0.99996 |
| $\text{Cs}_{0.15}\text{Tm}_{0.26}\text{YbS}_2$ | 5.96 | 5.898(7) | -15.7(7) | 0.9998 |
| $\text{Cs}_{0.15}\text{Yb}_{0.26}\text{YbS}_2$ | 5.10 | 4.99(2) | -45(2) | 0.99842 |

^a P_{cal} and P_{eff} : calculated and experimental effective magnetic moments per formula unit.

^b Weiss constant (θ_{p}) and goodness of fit (R^2) obtained from high temperature (100-300 K) data.

$\text{Cs}_{0.16}\text{Ho}_{0.30}\text{YbS}_2$. Splitting of the ground state terms for magnetic ions and disorder of Ln into the Yb(1) sites might be the reasons for such differences.

$\text{Cs}_{0.15}\text{Tb}_{0.29}\text{YbS}_2$ is different from the other compounds, with a slightly positive Weiss temperature 3.4(4) K in the high-temperature (HT) state, and an increase of the susceptibility as it is cooled through the ~50 K point. The observed moment (7.708(5) μ_B) is considerably larger than the calculated value (6.93 μ_B). All these behaviors could be due to strong ferromagnetic interactions among the Tb^{3+} and Yb^{3+} ions. One piece of supporting evidence for this argument is that $\text{Cs}_{0.15}\text{Tb}_{0.29}\text{YbS}_2$ has the shortest distances between magnetic atoms, as is shown in Figure 9.4 and Table 9.3.

XANES. Lanthanide LIII-edge X-ray absorption spectroscopy is commonly used to determine their valence state, and can be used to verify the results from magnetic susceptibility measurements. The focus is on the lanthanides that can be in more than one valence state, and we have chosen to focus on cerium, samarium, and ytterbium, along with neodymium for comparison. The normalized, energy-calibrated spectra of $\text{Cs}_{0.14}\text{Ce}_{0.30}\text{YbS}_2$, $\text{Cs}_{0.14}\text{Nd}_{0.29}\text{YbS}_2$, and $\text{Cs}_{0.15}\text{Sm}_{0.29}\text{YbS}_2$ (Figure 9.7, 9.8) support the conclusion that all lanthanides in these samples are in their trivalent state. This result is particularly clear in the Ce L_{III} edge data because the character of spectra from formally tetravalent cerium samples (such as the CeO_2 data in Figure 9.7(a)) includes a predominantly double-peaked structure with the first clear maximum at about 5727 eV, whereas trivalent cerium spectra contain a dominant single peak at about 5722 eV (Figure 9.7). There is no evidence of a peak at 5727 eV in the Ce L_{III} spectrum of $\text{Cs}_{0.14}\text{Ce}_{0.30}\text{YbS}_2$ (Fig. 7(a)). Nd and Sm L_{III} edge spectra also are dominated by a single peak, and the measured peak positions of 6210 eV and 6718 eV are consistent only with a

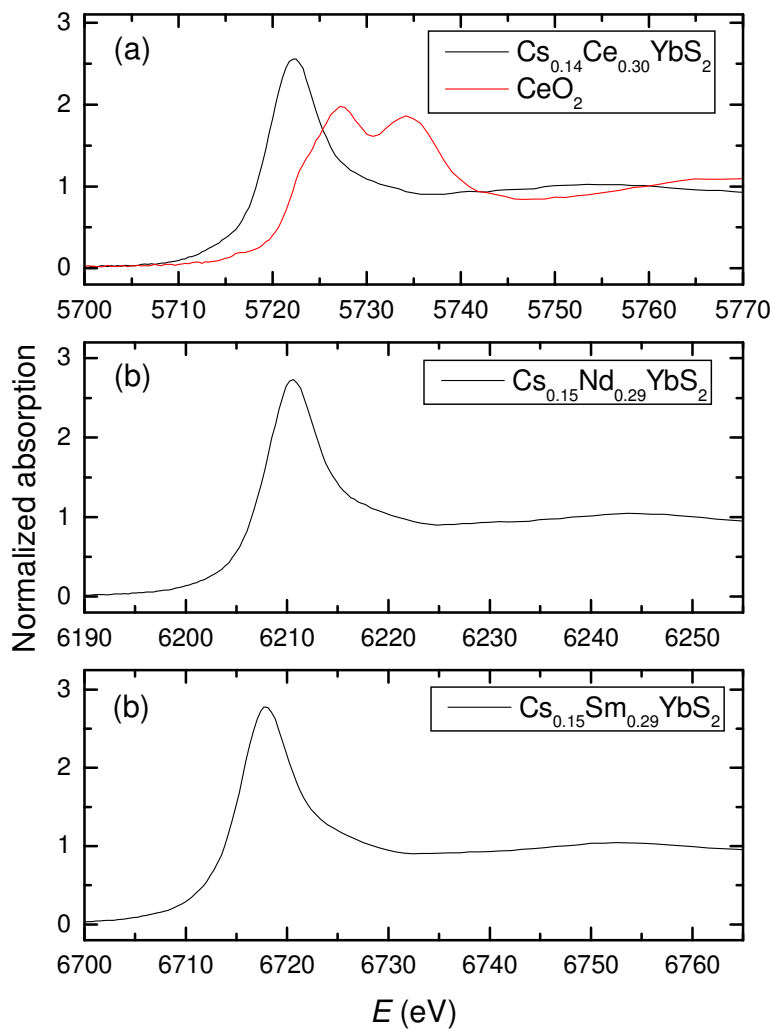


Figure 9.7. Ce, Nd, and Sm L_{III} edge x-ray absorption spectra of (a) $\text{Cs}_{0.14}\text{Ce}_{0.30}\text{YbS}_2$, (b) $\text{Cs}_{0.14}\text{Nd}_{0.29}\text{YbS}_2$, and (c) $\text{Cs}_{0.15}\text{Sm}_{0.29}\text{YbS}_2$, respectively. Also shown in (a) is the spectrum of CeO_2 as a reference. All data are calibrated to the first inflection point of the Nd L_{III} edge of Nd_2O_3 at 6208 eV. The sulfide spectra are consistent with a fully trivalent state for the relevant lanthanide.

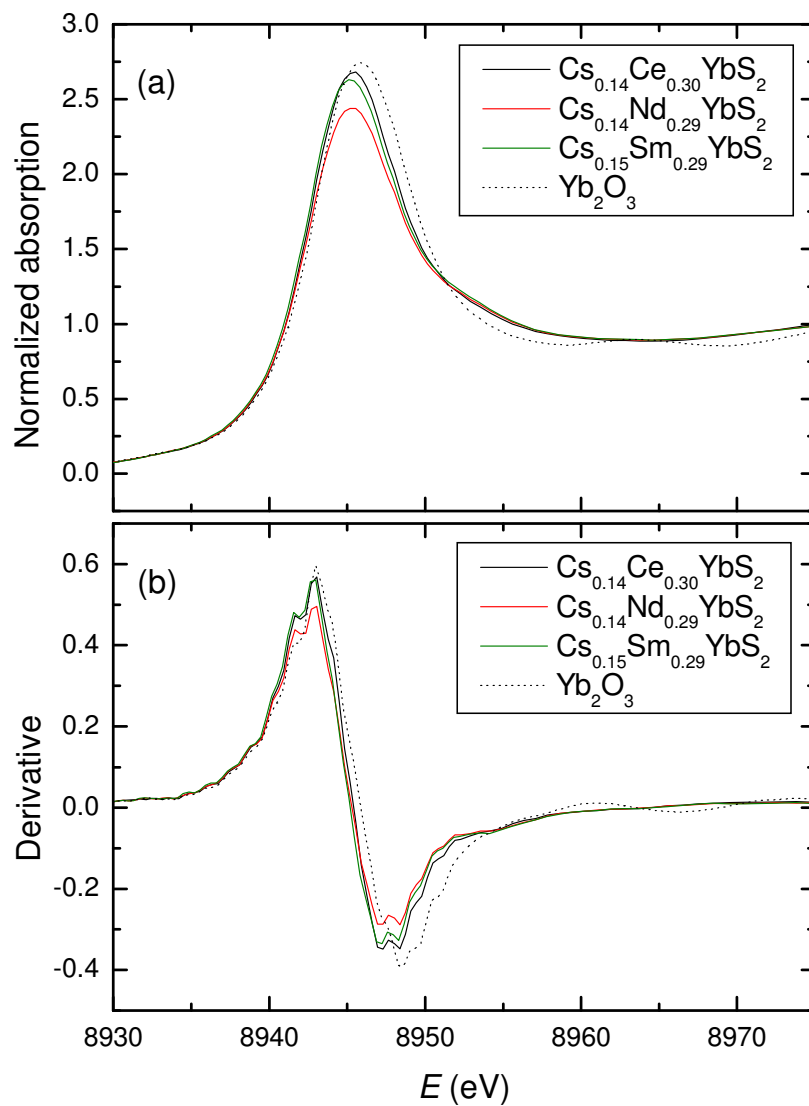


Figure 9.8. (a) Yb L_{III} edge spectra of the same samples in Fig. 7, and (b) the derivative of these spectra. These data are calibrated to the first inflection point of the Yb L_{III} edge of Yb_2O_3 at 8943 eV.

trivalent state.⁶⁸ The L_{III} threshold energy is about 8 eV lower in Sm(II) than Sm(III),⁶⁹ and we see no evidence of such a peak in the $\text{Cs}_{0.15}\text{Sm}_{0.29}\text{YbS}_2$ spectrum. A similar shift is expected in Yb L_{III} spectra between Yb(II) and Yb(III), and would appear as a shoulder on the main absorption edge Figure 9.8(a).⁷⁰ To emphasize this point, the derivative spectra in Figure 9.8(b) show no inflection point at the expected Yb(II) position of 8936 eV, below the main trivalent feature at 8943 eV.

Optical Properties. Many ternary alkali metal rare-earth chalcogenides have been synthesized, but few of them have had their optical properties examined in detail.⁵⁹⁻⁶⁷ Early work by B. Deng et al. have shown that RbLnSe_2 (Ln = La, Ce, Pr, Nd, Sm, Gd, Tb, Ho, Er, Lu) are direct band gap semiconductors.⁶⁷ The absorption in these compounds was attributed as the transition from a Se^{2-} valence band to a Ln^{3+} conduction band. Therefore the band gaps in the series ALnQ_2 is tunable based on the choice of lanthanide ion and chalcogen, which is also true for other ternary and quaternary chalcogenides.

In this present study, only the larger lanthanide site in $\text{Cs}_x\text{Ln}_y\text{YbS}_2$ has been systematically varied. The optical band gaps were measured using UV-vis-NIR spectroscopy. The gap of $\text{Cs}_{0.14}\text{Ce}_{0.30}\text{YbS}_2$ was determined to be approximately 2.1 eV and $\text{Cs}_{0.14}\text{La}_{0.30}\text{YbS}_2$, $\text{Cs}_{0.14}\text{Pr}_{0.30}\text{YbS}_2$, $\text{Cs}_{0.14}\text{Nd}_{0.29}\text{YbS}_2$, $\text{Cs}_{0.15}\text{Sm}_{0.29}\text{YbS}_2$ are ~2.3 eV, which are consistent with their red and yellow colors. For the brown compounds, the measured values of $\text{Cs}_{0.15}\text{Gd}_{0.29}\text{YbS}_2$, $\text{Cs}_{0.15}\text{Tb}_{0.29}\text{YbS}_2$ and $\text{Cs}_{0.16}\text{Dy}_{0.28}\text{YbS}_2$ are between 2.3 and 2.4 eV, while the band gap of $\text{Cs}_{0.16}\text{Ho}_{0.30}\text{YbS}_2$, $\text{Cs}_{0.17}\text{Er}_{0.32}\text{YbS}_2$, $\text{Cs}_{0.15}\text{Tm}_{0.26}\text{YbS}_2$ are about 2.2 eV. The brown color might be due to the absorptions before 2.0 eV, which are not shown in Figure 9.9. These band gaps are comparable to the

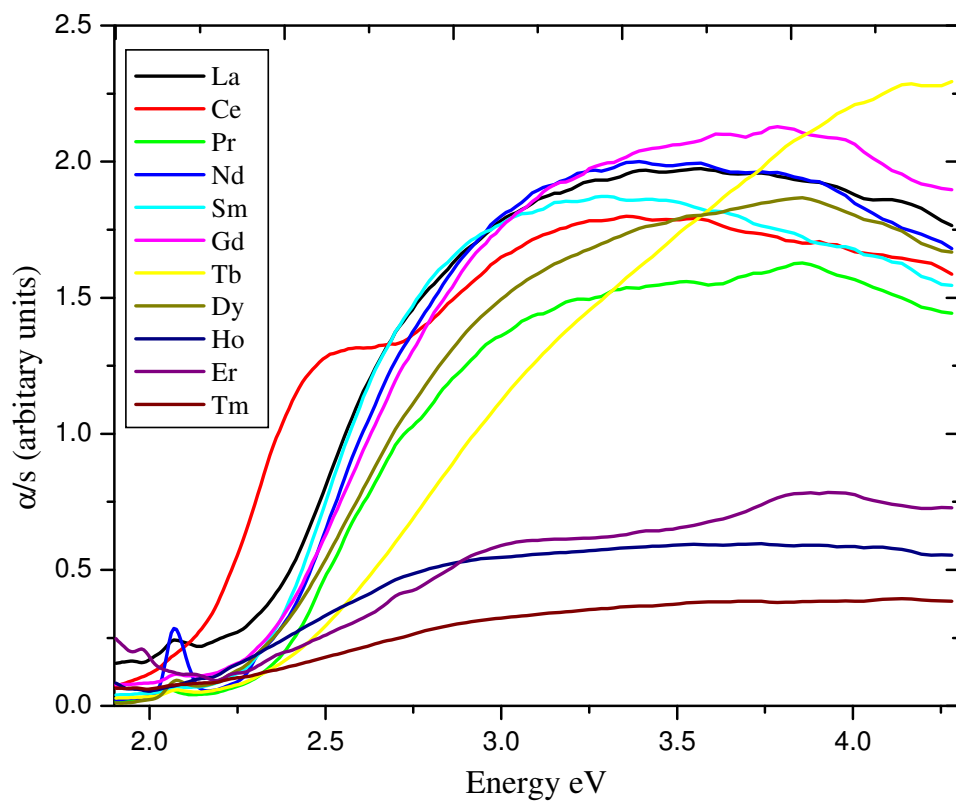


Figure 9.9 UV-vis diffuse reflectance spectra of $\text{Cs}_{0.14-0.17}\text{Ln}_{0.26-0.33}\text{YbS}_2$ (Ln = La, Ce, Pr, Nd, Sm, Gd, Tb, Dy, Ho, Er, Tm).

values reported for red NaCeS₃ (2.15 eV) and yellow NaLaS₃ (2.61 eV).⁶⁶ The Ce compounds often show the smallest band gaps of the series owing the high energy of the 4f¹ electron. The fine structure in these spectra are f-f transitions for the lanthanide ions.

CONCLUSIONS

In this present work we have prepared a new family of interlanthanide sulfide, Cs_xLn_yYbS₂ (x = 0.14 – 0.16; Ln = La-Nd, Sm-Yb; y = 0.26 – 0.33), using CsCl flux. These compounds are partially-filled mixed-lanthanide variants of the K₂Tm_{23.33}S₃₆ structure-type. The three-dimensional channel structure of Cs_xLn_yYbS₂ is constructed from one-dimensional edge-shared double rutile chains of [YbS₆] octahedral. Each chain is connected to four other identical neighbors to form two different hexagonal channels. The larger channels are nearly filled with Cs⁺ cations while the other is only partially filled with lanthanide (Ln) ions. In all but one of these compounds the magnetic interactions are antiferromagnetic in nature. However, in Cs_{0.15}Tb_{0.29}YbS₂ the coupling is ferromagnetic. The trivalency of all lanthanides for Cs_{0.14}Ce_{0.30}YbS₂, Cs_{0.14}Nd_{0.29}YbS₂, and Cs_{0.15}Sm_{0.29}YbS₂ have been confirmed by XANES measurements. The band gaps for these compounds are relatively constant except for the Ce-analog, which possess a notably smaller gap than the other compounds.

REFERENCES

1. Ramirez, A.P. in *Handbook of Magnetic Materials*, edited by K. J. H. Buschow (Elsevier, Amsterdam, 2001), Vol. 13.
2. Schiffer, P.; Ramirez, A. P. *Comments Condens. Matter Phys.* **1996**, *18*, 21.
3. Lau, G. C.; Freitas, R. S.; Ueland, B. G.; Schiffer, P.; Cava, R. J. *Phys. Rev. B* **2005**, *72*, 54411.
4. Buttgen, N.; Hemberger, J.; Fritsch, V.; Krimmel, A.; Mucksch, M.; Krug von Nidda, H. A.; Lunkenheimer, P.; Fichtl, R.; Tsurkan, V.; Loidl, A. *New J. Phys.* **2004**, *6*, 191.
5. Fritsch, V.; Hemberger, J.; Buttgen, N.; Scheidt, E. W.; Krug von Nidda, H. A.; Loidl, A.; Tsurkan, V. *Phys. Rev. Lett.* **2004**, *92*, 116401.
6. Tsurkan, V.; Mucksch, M.; Fritsch, V.; Hemberger, J.; Klemm, M.; Klimm, S.; Korner, S.; Krug von Nidda, H. A.; Samusi, D.; Scheidt, E. W.; Loidl, A.; Horn, S.; Tidecks, R. *Phys. Rev. B* **2003**, *68*, 134434.
7. Martinho, H.; Moreno, N. O.; Sanjurjo, J. A.; Rettori, C.; Garcia-Adeva, A. J.; Huber, D. L.; Oseroff, S. B.; Ratcliff II, W.; Cheong, S. W.; Pagliuso, P. G.; Sarrao, J. L.; Martins, G. B. *Phys. Rev. B* **2001**, *64*, 024408.
8. Wills, A. S.; Raju, N. P.; Morin, C. J.; Greedan, E. *Chem. Mater.* **1999**, *11*, 1936.
9. Hamedoun, M.; Silimani, M.; Sayouri, S.; Benyoussef, A. *Physica Status Solidi A: Applied Research* **1994**, *144*, 441.
10. Ostorero, J.; Mauger, A.; Guillot, M.; Derory, A.; Escorne, M.; Marchand, A. *Phys. Rev. B* **1989**, *40*, 391.
11. Pawlak, L.; Duczmal, M.; Zygmunt, A. *J. Magn. Magn. Mater.* **1988**, *76-7*, 199.

12. Bendor, L.; Shilo, I.; Felner, I. *J. Solid State Chem.* **1981**, *39*, 257.
13. Bendor, L.; Shilo, I. *J. Solid State Chem.* **1980**, *35*, 278.
14. Pokrzywnicki, S.; Pawlak, L.; Czopnik, A. *Physica B & C* **1977**, *86*, 1141.
15. Snyder, J.; Ueland, B. G.; Mizel, A.; Slusky, J. S.; Karunadasa, H.; Cava, R. J.; Schiffer, P. *Phys. Rev. B* **2004**, *70*, 184431.
16. Snyder, J.; Ueland, B. G.; Slusky, J. S.; Karunadasa, H.; Cava, R. J.; Schiffer, P. *Phys. Rev. B* **2004**, *69*, 064414.
17. Champion, J. D. M.; Harris, M. J.; Holdsworth, P. C. W.; Wills, A. S.; Balakrishnan, G.; Bramwell, S. T.; Cizmar, E.; Fennell, T.; Gardner, J. S.; Lago, J.; McMorro, D. F.; Orendac, M.; Orendacova, A.; Paul, D. McK.; Smith, R. I.; Telling, M. T. F.; Wildes, A. *Phys. Rev. B* **2003**, *68*, 020401(R).
18. Sakakibara, T.; Tayama, T.; Hiroi, Z.; Matsuhira, K.; Takagi, S. *Phys. Rev. Lett.* **2003**, *90*, 207205.
19. Snyder, J.; Ueland, B. G.; Slusky, J. S.; Karunadasa, H.; Cava, R. J.; Mizel, A.; Schiffer, P. *Phys. Rev. Lett.* **2003**, *91*, 107201.
20. Taira, N.; Wakeshima, M.; Hinatsu, Y. *J. Mater. Chem.* **2002**, *12*, 1475.
21. Ramirez, A. P.; Shastri, B. S.; Hayashi, A.; Krajewski, J. J.; Huse, D. A.; Cava, R. J. *Phys. Rev. Lett.* **2002**, *89*, 067202.
22. Hodges, J. A.; Bonville, P.; Forget, A.; Yaouanc, A.; Dalmas de Reotier, P.; Andre, G.; Rams, M.; Krolas, K.; Ritter, C.; Gubbens, P. C. M.; Kaiser, C. T.; King, P. J. C.; Baines, C. *Phys. Rev. Lett.* **2002**, *88*, 077204.
23. Fukazawa, H.; Melko, R. G.; Higashinaka, R.; Maeno, Y.; Gingras, M. J. P. *Phys. Rev. B* **2002**, *65*, 054410.

24. Bramwell, S. T.; Gingras, M. J. P. *Science* **2001**, *294*, 1495.
25. Snyder, J.; Slusky, J. S.; Cava, R. J.; Schiffer, P. *Nature* **2001**, *413*, 48.
26. Matsuhira, K.; Hinatsu, Y.; Tenya, K.; Sakakibara, T. *J. Phys.: Condens. Matter* **2000**, *12*, L649.
27. Gingras, M. J. P.; den Hertog, B. C.; Faucher, M.; Gardner, J. S.; Dunsiger, S. R.; Chang, L. J.; Gaulin, B. D.; Raju, N. P.; Greedan, J. E. *Phys. Rev. B* **2000**, *62*, 6496.
28. Ramirez, A. P.; Hayashi, A.; Cava, R. J.; Siddharthan, R.; Shastry, B. S. *Nature* **1999**, *399*, 333.
29. Taira, N.; Wakeshima, M.; Hinatsu, Y. *J. Phys.: Condens. Matter* **1999**, *11*, 6983.
30. Harris, M. J.; Bramwell, S. T.; Holdsworth, P. C. W.; Champion, J. D. M. *Phys. Rev. Lett.* **1998**, *81*, 4496.
31. Bramwell, S. T.; Harris, M. J. *J. Phys. Condens. Matter* **1998**, *10*, L215.
32. Harris, M. J.; Bramwell, S. T.; McMorro, D. F.; Zeiske, T.; Godfrey, K. W. *Phys. Rev. Lett.* **1997**, *79*, 2554.
33. Greedan, J. E.; Raju, N. P.; Maignan, A.; Simon, Ch.; Pedersen, J.S.; Niraimathi, A. N.; Melin, E. G.; Subramanian, M.A. *Phys. Rev. B* **1996**, *54*, 7189.
34. Harris, M. J.; Zinkin, M. P.; Tun, Z.; Wanklyn, B. M.; Swainson, I. P. *Phys. Rev. Lett.* **1994**, *73*, 189.
35. Gaulin, B. D.; Reimers, J. N.; Mason, T. E.; Greedan, J. E.; Tun, Z. *Phys. Rev. Lett.* **1992**, *69*, 3244.

36. Greedan, J. E.; Greedan, J. E.; Reimers, J. N.; Stager, C. V.; Penny, S. L. *Phys. Rev. B* **1991**, *43*, 5682.
37. J. E. Greedan, *J. Mater. Chem.* **2001**, *11*, 37.
38. Schiffer, P.; Ramirez, A. P. *Comments Condens. Matter Phys.* **1996**, *18*, 21.
39. Ramirez, A. P. *Annu. Rev. Mater. Sci.* **1994**, *24*, 453.
40. Shores, M. P.; Nytko, E. A.; Bartlett, B. M.; Nocera, D. G. *J. Am. Chem. Soc.* **2005**, *127*, 13462.
41. Elhajal, M.; Canals, B.; Sunyer, R.; Lacroix, C. *Phys. Rev. B* **2005**, *71*, 094420.
42. Elhajal, M.; Canals, B.; Lacroix, C. *J. Phys.: Condens. Matter* **2004**, *16*, S917.
43. Elhajal, M.; Canals, B.; Lacroix, C. *Phys. Rev. B* **2002**, *66*, 014422.
44. Bartlett, B. M.; Nocera, D. G. *J. Am. Chem. Soc.* **2005**, *127*, 8985.
45. Grohol, D.; Matan, K.; Cho, J.-H.; Lee, S.-H.; Lynn, J. W.; Nocera, D. G.; Lee, Y. S.; *Nat. Mater.* **2005**, *4*, 323.
46. Grohol, D.; Nocera, D. G.; Papoutsakis, D. *Phys. Rev. B* **2003**, *67*, 064401.
47. Inami, T.; Nishiyama, M.; Maegawa, S.; Oka, Y. *Phys. Rev. B* **2000**, *61*, 12181.
48. Wills, A. S.; Harrison, A.; Ritter, C.; Smith, R. I. *Phys. Rev. B* **2000**, *61*, 6156.
49. Lau, G. C.; Ueland, B. G.; Freitas, R. S.; Dahlberg, M. L.; Schiffer, P.; Cava, R. J. *Phys. Rev. B* **2006**, *73*, 012413.
50. Lemoine, Per P.; Tomas, A.; Carre, D.; Vovan Et M. Guittard, T. *Acta Cryst. C* **1989**, *45*, 350.
51. Sheldrick, G. M. *SHELLXTL PC, Version 6.12, An Integrated System for Solving, Refining, and Displaying Crystal Structures from Diffraction Data*; Siemens Analytical X-ray Instruments, Inc.: Madison, WI, 2001.

52. Sheldrick, G. M. *SADABS 2001, Program for absorption correction using SMART CCD based on the method of Blessing*: R. H. Blessing, *Acta Crystallogr.* **1995**, *A51*, 33.
53. Lugscheider, W.; Pink, H.; Weber, K.; Zinn, W. *Zeitschrift fuer Angewandte Physik* **1970**, *30*, 36.
54. Shannon, R. D. *Acta Crystallogr.* **1976**, *A 32*, 751.
55. Brese, N. E.; Okeeffe, M. *Acta Cryst.* **1991**, *B47*, 192.
56. Wendlandt, W. W.; Hecht, H. G. *Reflectance Spectroscopy*. Interscience Publishers: New York, 1966.
57. Karunadasa, H.; Huang, Q.; Ueland, B. G.; Lynn, J. W.; Schiffer, P.; Regan, K. A.; Cava, R. J. *Phys. Rev. B* **2005**, *71*, 144414.
58. Doi, Y.; Nakamori, W.; Hinatsu, Y. *J. Phys. Condens. Matter* **2006**, *18*, 333.
59. Tromme, M. *C. R. Acad. Sci. Ser. C* **1971**, *273*, 849.
60. Sato, M.; Adachi, G.; Shiokawa, J. *Mater. Res. Bull.* **1984**, *19*, 1215.
61. Ohtani, T.; Honjo, H.; Wada, H. *Mater. Res. Bull.* **1987**, *22*, 829.
62. Schleid, T.; Lissner, F. *Eur. J. Solid State Inorg. Chem.* **1993**, *30*, 829.
63. Foran, B.; Lee, S.; Aronson, M. *Chem. Mater.* **1993**, *5*, 974.
64. Bronger, W.; Bruggemann, W.; von der Ahe, M.; Schmitz, D. *J. Alloys Compd.* **1993**, *200*, 205.
65. Bronger, W.; Eyck, J.; Kruse, K.; Schmitz, D. *Eur. J. Solid State Inorg. Chem.* **1996**, *33*, 213.
66. Sutorik, A. C.; Kanatzidis, M. G. *Chem. Mater.* **1997**, *9*, 387.
67. Deng, B.; Ellis, D. E.; Ibers, J. A. *Inorg. Chem.* **2002**, *41*, 5716.

68. Nitani, H.; Nakagawa, T.; Yananouchi, M.; Osuki, T.; Yuya, M.; Yamamoto, A. *Mater. Lett.* **2004**, *58*, 2076.
69. Shimizugawa, Y.; Sawaguchi, N.; Kawamura, K.; Hirao, K. *J. Appl. Phys.* **1997**, *81*, 6657.
70. Sarrao, J. L.; Immer, C. D.; Fisk, Z.; Booth, C. H.; Figueroa, E.; Lawrence, J. M.; Modler, R.; Cornelius, A. L.; Hundley, M. F.; Kwei, G. H.; Thompson, J. D.; Bridges, F. *Phys. Rev. B* **1999**, *59*, 6855.
71. Li, G. G.; Bridges, F.; Booth, C. H. *Phys. Rev. B* **1995**, *52*, 6332.

CHAPTER 10

SUMMARY

Syntheses and characterizations of new lanthanide chalcogenides have been discussed in Chapter 2 through Chapter 9. All these compounds were prepared by solid-state reactions of corresponding elements using alkali metal halides or Sb_2Q_3 ($\text{Q} = \text{S}, \text{Se}$) fluxes. Single crystal X-ray diffraction, UV-vis-NIR diffuse reflectance spectroscopy, magnetic susceptibility measurements, Mössbauer spectroscopy, and X-ray Absorption Near Edge Spectroscopy were used to determine their structures and physical properties. A list of new compounds and their crystallographic, magnetic, and optical properties are presented in Table 10.1a and Table 10.1b.

Chapter 2 and Chapter 3 report three ternary europium pnictogen chalcogenide compounds, $\text{Eu}_6\text{Sb}_6\text{S}_{17}$ and EuPnSe_3 ($\text{Pn} = \text{Sb}, \text{Bi}$). All of them have three-dimensional complex structures in a chiral space group. These compounds follow essentially Curie behavior from 300 K to 5 K, and undergo an apparently antiferromagnetic transition below 5 K. Magnetic susceptibility measurements and ^{151}Eu and ^{121}Sb Mössbauer spectroscopy studies have revealed the presence of divalent europium and trivalent antimony.

Chapters 4 to Chapter 6 discuss the synthesis of ternary interlanthanide chalcogenides using Sb_2Q_3 ($\text{Q} = \text{S}, \text{Se}$) fluxes. Structures and physical properties of these compounds depend highly on the choices of lanthanides and chalcogenides. They have

Table 10.1a. A list of new compounds and some of their properties, contained in this dissertation.

| Formula | Chapter | Space Group | Magnetism | Color/Band Gap (eV) |
|---|---------|--------------|--------------------|---------------------|
| $\text{Eu}_6\text{Sb}_6\text{S}_{17}$ | 2 | $P2_12_12_1$ | Antiferromagnetism | Black/N/A |
| EuPnSe_3 (Pn = Sb, Bi) | 3 | $P2_12_12_1$ | Antiferromagnetism | Black/N/A |
| $\gamma\text{-LaLn}'\text{S}_3$ (Ln' = Er, Tm, Yb) | 4 | $Pnma$ | Paramagnetism | Dark Red/1.6 |
| $\gamma\text{-CeLn}'\text{S}_3$ (Ln' = Er, Tm, Yb) | 4 | $Pnma$ | Paramagnetism | Black/1.3 |
| $\delta\text{-Ce}_{1.30}\text{Lu}_{0.70}\text{S}_3$ | 5 | $P2_1/m$ | Paramagnetism | Black/1.25 |
| $\delta\text{-Pr}_{1.29}\text{Lu}_{0.71}\text{S}_3$ | 5 | $P2_1/m$ | Paramagnetism | Dark Red/1.38 |
| $\delta\text{-Nd}_{1.33}\text{Lu}_{0.67}\text{S}_3$ | 5 | $P2_1/m$ | Paramagnetism | Dark Red/1.50 |
| La_3LuSe_6 | 6 | $Pnnm$ | Diamagnetism | Black/1.26 |
| Ce_3LuSe_6 | 6 | $Pnnm$ | Ferromagnetism | Black/1.10 |
| $\beta\text{-PrLuSe}_3$ | 6 | $Cmcm$ | Paramagnetism | Black/1.56 |

Table 10.1b. A list of new compounds and some of their properties, contained in this dissertation.

| Formula | Chapter | Space Group | Magnetism | Color/Band Gap (eV) |
|---|---------|-------------------------|----------------------------|---------------------------------|
| β -NdLuSe ₃ | 6 | <i>Cmcm</i> | Paramagnetism | Black/1.61 |
| Sm _{1.82} Lu _{2.18} Se ₆ | 6 | <i>P2₁/m</i> | van Vleck Paramagnetism | Black/1.51 |
| Gd _{1.87} Lu _{2.13} Se ₆ | 6 | <i>P2₁/m</i> | Antiferromagnetism | Black/1.56 |
| Ln ₂ YbCuS ₅ (Ln = La, Ce, Pr, Nd) | 8 | <i>Pnma</i> | Paramagnetism | Black/1.45, 1.37, 1.25, 1.35 |
| Sm ₂ YbCuQ ₅ | 8 | <i>Pnma</i> | Spin Glass? | Black/1.28 |
| Ln ₂ YbCuSe ₅ (Ln = La, Ce) | 8 | <i>Pnma</i> | Paramagnetism | Black/1.05, 1.15 |
| Cs _x Ln _y YbS ₂ (Ln = La, Pr, Nd, Sm) | 9 | <i>P6₃/m</i> | Paramagnetism | Yellow/2.3 |
| Cs _{0.14} Ce _{0.30} YbS ₂ | 9 | <i>P6₃/m</i> | Paramagnetism | Red/2.1 |
| Cs _x Ln _y YbS ₂ (Ln = Gd, Tb, Dy) | 9 | <i>P6₃/m</i> | Paramagnetism | Brown/2.3-2.4 |
| Cs _x Ln _y YbS ₂ (Ln = Ho, Er, Tm) | 9 | <i>P6₃/m</i> | Paramagnetism | Brown/2.2 |
| Ln ₂ YbCuS ₅ (Ln = La, Ce, Pr, Nd) | 8 | <i>Pnma</i> | Paramagnetism | Black/1.45, 1.37, 1.25, 1.35 |

shown a variety of structures including ordered and disordered types under different reaction conditions. Most of compounds are semiconductors with wide tunable band gaps. Different magnetic behaviors have been found in these systems, namely Curie-Weiss type paramagnetism, van Vleck paramagnetism, antiferromagnetism, ferromagnetism, and spin glass performance. Possible spin-frustrations in some of these interlanthanide compounds were also discussed.

Chapter 7 presents the first two partially ordered quaternary interlanthanide sulfides $\text{PrLnYb}_2\text{S}_6$ ($\text{Ln} = \text{Tb}, \text{Dy}$). They were prepared using intermediate lanthanides to substitute in the disordered sites in already known ternary $\text{F-Ln}_2\text{S}_3$ type structures. The elemental analysis and magnetic susceptibility measurements are consistent with the proposed formula.

In Chapter 8, a new series of ordered quaternary interlanthanide copper chalcogenides, $\text{Ln}_2\text{YbCuQ}_5$ ($\text{Ln} = \text{La}, \text{Ce}, \text{Pr}, \text{Nd}, \text{Sm}$; $\text{Q} = \text{S}, \text{Se}$) are reported. These compounds crystallize in a new structure type that is realized by including two different lanthanides with large size difference, which tend to have distinct coordination environments. Magnetic measurements have shown that $\text{Ce}_2\text{YbCuSe}_5$, $\text{La}_2\text{YbCuS}_5$, $\text{Ce}_2\text{YbCuS}_5$, and $\text{Pr}_2\text{YbCuS}_5$ are Curie-Weiss paramagnets. $\text{La}_2\text{YbCuSe}_5$ and $\text{Nd}_2\text{YbCuS}_5$ have short-range antiferromagnetic ordering at low temperature. $\text{Sm}_2\text{YbCuS}_5$ exhibits an interesting magnetic transition below 7 K. The UV-vis-NIR diffuse reflectance measurements show these compounds to be wide band-gap semiconductors.

Finally, Chapter 9 encloses a new family of interlanthanide sulfide, $\text{Cs}_x\text{Ln}_y\text{YbS}_2$ ($x = 0.14 - 0.16$; $\text{Ln} = \text{La-Nd}, \text{Sm-Yb}$; $y = 0.26 - 0.33$). These compounds are partially-filled mixed-lanthanide variants of the $\text{K}_2\text{Tm}_{23.33}\text{S}_{36}$ structure-type. In all but one of these

compounds the magnetic interactions are antiferromagnetic in nature. However, in $\text{Cs}_{0.15}\text{Tb}_{0.29}\text{YbS}_2$ the coupling is ferromagnetic. The trivalency of all lanthanides for $\text{Cs}_{0.14}\text{Ce}_{0.30}\text{YbS}_2$, $\text{Cs}_{0.14}\text{Nd}_{0.29}\text{YbS}_2$, and $\text{Cs}_{0.15}\text{Sm}_{0.29}\text{YbS}_2$ have been confirmed by XANES measurements. The band gaps for these compounds are relatively constant except for the Ce analog, which possesses a notably smaller gap than the other compounds. Possible spin-frustrations in these interlanthanide compounds were also examined.